SISSA
Scuola
Internazionale
Superiore di
Studi Avanzati

Physics Area - PhD course in
Astroparticle Physics

The strong gravitational field regime of compact objects beyond General Relativity

Candidate:
José Guillermo
Lara Delgado

Advisor:
Enrico Barausse

Academic Year 2021-22

Abstract

The maturity of experimental probes of the strong field regime of gravity, both in terms of sensitivity and number of observations, offers hope in discriminating General Relativity (GR) from alternative theories of gravity in the near future. At present, such probes include gravitational-wave observations with ground-based interferometers, 1.3 mm electromagnetic observations with Very-Large-Baseline Interferometry (VLBI) and binary pulsar observations. For these, a prominent role is played by compact objects, which source strong (and in some cases highly dynamical) gravitational fields, and therefore make up the main target of such observations. Most efforts so far have focused on computing strong field predictions for compact objects in GR. However, if one aims to fairly discriminate among them, the same predictions need to be obtained for theories beyond GR.

The purpose of this Thesis is to explore various aspects of compact objects in theories beyond GR where strong gravitational fields are relevant.

We begin by studying k-essence, a scalar-tensor theory motivated as a viable dynamical explanation for Dark Energy. Derivative self-interactions provide (through a kinetic screening mechanism) the suppression of the extra scalar force needed to satisfy local gravitational constraints. We first explore ways to ensure that the theory admits a well-posed initial-value problem, a mathematical property that is essential for obtaining predictions in the strong field with numerical relativity. We then show how some of the lessons learned for k-essence can also be applied to self-interacting massive vector theories. In addition, we explore the resilience of kinetic screening with different possibilities in which the scalar can couple to the matter sector.

We then turn our attention to the question of whether gravity can be constrained with black hole images from VLBI, and whether this can be done in spite of uncertainties in the astrophysical modelling of the system. We present a proof-of-principle demonstration of a theory-agnostic framework to reconstruct simultaneously both the underlying geometry and accretion behind these images. Our framework makes use of a general parametrization for these properties and of a Principal Component Analysis to mitigate the degeneracies linked to the presence of a large number of parameters.

Finally, we consider the question of whether quantum gravity can provide a resolution to the issue of singularities inside black holes. We do so in the context of (2+1) projectable Hořava gravity, a Lorentz-violating quantum gravity candidate that has been shown to be renormalizable (beyond power counting) and ultraviolet complete. We obtain all circularly-symmetric stationary solutions and show that, in spite of naive expectations, solutions that reduce to BHs at low-energies remain singular in the interior.

Acknowledgements

This Thesis would not have been possible without the support of many people.

First and foremost, I would like to thank my advisor Enrico Barausse for his helpful and patient guidance as well as for enthusiastically suggesting many interesting collaborations and projects in a broad range of topics.

I would like to thank my collaborators, Enrico Barausse, Miguel Bezares, Marco Crisostomi, Mario Herrero-Valea, Sergey Sibiryakov and Sebastian Völkel for teaching a great deal of physics. Special thanks go to Miguel for thoroughly and very patiently introducing me to the field of Numerical Relativity. People in the GRAMS group, Mateja Boskovic, Alexandru Dima, Nicola Franchini, Aron Kovacs, Sourabh Nampalliwar, Marcelo Rubio, Lotte ter Haar, and also Jaumila Gonzalez. I would also like to thank the people with whom we had interesting discussions or gave insightful comments and information on the work presented here, Miguel Bezares, Nicola Franchini, Lotte ter Haar, Marco Crisostomi, Luis Lehner, Carlos Palenzuela, Avery Broderick, Boris Georgiev, Luciano Rezzolla, Maciek Wielgus, Stefano Liberati and S. Solodukhin. To my mentors and teachers throughout the years, Alexandra Velázquez, Eric Vázquez-Jáuregui, Alejandro Ayala, Jerónimo Cortez and Paolo Creminelli. As well as people in the physics community who have supported me and with whom I have enjoyed talking about physics, Julián Rey, Vicharit Yingcharoenrat, Mehrdad Mirbabayi and Fernando Quevedo.

I am deeply grateful to my family for their unwavering support. I love you. I dedicate this thesis to the memory of my grandfather, Pedro Delgado, who gifted me a little book on Astronomy that talked about strange objects called Black Holes. Thank you for supporting me to follow my dreams.

I am also very grateful to my friends in Trieste, Miguel and Ani, Nicola, Lotte, Sebastian, Paola and Uriel. My dance partners and friends from *The Swing Freaks*, Francesca, Nadia and Jean, Marco and Alessia. And elsewhere, Samantha, Nastia, Pedro, Santiago, Julián, Rodrigo, Jessica P., Jessica V., Alan and David. Thank you Francesca and Nicola for making our apartment a warm place I could call home. Also many thanks to my officemates, Lotte, Alessandro, Miguel, Oleg and Mateja. And to the SISSA Student Secretariat, Marco and Riccardo for helping me many may times to get through the bureaucracy in a foreign country. And to the many wonderful people I have met during my time in Trieste. I am also grateful to the essential workers that allowed me to continue doing science during the toughest times in the COVID-19 pandemic.

Finally, I would like to thank the Abdus Salam International Centre for Theoretical Physics (ICTP) for hospitality during the duration of my studies, and the Perimeter Institute for Theoretical Physics for hospitality during my stay in

May 2022.

Contents

Preface

The year 2015 saw a landmark achievement in experimental physics and astronomy. Gravitational waves (GWs), originating from the cataclysmic coalescence of two black holes (BHs) roughly 1.4 billion light years away from Earth, were detected for the first time by ground-based GW interferometers of the LIGO-Virgo Collaboration [1]. Although General Relativity (GR) had long predicted that the merger of stellar-mass compact objects would produce such ripples in the fabric of spacetime, a massive theoretical and experimental effort (spanning almost a century), was needed to provide the final confirmation of their existence –the first indirect evidence was observed in the Hulse-Taylor binary pulsar system [2, 3]. Since then, GW observations have become routine in the newborn field of GW astronomy, allowing for unprecedented tests of strong and highly dynamical gravity, as well as on the astrophysics of compact objects –see e.g. Refs. [4–8].

Meanwhile, another experimental breakthrough occurred in the field of radio astronomy. During the spring of 2017, a global observation campaign by eight radio observatories scattered across the Earth, grouped under the Event Horizon Telescope (EHT) Collaboration, led to the first high-resolution images of the supermassive black hole (SMBH) at the center of the neighbouring galaxy M87, and of our own galaxy, the Milky Way [9, 10]. These new electromagnetic observations open up the possibility to test the strong lensing predictions of GR, astrophysical BH environment models, and possibly, the nature of the underlying compact objects behind these images –see e.g. Refs. [11–13].

Although these novel observations can (so far) all be explained within the framework of GR, there are a number of reasons to look *beyond*. From the experimental side, cosmological observations have uncovered the existence of a new dark sector. Dark Matter accounts for the missing matter content of the Universe, whereas Dark Energy is responsible for the accelerated expansion of the Universe. In particular, efforts to provide a dynamical explanation for the latter have led to the development of a large family of new theories beyond GR, among which are scalar-tensor theories.

From the theoretical side, the quantum revolution that happened in parallel to the development of modern gravitational physics supports the view that

GR may only be the leading-order approximation to a (yet unknown) full theory of Quantum Gravity (QG). Among prominent candidates (such as String Theory), a relatively recent proposal is Hořava gravity [14], a theory that aims to enforce renormalizability by introducing higher order spatial-derivative terms, which break Local Lorentz Invariance.

In order to fully exploit the potential to uncover new fundamental physics from these new kinds of gravitational and electromagnetic observations, accurate theoretical predictions for the strong (and highly-dynamical) gravitational fields around compact objects are needed. For General Relativity, a half-century-long effort to compute these predictions has led, for instance, to the development of sophisticated tools in Numerical Relativity and Magneto-hydrodynamics –both of which have become ubiquitous in the analysis of current experimental data. However, the strong, highly-dynamical and nonlinear regime in alternatives to GR remains vastly unexplored. New phenomena waiting to be fully studied include new scalarized compact objects, new gravitational polarizations and nonlinear screening mechanisms.

Indeed there is a *pressing* need to do so. For GW astronomy, the foreseeable future promises it to become a *data-rich* field. For instance, after major upgrades, the next observation run (O4) of the LIGO, Virgo and Kagra detectors will start next year (2023). Third-generation GW observatories, such as the Einstein Telescope [1] and Cosmic Explorer [2], have also been planned for the future. And the Laser Interferometer Space Antenna (LISA) [3] [15], a space-borne GW observatory, which will be sensitive to an almost entirely different range of sources, will be commissioned in about a decade. For electromagnetic observations with VLBI, improved observation campaigns are planned under the next-generation Event Horizon Telescope (ngEHT) [4]. Finally, binary pulsar observations continue delivering measurements with increasing precision [16].

So, *which* theories should one study in the strong field regime? There are a number of guides, both experimental and theoretical, one could use to focus efforts. One example of an experimental guide is the observation of the coincident arrival of the GW signal and short gamma-ray burst originating from the neutron star binary merger GW170817 [17], which allowed to determine that GWs travel at the speed of light to an astounding precision [18]. We will see in Part I that the number of Dark Energy models consistent with this observation has already been greatly reduced. As for the theoretical guides, one could use requirements on the mathematical/physical consistency of the theory. For instance, one could seek for

[1] http://www.et-gw.eu/
[2] http://cosmicexplorer.org/
[3] https://www.elisascience.org/
[4] https://www.ngeht.org/

compatibility at multiple scales (e.g. Dark Energy models or QG theories should also be compatible with Solar System scale physics), or require that the theory admits a well-posed initial-value problem [19] (such that solutions are unique and smooth with respect the boundary conditions). In this Thesis we explore a number of alternative theories of GR guided by some of these requirements.

This Thesis is organized as follows. We begin in Part I with some brief contextual background for the rest of the Thesis. In Part II, we focus on k-essence, a self-interacting scalar tensor theory motivated as a dynamical explanation to Dark Energy. In particular, in Chapter 2 we investigate ways to obtain a well-posed initial value problem in this theory. In Chapter 3, we comment on the applications of the tools developed for k-essence to theories involving massive vector fields. Towards the end of this Part, in Chapter 4, we investigate whether the mechanism necessary to shield local scales from additional scalar forces (known as kinetic screening) prevails when the coupling to matter is generalized. In Part III, we look at the inverse problem of BH imaging, and how to mitigate the impact of uncertainty in the details of the astrophysical environment. Finally, in Part IV, we explore whether projectable Hořava gravity, a candidate for a full theory of QG, can help resolve singularities inside BHs. We conclude in Part V. Additional technical details are provided in Appendices A, B, C, D and E.

List of Publications

The research presented in this Thesis is the product of my work, as well as work done within the scientific collaborations detailed below. This Thesis contains material included in the following publications:

Part II:

1. Guillermo Lara, Miguel Bezares, and Enrico Barausse, "UV completions, fixing the equations, and nonlinearities in k-essence", Phys. Rev. D 105, 064058, arXiv: 2112.09186.
2. Enrico Barausse, Miguel Bezares, Marco Crisostomi, and Guillermo Lara, "The well-posedness of the Cauchy problem for self-interacting vector fields", arXiv:2207.00443.
3. Guillermo Lara, Marco Crisostomi, Miguel Bezares, and Enrico Barausse, "Robustness of kinetic screening against matter coupling", Phys. Rev. D *(in review)*, arXiv: 2207.03437.

Part III:

4. Guillermo Lara, Sebastian H. Völkel, and Enrico Barausse, "Separating astrophysics and geometry in black hole images", Phys. Rev. D 104, 124041, arXiv: 2110.00026.

Part IV:

5. Guillermo Lara, Mario Herrero-Valea, Enrico Barausse, and Sergey M. Sibiryakov, "Black holes in ultraviolet-complete Hořava gravity", Phys. Rev. D 103, 104007, arXiv: 2103.01975.

Part I

Preliminaries

Chapter 1

The nature of gravity

In this Chapter we give an overview of different possible descriptions of gravity. Various classifications of alternative theories of gravity have been given in the literature, e.g. in terms of the fundamental assumptions that they break (with respect to uniqueness theorems such as Lovelock's theorem [20, 21]), or depending on the number and type of additional fields they include (with respect to the spin-2 field describing the metric) –see e.g. Refs. [22, 23]. In the following we will not attempt to describe all of them and will mainly discuss those that are of direct relevance for this Thesis.

We start off this Chapter with GR and list few of its most important consequences, from the existence of BHs to the prediction of GWs. We then, in Sec. 1.2, we turn our attention to scalar-tensor theories, with particular emphasis on those that provide a dynamical explanation to Dark Energy, and among which we highlight k-essence. Next, in Sec. 1.3, we briefly present theories that break Local Lorentz Invariance by incorporating a preferred frame. In particular, a subset of these theories can be understood as the low-energy limit of a theory of QG known as Hořava gravity. In Sec. 1.4, we briefly describe how to capture the effects of many different possible descriptions all at once with theory-independent parametrizations of gravity. Finally, at the end of this Chapter (Sec. 1.5), we briefly summarize current tests of gravity. Throughout this Chapter, and unless otherwise stated, we use units in which $c = 1$ and $-+++$ metric signature.

1.1 The standard theory of gravitation

The General Theory of Relativity [24] (or General Relativity for short) was devised by Albert Einstein between the years 1905 and 1915, as a generalization of Special Relativity [25] and in an attempt to reconcile the Equivalence Principle with gravitational phenomena. The Equivalence Principle can be formulated in many different flavors and forms. In particular, the Einstein Equivalence Principle

(EEP) encompasses the universality of free fall (also called the Weak Equivalence Principle) and the requirement that the non-gravitational laws of physics are the same in any (freely falling) frame of reference used to describe them. Whereas, the Strong Equivalence Principle essentially generalizes the EEP to include also gravitational interactions. When describing gravity in terms of an action, some of these properties can be included through *diffeomorphism-invariance* [i.e. invariance under arbitrary changes of coordinates $x^\mu \to \tilde{x}^\mu \equiv f^\mu(x^\alpha)$], and through the "universal coupling" of the metric $g_{\mu\nu}$ with the additional matter and gauge fields Ψ_m in the Standard Model of Particle Physics –see Ref. [26] for a more detailed discussion of the formulations of the Equivalence Principle.

General Relativity can be summarized in the Einstein-Hilbert action [1] [27]

$$S\left[g_{\mu\nu}, \Psi_m\right] = \int d^4x \, \frac{\sqrt{-g}}{2\kappa} \, R + S_m\left[g_{\mu\nu}, \Psi_m\right] \ , \tag{1.1}$$

where $\kappa = 8\pi G$, G is the Newton constant, $R_{\mu\nu}$ is the Ricci tensor with trace $R \equiv g^{\mu\nu} R_{\mu\nu}$, and $g \equiv \det(g_{\mu\nu})$. Variation of action (1.1) with respect to the metric yields Einstein field equations,

$$G_{\mu\nu} = \kappa \, T_{\mu\nu} \ , \tag{1.2}$$

where $G_{\mu\nu} \equiv R_{\mu\nu} - (R/2) g_{\mu\nu}$ is the Einstein tensor, and

$$T^{\mu\nu} \equiv \frac{2}{\sqrt{-g}} \frac{\delta S_m}{\delta g_{\mu\nu}} \ , \tag{1.3}$$

is the stress-energy tensor of matter. While the (contracted) Bianchi Identity yields $\nabla_\mu T^{\mu\nu} = 0$, i.e. the conservation of the stress-energy tensor.

Among the early achievements of General Relativity are the recovery of the known results by the Newtonian theory of gravitation [28], for instance, the reconcilement of the perihelion advance of Mercury and the prediction of the bending of light by massive bodies such as the Sun [26]. In the following, we highlight a few of the most relevant concepts and results for this Thesis.

1.1.1 Black holes and the Kerr hypothesis

One of the most startling consequences of GR is the prediction of the existence of *black holes*. These are regions of warped spacetime characterized by the presence of an *event horizon* [2], which is a causal barrier separating a region of spacetime

[1] We take the view that the cosmological constant enters the right-hand-side of Einstein field equations (1.2) as $T_{\mu\nu} = -\Lambda g_{\mu\nu} + \cdots$.

[2] Several definitions of black hole horizons find utility in different applications, among them are *apparent* horizons, which are defined as the boundary of the trapped region of outgoing null

(the interior of the BH) from the future of all outgoing null rays –see e.g. Ref. [30]. This for instance would make it impossible for a space probe entering a BH to transmit any information about potential measurements to physicists on Earth.

After decades of debate, today it is established that BHs are physical and that they are commonly present throughout the Universe. For instance, stellar-mass BHs can form directly from the core collapse of massive stars once they have exhausted their nuclear fuel, whereas binary BHs can form by evolving through a common envelope phase or through dynamical encounters [31]. Supermassive BHs (SMBHs), on the other hand, are thought to reside at the core of most galaxies [32], and have achieved their large masses mainly through accretion, with several possible mechanisms behind their original seeds [33]. The radiation from hot accretion gas in their environments and the gravitational effects on nearby stars make it possible to study them with electromagnetic probes, from the radio band to X-rays [31]. And since 2015, stellar-mass BH binaries are commonly observed with gravitational wave observations [34].

Form the theoretical point of view, BHs also provide rich playgrounds. During the '70s, it was realized that there is a deep connection between BH horizons and the laws of thermodynamics, and that BHs should posses both temperature and entropy [35, 36]. Moreover, it was realized that they should *radiate* (thermally) by emitting Hawking radiation [37]. In the interior of BHs, it has been shown that the formation of curvature *singularities*, and thus the breakdown of GR, is an inevitable consequence of Einstein equations –and a number of reasonable assumptions [38].

BH (vacuum) spacetimes can be found by solving Einstein field equations [Eq. (1.2)] with $T_{\mu\nu} \equiv 0$. Despite the highly nonlinear nature of these equations, analytical solutions have been obtained with the aid of symmetry assumptions. The first solution for a nonrotating BH spacetime was found in 1916 by Karl Schwarzschild [39], merely a year after Einstein arrived to the final form of Eq. (1.2). The solution for a rotating BH spacetime was found by Kerr in 1963 [40]. In Boyer-Lindquist coordinates (t, r, θ, ϕ) (and in $G = 1$ units), the Kerr metric is given by [41]

$$ds^2 = -\Big(1 - \frac{2Mr}{\rho^2}\Big)dt^2 - \frac{4aMr\sin^2\theta}{\rho^2}dtd\phi + \frac{\rho^2}{\Delta}dr^2 + \rho^2 d\theta^2 + \Big(r^2 + a^2 + \frac{2a^2Mr\sin^2\theta}{\rho^2}\Big)\sin^2\theta d\phi^2\,, \quad (1.4)$$

where M is the mass of the BH, a is the spin parameter, $\Delta \equiv r^2 - 2Mr + a^2$, and $\rho^2 \equiv r^2 + a^2\cos^2\theta$. The Schwarzschild metric can be obtained as a particular

rays –see e.g. Ref. [29] for more details. We will encounter the latter in Ch. 2.

solution of Eq. (1.4) when $a = 0$.

The exterior spacetime of astrophysical BHs, in vacuum and at a sufficiently long time after formation, are believed to be described by the Kerr metric [3] [Eq. (1.4)]. This expectation is usually called the *Kerr hypothesis*, and is based upon a series of results demonstrating the uniqueness and robustness of the Kerr metric [43–45]. It paints BHs as remarkably simple objects, described only by their mass M and spin a. Moreover, the oscillation frequencies of small perturbations of this spacetime, known as *quasinormal modes* (QNMs), are also described by these two parameters [46].

1.1.2 Neutron stars

Towards the end of their lifetime, the most massive stars [4] usually leave behind BH remnants, whereas for stars with more moderate masses, other possible endpoints are the formation of neutron star (NS) and white dwarf (WD) remnants.

First proposed by Baade and Zwicky in 1934 [47], NSs are among the most compact objects thought to exist within the physics of action (1.1). If we define the compactness $\mathcal{C} \equiv GM/R$ [48, 49], where M is the mass of the star and R is its radius, neutron stars have $\mathcal{C} \sim 0.3$ –for comparison, a non-rotating BH has compactness $\mathcal{C} = 1/2$, whereas a main-sequence star like the Sun has $\mathcal{C} \sim 10^{-6}$.

Moreover, strongly magnetized NSs may emit electromagnetic radiation along jets which may not be aligned with the rotation axis, as thus it would appear to an observer as a source of pulsating bursts of radiation. In this way, *pulsars* can act as cosmic "lighthouses". The first known pulsar was discovered in 1967 by J. Bell-Burnell, working with A. Hewish, and the connection with NSs was made until further pulsars were observed [50, 51]. Today, the fastest known millisecond pulsar has an observed frequency of $\sim 0.7\,\mathrm{kHz}$ [52].

For our purposes, NSs can be approximately described as a perfect fluid,

$$T_{\mu\nu} \equiv [\rho_0 (1 + \epsilon) + P]\, u_\mu u_\nu + P g_{\mu\nu} \ , \tag{1.5}$$

where u^μ is the 4-velocity of the fluid, and $\{\rho_0, \epsilon, P\}$ are macroscopic thermodynamic variables: the rest-mass density, internal energy density, and pressure, respectively. In this way, the nuclear physics processes describing the interior of these objects are parameterized in terms of an *equation of state* (EOS) relating the different thermodynamical variables. Many models have been proposed to

[3] Although the Kerr-Newman spacetime [42] generalizes the Kerr metric to BHs with electric charge, it is widely believed that astrophysical BHs are mostly neutral.

[4] For stars with $50\,M_\odot \lesssim M \lesssim 120\,M_\odot$, the formation antimatter inside the star and which may lead to a catastrophic destruction of the star (through a pair-instability supernova) before it fully collapses. This process may thus give rise to a pair-instability mass gap [31].

describe the EOS, with varying levels of detail, and each of them can provide different predictions for the observables, e.g. mass-radius relations, tidal Love numbers, oscillation modes, etc. –however, universal relations among them may be found, see e.g. Ref. [53]. Among the simplest of these is the family of polytropic EOS, for which a simple relation is assumed to hold between the thermodynamic variables. Namely, $P \propto \rho_0^{\Gamma}$, where Γ is called the adiabatic index. Due to their simplicity, we will use this type of EOS in Ch. 4 to study neutron stars in gravity beyond GR.

Once neutron star matter is modelled in this way, stationary solutions in spherical symmetry can be obtained by solving the Tolman-Oppenheimer-Volkoff (TOV) equations [54]. The latter are a set of ordinary-differential-equations, written in schematic form as $\partial_r \boldsymbol{U} = \boldsymbol{V}[\boldsymbol{U}, r]$, where $\boldsymbol{U}$ is a vector containing the relevant gravitational and thermodynamical variables –e.g. the pressure and (derivatives of) the metric functions. Different properties may be studied with the solutions of these equations. For instance, both stable and unstable families of NSs with different mass-radius relations can be constructed. Stable stars are robust under small perturbations of the energy density, whereas unstable stars migrate to a stable solution or collapse to a BH. Furthermore, EOS-dependent predictions for the maximum mass of (non-rotating) NS can be obtained in this way –see e.g. Ref. [55]. Away from spherical symmetry, generalizations to spinning NSs in axisymmetry and NS binary mergers, with their associated observables, have also been studied –see e.g. Ref. [51].

1.1.3 The standard model of Cosmology

Another great success of GR has been the description of the Universe on its largest scales. Guided by the observation of the homogeneous and isotropic nature of the Universe and the recession of faraway galaxies, the spacetime of the Universe (as a whole) can be approximated by the Friedmann-Lemaitre-Robertson-Walker (FLRW) metric [5]

$$ds^2 = -dt^2 + a\,(t)^2\,\delta_{ij} dx^i dx^j \ , \tag{1.6}$$

where x^i are the spatial coordinates, δ_{ij} is the Kronecker delta, and the dynamics of expansion parameter $a(t)$ can be found by solving Einstein field equations (1.2), with $T_{\mu\nu}$ being replaced by a homogeneous and isotropic mix of the contents of the Universe. The rate of the expansion of the Universe is described by the *Hubble*

[5] We write for simplicity the *flat* FLRW metric, as curvature makes less than one percent of the energy budget of the Universe [56].

parameter, $H \equiv d\log a/dt$, and its present value is [6] $H_0 = 67.32\,\mathrm{km\,s^{-1}\,Mpc^{-1}}$ [58].

In brief, the current standard paradigm in Cosmology is the ΛCDM model (where CDM stands for Cold Dark Matter), which makes use of Eq. (1.6) (and perturbations around it) and identifies, in addition to neutral baryonic matter (nuclei and electrons) and radiation (photons and neutrinos), a non-zero contribution of cold *Dark Matter* (up to $\sim 27\%$ of the energy budget of the Universe) and *Dark Energy* (up to $\sim 68\%$ of the energy budget of the Universe) [56]. In particular, the latter describes the current phase of *accelerated* expansion of the Universe (first observed in supenovae Type IA measurements [59, 60]) and is a component that behaves like the energy density of the vacuum (with EOS given by $P = -\rho$), e.g. the behavior of the *Cosmological Constant* Λ. Precise measurements of the Cosmic Microwave Background (CMB) radiation, the afterglow radiation of the Big Bang formed when photons decoupled from the primordial plasma, have played a key role in determining this composition of the Universe.

The cosmological evolution of the Universe also provides an interesting playground for theoretical physics, and the puzzles it poses may yield a window to new fundamental physics. As the history of the Universe is rewinded back in time, and as the Universe becomes increasingly dense, GR predicts inevitably (under certain assumptions) a singularity at the beginning of time [61]. As with the singularities inside BHs, the description given by GR breaks down and QG effects are expected to become important [61]. Furthermore, it is widely believed that the peculiar initial conditions of the ΛCDM model, in particular homogeneity, are a consequence of an early epoch of accelerated expansion called *inflation* [62]. Moreover, this epoch predicts a signature imprinted in the GW background radiation [63]. Finally, as we will see in Sec. 1.2, the search for a dynamical explanation for Dark Energy has prompted the development of a large family of scalar-theories of gravity.

1.1.4 Gravitational waves

Gravitational waves (GWs) are ripples in the fabric of spacetime, first predicted by Einstein in 1916 [64, 65]. For a long time, however, physicists were confused on whether these type of waves were actually physical [66].

In vacuum flat space, (the linearized) Einstein field equations (1.2) imply that GWs, follow the wave equation

$$\Box h^{\mathrm{TT}}_{\mu\nu} = 0\ , \tag{1.7}$$

[6] There is, however, and ongoing debate over a tension ($\sim 4\sigma - 6\sigma$ disagreement) between the early and late time measurements of H_0 –for a review, see Ref. [57].

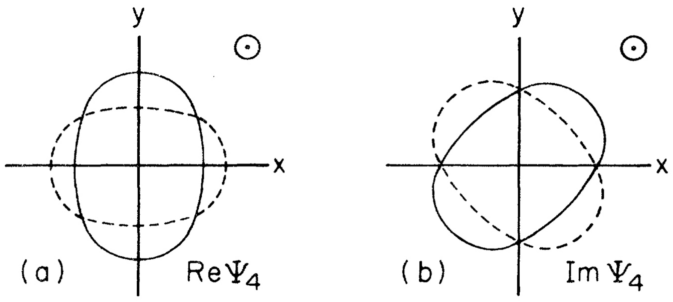

Figure 1.1: *Gravitational wave polarizations.* The effect of the two GW polarizations, + ("plus") on panel (a) and × ("cross") on panel (b), is illustrated on the effect it produces on a ring of test particles. Here, the plane GW travels in the z-direction, perpendicular to the plane of the Figure. In the Newman-Penrose formalism [68] each polarization is associated to the real and imaginary parts of the Ψ_4 projection of the Riemann tensor. Taken from Eardley, *et al* [69].

where $h^{\rm TT}_{\mu\nu}$ is the metric perturbation $h_{\mu\nu} \equiv g_{\mu\nu} - \eta_{\mu\nu}$ written in the transverse-traceless (TT) gauge (defined by $h^{0\mu} = h^i{}_i = \partial^i h_{ij} = 0$), the (background) Minkowski space metric is $\eta_{\mu\nu}$, and $\Box \equiv \eta^{\mu\nu}\partial_\mu\partial_\nu$ is the wave operator in flat space. GWs come in two polarizations, + ("plus") and × ("cross"), corresponding to the two propagating degrees of freedom of GR. Each of these polarizations exhibits a compress and stretch pattern in the spacetime between test masses [67] –see Fig. 1.1. For an L-shaped gravitational wave (Michelson) interferometer, the compress and stretch pattern translates into difference in the optical path followed by laser beams in each arm. When the beams are recombined, the resulting phase difference between the beams produces an interference pattern and a measurable EM power variation at a photodetector. Among different detection pipelines, the GW signal can be compared with theoretical templates through *match filtering* –and offline for parameter estimation [67].

The earliest experimental indication of the existence of GWs came in 1974 from the observation of orbital variation, due to energy lost in GWs, of the Hulse-Taylor binary pulsar system [26]. However, it took nearly a century until GWs, originating from a binary black hole merger (GW150914), were first detected directly by the LIGO-Virgo Collaboration [1].

Currently observed sources include merging compact binary BH systems with masses up to $\sim 100\,M_\odot$, binary NS systems, and mixed BN-NS systems, with gravitational wave frequencies $\sim 100\,$Hz [70]. Nevertheless, there exist many other potential sources waiting to be discovered such as supernovae [71] and continuous sources from neutron stars [72]. In the LISA band ($\sim 10^{-3}\,$Hz), expected sources include massive BH binaries (with component masses $\sim (10^3 - 10^7)\,M_\odot$) and extreme-mass-ratio inspirals (EMRIs) –where the latter correspond to compact

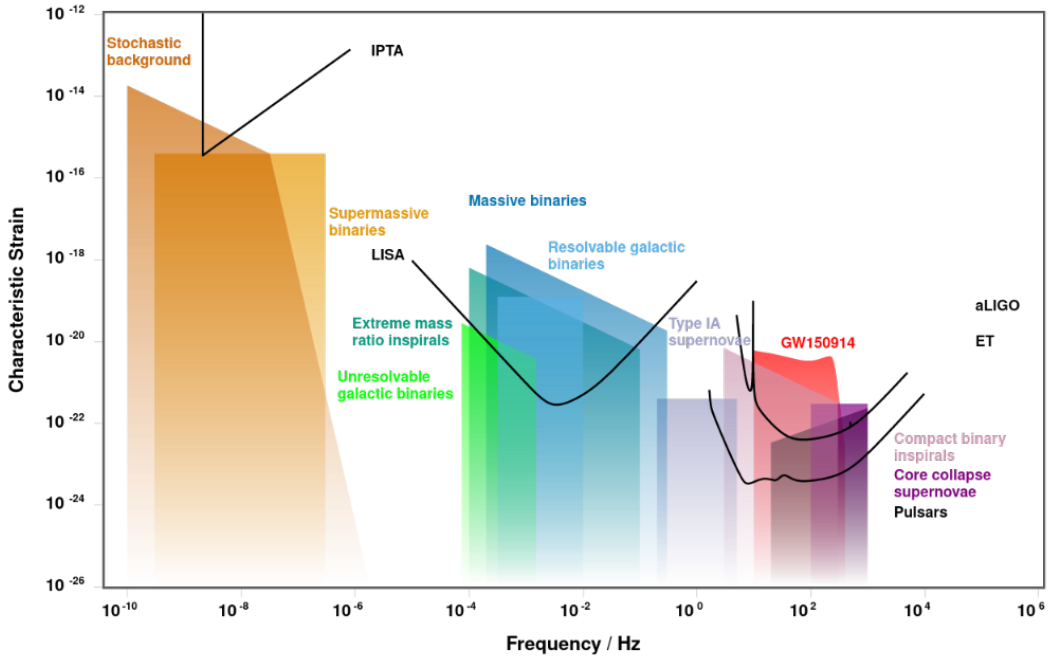

Figure 1.2: *Gravitational wave sources and detectability.* Solid color regions illustrate sources of GWs with their characteristic strain and frequency ranges. For comparison, the sensitivity curves for various current and future observatories are included. From left to right, the International Pulsar Timing Array (IPTA), the Laser Interferometer Space Antenna (LISA), Einstein Telescope (ET) and the Advanced LIGO observatories. Produced with the software in Ref. [76].

object binaries with mass ratios $q \sim 10^{-7} - 10^{-5}$ [73, 74]. And finally, in the pulsar timing-array (PTA) band ($\sim 10^{-9}$ Hz), a potential source is the stochastic GW background [75]. Further sources are illustrated in Fig. 1.2.

1.2 Scalar-tensor theories

Scalar-tensor theories postulate the existence of a dynamical scalar degree of freedom in addition to the tensor degrees of freedom of the metric, the latter corresponding to the two GW polarizations. They are useful in providing a dynamical explanation to Dark Energy, and thus to the accelerated expansion of the Universe. Such scalar fields have proven to be useful in other areas. For instance, the inflationary period in Cosmology is driven by the dynamics of the inflaton [56], and in particle physics, the Higgs boson is associated to the mechanism that provides the masses to quarks and leptons [77].

1.2.1 Horndeski theory

The most general scalar-tensor theory with second-order equations of motion (as to avoid Ostrogradski instabilities [78]), is known as Horndeski theory [79].

However, since we are interested in cosmological applications, we will consider the shift-symmetric [7] ($\varphi \to \varphi + c$) version of the theory, capable of describing Dark Energy with a massless scalar. The action is given by

$$S_{\rm H}\left[g_{\mu\nu},\varphi,\Psi_m\right] = \int d^4x\,\sqrt{-g}\sum_{i=2}^{5}\mathcal{L}_i + S_m[\Phi^{-1}g_{\mu\nu},\Psi_m]\ , \tag{1.8}$$

where we have defined

$$\begin{aligned}
&\mathcal{L}_2 \equiv G_2\left(X\right)\ ,\\
&\mathcal{L}_3 \equiv G_3\left(X\right)\left[\Theta\right]\ ,\\
&\mathcal{L}_4 \equiv G_4\left(X\right)R - 2\partial_X G_4\left(X\right)\left(\left[\Theta\right]^2 - \left[\Theta^2\right]\right)\ ,\\
&\mathcal{L}_5 \equiv G_5\left(X\right)G_{\mu\nu}\Theta^{\mu\nu} + \frac{1}{3}\partial_X G_5\left(X\right)\left(\left[\Theta\right]^3 - 3\left[\Theta\right]\left[\Theta^2\right] + 2\left[\Theta^2\right]\right)\ ,
\end{aligned} \tag{1.9}$$

$X \equiv \nabla_\mu\varphi\nabla^\mu\varphi$, and $\Theta_{\mu\nu} \equiv \nabla_\mu\nabla_\nu\,\varphi$, the bracket notation indicates traces of these objects (e.g. $[\Theta] = \Box\varphi$), and Φ is a function on the scalar field that allows for the metric to couple non-minimally to matter. The approximate [8] Galilean symmetry ($\varphi \to \varphi + b_\mu x^\mu + c$) ensures a good behavior against radiative corrections [80, 81].

This theory can be further generalized to include *beyond Horndeski* operators [82–84] and to degenerate-higher-order scalar-tensor (DHOST) theories [82, 85–87], which propagate the right number of degrees of freedom (two tensor and one scalar).

As a side-note, an interesting subset of Eqs. (1.8)-(1.9) that has attracted interest in recent years is defined by the quintic Horndeski operator $G_5(X) = \log(X)$ [88]. The theory defined by this operator has been shown to be equivalent to (linear) scalar Gauss-Bonnet theory,

$$S_{\rm sGB}\left[g_{\mu\nu},\varphi,\Psi_m\right] = \int d^4x\,\sqrt{-g}\left[\frac{R}{2\kappa} - \frac{X}{2} + f\left(\varphi\right)\mathcal{G}_{\rm GB}\right] + S_m\left[\Psi_m\right]\ , \tag{1.10}$$

where $\mathcal{G}_{\rm GB} \equiv R_{\mu\nu\rho\sigma}R^{\mu\nu\rho\sigma} - 4R_{\mu\nu}R^{\mu\nu} + R^2$ is the Gauss-Bonnet invariant, $f(\varphi) = \lambda\varphi$, and λ a dimensionful coupling constant. Generalizations of $f(\varphi)$ to non-shift symmetric forms have also been widely studied, most recently to study BH solutions with scalar *hair* as well as dynamical evolutions beyond GR –see e.g. Refs. [89–94].

[7] Except possibly for a weak breaking of this symmetry in the coupling to matter.
[8] Exact in Minkowski space.

1.2.2 Constraints from gravitational wave propagation

Scalar-tensor theories generically alter the propagation speed of GWs, with such modifications depending on the coupling constants and particular details of the theory. Thus, any constraints on the deviation of the speed of GWs from the speed of light c (which we make explicit in this section), the GR prediction, can be turned into bounds on such theories [95]. For instance, the difference in time of arrival of the GW signal between the two Advanced LIGO detectors can be used to constrain the speed of tensor modes to $0 \lesssim c_T/c - 1 \lesssim 0.7$ [96]. Other constrains come from observations of the Hulse-Taylor binary pulsar –under certain assumptions on how a different GW speed might alter the quadrupole formula [97]. And a lower bound, $-10^{-15} \lesssim c_T/c - 1 < 0$ (for the case $c_T < c$), for high-frequency GWs ($\sim 10^{25}\,\mathrm{Hz}$), comes from the absence of gravitational Cherenkov radiation in high-energy cosmic rays [98].

A remarkable improvement was achieved with the first multimessenger observation in 2017 of the gravitational wave signal from a binary NS merger event (GW170817) [17] –see Fig. 1.3 for more details on this observation. The identification of an electromagnetic follow-up, consisting of a short Gamma-ray Burst (GRB 170817A), allowed to cast the strongest bounds yet on the speed of tensor modes, $-3 \times 10^{-15} \lesssim c_T/c - 1 \lesssim 7 \times 10^{-16}$ [18].

The bounds from GW170817 have been used to cast stringent [9] constraints for large part of DE models described by action (1.8) [102–105]. In particular, the analysis carried out in Refs. [102] set these constraints by exploiting the mapping of shift-symmetric Horndeski theories (and their generalizations) into the effective field theory of Dark Energy (EFT of DE) [106, 107]. Further *theoretical* constraints can be imposed by ruling out the interactions of the tensor modes with the scalar which might lead to GWs decaying into Dark Energy [108, 109] or to instabilities for Dark Energy perturbations due to the presence of GWs [110].

In summary, the situation when all of the above constraints are combined leaves essentially only the $\mathcal{L}_2$ term in Eq. (1.8) (also known as k-essence) as the viable theory, as well as theories related to k-essence by the conformal transformations [110]. Therefore, in the remainder of this section we will concentrate on k-essence.

[9] However, a potential caveat to these bounds is that, due to the strong coupling scale of Dark Energy lying close to the scale of the GW170817 observations, the speed of GWs may be luminal ($c_T = 1$) at short scales while remaining subluminal ($c_T < 1$) at long (or cosmological) scales [101].

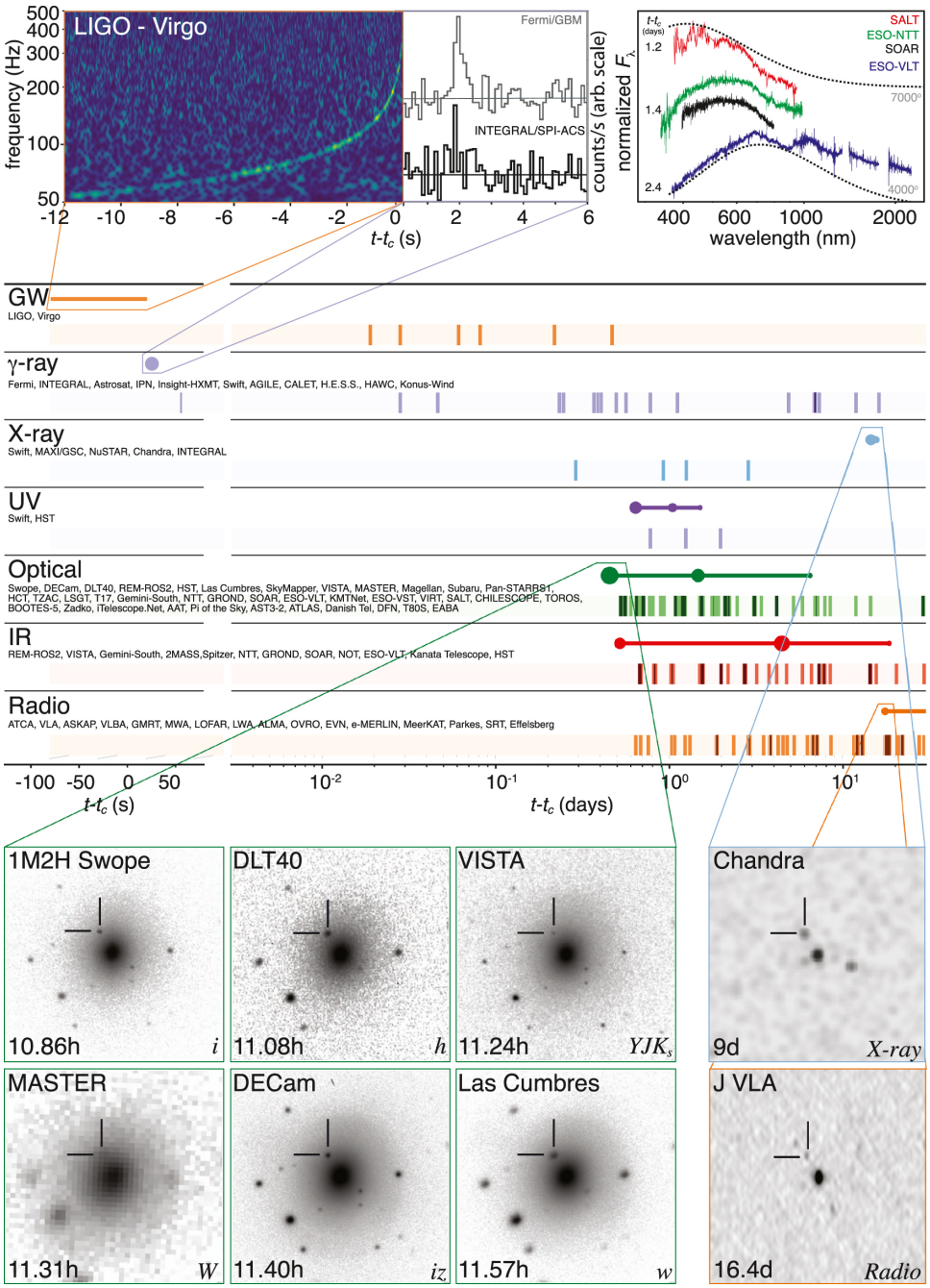

Figure 1.3: *Multimessenger observation of GW170817.* Top left, inset. Combined GW chirp signal from the Advanced LIGO detectors, produced by the merger of two neutron stars (with component masses $m_1 \approx (1.36-2.26)M_\odot$ and $m_2 \approx (0.86-1.36)M_\odot$) in the NGC4993 galaxy –see also Ref. [99]. The GW signal is followed, 1.7 s later, by short Gamma-Ray Bursts observed by Fermi-GBM (top) and INTEGRAL (down). Top right panel. Representative early spectra indicative of a possible kilonova. Middle panel. Timeline of multimessenger observations in GW and all across the EM spectrum, with respect to the GW observation time t_c. Lower left inset. Optical transient observations. Lower right, first X-ray and radio observations. Taken from LIGO Scientific Collaboration and Virgo Collaboration, *et al* [100]. See original source for more details.

1.2.3 Kinetic screening in k-essence

The action of k-essence [111, 112] is given by

$$S_{\rm K}\left[g_{\mu\nu},\varphi,\Psi_m\right]=\int d^4x\sqrt{-g}\left[\frac{R}{2\kappa}+K\left(X\right)\right]+S_m\left[\Phi^{-1}g_{\mu\nu},\Psi_m\right]\ , \tag{1.11}$$

where $K(X)$ is a function of the kinetic term X, and it determines the nonlinear derivative self-interactions of the scalar field. Its particular form is not restricted by the constraints of Sec. 1.2.2. The lowest order terms can be obtained from the expansion

$$K\left(X\right)=-\frac{1}{2}X+\frac{\beta}{4\Lambda^4}X^2-\frac{\gamma}{8\Lambda^8}X^3+\mathcal{O}\left(X^4\Lambda^{-12}\right)\ , \tag{1.12}$$

where $\beta,\gamma\sim\mathcal{O}(1)$ and Λ is the strong-coupling scale of the theory. In the literature, this theory is also known in flat space as $P(X)$ theory and has been studied extensively as a dynamical explanation for DE, for which $\Lambda^4\sim(H_0M_{\rm Pl})^2c\hbar^{-1}\sim(5\,{\rm meV})^4$, where $M_{\rm Pl}$ is the (reduced) Planck mass [113]. Historically one of the first scalar tensor theories to be considered is Fierz-Jordan-Brans-Dicke (FJBD) theory [114–116], which corresponds to the case when no derivative self-interactions (besides the standard kinetic term) are included –i.e. this theory corresponds to $K(X)=-X/2$.

Although it is desirable that the predictions of k-essence depart from GR at the largest scales (as to explain Dark Energy), at astrophysical scales (e.g. the scales the Solar System), the theory must be consistent with known gravitational measurements –see Sec. 1.5. In vacuum, no-hair theorems constrain BH solutions to be the same as in GR [117, 118]. On the other hand, for matter spacetimes, this consistency is achieved due to the nonlinear (derivative) interactions of k-essence, via the *kinetic screening* mechanism [10] (also known as k-mouflage).

In analogy to Newtonian gravity, where the gravitational potential force is the gradient $\partial_i\psi$ of the gravitational potential ψ (obeying Poisson equation $\nabla^2\psi=4\pi G\rho$, with ρ the mass density), the scalar fifth force can be identified with the gradient of the k-essence scalar. The role of the screening mechanism is then to ensure the suppression (through nonlinear self-interactions) of such a scalar fifth force in presence of matter, e.g. in the vicinity of the Sun or a NS [120] –see Fig. 1.4.

In Fig. 1.5, we focus on a specific choice of $K(X)$ defined by $\beta=0$ and $\gamma>0$, which guarantees the presence of kinetic screening [113] –although screening can be achieved with more general forms of $K(X)$. We can observe that radial profile

[10] For scalar tensor theories, there might exist other types of screening mechanisms, such as *Vainshtein screening* and *chameleon screening*. See Ref. [119] for a review on the subject.

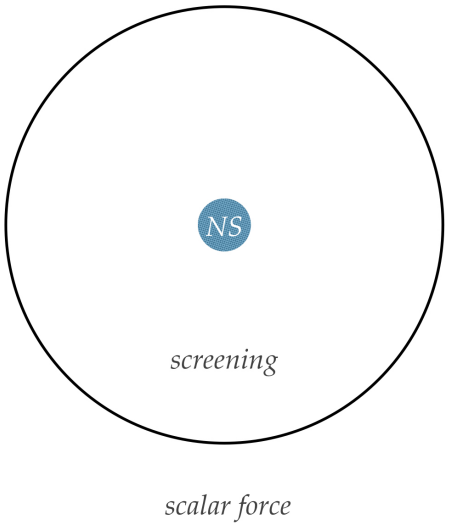

Figure 1.4: *Kinetic screening sketch.* When kinetic screening is active, the scalar force is suppressed in the vicinity of matter distributions, e.g. a neutron star (NS). Outside the Vainshtein radius (black circle, not to scale), the scalar force is not suppressed and the scalar behaves as Dark Energy.

of the scalar gradient (the fifth force) in k-essence (solid red) is suppressed in comparison with FJBD theory (dashed green) in the region $r/M_\odot \sim 10^{-18} - 10^{11}$. Nonlinear scalar effects produce the observed changes in slope or "knees" for k-essence: one near the center of the star ($r/M_\odot \sim 0$), another at the star surface ($r/M_\odot \sim 10$), and the last one is located at the so-called *Vainshtein radius* ($r/M_\odot \sim 10^{11}$).

1.3 Lorentz-violating theories

Alternative theories of gravity can also be obtained by relaxing the fundamental symmetries upon which GR is built. Namely, diffeomorphism invariance. In this section, we briefly review theories that introduce a preferred direction or a preferred frame (given, for instance, by a timelike *aether*) that locally breaks the symmetry under boosts. Among these theories, *Hořava* gravity provides a candidate for a renormalizable theory of QG [14].

1.3.1 Einstein-aether and the low-energy limit of Hořava gravity

In order to break Lorentz invariance, we introduce a timelike *aether* vector field u^μ in the action

$$S_{\text{Æ}}\left[g_{\mu\nu}, u^\mu, \Psi_m\right] = \frac{1}{2\kappa}\int d^4x\,\sqrt{-g}\Big[R + M_{\mu\rho\nu\sigma}\nabla^\mu u^\nu \nabla^\rho u^\sigma + \lambda\left(u_\mu u^\mu + 1\right)\Big]$$

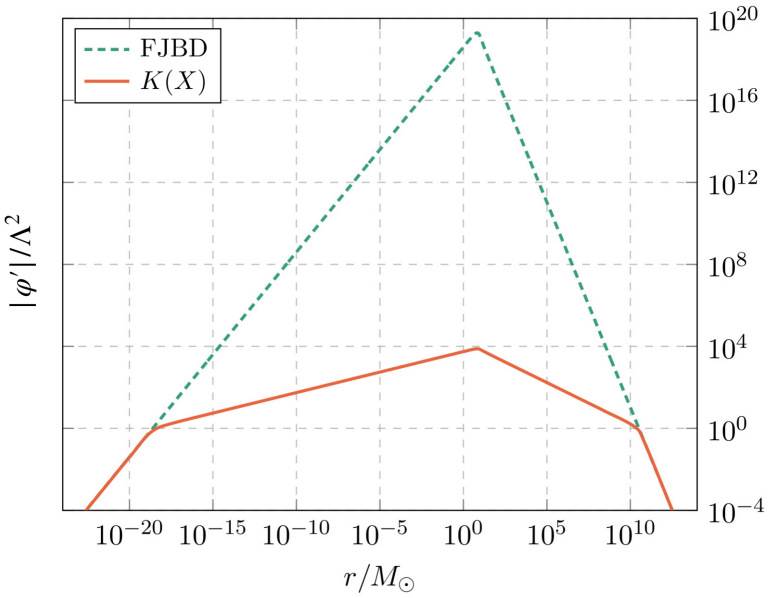

Figure 1.5: *Kinetic Screening Example.* The normalized scalar gradient for k-essence (solid red), with $\beta = 0$ and $\gamma > 0$, and FJBD theory (dashed green) are shown. Suppression of the scalar fifth force (proportional to the scalar gradient) due kinetic screening is evident. For k-essence, the Vainshtein radius is located near the last "knee". Taken from ter Haar, *et al* [113].

$$+ S_m[g_{\mu\nu}, \Psi_m] \ , \quad (1.13)$$

where $M_{\mu\rho\nu\sigma} \equiv c_1 g_{\mu\rho} g_{\nu\sigma} + c_2 g_{\mu\nu} g_{\rho\sigma} + c_3 g_{\mu\sigma} g_{\nu\rho} + c_4 g_{\nu\sigma} u_\mu u_\rho$, c_i are coupling constants, and λ is a Lagrange multiplier that imposes the constraint $u_\mu u^\mu = -1$. The theory described by action (1.13) is called *Einstein-aether* theory [121, 122].

A particular version of this theory, known as *khronometric* theory is obtained if one makes the extra assumption that the aether field is hypersurface-orthogonal. In other words, this condition means that the aether given by the gradient of a scalar function (i.e. $u_\mu \propto \partial_\mu t$, for t a scalar function), which also induces relations between the couplings c_i. The latter can be seen to arise as the low-energy limit [123] of a renormalizable [11] quantum theory of gravity known as [12] *Hořava gravity* [14].

The reduced symmetry in Hořava gravity is that of *foliation-preserving* diffeomorphisms (FDiff), given by

$$t \to \tilde{t}(t), \quad x^i \to \tilde{x}^i(t, x), \quad (1.14)$$

where t is the preferred time direction defining the preferred foliation. Schemat-

[11] Although power counting renormalizability is encouraging, formal renormalizability has been proven only for the so-called *projectable* version [124].

[12] More precisely, from the *non-projectable* version [125] of the theory.

ically, the action of Hořava gravity (in vacuum) can be written as [126]

$$S_{\rm HL}\left[N, N^i, \gamma_{ij}, a_i\right] = \frac{1}{2\kappa}\int dt\, d^3x\, N\sqrt{\det\gamma_{ij}}\left[\mathcal{L}_2 + \frac{1}{\Lambda_\star^2}\mathcal{L}_4 + \frac{1}{\Lambda_\star^4}\mathcal{L}_6\right] \ , \qquad (1.15)$$

where we have performed an Arnowitt-Deser-Misner (ADM) decomposition of the metric [127], $ds^2 = -N^2dt^2 + \gamma_{ij}(dx^i + N^i dt)(dx^j + N^j dt)$, for which N and N^i are respectively the lapse function and shift vector, and γ_{ij} is the metric of the spatial hypersurfaces. In action (1.15), the $\mathcal{L}_2$ term represents khronometric theory written in the 3+1 decomposition. On the other hand, $\mathcal{L}_4$ and $\mathcal{L}_6$ represent terms containing fourth and sixth spatial derivatives of the metric and the acceleration $a_i \equiv \partial_i \log N$, and are suppressed by a new physical scale $\Lambda_\star$. A viable range of values for $\Lambda_\star$ has been identified to be roughly $(10^{10} - 10^{16})$ GeV (in natural $\hbar = 1$ units), where strong coupling at low energies is avoided, and where the theory satisfies both gravitational constraints from Solar System tests and Cosmology, as well as constraints from Lorentz-violations in matter [128]. At the quantum level, the higher-derivative terms are responsible for the power-counting renormalizability properties of action (1.15) –see Ref. [129] for an argument of how this argument works out in the simplified setting of a Lifshitz scalar.

1.3.2 Black hole phenomenology

The concept of a BH is subtle in Einstein-aether theory [Eq. (1.13)], and the main reason for this is the fact that the theory propagates spin-0 and spin-1 degrees of freedom in addition to the usual spin-2 modes, and each of these may propagate with a different (but finite) speed [126]. However, in order to avoid gravitational Cherenkov radiation from cosmic rays, these speeds must be larger than the speed of light [130]. This in turn results in the possibility of defining different (Killing) horizons for each mode. However, the BH horizon which constitutes a causal barrier of spacetime (for all of these modes) corresponds to the innermost of these horizons –i.e. the horizon defined by the modes with the largest speed.

Although we can define Einstein-aether BHs in such a way, a more peculiar causal barrier for modes of arbitrarily high speeds, called the *universal horizon* [13], has been identified [126, 132]. Such modes arise naturally in Hořava gravity, where higher-order spatial derivative operators in the action give rise to high energy modes (with frequency ω and spatial momentum $\boldsymbol{k}$) propagating according to a dispersion relations of the form $\omega^2 \approx \alpha^2|\boldsymbol{k}|^{2p}/\Lambda_\star^{2p-2}$, with $p > 1$ [133]. Therefore, the universal horizon aids in defining the concept of a BH in the

[13] A formal definition of the universal horizon has been given in Ref. [131]. For stationary solutions with associated Killing field χ^μ, the universal horizon is defined by the location where $u_\mu\chi^\mu = 0$ and $a_\mu\chi^\mu \neq 0$, where we have defined the 4-acceleration $a^\mu \equiv u^\sigma\nabla_\sigma u^\mu$.

presence of modes that travel with arbitrarily large (as $|\boldsymbol{k}| \to \infty$) group velocities $v^2 \equiv |d\omega/d\boldsymbol{k}|^2 \approx \alpha^2(|\boldsymbol{k}|/\Lambda_\star)^{2p-2}$.

Non-spinning and slowly-rotating BHs in Einstein-aether/khronometric theory have been studied e.g. in Refs. [126, 134, 135]. Most recently, fully rotating solutions, mildly departing from the Kerr metric (1.4), have been obtained in Ref. [136], in the unconstrained regions of the parameter space –although in the latter study no universal horizons where identified.

1.4 Theory-independent parameterizations

Given the vast array of possible modifications to gravity, computing the observables for each theory individually, with the aim of constraining its couplings and charges, may become a tedious task. A useful alternative to such a program is to compute the observables for a general parametrization capable of capturing the effects of many of these theories. Once experimental bounds are cast on these generalized parameters, such constrains are mapped to the couplings and charges of each theory. In the following, we review a few examples of this approach. We concentrate on stationary BH spacetimes and on the EFT approach. Other possible ways to give theory-independent parameterizations of gravitational observables include: the Parameterized Post-Newtonian framework (for Solar System applications up to 1 Post-Newtonian order) [26] and template-free reconstructions of GW signals [137].

1.4.1 Stationary black hole spacetimes

Given that alternative theories often break symmetries or introduce additional fields, one might generically expect that the solutions for BH spacetimes are different from the Kerr/Schwarzschild metric. Since EM and GW probes (e.g. light emitted by an accretion disk or GWs from an EMRI) may provide information about the spacetime geometry of a BH, one would like to find a way to describe the metric in a general way. In this section, we look at how this can be done for stationary BH solutions in spherical symmetry.

In polar coordinates, the metric can be written as

$$ds^2 = -N^2(r)\,dt^2 + \frac{B^2(r)}{N^2(r)}\,dr^2 + r^2\,d\Omega^2, \tag{1.16}$$

where $d\Omega^2 = d\theta^2 + \sin^2(\theta)\,d\phi^2$. For a Schwarzschild BH in GR, these functions take the form $N^2(r) = 1 - 2M/r$ and $B(r) = 1$, where M is the BH mass.

In order to describe BHs in an unspecified theory, one must first choose a

way to parameterize the metric functions $N(r)$ and $B(r)$. This choice may be motivated by different arguments. For instance, one possibility, if one wishes to ensure that any arbitrary smooth solution be captured (i.e. one wishes to ensure *completeness*), one may choose a Fourier basis, with parameters a_k as defined by the Fourier transform $\tilde{f}(k) \equiv \sum_k a_k e^{ikr}$. However, a disadvantage of such a choice may be that a large (possibly infinite) number of parameters may be required. In Part III, we employ data analysis techniques to mitigate the problems due to the inclusion of a large number of parameters and apply it to compute BH images.

Another approach is to write the parametrization guided by physical arguments or empirical expectations, for instance, to ensure that only few parameters are needed to describe the most interesting spacetimes or that at large distances one does not require extreme fine tuning to recover the GR asymptotics. One may also wish to ensure a BH horizon is present.

An example of the latter description is given by the Rezzolla-Zhidenko (RZ) parametrization [138], which has been shown to reproduce a wide family of BH solutions –see e.g. [139] and see also Ref. [140] for a generalization to rotating spacetimes. In this parametrization, one first introduces a compactified coordinate $x \equiv 1 - r_0/r$, with r_0 the location of the event horizon. Then, the parameters $\{\varepsilon, a_0, b_0\}$, which mainly describe the large distance behavior are defined by

$$\begin{aligned} A(x) &= 1 - \varepsilon(1-x) + (a_0 - \varepsilon)(1-x)^2 + \tilde{A}(x)(1-x)^3, \\ B(x) &= 1 + b_0(1-x) + \tilde{B}(x)(1-x)^2, \end{aligned} \tag{1.17}$$

where $xA^2(x) = N^2(r)$, $A(x) > 0$ for $0 < x < 1$. Finally, the rest of the parameters $\{a_i, b_i\}_{i=2}^{\infty}$ are defined in terms of Padé approximants (see e.g. Ref. [141]) as

$$\tilde{A}(x) = \frac{a_1}{1 + \frac{a_2 x}{1 + \frac{a_3 x}{1 + \ldots}}}\,, \qquad\qquad \tilde{B}(x) = \frac{b_1}{1 + \frac{b_2 x}{1 + \frac{b_3 x}{1 + \ldots}}}\,. \tag{1.18}$$

Applications of this parametrization include the computation of BH shadows [142–144], BH QNMs [145, 146] and X-rays [146, 147].

1.4.2 Effective field theory approach

Consider an action $S_{\rm IR}$ describing physics below a certain energy scale $E \ll \Lambda_{\rm cut}$ (or for length scales $L \gg 1/\Lambda_{\rm cut}$) and involving fields with masses much smaller than $\Lambda_{\rm cut}$ –in this section we set $\hbar = 1$. The idea of EFT is to complete the action $S_{\rm IR}$ with all possible local operators (interactions) compatible with a given set of the fundamental symmetries and fields, and which we denote $\Delta S_{\rm IR}$. On dimensional grounds, the coupling constants associated with higher-dimensional

operators (i.e. those with increasing number of fields or derivatives) can be written in terms of dimensionless parameters suppressed by powers of energy/length scales of order $\Lambda_{\rm cut}$. Thus, they are expected to provide small corrections to the leading-order operators, provided $E \ll \Lambda_{\rm cut}$. In this way, one obtains the *effective field theory* $S_{\rm EFT} = S_{\rm IR} + \Delta S_{\rm IR}$, valid for $E \ll \Lambda_{\rm cut}$.

Outside this range, at scales $E \gtrsim \Lambda_{\rm cut}$ (or $L \lesssim 1/\Lambda_{\rm cut}$), perturbative control may be lost, and $S_{\rm EFT}$ can no longer be trusted. Instead, it should be replaced with the action of a more fundamental theory, or *a UV completion* $S_{\rm UV}$, that is able to describe physics at such scales –and from which the low-energy EFT can be derived. A classic example of an EFT in Particle Physics is the Fermi theory of weak interactions, which can be UV-completed by the electroweak sector of the Standard Model of Particle Physics –see e.g. Ref. [77]. To make an analogy with Sec. 1.4.1, one can think that all of the coefficients of a general metric parametrization could be computed from the exact solution for the metric in a given theory of gravity. However, it is often the case that for many theories of interest such a UV completion may not be available.

In brief, the EFT approach provides a way to parameterize the unknown in a way that allows us to make predictions with incomplete information. Indeed, this approach has found utility in a number of applications in gravity and Cosmology, including Dark Energy [106, 107], inflation [148], BHs [149, 150] and GWs [151].

Another relevant example is the EFT extension of GR in vacuum given in Ref. [152]. Including up to eight-derivative corrections, the action is given by

$$S_{\text{EFT of GR}}\left[g_{\mu\nu}\right] = \frac{1}{2\kappa}\int d^4x\,\sqrt{-g}\left[R - \frac{\mathcal{C}^2}{\Lambda_\star^6} - \frac{\tilde{\mathcal{C}}^2}{\tilde{\Lambda}^6} - \frac{\mathcal{C}\tilde{\mathcal{C}}}{\Lambda_-^6} + \cdots\right], \tag{1.19}$$

where $\mathcal{C} \equiv R_{\mu\nu\sigma\rho}R^{\mu\nu\sigma\rho}$ and $\tilde{\mathcal{C}} \equiv R_{\mu\nu\sigma\rho}\tilde{R}^{\mu\nu\sigma\rho}$. Notice that the higher-order operators [14] depend only the contractions of products of the Riemann tensor and its dual $\tilde{R}^{\mu\nu\sigma\rho} \equiv \epsilon^{\mu\nu}{}_{\alpha\beta}R^{\alpha\beta\rho\sigma}$, and are suppressed by new energy scales $\Lambda_\star$, $\tilde{\Lambda}$ and Λ_- –where the latter are unknown parameters that need not coincide with the Planck mass $M_{\rm Pl}$.

And advantage of the EFT approach, with respect to the one of section 1.4.1, is that it also parameterizes deviations in the dynamics of the metric, and not just deviations of the stationary solutions. Indeed, bounds on the new energy scales of action (1.19) have been found in Ref. [153] by computing deviations GW phase during the early inspiral of BH binaries and comparing with LIGO-Virgo events. Furthermore, the new terms in action (1.19) may also lead to modifications of the QNMs and horizon properties of BHs [154].

[14] In principle, operators suppressed by powers of Λ^{-4} may also be present. However, Ref. [152] omits them based on subtle theoretical assumptions.

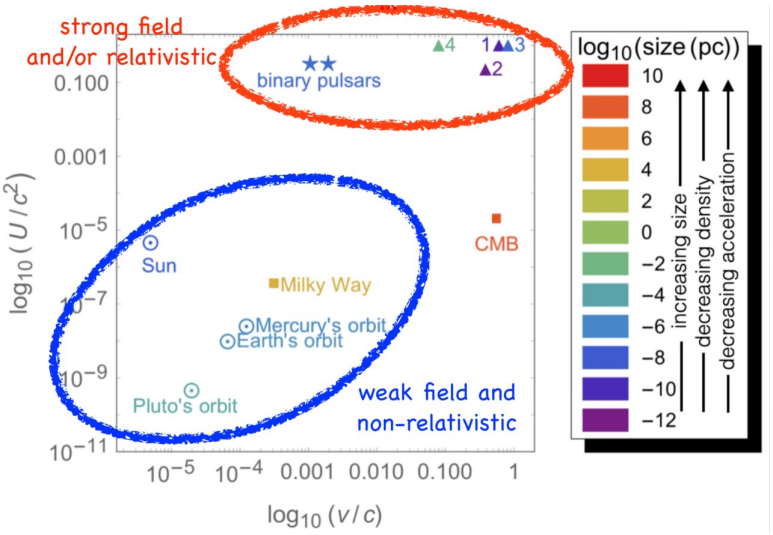

Figure 1.6: *Chart of gravitational regimes.* In the horizontal plane, the binding energy of the system U and representative speed v, normalized by powers of c. In color code, the representative size of the system, and (inversely) proportional to the latter are the density (acceleration). The weak and non-relativistic regime is located towards the lower left corner, whereas the strong and relativistic regime towards the top right corner. Markers indicate example probes of different parts of this chart. The triangular markers correspond to: (1) binary BH systems with LIGO-Virgo, (2) binary NS systems with LIGO-Virgo, (3) binary BH systems with LISA, and (4) binary BH systems with Pulsar-Timing Arrays (PTA). Courtesy of Enrico Barausse.

1.5 Summary of current tests of gravity

In the previous sections, we provided a brief overview of a number of different descriptions of gravity. In this section, we summarize both classical (mainly weak field) and modern (mainly strong field) tests of gravity. Until recently, GR had been extensively tested mostly in the weak and mildly relativistic regime, or in cosmological settings. With the maturity of GW interferometers and Very Large Baseline Interferometry, a new campaign to test the strong field of gravity has just begun.

A map of the different regimes of gravity is provided in Fig. 1.6, where gravitational systems are characterized by some representative speed v (horizontal axis), their (binding) energy content U (vertical axis), and a representative length/size (color bar). Marks indicate examples of probes for different parts of this parameter space, from Solar System scales (lower left) to compact object binaries (upper right). In Fig. 1.6, the *weak field* and non- (or mildly) relativistic regime can be identified as the lower left corner, whereas the *strong* and highly dynamical (relativistic) is identified as the upper right corner. Solar System probes, for instance, clearly belong to the former, as GWs from binary BH mergers belong to the latter.

1.5.1 Weak field tests

Here we summarize the "classical" weak field tests following Will [26]. Predictions for the observables in the weak and mildly relativistic regime are often computed by means of the Post-Newtonian (PN) framework which relies on an expansion in v/c, with terms of order $(v/c)^{2n}$ referred to as being of nPN order [26, 155].

The first kind of tests probe the gravitational deflection of light. In Solar System, category includes the classical Eddington experiment where the deflection of background starlight caused by the Sun was measured, and subsequent improvements of these type of observations –see Fig. 7.2 of Will [26] for a plot comparing Eddington's results with modern measurements.

The second type of tests probe the relativistic delay (with respect to Newtonian gravity) in the arrival time of light signals moving across a gravitational field –often called Shapiro time delay in honor of Irwin Shapiro, who first predicted it in 1964 [156]. For example, this delay occurs for a radar signal travelling across the gravitational field of the Sun, and bouncing off a third body, such as a planet or a spacecraft. Indeed, the most accurate measurements of these effects have been made with radar-ranging measurements of the Cassini spacecraft [26, 157].

Finally, the third classical test probes the perihelion advance of an orbiting body such as Mercury. This effect is of great historical relevance as it evidenced the shortcomings of Newtonian gravity [158] and became one of the first predictions Einstein computed using GR [159]. The perihelion advance is naturally included in the PN equations of motion, and is generically present in orbiting systems. For instance, this effect has been identified by the GRAVITY Collaboration for the orbits of stars around the SMBH at the center of the Milky Way, Sag A* [160].

Other weak field probes include the Nordtvedt effect [161, 162], which can be used to test the validity of the Strong Equivalence Principle, the Lense-Thirring effect [163, 164], which probes the frame-dragging effect [26].

1.5.2 Strong field tests

In the mildly relativistic strong field regime (upper center part in Fig. 1.6), the first indirect evidence of the existence of GWs was provided by measurements of the change in the orbital period (due to GW damping) in the Hulse-Taylor binary pulsar system [2, 3]. Today, the double pulsar system PSR J0737–3039A/B allows for very precise tests of strong field effects of GR. For instance, Kramer, *et al.* [16] measure the change in the orbital period due GW damping to be $\dot{P}^{\rm GW}/\dot{P}^{\rm GW,\,GR} = 0.999963(63)$, with respect to the orbital change $\dot{P}^{\rm GW,\,GR}$ predicted in GR using the quadrupole formula. This measurement is a factor of 25 more precise than

that for the Hulse-Taylor pulsar [165] –see Fig. 1.7.

With regards to theories beyond-GR, this system can also be used to cast bounds on the parameters of Damour-Esposito-Farèse (DEF) theory –a FJBD theory in the terminology of Sec. 1.2.3 [16]. However, systems where one pulsar companion is a white dwarf (WD), cast the stringier bounds for most of the parameter space of DEF theory –see e.g. Refs. [16, 166, 167].

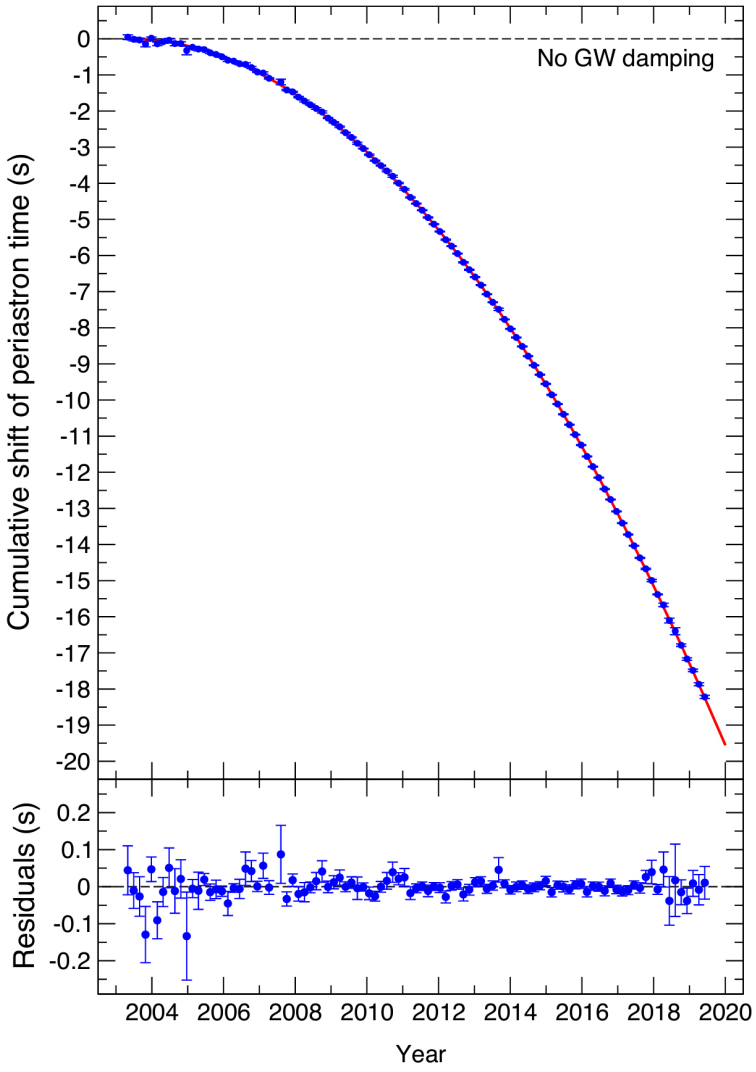

Figure 1.7: *Gravitational wave damping in the double pulsar system PSR J0737–3039A/B* . Top panel. Cumulative shift of the times of periastron passage relative to a model with no GW damping. Each data point represents 60 days of data to which a Keplerian orbit is fitted. In solid red, the GR prediction based on measurements of the masses reported in Kramer, *et al* [16]. Bottom panel. Residuals of the deviation with respect to the GR prediction. See original source for more details. Taken from Kramer *et al* [16].

In recent years, the increasing number of GW events in the LIGO-Virgo catalogues have already allowed for numerous novel tests of the strong and highly dynamical regime of gravity –see Refs. [4–8]. Such kinds of tests are referred to

as *null tests of GR* and make no use of high-accuracy waveforms in alternative theories of gravity –we will describe efforts in this direction in Part II. Instead, the latter look for deviations from GR with different consistency and parameterized tests. Among them: consistency tests between the low- and high-frequency parts of the signal (also known as Inspiral-Merger-Ringdown tests), probes of additional GW polarizations, ringdown tests, and constraints on PN parameters. No evidence for physics beyond GR has been reported so far [8].

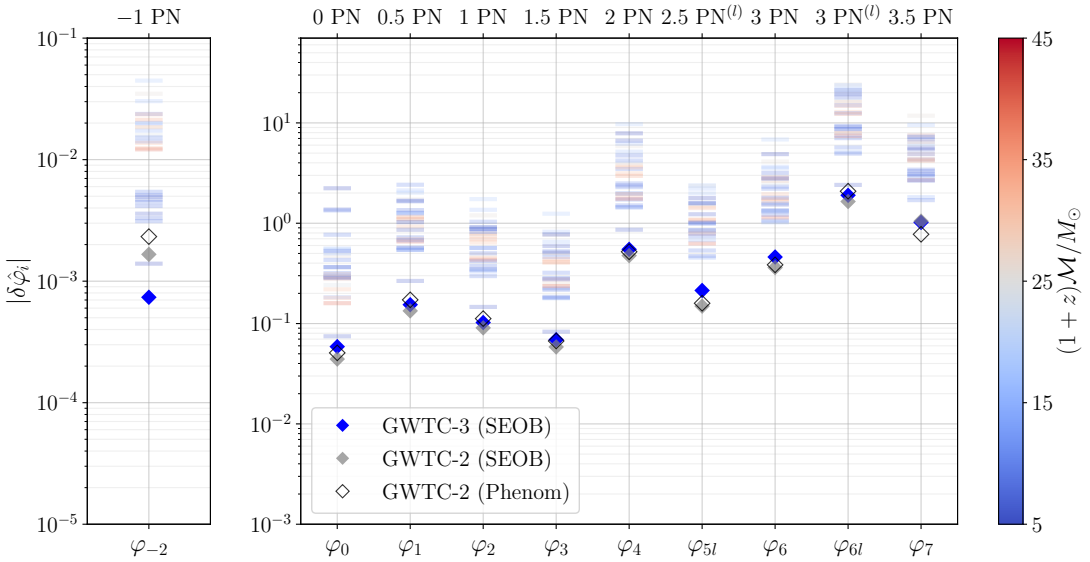

Figure 1.8: *Bounds on parameterized PN coefficients of the GW phase.* See main text for the definition of the coefficients $\delta\varphi_i$. Blue and gray diamonds indicate bounds obtained using the SEOBNRv4_ROM with the GWTC-3 [8] and GWTC-2 [7] catalogues, respectively. White diamonds used the IMRPhenomPv2 model for GWTC-2 data. The diamond markers are the combined bounds for the eligible GW events, and assume that the deviations take the same values for events. Horizontal colored bars indicate bounds from individual events labeled by their redshifted total mass. See main source for more details. Taken from Ref. *et al* [8].

As an example of the latter family of tests, constraints from GW observations on PN parameters are reported [8] as fractional deviation terms applied to the GW phase $\varphi_{\rm PN}(f)$ described by the 3.5PN TaylorF2 approximant [168],

$$\varphi_{\rm PN}(f) = 2\pi\, f\, t_{\rm c} - \varphi_{\rm c} - \frac{\pi}{4} + \frac{3}{128\eta}\left(\pi\tilde{f}\right)^{-5/3} \sum_{i=0}^{7} \left[\varphi_i + \varphi_{i\,l}\log(\pi\tilde{f})\right]\left(\pi\tilde{f}\right)^{i/3} , \tag{1.20}$$

where $\tilde{f} = GM(1+z)f/c^3$, $M(1+z)$ is the redshifted total mass of the binary, φ_c, t_c are the coalescence phase and time, and η the symmetric mass ratio. In GR, the coefficients $\{\varphi_i\}$ are uniquely determined, and their values are reported in Ref. [168]. In Fig. 1.8, upper bounds are reported on the fractional

deviation terms $\delta\varphi_i$, when they are varied one at a time, obtained through [15] $\varphi_i \to (1+\delta\varphi_i)\varphi_i$ [5]. In particular, Fig. 1.8 shows stringent constraints on the $\delta\varphi_{-2}$, which in GR its value is identically zero –and therefore represents and absolute (normalized) deviation. Physically, the $\delta\varphi_{-2}$ term represents the contribution to the GW phase of dipolar radiation, which is not present in GR, but is generically predicted in many alternative theories of gravity –such as FJBD theory-like theories, see e.g. Ref. [169].

For electromagnetic probes, recent observations in the radio band have yielded the first horizon-scale images of the SMBH Sag A* and M87*. Based on these measurements, the EHT Collaboration has recently performed tests of GR [10, 12, 170]. One example of the tests reported in Ref. [12] is shown in Fig. 1.9, where a comparison of the inferred shadow size is performed against various non-Kerr metrics [16]. This comparison is done in terms of the fractional diameter deviation $\delta \equiv (d_{\rm sh}/d_{\rm sh,Sch}) - 1$, where $d_{\rm sh}$ is the inferred diameter of the shadow and $d_{\rm sh,Sch}$ is its value for the Schwarzschild metric. White regions indicate sizes consistent at 68 % CL with the inferred size of Sag A*. From this plot it can be seen that large values of the (normalized) charges in the various examples (solid lines) are disfavoured. Although this plot concerns non-rotating BH spacetimes, it is argued that spin introduces minor corrections.

[15] In the analysis of Ref. [5], these deviations are turned off at a maximum cutoff frequency –see the original reference for more details.

[16] See also Volkel, *et al.* [171], for a comparison of the shadow size of M87* against predictions made with the RZ parametrization [138] of Sec. 1.4.1.

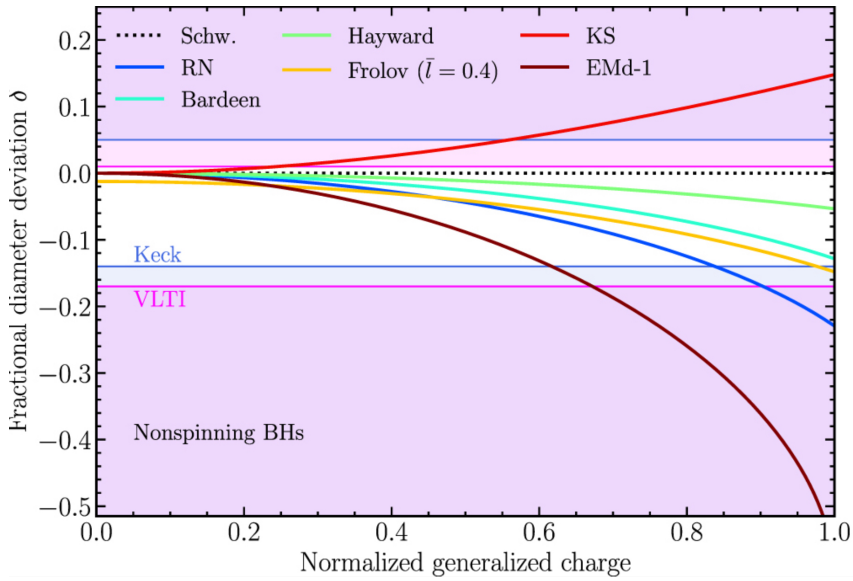

Figure 1.9: *Bounds on charges for non-rotating metrics.* Comparison of the shadow sizes consistent the the measurement of Sag A*. White regions (using two different values for the distance to Sag A*, labelled Keck and VLTI) indicate consistency at 68 % CL with the inferred value of the shadow. The latter is described by the fractional diameter deviation δ. In dashed black, the value of the shadow for the Schwarzschild metric. In solid lines, the shadow size as a function of the a single charge (normalized to its maximum value) parameterizing various nonrotating BH metrics: Reissner–Nordström (RN), Bardeen, Hayward, Frolov, the Kazakov & Solodukhin (KS) and the Gibbons–Maeda–Garfinkle–Horowitz–Strominger solution for Einstein–Maxwell–dilaton–axion theory (EMd–1). See original source for more details. Taken from Ref. *et al* [12].

Part II

The strong field regime in k-essence

Chapter 2

UV completions, fixing the equations and nonlinearities in k-essence

In Sec. 1.2.3, we have introduced k-essence, a scalar-tensor theory with first-derivative self interactions and which may provide interesting phenomenology on cosmological scales. On smaller scales, however, initial value evolutions (which are crucial for predicting the behavior of astrophysical systems, such as binaries of compact objects) may run into instabilities related to the Cauchy problem becoming potentially ill-posed. Moreover, on local scales the dynamics may enter in the nonlinear regime, which may lie beyond the range of validity of the infrared theory. Completions of k-essence in the ultraviolet, when they are known to exist, mitigate these problems, as they both render Cauchy evolutions well-posed at all times, and allow for checking the relation between nonlinearities and the low energy theory's range of validity.

In this Chapter, we explore these issues explicitly by considering an ultraviolet completion to k-essence and performing vacuum 1+1 dynamical evolutions within it. The results are compared to those obtained with the low-energy theory, and with the low-energy theory suitably deformed with a phenomenological "fixing the equations" approach. We confirm that the ultraviolet completion does not incur in any breakdown of the Cauchy problem's well-posedness, and we find that evolutions agree with the results of the low-energy theory, when the system is within the regime of validity of the latter. However, we also find that the nonlinear behavior of k-essence lies (for the most part) outside this regime.

Throughout this Chapter, and for the rest of Part II (unless otherwise stated), we use the metric signature $-+++$ and work in units where $c = 1$. Greek letters μ, $\nu, \ldots$ denote spacetime indices ranging from 0 to 3, while Roman letters near the middle i, $j, \ldots$ range from 1 to 3, denoting spatial indices.

2.1 Motivation and outline

As we have seen in Sec. 1.2.2, k-essence theories [111, 112] are among the very few terms in the DHOST class that remain experimentally viable despite constraints from GW propagation [108, 110, 172–178]. Potentially even tighter constraints may come from the *generation* (rather than just the propagation) of GWs [179, 180]. However, obtaining predictions for GW generation is far more difficult than for propagation, as the nonlinear self interactions of the k-essence scalar are believed to dominate the dynamics on the small scales characterizing compact binary systems. In fact, this expectation comes from calculations of static and quasi-static systems (such as stars), on whose scales the scalar self interactions are important and tend to suppress deviations from GR [113, 120]. This nonlinear mechanism, known as "screening" (of local scales from GR deviations), is common to other theories in the DHOST class (see e.g. Refs. [181–184]) and is both a blessing and a curse. On the one hand it allows k-essence to pass solar-system tests of gravity [113, 179], but on the other hand it renders the calculation of GW generation conceptually and practically involved [113, 179, 180, 185, 186].

In fact, because of the nonlinear scalar derivative self-interactions, evolutions to the future of initial configurations of interest (on which calculations of GW generation in the highly relativistic and strong-field regime of compact binaries are based) may become "unstable", i.e. they may depend "discontinuously" on the initial data and/or exhibit fast exponential growth. (See e.g. Refs. [185, 187–189].) In mathematical jargon, this corresponds to the Cauchy (i.e. initial value) problem becoming ill-posed [19]. While for astrophysically relevant initial conditions (such as neutron star binaries or gravitational collapse) this breakdown of the Cauchy problem can be avoided by a judicious choice of gauge [180] (at least in specific k-essence theories), for general theories/configurations this may not always be possible. In fact, a more robust approach to "fixing" the Cauchy problem is to complete k-essence to the ultraviolet (UV) [190] (when that is allowed by positivity bounds [191]) or to "deform" the evolution (by adding an auxiliary field that drives the dynamics to the "real" one on long timescales). This second approach to "fix the equations" was proposed by Cayuso, Ortiz and Lehner in Ref. [192] (see also Refs. [154, 193]), partly inspired by dissipative hydrodynamics, and was successfully applied to gravitational collapse in k-essence by Refs. [179, 180] (where it was shown to reproduce the results obtained in a gauge where breakdowns of the Cauchy problem are avoided). On a similar note, shocks/caustics in k-essence [185, 194, 195] may also be resolved by resorting to a UV completion. In Ref. [196], it was illustrated that the transfer of energy to an additional (UV) degree of freedom may allow for the smoothening of shock/caustic fronts in k-essence.

In this Chapter, we take a step back and investigate in depth the relation between first-derivative self interactions of the scalar, well-posedness of the Cauchy problem and UV completions (in both the standard and "fixing the equations" approaches). To this purpose, we consider a k-essence model that potentially suffers from both Tricomi-type and Keldysh-type breakdowns of initial-data evolutions [185, 186]. In more detail, the former corresponds to the equations becoming parabolic (and then elliptic) along the evolution, while the latter are caused by diverging (coordinate) characteristic speeds for the scalar mode. By suitably choosing the sign of the coupling of the first-derivative scalar self interactions in the action, we can then extend the k-essence model to a standard $U(1)$ symmetric UV completion [190]. Solutions in the UV-complete theory are compared to ones in the low-energy k-essence theory (as long as the Cauchy problem in the latter remains well-posed) and to ones in a "fixing the equations" completion. We also explore the relation between the regime in which the scalar self-interactions become important and the domain of validity of the low-energy EFT, finding that the two are closely connected for the example that we study.

In more detail, this Chapter is organized as follows. First, in Sec. 2.2 we review the k-essence model that we adopt as our case study. We then introduce its standard UV-completion in Sec. 2.2.1, while our "fixing the equations" approach is introduced and applied in Sec. 2.2.2. We describe our numerical implementation in Sec. 2.3 and present our results in Sec. 4.4. Our findings are discussed and conclusions drawn in Sec.2.5. In Appendix B.1, we present an additional example, and in Appendix B.2 we elaborate on details regarding the constraint propagation in the "fixed" theory. For convenience in the notation, in contrast to Part I, and only for this Chapter, we will denote the k-essence scalar field as $\pi(x)$.

2.2 Quadratic k-essence

The action of k-essence in vacuum is given by [cf. (1.11)]

$$S_{\rm K}\left[g_{\mu\nu},\pi\right]=\int d^4x\sqrt{-g}\left[\frac{R}{2\kappa}+K\left(X\right)\right]\ , \tag{2.1}$$

where $K\left(X\right)$ is a function of the standard kinetic term of the scalar field $\pi(x)$, given by $X=\nabla^\mu\pi\nabla_\mu\pi$. The quadratic model is defined by keeping only the leading first derivative self interaction, i.e.

$$K(X)=-\frac{1}{2}X+\frac{\beta}{4\Lambda^4}X^2+O\left(\Lambda^{-8}X^3\right)\ , \tag{2.2}$$

with $\beta \sim O(1)$ a dimensionless coupling constant and Λ the EFT strong coupling scale. Note that in the presence of matter, screening is present only in the $\beta < 0$ branch [113, 120, 186]. However, positivity bounds select the branch with $\beta > 0$ as the one consistent with embedding in a UV theory [191].

The vacuum field equations derived from action (2.1) are given by

$$G_{\mu\nu} = \kappa\, T^{(\pi)}_{\mu\nu} \ , \tag{2.3}$$

where $G_{\mu\nu}$ is the Einstein tensor and

$$T^{(\pi)}_{\mu\nu} = K\left(X\right) g_{\mu\nu} - 2K'\left(X\right) \nabla_\mu \pi \nabla_\nu \pi \ , \tag{2.4}$$

is the energy-momentum tensor of the k-essence field. The equation for the scalar field can be written as

$$\gamma^{\mu\nu} \nabla_\mu \nabla_\nu \pi = 0 \ , \tag{2.5}$$

where

$$\gamma^{\mu\nu} = g^{\mu\nu} + \frac{2K''(X)}{K'(X)} \nabla^\mu \pi \nabla^\nu \pi \ , \tag{2.6}$$

is an effective metric for the scalar field. From Eq. (2.6), it is evident that the scalar equation (2.5) may develop shocks/caustics (e.g. discontinuities) if the scalar gradients become large, even in situations when the initial data for the scalar field is smooth [185, 194, 195]. Additionally, other pathologies may arise if $K'\left(X\right)$ approaches zero [188].

In order to study the non-linear dynamical regime, the *well-posedness* of the Cauchy problem must first be assessed. According to Hadamard's criteria [19], the Cauchy initial value problem governed by Eqs. (2.3) and (2.5) is well-posed if a unique solution exists and depends continuously on the initial data. This can be shown to occur if the associated system of equations is *strongly hyperbolic* [197, 198], i.e. if the system of equations can be written as a quasilinear first-order system and its principal part (consisting of the terms with the highest derivatives) has real eigenvalues and a complete set of eigenvectors [199, 200]. In our case, one can restrict the analysis to the scalar equation (2.5), since the evolution equations for the metric variables [Eq. (2.3)] take the same form as in GR (which is well-posed [201]) and the source terms involve only derivatives that are lower-order than the principal part.

In the following, we will restrict to spherical symmetry, where the metric can

be written in the form

$$ds^2 = -\alpha^2(t,r)\,dt^2 + g_{rr}(t,r)\,dr^2 + r^2 g_{\theta\theta}(t,r)\,d\Omega^2 \ , \tag{2.7}$$

where $\alpha(t,r)$ is the lapse function, and $g_{rr}(t,r)$ and $g_{\theta\theta}(t,r)$ are the spatial components of the metric and $d\Omega^2 = d\theta^2 + \sin^2(\theta)\,d\phi^2$. The scalar equation (2.5) can be written as a first-order system of equations of the form

$$\partial_t \boldsymbol{U} + \mathbb{V}\,\partial_r \boldsymbol{U} = \boldsymbol{\mathcal{S}}(\boldsymbol{U}) \,, \tag{2.8}$$

where $\boldsymbol{U} = (\partial_t\pi, \partial_r\pi)$, $\boldsymbol{\mathcal{S}}(\boldsymbol{U})$ is a source term, and we have made use of the consistency equation $\partial_t\partial_r\pi = \partial_r\partial_t\pi$. The *characteristic speeds*, corresponding to the eigenvalues of the characteristic matrix $\mathbb{V}$, are given by

$$V_\pm = -\frac{\gamma^{tr}}{\gamma^{tt}} \pm \sqrt{\frac{-\det(\gamma^{\mu\nu})}{(\gamma^{tt})^2}} \ , \tag{2.9}$$

where $\det(\gamma^{\mu\nu})$ should be understood as the determinant of the effective metric in the (t,r) subspace, i.e.

$$\det(\gamma^{\mu\nu}) = \gamma^{tt}\gamma^{rr} - \left(\gamma^{tr}\right)^2 \ . \tag{2.10}$$

If these speeds are real and distinct, the corresponding eigenvectors form a complete set, and thus the scalar sector is strongly hyperbolic.

Since the characteristic speeds (2.9) depend on the effective metric (which differs in general from the spacetime metric $g_{\mu\nu}$), two situations may arise that can cause a breakdown of strong hyperbolicity. The first problem occurs when the scalar equation (2.5) changes character from hyperbolic to parabolic, i.e. when one of the eigenvalues of the effective metric [Eq. (2.6)],

$$\lambda_\pm = \frac{1}{2}\left(\gamma^{tt} + \gamma^{rr} \pm \sqrt{(\gamma^{tt}-\gamma^{rr})^2 - (2\gamma^{tr})^2}\right) \ , \tag{2.11}$$

vanishes, implying $\det(\gamma^{\mu\nu}) \to 0$. This referred to as a *Tricomi-type* breakdown [202] (see also Ref. [185]) due to its resemblance to the behavior of the Tricomi equation,

$$\partial_t^2 u(t,r) + t\,\partial_r^2 u(t,r) = 0 \ , \tag{2.12}$$

which is hyperbolic for $t < 0$ (as it has characteristic speeds $\pm(-t)^{1/2}$) and elliptic for $t > 0$. The system of evolution equations, including those for the metric, then becomes of mixed-type, with parabolic and hyperbolic sectors [203]. The second

problem occurs when the characteristic speeds diverge. This referred to as a *Keldyish-type* breakdown [202] (see also Ref. [185]), in analogy with the Keldyish equation,

$$t\,\partial_t^2 u(t,r) + \partial_r^2 u(t,r) = 0\ . \tag{2.13}$$

which has characteristic speeds $\pm\,(-t)^{-1/2}$ diverging as $t \to 0^-$.

Both problems may be solved by a suitable UV completion of the EFT. In fact, in the following we will review a UV completion of the quadratic k-essence model given by (2.2) (for $\beta > 0$), and show that it allows for avoiding both Keldysh and Tricomi breakdowns of the Cauchy problem. Similarly, the "fixing the equations" approach [192] may also improve the behavior of initial-value evolutions in the branch $\beta < 0$.

2.2.1 $U(1)$ UV completion

The positive branch ($\beta > 0$) of quadratic k-essence can be obtained as the low-energy description of a UV completion given by the $U(1)$-symmetric action[1]

$$S_{\rm UV}\left[g_{\mu\nu},\phi\right] = \int \mathrm{d}^4x\,\sqrt{-g}\left[\frac{R}{2\kappa} - \partial_\mu\phi^\star\partial^\mu\phi - V\left(\phi^\star\phi\right)\right], \tag{2.14}$$

with a potential

$$V(\phi^\star\phi) = \frac{\lambda}{2}\left(\phi^\star\phi - \frac{v^2}{2}\right)^2, \tag{2.15}$$

where ϕ is a complex scalar field (with $\phi^\star$ its complex conjugate), $\lambda > 0$ is a dimensionful coupling constant and v can be interpreted as the scale of the vacuum expectation value of ϕ, i.e. the magnitude of ϕ that minimizes $V\left(\phi^\star\phi\right)$.

In Minkowski space, quadratic k-essence is recovered at low energies when the $U(1)$ symmetry of action (2.14) is broken spontaneously [190]. When gravity is considered the same result holds at leading order. Indeed, by expanding ϕ around the degenerate vacuum of the potential,

$$\phi(x) = \frac{v}{\sqrt{2}}\left[1+\rho(x)\right]e^{i\theta(x)}\ , \tag{2.16}$$

it can be seen, by substituting in action (2.14), that the radial field $\rho(x)$ acquires a "mass" [2] $M_\rho = \sqrt{\lambda}\,v$, while the phase field $\theta(x)$ (i.e. the "Goldstone boson" [204])

[1] To be precise, this is a *partial* UV completion as it only describes the scalar degree of freedom at higher energies. A *full* UV completion would also describe the gravitational degrees of freedom, e.g. in a full theory of quantum gravity.

[2] In our units $c = 1$, the "mass" M_ρ is actually the inverse of the Compton wavelength, i.e.

remains massless. At energies much lower than M_ρ, one can use the equation of motion of the radial field, $-\Box\rho + (1+\rho)\,\partial_\mu\theta\partial^\mu\theta + v^{-2}\partial V/\partial\rho = 0$, to integrate it out of action (2.14). More precisely, one can solve perturbatively for ρ as

$$\rho = -\frac{1}{M_\rho^2}\partial_\mu\theta\partial^\mu\theta + \mathcal{O}\left(M_\rho^{-4}\right) \ , \tag{2.17}$$

and substitute in the action (2.14) to obtain the effective action for the phase field $\theta(x)$. The latter takes the same form as Eq. (2.1), i.e.

$$S_{\rm eff}\left[g_{\mu\nu},\theta\right] = \int d^4x\sqrt{-g}\left[\frac{R}{2\kappa} + v^2\left(-\frac{1}{2}\partial_\mu\theta\partial^\mu\theta + \frac{1}{2M_\rho^2}\left(\partial_\mu\theta\partial^\mu\theta\right)^2\right)\right] + \mathcal{O}(v^2M_\rho^{-4}\nabla^6) \ , \tag{2.18}$$

where $\mathcal{O}(v^2M_\rho^{-4}\nabla^6)$ denotes higher order terms (in M_ρ^{-2}) with at least six derivatives. Therefore, this UV completion reproduces the dynamics of quadratic k-essence at leading order, and the k-essence field is interpreted as given by the dimensionful "phase" field

$$\pi^{(\rm UV)}(x) = v\,\theta(x) \ . \tag{2.19}$$

Direct comparison between the actions (2.1) and (2.18) yields the relation between the coupling constants in the two theories,

$$\frac{\beta}{2\Lambda^4} = \frac{1}{M_\rho^2v^2} \geq 0 \ , \tag{2.20}$$

and selects the positive branch of quadratic k-essence (for which there is no screening mechanism in the presence of matter), consistently with positivity bounds [191]. At next-to-leading order, the higher order terms do not reproduce k-essence, since the UV completion introduces other six-derivative terms in addition to the cubic term appearing in Eq. (2.2) – see e.g. Ref. [190].

We now turn to the question of whether this UV completion admits a well-posed Cauchy problem. Since the scalar field ϕ is minimally coupled to the metric, the evolution equations for the metric are

$$G_{\mu\nu} = \kappa\,T^{(\phi)}_{\mu\nu} \ , \tag{2.21}$$

where now

$$T^{(\phi)}_{\mu\nu} = \nabla_\mu\phi^\star\nabla_\nu\phi + \nabla_\mu\phi\nabla_\nu\phi^\star - g_{\mu\nu}\left[\nabla^\sigma\phi\nabla_\sigma\phi + V\left(\phi^\star\phi\right)\right] \ . \tag{2.22}$$

the real mass is $m_\rho = M_\rho\hbar$.

As before, it can be shown that the system is strongly hyperbolic [205]. The scalar equation,

$$\Box\phi - \frac{\partial V}{\partial|\phi|^2}\phi = 0 \ , \tag{2.23}$$

is also manifestly strongly hyperbolic since it is a wave equation. We split the complex scalar

$$\phi = \phi_R + i\,\phi_I \tag{2.24}$$

in its real and imaginary parts, ϕ_R and ϕ_I. Then the associated characteristic speeds are given by

$$V_\pm^{(\phi_R)} = V_\pm^{(\phi_I)} = \pm\frac{\alpha}{\sqrt{g_{rr}}} \ , \tag{2.25}$$

which are always real and distinct (hence implying the existence of a complete set of eigenvectors).

2.2.2 Fixing the equations

The "fixing the equations" approach [192] (see also Refs. [154, 193]) provides a prescription to control the high frequency behavior of an EFT, which may be the cause of ill-posedness of the Cauchy problem. In the following, we will apply this prescription to k-essence. Unlike for the case of the $U(1)$ UV completion presented in the previous section, we do not make here any assumptions on the sign of β.

In order to deal with shocks (c.f. Sec. 2.3), it is convenient to rewrite the scalar equation (2.5) in conservative form (as made possible by the shift-symmetry of the theory):

$$\nabla_\mu \left(K'(X)\nabla^\mu\pi\right) = 0 \ . \tag{2.26}$$

Since large gradients may occur due to the $K'(X)$ factor, triggering a breakdown of the Cauchy problem, we "fix" the scalar equation (2.26) by replacing $K'(X)$ with a *new* dynamical field Σ, which in turn is prescribed to approach $K'(X)$ by a "driver" equation. The system of equations that we adopt (see also Ref. [179, 180]) is therefore

$$\nabla_\mu(\Sigma\nabla^\mu\pi) = 0 \ , \tag{2.27}$$

$$\tau\,\partial_t\Sigma = -\left[\Sigma - K'\left(X\right)\right] \ , \tag{2.28}$$

where τ is a constant timescale, whose precise value controls the rate of approach of Σ to $K'(X)$ and which damps frequencies ω in the range $\tau^{-1} \lesssim \omega$ [192, 206]. For the metric, the evolution equations remain unaltered and are given by Eq. (2.3).

The characteristic speeds of the "fixed" theory, for $\Sigma \neq 0$, are

$$V_{\pm}^{(\mathrm{FE})} = \pm \frac{\alpha}{\sqrt{g_{rr}}} \,, \tag{2.29}$$

with an additional speed $V_3^{(\mathrm{FE})} = 0$ due to the presence of the new variable Σ. These speeds are always real and distinct (hence implying the existence of a complete set of eigenvectors). Therefore, as long as $\Sigma \neq 0$, the system of equations of the "fixed" theory is strongly hyperbolic.

However, if Σ approaches zero during the evolution, a pathological situation occurs. This can be seen as follows: rewriting Eq. (2.27) as $\Sigma \Box\pi + \nabla_\mu \Sigma \nabla^\mu \pi = 0$, it is evident that when $\Sigma \to 0$ the principal part of this equation (i.e. the part consisting of the highest derivative terms) vanishes, and therefore the system (2.27)-(2.28) changes from second order to first order.

Finally, in contrast with the UV completion of Sec. 2.2.1, there are no restrictions on the sign of the quadratic k-essence coupling constant β, and the "fixing the equations" prescription can also be applied to the branch with screening ($\beta < 0$).

2.3 Methodology

In order to explore the well-posedness of the Cauchy problem and the nonlinear dynamics in k-essence, in its $U(1)$ UV completion and in the "fixing the equations" approach, the fully nonlinear equations must be considered. In the following, we present the evolution equations in a 1+1 decomposition of the spacetime restricted to spherical symmetry and describe the details of our numerical implementation. First, in Sec. 2.3.1 we present the evolution equations for the scalar sector in a first-order conservative form. We specify our working units in Sec. 2.3.3 and then, in Sec. 2.3.2 we describe in detail the procedure used to construct initial data. In Sec. 2.3.4, we describe the numerical evolution scheme and code. Finally, in Sec. 2.3.5, we describe additional diagnostic tools needed to compare and interpret our numerical simulations.

2.3.1 Evolution equations

We decompose the metric into space and time components by using the line element in spherical symmetry given by Eq. (A.2). In the 1+1 decomposition, the

Einstein equations [Eq. (2.3) for k-essence and the "fixed" theory and Eq. (2.21) for the $U(1)$ UV completion] can be written in first-order form [analogous to Eq. (2.33)] by using the $Z3$ formulation, which is strongly hyperbolic [207–209] – see Appendix A for more details. We write the evolution equations for the metric as a first order system by defining the variables

$$A_r = \frac{1}{\alpha}\partial_r\alpha \ , \qquad D_{rr}{}^r = \frac{1}{2g_{rr}}\partial_r g_{rr} \ , \qquad D_{r\theta}{}^\theta = \frac{1}{2g_{\theta\theta}}\partial_r g_{\theta\theta} \ , \tag{2.30}$$

and the extrinsic curvature

$$K_{ij} = -\frac{1}{2}\mathcal{L}_n g_{ij} \ , \tag{2.31}$$

where g_{ij} is the spatial metric and $n_\mu = (-\alpha, 0)$ is the normal vector to the foliation. We close the evolution system by prescribing the singularity-avoidance 1+log slicing condition, $\partial_t \log\alpha = -2\,\mathcal{K}$, where the trace of the extrinsic curvature is $\mathcal{K} = K_r{}^r + 2K_\theta{}^\theta$ [210]. The final set of evolution fields for the $Z3$ formulation in spherical symmetry can be found in Appendix A.

In the following, we will also describe the scalar equation in k-essence, in its $U(1)$ UV completion and in the "fixing the equations" approach, and write it in first-order form.

2.3.1.1 Quadratic k-essence

Defining the following first-order variables

$$\Phi = \partial_r\pi \ , \qquad\qquad \Pi = -\frac{1}{\alpha}\partial_t\pi \ , \tag{2.32}$$

one can write the scalar equation (2.5) in first-order conservative form as

$$\begin{aligned} &\partial_t\pi + \alpha\Pi = 0 \ , \\ &\partial_t\Phi + \partial_r[\alpha\Pi] = 0 \ , \\ &\partial_t\Psi + \partial_r F_\Psi = -\frac{2}{r}F_\Psi \ , \end{aligned} \tag{2.33}$$

where

$$\Psi = \sqrt{g_{rr}}\, g_{\theta\theta} K'(X)\,\Pi \ , \tag{2.34}$$

$$F_\Psi = \frac{\alpha g_{\theta\theta}}{\sqrt{g_{rr}}} K'(X)\,\Phi \ . \tag{2.35}$$

At each time step, Π is obtained (numerically) by solving the non-linear equation (2.34).

2.3.1.2 $U(1)$ UV completion

For the $U(1)$ UV completion, the scalar equation (2.23) defines two real systems of equations for the real ϕ_R and imaginary ϕ_I parts. As before, we define the first-order scalar variables

$$\Phi_{R,I} = \partial_r \phi_{R,I} \ , \qquad \Pi_{R,I} = -\frac{1}{\alpha}\partial_t \phi_{R,I} \ . \tag{2.36}$$

Then, the real scalar system for $\phi_{R,I}$ can be written as

$$\begin{aligned} &\partial_t \phi_{R,I} + \alpha \Pi_{R,I} = 0 \ , \\ &\partial_t \Phi_{R,I} + \partial_r [\alpha \Pi_{R,I}] = 0 \ , \\ &\partial_t \Pi_{R,I} + \partial_r \left[\frac{\alpha}{g_{rr}} \Phi_{R,I} \right] = S_{\Pi_{R,I}} \ , \end{aligned} \tag{2.37}$$

with source term

$$\begin{aligned} S_{\Pi_{R,I}} = \alpha \Bigg[&\left(K_r{}^r + 2K_\theta{}^\theta \right) \Pi_{R,I} + \\ &- \frac{1}{g_{rr}} \left(\frac{2}{r} + D_{rr}{}^r + 2D_{r\theta}{}^\theta \right) \Phi_{R,I} + \frac{\partial V}{\partial |\phi|^2} \phi_{R,I} \Bigg] \ . \end{aligned} \tag{2.38}$$

2.3.1.3 Fixing the equations

Finally, for the "fixed" theory, the first order system of equations can be written in the same form as in k-essence (Sec. 2.3.1.1), but replacing $K'(X) \to \Sigma$ and including the "driver" equation (2.28).

2.3.2 Initial data

We will now describe in detail the construction of initial data in isotropic coordinates, corresponding to an initially stationary scalar "shell" in k-essence (Sec. 2.3.2.1). We will then comment on how this procedure can be generalized to the $U(1)$ UV completion (Sec. 2.3.2.2) and the "fixed" theory (Sec. 2.3.2.3).

2.3.2.1 Quadratic k-essence

On the initial slice at time $t = 0$, we adopt isotropic coordinates given by

$$ds^2 = -\alpha^2(r)\, dt^2 + \psi^4(r) \left(dr^2 + r^2\, d\Omega^2 \right) \ , \tag{2.39}$$

and prescribe the initial profile of the lapse function to be constant and equal to unity – i.e. $\alpha(r)|_{t=0} = 1$.

In these coordinates, the Hamiltonian and momentum constraints for k-essence take the form

$$\frac{1}{r^2}\frac{\partial}{\partial r}\left(r^2\frac{\partial\psi}{\partial r}\right) = \frac{1}{4}\psi^5 K_\theta{}^\theta\left(2K_r{}^r + K_\theta{}^\theta\right) + P\left[\alpha,\psi,\partial_t\pi,\partial_r\pi,\pi\right] \ , \tag{2.40}$$

$$\frac{\partial K_\theta{}^\theta}{\partial r} = \frac{1}{r\psi}\left(K_r{}^r - K_\theta{}^\theta\right)\left(\psi + 2r\frac{\partial\psi}{\partial r}\right) + Q\left[\alpha,\psi,\partial_t\pi,\partial_r\pi,\pi\right] \ , \tag{2.41}$$

respectively, where

$$\begin{aligned} P[\alpha,\psi,\partial_t\pi,\partial_r\pi,\pi] &= \frac{1}{4}\kappa\psi^5\left[K\left(X\right) + 2\Pi^2 K'\left(X\right)\right] \ , \\ Q[\alpha,\psi,\partial_t\pi,\partial_r\pi,\pi] &= \kappa\,\Pi\Phi K'\left(X\right) \ . \end{aligned} \tag{2.42}$$

We will consider initially stationary configurations by imposing $\partial_t\pi = K_\theta{}^\theta = \mathcal{K} = 0$ for which $K_r{}^r$ and $Q \equiv 0$. Therefore, Eq. (2.41) is trivially satisfied and we only need to solve Eq. (2.40) for ψ.

The initial profile for the k-essence field [the *free data* in Eqs. (2.40)-(2.41)] is specified as

$$\begin{aligned} \partial_r\pi|_{t=0} &= A\exp\left[-\frac{\left(r-r_c\right)^2}{\sigma^2}\right]\cos\left(\frac{\pi}{10}r\right) \ , \\ \partial_t\pi|_{t=0} &= 0 \ , \end{aligned} \tag{2.43}$$

where A is the amplitude of the pulse, and r_c and σ are parameters specifying the location and root-mean-square width of the Gaussian envelope of the pulse. Note that this form resembles the initial data used in Ref. [185].

We implement our initial data solver in *Mathematica* [211]. First, regularity at the origin is imposed by solving Eq. (2.40) perturbatively near the origin. The perturbative solution for $\psi(r)$, which depends on one integration constant $\psi(0)$, is then used as initial data in an outward-bound integration (in radius) starting from a small non-zero radius. Finally, using a shooting method, we fix $\psi(0)$ by requiring that the exterior Robin boundary condition

$$-1 + \psi + r\frac{\partial\psi}{\partial r}\bigg|_{r\to\infty} = 0 \tag{2.44}$$

is satisfied. Note that this boundary condition corresponds to imposing that ψ reduces to the asymptotically flat solution of Eq. (2.40) (c.f. Birkhoff's Theorem [30]), $\psi\left(r\to\infty\right) \approx 1 + m_0/\left(2r\right)$, where m_0 is the (unknown) Arnowitt-Deser-Misner (ADM) mass.

2.3.2.2 $U(1)$ UV-completion

The construction of the initial data for the metric variables proceeds as in Sec. 2.3.2.1. In this case, the P and Q terms in Eqs. (2.40)-(2.41) are replaced by

$$P[\alpha,\psi,\partial_t\phi_{R,I},\partial_r\phi_{R,I},\phi_{R,I}] = -\frac{1}{8}\kappa\psi\left[\psi^4\left(\Pi_R^2+\Pi_I^2\right)+\Phi_R^2+\Phi_I^2+\psi^4 V\left(\phi^\star\phi\right)\right] ,$$
$$Q[\alpha,\psi,\partial_t\phi_{R,I},\partial_r\phi_{R,I},\phi_{R,I}] = -\frac{1}{2}\kappa\left(\Pi_R\Phi_R+\Pi_I\Phi_I\right) . \tag{2.45}$$

From the initial profile of the k-essence (phase) field [Eqs. (2.43)], we can construct the initial configurations for the fields $\phi_{R,I}$ by direct application of Eqs. (2.16) and (2.17).

Finally, let us comment on a subtlety regarding the initial profile for the complex scalar field. When specifying the initial configuration of the radial field ρ [Eq. (2.17)], one needs to provide also information on the configuration of the metric function $\psi(r)$ in k-essence, which we denote by $\psi^K(r)$. The latter is obtained from the solution of the Hamiltonian constraint [Eq. (2.40)]. This complicates the solution of Eq. (2.40) for the $U(1)$ UV completion, since it would require the use of an interpolated function for $\psi^K(r)$. For the cases that we consider below, $\psi^K(r)\approx 1$. Thus, we avoid this problem by using the *approximation* $\psi^K(r)\equiv 1$ in Eq. (2.17). We stress that the Hamiltonian constraint [Eq. (2.40)] in this UV completion *should not* be solved by considering $\psi^K(r)=\psi(r)$.

2.3.2.3 Fixing the equations

The initial data in the "fixing the equations" approach is prescribed in exactly the same way as in Sec. 2.3.2.1. The only additional information that we need to include is the initial profile of the Σ field, which we specify to be

$$\Sigma|_{t=0} = K'(X)|_{t=0} . \tag{2.46}$$

2.3.3 Units

For convenience in the numerical implementation, we will measure physical quantities with respect to the following energy, length and time units $E_\Lambda\equiv\Lambda^{-2}\kappa^{-3/2}$, $L_\Lambda\equiv\Lambda^{-2}\kappa^{-1/2}$, and $T_\Lambda\equiv L_\Lambda$, respectively.

2.3.4 Evolution scheme

For this Chapter, we extend the code of Ref. [209], which was initially written for one dimensional black hole simulations, but which was later adapted in Refs. [212] to perform dynamical evolutions of boson stars, fermion-boson

stars [213], anisotropic stars [214], and also in Refs. [113, 179, 186] and in Ref. [215] for neutron stars in k-essence and chameleon screening, respectively. The metric equations are evolved using a high-resolution shock-capturing finite-difference (HRSC) scheme, described in Ref. [209, 216], to discretize the spacetime variables. This method can be interpreted as a fourth-order finite difference scheme plus third-order adaptive dissipation, where the dissipation coefficient is given by the maximum propagation speed at each grid point. For the scalar field sector, a more robust HRSC second-order method is employed, which is based on the Local-Lax-Friedrichs flux formula with a monotonic-centred limiter [217]. Integrations in time are carried out through the method of lines, by using a third-order accurate strong stability preserving Runge-Kutta integration scheme, with a Courant factor of $\Delta t/\Delta r = 0.25\, T_\Lambda/L_\Lambda$, such that the Courant-Friedrichs-Levy condition is satisfied.

We have used a spatial resolution of $\Delta r = 0.01\, L_\Lambda$ and a spatial domain with outer boundary located at $r = 480\, L_\Lambda$. We have checked that the results do not vary significantly with the position of the outer boundary or with resolution. For the spacetime variables, we use maximally dissipative boundary conditions, whereas for the scalar fields we use outgoing boundary conditions.

2.3.5 Diagnostic quantities

In the $U(1)$ UV completion, the phase field derivatives can be computed at each time step from

$$\partial_r \pi = v \left(\frac{\phi_R \partial_r \phi_I - \phi_I \partial_r \phi_R}{\phi_R^2 + \phi_I^2} \right), \tag{2.47a}$$

$$\partial_t \pi = v \left(\frac{\phi_R \partial_t \phi_I - \phi_I \partial_t \phi_R}{\phi_R^2 + \phi_I^2} \right). \tag{2.47b}$$

The phase field $\pi(t, r)$ itself, which at low energies is expected to reduce to the k-essence field, can be obtained by integrating Eq. (2.47b) along with the evolution equations. In the "fixing the equations" approach, this procedure is instead not needed.

Once the phase field and its derivatives are known, one can compute the k-essence "characteristic speeds" from Eq. (2.9). We emphasize, however, that the *true* characteristic speeds in the $U(1)$ UV completion and in the "fixed" theory are given by Eqs. (2.25) and (2.29), respectively.

If an apparent horizon (defined as the outermost trapped surface) is present, its location $r_{\rm AH}$ is given by the zeros of the expansion of outgoing null rays

[Eq. (4.4) of Ref. [186]] [3]

$$\Theta = \frac{1}{\sqrt{g_{rr}}}\left(2D_{r\theta}{}^{\theta} + \frac{2}{r}\right) - 2K_{\theta}{}^{\theta} \ . \tag{2.48}$$

Similarly, for the k-essence field, we find the location of a sound horizon (if present) by looking for the zeros of the expansion of outgoing null rays with respect to the effective metric $\gamma^{\mu\nu}$ [Eq. (4.5) of Ref. [186]],

$$\mathcal{S} = r^2 g_{\theta\theta}\left[(rD_{r\theta}{}^{\theta}+2)^2\gamma^{rr} + rK_{\theta}{}^{\theta}\alpha\left(r\gamma^{tt}K_{\theta}{}^{\theta}\alpha - 2\left(rD_{r\theta}{}^{\theta}+2\right)\gamma^{tr}\right)\right] . \tag{2.49}$$

Finally, we compare the evolutions in two theories A and B by calculating a *discrepancy* measure for a given field χ as

$$\mathbb{E}_{A,B}\left[\chi\right](t) = \frac{\left\|\chi^{(A)} - \chi^{(B)}\right\|_{\rm AH}}{\left\|\chi^{(B)}\right\|_{\rm AH}} \ , \tag{2.50}$$

where the L_2-norm of a function ξ is defined as

$$\|\xi\|^2_{\rm AH} = \int_{\max_{A,B}(r_{\rm AH})}^{\infty} |\xi(t,r)|^2 \ dr \ , \tag{2.51}$$

with integration domain only covering the exterior of the apparent horizons $r_{\rm AH}$ of *both* theories A and B. This measure is inspired in a similar measure introduced for Minkowski space in Ref. [193].

2.4 Results

In this section, we will compare the dynamics of quadratic k-essence, the $U(1)$ UV completion and the "fixed" theory during the gravitational collapse of a scalar "shell". We will first study in Sec. 2.4.1 the initial stage of gravitational collapse, when the Cauchy problem in k-essence is well-posed, and confirm that the $U(1)$ UV and the "fixed" theory reproduce the same dynamics of quadratic k-essence. After a Tricomi-type breakdown of k-essence, we will continue the evolution with the $U(1)$ UV completion and the "fixed" theory to determine in Sec. 2.4.2 that the endstate of the system corresponds to that of a black hole. Finally, in Sec. 2.4.3, we will show that the system enters the nonlinear regime and compare the dynamics of the $U(1)$ UV completion and the "fixed" theory within it. This will serve as a "validation" test of the "fixing the equations" approach in a setting where we have access to the UV physics, and it will also allow us to explore the relation between the nonlinear regime and the range of validity of the EFT. Additional

[3] We correct here a typo in Eq. (4.4) in Ref. [186].

comments for the case of a large coupling constant β are given in Sec. 2.4.4. In the following, we will explore the case corresponding to initial data [Eq. (2.43)] generated with parameters $r_c = 55\,L_\Lambda$, $\sigma = 1.5\,L_\Lambda$, and $A = 0.14\,L_\Lambda$ and coupling constants $\beta = 1$, $M_\rho^2 = 2\,L_\Lambda^{-2}$, $v^2\,E_\Lambda^{-1}L_\Lambda = 1$ and $\tau\,T_\Lambda^{-1} = 1$. In Appendix B.1, we present an additional example with weak initial data, where no breakdown of the Cauchy problem or black hole formation occurs.

2.4.1 EFT evolution and Tricomi-type breakdown

By construction, the initial radial profile of the k-essence field $\pi|_{t=0}$ agrees with the profiles from the $U(1)$ UV completion phase field $\pi^{(\mathrm{UV})}|_{t=0}$ and from the π-field of the "fixed" theory. [Recall that in the $U(1)$ UV completion, the k-essence field is described at low energies by the (dimensionful) phase mode [Eqs. (2.16)] and (2.19) of the complex scalar ϕ and needs to be computed from Eqs. (2.47).] The initial data for the metric variables, obtained after solving the constraint equations, is also in agreement. In particular, for the $U(1)$ UV completion, this is not a trivial statement, as the agreement in the metric occurs because the extra degree of freedom (the radial mode of the complex scalar [Eq. (2.16)]) contains a negligible fraction of the scalar energy content. Thus, we can say that the initial data is in the regime of validity of the EFT description of k-essence.

In the early stage of collapse in k-essence, from $t = 0$ to $t \sim 55\,T_\Lambda$, the scalar pulse splits into an in-going (collapsing) pulse travelling towards the origin, and into an out-going (radiated) pulse moving towards the outer boundary of the numerical grid. In the following, we will concentrate on the former. This stage is reproduced by the $U(1)$ UV completion and the "fixed" theory. In Fig. 2.1, in the first panel, we can observe that the k-essence scalar field at $t \sim 50\,T_\Lambda$ and $r \sim 7\ L_\Lambda$ is almost indistinguishable in the $U(1)$ UV completion and in the "fixed" theory. We quantify this agreement by plotting the absolute difference of these profiles in the second panel. In the third and fourth panels, we also plot the relative difference of g_{rr} and $g_{\theta\theta}$, respectively, showing that the metric is also very well recovered, with a relative error of $\lesssim 0.01\%$.

As the pulse approaches the origin, the k-essence scalar gradients increase. At $t \sim 56.5\,T_\Lambda$, large gradients trigger a Tricomi-type breakdown, by which the scalar equation (2.5) transitions from hyperbolic to parabolic and then elliptic. From the discussion in Sec. 2.2, this occurs when, at any point of the spatial grid, the determinant of the effective metric (2.6) vanishes, or equivalently, when at least one eigenvalue of the latter becomes zero. We can gain some insight by tracking the spatial maximum and minimum of the eigenvalues of the effective metric [Eq. (2.11)] as a function of time, as can be seen in the first panel of Fig. 2.2. Note that for the $U(1)$ UV completion and the "fixed" theory, the effective metric

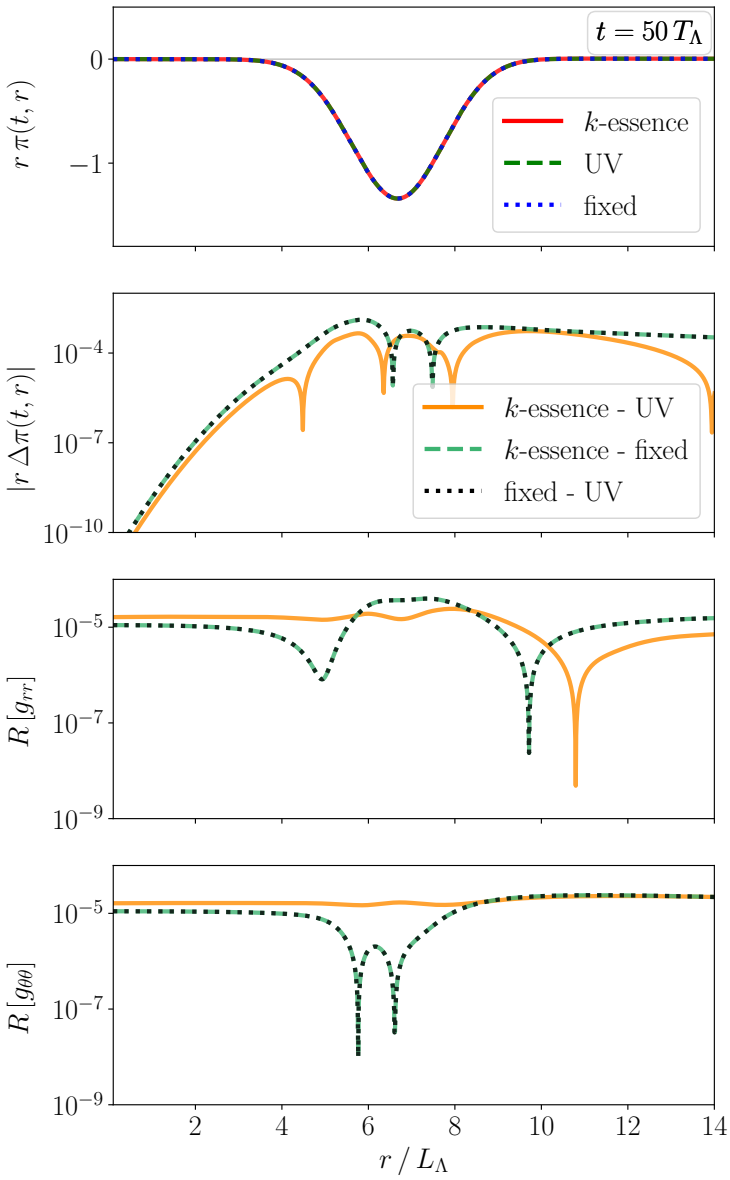

Figure 2.1: *EFT evolution.* First panel: The radial profile of the k-essence field multiplied by r, at time $t = 50\,T_\Lambda$ (red solid line) compared with the phase field of the $U(1)$ UV completion (green dashed line) and the π-scalar of "fixed" theory (blue dotted line), showing that they are indistinguishable from each other. Second panel: Absolute differences $\Delta\pi \equiv \pi^{(A)} - \pi^{(B)}$ for theories A vs. B; namely, k-essence vs. UV (orange solid lines), k-essence vs. "fixed" (light green dashed lines) and "fixed" vs. UV (black dotted lines). Third and fourth panels: relative differences, $R\,[g] \equiv \left|\left(g^{(A)} - g^{(B)}\right)/g^{(B)}\right|$, of the metric functions $g = g_{rr}, g_{\theta\theta}$ for theories A vs. B.

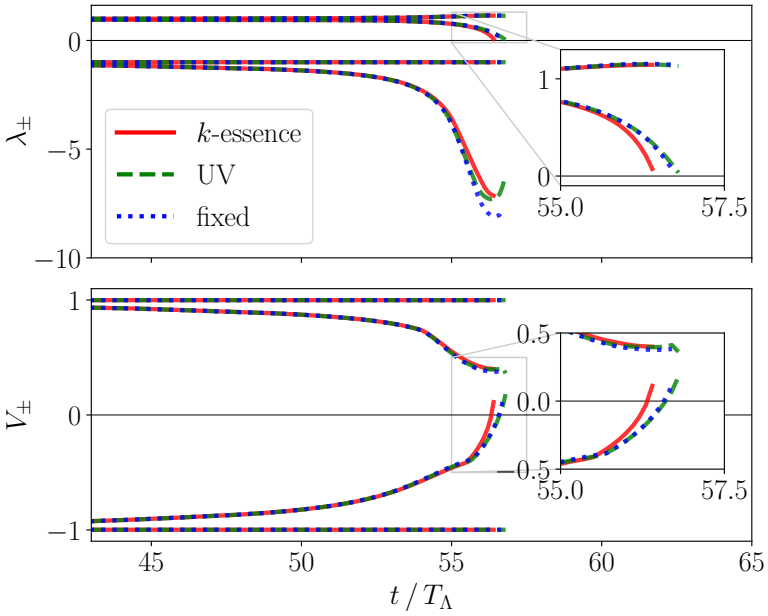

Figure 2.2: *Character of the k-essence scalar equation.* First panel: the minimum and maximum values of the eigenvalues of the effective metric in k-essence (red solid line), $U(1)$ UV completion (green dashed line) and the "fixed" theory (blue dotted line). For the last two, the effective metric is not a fundamental quantity but "emergent" at low energies. From top to bottom: $\max(\lambda_+)$, $\min(\lambda_+)$, $\max(\lambda_-)$, $\min(\lambda_-)$. The Tricomi-type breakdown is signaled by $\min\lambda_+ \to 0$ at $t \sim 56.5\,T_\Lambda$. Second panel: the minimum and maximum values of the characteristic speeds. In this panel, from top to bottom: $\max(V_+)$, $\min(V_+)$, $\max(V_-)$, $\min(V_-)$. Notice that, at $t \sim 56.5\,T_\Lambda$, $|\min(V_+) - \max(V_-)| \to 0$, signaling a Tricomi-type breakdown.

is not a fundamental but an "emergent" quantity, therefore, these eigenvalues have been computed from Eqs. (2.11) and (2.47). Initially, $\lambda_\pm \approx \pm 1$. As the evolution progresses, the Tricomi-type breakdown is signaled in this plot by one of the eigenvalues approaching zero. Specifically, we observe that $\min(\lambda_+) \to 0$. In the second panel, we plot the spatial maximum and minimum values of the characteristic speeds of k-essence [Eq. (2.9)] as a function of time. In the early evolution, the system is clearly strongly hyperbolic since $V_\pm$ are real and distinct. As the pulse approaches the origin, first, we observe the formation of a sound horizon (roughly when $\max(V_-) \approx 0$[4]). Then, the Tricomi-type breakdown occurs when the characteristic speeds become equal. Indeed, we observe that $|\min(V_+) - \max(V_-)| \to 0$, indicating that strong hyperbolicity is lost[5]. Note that, as before, for the $U(1)$ UV completion and the "fixed" theory, the values of $V_\pm$ have been computed using Eqs. (2.9) and (2.47).

[4]As mentioned earlier, we define the location of the (apparent) sound horizon as the zero of the effective metric's null ray expansion (2.49). In areal coordinates, that condition is exactly equivalent to $V_- = 0$, and this equivalence carries on (albeit approximately) also in the isotropic coordinates that we utilize.

[5]This is actually a necessary and not sufficient condition for the loss of hyperbolicity, but we have checked that the effective metric also becomes degenerate when $V_+ = V_-$.

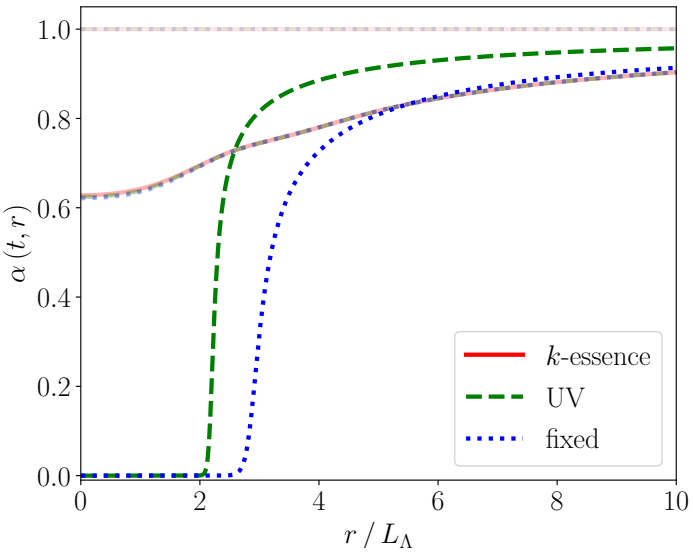

Figure 2.3: *Gravitational collapse of the pulse.* Radial profiles of the lapse α at times $t/T_\Lambda = 30,\ 55,\ 80$ in k-essence (red solid lines), $U(1)$ UV completion (green dashed lines) and the "fixed" theory (blue dotted lines). Increasing times are denoted by increasing intensity of the color. The lapse approaching zero near the origin is a typical effect signaling the formation of a black hole. Note that k-essence experiences a Tricomi breakdown at $t \sim 55.6\,T_\Lambda$, much before any apparent horizon formation.

We argue that the change of character of the scalar equation (2.5) occurs within the EFT regime since all three theories predict that the effective metric becomes degenerate (corresponding to a Tricomi transition in the low energy k-essence theory) at similar times. Past this point, only with the $U(1)$ UV completion and the "fixed" theory, for which the Cauchy problem remains well-posed, can the scalar and metric be evolved smoothly and the final fate of the system be predicted.

2.4.2 Endstate

In both the $U(1)$ UV completion and the "fixed" theory, the system collapses to form a black hole. In Fig. 2.3, we show the lapse function approaching zero near the origin at different representative times, a typical behavior leading up to the formation of a black hole [205]. We confirm this conclusion by identifying the appearance of an apparent horizon, which we indicate with solid vertical lines in Fig. 2.6. For the "fixed" theory, we have checked that the final state is a black hole when varying $\tau/T_\Lambda \in [1, 10]$. This endstate remains inaccessible with the low-energy k-essence model, where the Tricomi-type breakdown occurs well before the lapse gets close to zero.

With our numerical implementation (Sec. 2.3.4), we can only track the evolution of the black hole horizon for some time after formation. This is due to

the formation of steep gradients in the collapse front of the lapse [209]. Finally, in the $U(1)$ UV completion, the final area is $A_{\rm BH} = 4\pi\mathcal{R}^2_{\rm AH} \sim 5.2\, L^2_\Lambda$, where $\mathcal{R}_{\rm AH} \sim 0.64\, L_\Lambda$ is the polar radius of the apparent horizon. In the "fixed" theory, the initial value of the black hole area is $A_{\rm BH} \sim 7.1\, L^2_\Lambda$ (37% larger) with $\mathcal{R}_{\rm AH} \sim 0.75\, L_\Lambda$ (17% larger). However, we cannot accurately determine the final value of the area due to additional constraint violation contributions with respect to the $U(1)$ UV completion: in the "fixed" theory the stress-energy tensor is only strictly conserved in the limit $\Sigma \to K'(X)$, thus, the Hamiltonian constraint time derivative is only strictly vanishing in the limit $\Sigma \to K'(X)$. We will elaborate on this point in Appendix B.2.

2.4.3 Nonlinear vs. UV regime

Having confirmed that the k-essence dynamics is recovered at early times (Sec. 2.4.1) and that the evolution can be continued past the Tricomi transition to determine the final fate of the system (Sec. 2.4.2), we will now proceed to compare the $U(1)$ UV completion and the "fixed" theory in the nonlinear regime. This will allow us to explore the relation between the latter and the range of validity of the EFT (defined by the difference between the $U(1)$ UV completion and quadratic k-essence evolved within the "fixing the equations" approach).

To establish whether the dynamics enters the nonlinear regime, we monitor the ratio of the first k-essence self-interaction operator to the kinetic term, i.e. $\mathrm{NL} \equiv |\beta\Lambda^{-4}X| = \left|2M_\rho^{-2}v^{-2}X\right|$. As can be seen, this can be rewritten, using Eqs. (2.1) and (2.17), as simply $\mathrm{NL} = 2\,|\rho|$. One therefore expects the nonlinear regime [i.e. $\mathrm{NL} \sim \mathcal{O}(1)$] to be closely related, if not equivalent, to the range of validity of the low energy theory, to which the $U(1)$ UV completion only reduces when ρ becomes non-dynamical and can be integrated out (thus implying that $\mathrm{NL} = 2\,|\rho|$ is small). We will verify this conjecture with our numerical simulations in the following.

Let us first analyze when the nonlinear regime is attained. In Fig. 2.4, we plot the spatial maximum of NL as a function of time in the region outside the apparent horizon (if present). We denote this quantity as $\max_{\rm AH}(\mathrm{NL})$. During the early evolution, this ratio is small, signaling that the dynamics is linear. However, as the pulse approaches the origin and scalar gradients grow, both the $U(1)$ UV completion and the "fixed" theory enter the nonlinear regime. In particular, for the "fixed" theory, the growth of the gradients within the nonlinear regime is damped in comparison to the $U(1)$ UV completion, and we observe a milder growth in $\max_{\rm AH}(\mathrm{NL})$. Recall that in the "fixed" theory, high frequency modes are suppressed by construction. Finally, once the black hole forms, the nonlinear regions become hidden behind the apparent horizon, and we observe a

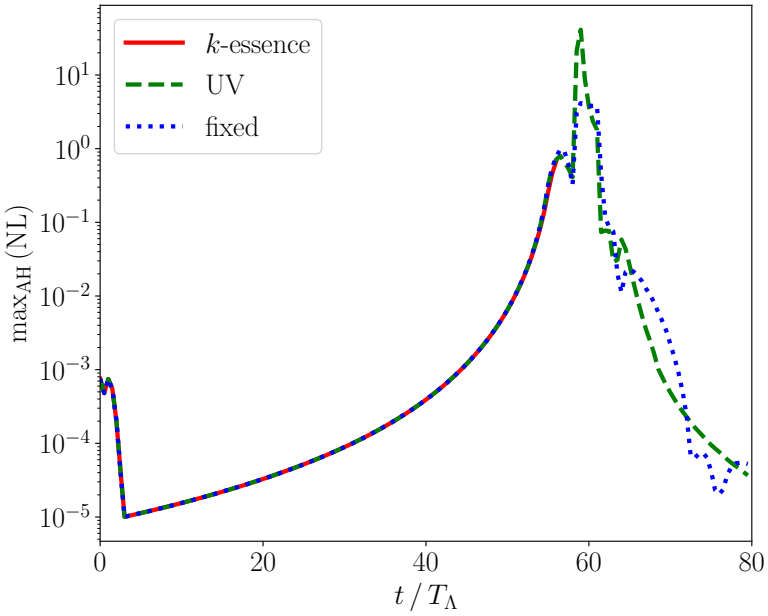

Figure 2.4: *Nonlinear regime assessment.* The spatial maximum of the ratio of the self-interaction term to the kinetic term for k-essence (red solid line), the $U(1)$ UV completion (green dashed line) and the "fixed" theory (blue dotted line). The maximum is taken in the region outside the apparent horizon, if present. During the early evolution, this measure is small ($\lesssim 10^{-2}$). As the pulse approaches the origin, the system enters the nonlinear regime $\max_{\rm AH}\,({\rm NL}) \sim \mathcal{O}(1)$, shortly after the Tricomi transition at $t \sim 56.5\,T_\Lambda$. This measure decreases in the later stage once the black hole is formed and nonlinearities are hidden behind the apparent horizon.

decrease in $\max_{\rm AH}\,({\rm NL})$.

We now proceed to compare the k-essence (phase) field profiles in the nonlinear regime. In Fig. 2.5, we plot the *discrepancy* measure $\mathbb{E}_{AB}\,[\pi]$, between the k-essence scalar profiles of theories A and B, as defined in Eq. (2.50). (Note that the plot for the discrepancy of the kinetic energy X would look qualitatively similar and lead to the same conclusions.) We denote in colored diamonds the approximate time of formation of sound horizons, and in colored squares the approximate time of formation of apparent horizons in each theory. We focus on the discrepancy between the "fixed" theory (theory A) and the $U(1)$ UV completion (theory B), plotted in blue dotted lines. This provides a measure of how much the EFT and UV dynamics differ, i.e. it allows for understanding the range of validity of the EFT. During the early evolution the agreement is clear ($\mathbb{E}_{AB}\,[\pi] < 10^{-3}$), i.e. the EFT is a good description of the full dynamics. As the system enters the nonlinear regime, indicated with a black star, the discrepancy increases to $\mathcal{O}\,(1)$, which would seem to indicate that the dynamics exits the range of validity of the (fixed) low energy EFT. However, the comparison of the scalar profiles is subtle and we should examine them in more detail.

In Fig. 2.6, in the left panels, we show snapshots of the scalar profiles of the k-essence (phase) field close to when the nonlinear regime is reached, as well as

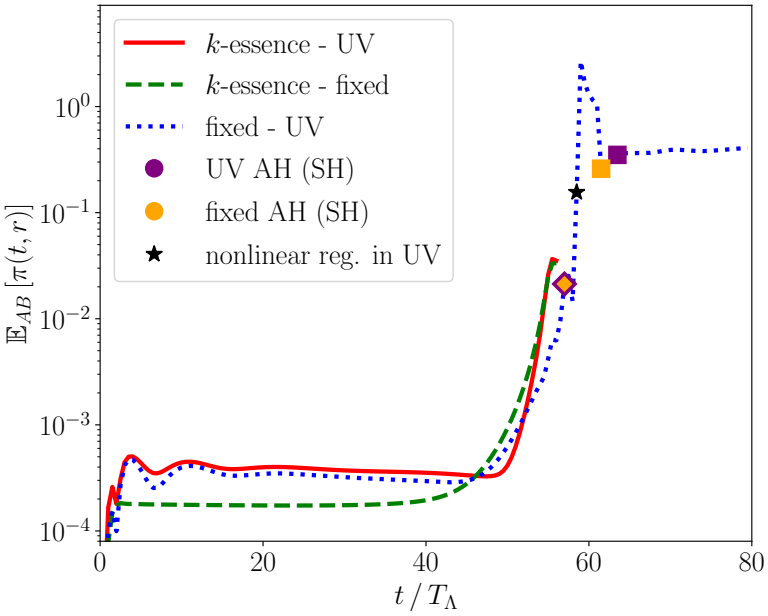

Figure 2.5: *Discrepancy of the k-essence scalar.* The discrepancy measure $\mathbb{E}_{AB}$ of the k-essence scalar π of theories A vs. B, defined in Eq. (2.50); namely, k-essence vs. $U(1)$ UV completion (red solid line), k-essence vs. "fixed" theory (green dashed line), and "fixed" theory vs. $U(1)$ UV completion (blue dot-dashed line). The discrepancy measures involving k-essence stop at the Cauchy breakdown of the theory. The colored diamonds and square markers, denote the (approximate) time of formation of the sound horizon (SH) and apparent horizon (AH) in each theory, respectively. Note that, the diamonds are superposed since both theories agree in the EFT regime. The black star marker denotes the approximate time where $\max_{\rm AH}\,({\rm NL}) \approx 1$ in the $U(1)$ UV theory –see also Fig. 2.4.

at later times. In the top left panel, at $t = 55\,T_\Lambda$, and right before the Tricomi transition, we observe that the scalar field is indistinguishable in k-essence, in the $U(1)$ UV theory and in the "fixed" theory. In the following panels, only the profiles of the last two theories are shown, as k-essence undergoes a Cauchy (Tricomi) breakdown, as mentioned earlier. We notice that the scalar profile of the "fixed" theory exhibits a qualitatively similar behavior of that of the $U(1)$ UV theory. From this figure, the $\mathcal{O}(1)$ discrepancies in Fig. 2.5 are then seen to originate mostly as a consequence of a "lag" between the scalar profiles. Once the black hole forms, the largest sources of discrepancy are hidden behind the apparent horizon, as can be seen for times $t \gtrsim 61\,T_\Lambda$ in Fig. 2.5. From the right panels of Fig. 2.6, we notice that the "fixed" theory also qualitatively follows the radiated (outgoing) scalar field of the $U(1)$ UV completion. Note that the observed difference in amplitude is small but is magnified by the factor r. In Fig. 2.5 it can be seen that the discrepancy is approximately $\mathcal{O}\,(10^{-1})$.

The observed "lag" in Fig. 2.6 can be traced, at least partly, to the form of the "driver" equation [Eq. (2.28)] and its associated timescale τ, which controls how fast the field Σ relaxes to $K'\,(X)$. By decreasing (increasing) the value of τ, we

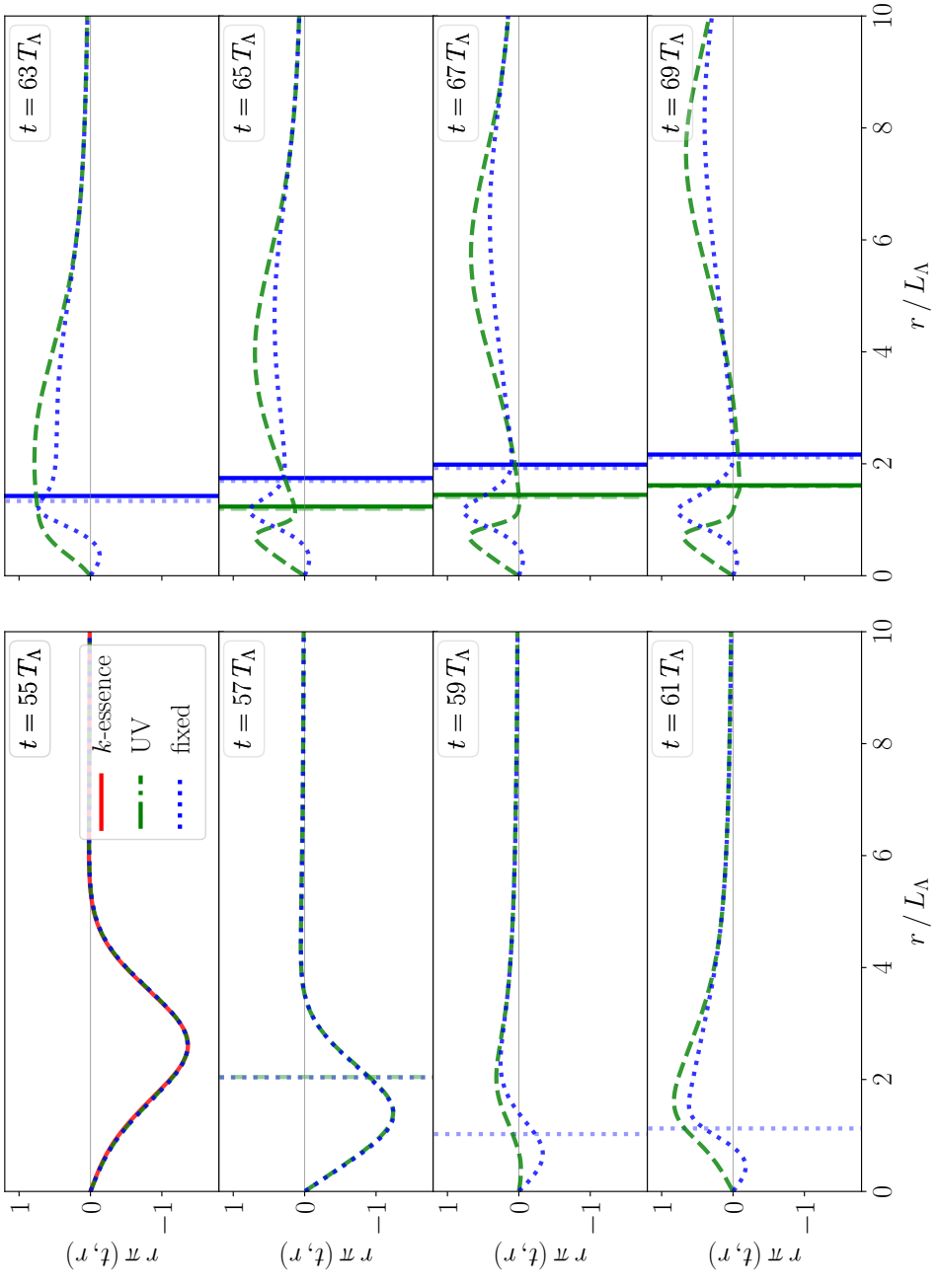

Figure 2.6: *Dynamics of the pulse in the nonlinear regime.* Time snapshots of the k-essence scalar for representative times from $t = 55\,T_\Lambda$ to $t = 69\,T_\Lambda$ for k-essence (red solid lines), the phase field of the $U(1)$ UV completion (green dashed lines) and the π-scalar of the "fixed" theory (blue dotted lines). The profiles corresponding to the quadratic model of k-essence exist only up to the Tricomi-type breakdown of the theory (at $t \sim 56.5\,T_\Lambda$), and hence, they are only shown in the first panel. The "fixed" theory exhibits a qualitatively similar behavior to that of the $U(1)$ UV completion. The solid vertical lines indicate the location of the apparent horizon, while the dashed and dotted vertical lines denote the location of the low-energy sound horizon. The appearance and disappearance of the sound horizon between frames $t = 57\,T_\Lambda$ and $t = 65\,T_\Lambda$ occurs due to the theory entering the nonlinear/UV regime. The singularity-avoidance prescription chosen for the lapse causes the "freezing" of the scalar profile near the origin, once the black hole forms.

can partly reduce (increase) the "lag" in scalar profiles. Other sources of "delay" may be due to the slightly different evolution of the lapse in the two theories – see Fig. 2.3. The latter observation illustrates that one must be careful when comparing fixed time scalar profiles from different evolutions. To overcome these ambiguities, better measures of comparison may be defined from observables such as the scalar radiation detected by an asymptotic observer –see e.g. Ref. [180].

Finally, we briefly comment on the low-energy sound horizons, which form prior to the formation of the black hole. Since physical modes in the $U(1)$ UV completion move along null geodesics [c.f. Eq. (2.23)] and are no longer (at least in principle) well described by the k-essence scalar equation (2.5), the sound horizons may lose physical meaning. This causes a strange behavior of the sound horizon in our simulations, as illustrated e.g. in Fig. 2.6. At $t = 57\,T_\Lambda$, the sound horizon has already formed in the $U(1)$ UV theory, and is marked by a green dashed vertical line. This horizon disappears shortly after and is not shown in subsequent frames. At $t = 65\,T_\Lambda$, the sound horizon instead reappears. Again, we stress that this is probably due to the sound horizon losing physical meaning in the UV regime.

2.4.4 Large coupling

In astrophysical settings, where masses and lengths are respectively of order $M_\odot$ and km (or larger), one typically has to employ units adapted to the system under scrutiny to simulate it, e.g. ones in which $G = c = M_\odot = 1$. In these units, the numerical value of the coupling constant $\beta\Lambda^{-4}$ is extremely large [113, 179, 180]. This coefficient is intimately connected to the scales M_ρ and v in the $U(1)$ UV completion by Eq. (2.20). Fixing $v^2 = E_\Lambda/L_\Lambda$ to avoid short wavelength oscillations in the complex scalar $\phi \propto \exp\left[i\pi^{(\mathrm{UV})}/v\right]$ [Eqs. (2.16) and (2.19)], larger values of $\beta\Lambda^{-4}$ correspond to smaller values of M_ρ. This, in turn, means a weaker suppression of higher-order terms, suppressed by powers of $M_\rho^{-2}v^{-2}$. Therefore, for fixed initial data parameters $\{A, \sigma, r_c\}$ [Eq. (2.43)], larger values of $\beta\Lambda^{-4}$ will push the initial data out of the linear regime and potentially also out of the EFT's regime of validity. One symptom of this is an increased disagreement by the metric coefficients obtained by solving the Hamiltonian constraint [Eq. (2.40)] at $t = 0$. This is due to the radial ρ field [in Eq. (2.16)] containing an increasing fraction of the scalar energy content in the $U(1)$ UV theory, which is not accounted for in k-essence (nor in the "fixed" theory), and resulting in "deeper" gravitational "potential wells". One way to return to the linear regime and to the EFT regime is to weaken the initial data by decreasing the amplitude A and/or choosing milder initial scalar gradients by increasing the root-mean-square width σ.

Finally, in Sec. 2.2.2, we highlighted a caveat with the strongly hyperbolic

nature of the "fixed" theory's scalar system of equations (2.27)-(2.28). Namely, when $\Sigma \to 0$, the system becomes pathological. We have performed numerical evolutions with larger values of β (and correspondingly smaller values of M_ρ) and observe that the $U(1)$ UV completion evolution may drive the reconstructed value of $K'(X)$ to zero. In the "fixed" theory, $K'(X)$ may also vanish dynamically, driving Σ to zero with it, and causing the code to crash. Moreover, this may happen in regions not censored by an apparent horizon (see also Ref. [188]). This problem may be avoided in other versions of k-essence. For instance, in cubic k-essence the particular functional form of $K(X)$ may keep $|K'(X)| \geq q^2 > 0$, where q is a constant –see e.g. Refs. [113, 179, 180, 186]. Alternatively, one may look for a different way to implement the "fixing the equations" approach.

2.5 Final comments

In this Chapter, we have studied two general strategies to deal with the breakdown of the Cauchy problem in k-essence. The first was to resort to a UV completion of the theory, which allows for an initial-value problem that remains well-posed at all times. Unfortunately, while this was possible for the k-essence model considered in this paper, it is not possible for generic ones, e.g. for those that possess screening mechanisms, for which such UV completions remain unknown (if existing at all [191]). The second strategy consisted in "fixing the equations" [192] of k-essence to control the high frequency behavior suspected of leading to the Cauchy breakdown. Both strategies were studied before in Minkowski space by Allwright and Lehner [193] to demonstrate their technical viability.[6] Here we have generalized them to include gravity.

By considering the specific case of quadratic k-essence, we have shown that both approaches reproduce the EFT dynamics of k-essence up to a "Tricomi-type" breakdown of the Cauchy problem, where the scalar equation changes character from hyperbolic to parabolic and then elliptic. Furthermore, both the UV completion and the "fixing the equations" approach allow for evolving the dynamics past the Cauchy breakdown to the physical end state of the evolution (in our example, the formation of a black hole). This should be contrasted with previous efforts to "chart" the space of initial data in k-essence, in order to rule out regions leading to ill-posed problems –see e.g. Ref. [185, 186, 220, 221]. With the two strategies described above, (most of) these regions need not be excluded. In the context of compact binaries, in particular, this opens up the possibility of simulating their coalescence, allowing the study of the entire dynamics and the

[6] See also Refs. [218, 219] where this UV theory and its corresponding EFT description were studied without considering the coupling to gravity, and Ref. [196], where it is shown that shocks/caustics in k-essence may be smoothed by a suitable UV completion.

emission of gravitational/scalar radiation in more generic k-essence models than currently possible [180].

Moreover, since we have access to the high-energy regime of k-essence thanks to its UV completion, our results for the scalar evolution provide a validation test of the "fixing the equations" approach. It is important to stress that this approach, albeit agnostic of the details of the UV completion, qualitatively agrees with the dynamics of the latter well into the nonlinear regime of k-essence. One can therefore argue that this nonlinear regime can be at least qualitatively captured by the low-energy EFT. In fact, we find that only in the high curvature/gradient region inside the black hole apparent horizon does the "fixing the equations" approach significantly deviate from the UV completion evolution. This is expected, as it is in those regions that the key assumption of the "fixing the equations" approach, i.e. the requirement that energy does not cascade into high energy modes [192], is violated. This provides hope that even the screening mechanism, which depends crucially on the non-linear dynamics of k-essence, may be within reach of the low-energy EFT, at least qualitatively.

Chapter 3

The well-posedness of the Cauchy problem for self-interacting vector fields

Massive vector fields are ubiquitous in physics, e.g. as mediators of the weak interaction, dark matter candidates and superconductivity. Recently, considerable interest has grown around possible pathologies that allegedly arise when self-interactions are considered for these fields. In more detail, in the presence of gravity, the action for a real vector field A_μ with mass m is given by

$$S\left[g_{\mu\nu}, A_\mu\right] = \int d^4x\sqrt{-g}\left[\frac{R}{2\kappa} - \frac{1}{4}F_{\mu\nu}F^{\mu\nu} - \frac{1}{2}m^2 A_\mu A^\mu + \lambda\left(A_\mu A^\mu\right)^2 + \cdots\right], \tag{3.1}$$

where $F_{\mu\nu} \equiv \nabla_\mu A_\nu - \nabla_\nu A_\mu$ and we have introduced the coupling constant λ for the lowest order self-interaction (the dots denote higher-order operators). Ref. [222] has shown that numerical initial-value (Cauchy) evolutions of such a vector field on a black hole background break down, and attributes this feature to the appearance of ghost (or tachyonic) instabilities. Soon afterwards, Ref. [223] and [224] have identified the same problem, although in a simplified set-up.

In this short Chapter, we wish to stress that those pathologies are not surprising when the action is rewritten in the Stueckelberg language, and that they are actually related to the (breakdown of the) well-posedness of the Cauchy problem in the set-up considered by these works. [1] Indeed, introducing a new scalar field φ, we can restore the $U(1)$ gauge symmetry of the action by performing the transformation

$$A_\mu \to A_\mu + \frac{1}{m}\nabla_\mu\varphi\,, \tag{3.2}$$

[1] See also Ref. [225] where the Stueckelberg formulation for self-interacting vector fields is presented in the context of stationary Proca stars.

which renders the longitudinal mode of the massive vector field explicit. We can now choose the "unitary" gauge $\varphi = 0$ and get back the original Lagrangian given by Eq. (3.1), or we can choose a different gauge, e.g. the Lorentz gauge $\nabla_\mu A^\mu = 0$. The latter is particularly useful when one focuses on the relatively high-energy limit of the theory (where one retains only the highest derivative terms in the action), since it decouples the scalar from the vector field and gives

$$S\left[g_{\mu\nu}, A_\mu, \varphi\right] = \int d^4x\sqrt{-g}\left[\frac{R}{2\kappa} - \frac{1}{4}F_{\mu\nu}F^{\mu\nu} - \frac{1}{2}\nabla_\mu\varphi\nabla^\mu\varphi + \frac{\lambda}{m^4}\left(\nabla_\mu\varphi\nabla^\mu\varphi\right)^2 + \mathcal{O}\left(\frac{\nabla}{m}\right)^3\right]. \quad (3.3)$$

In this form, it is straightforward to realize that the (seemingly innocuous) self-interactions of the original vector field actually hide derivative self-interactions, which modify the principal part of the evolution system. In particular, the Stueckelberg field presents first-order derivative self-interactions, which have been extensively studied in the literature (where they are often referred to as k-essence) and shown [113, 179, 180, 185, 186, 220, 226] to cause problems akin to those encountered in [222–224].

These problems arise from the breakdown of strong hyperbolicity (and thus of the well-posedness of the Cauchy problem) for the Stueckelberg field equations. A system of partial differential equations is strongly hyperbolic if the characteristic matrix of the principal part has real eigenvalues and a complete set of eigenvectors; a sufficient requirement for this is that the eigenvalues (i.e. the characteristic speeds) are real and distinct. Because of the derivative self-interactions in Eq. (3.3), the characteristic speeds depend on the scalar field gradients [113, 185, 186], potentially leading to several issues.

As we have seen in Chapter 2, if the characteristic speeds cease to be real and distinct along an initial value evolution, the system may become parabolic or elliptic. An example of this kind [203] is provided by the Tricomi equation [cf. Eq. (2.12)] [185, 220, 226]

$$\partial_t^2\varphi(t,r) + t\,\partial_r^2\varphi(t,r) = 0\ , \quad (3.4)$$

which is hyperbolic for $t < 0$ (as it has characteristic speeds $\pm\left(-t\right)^{1/2}$) and elliptic for $t > 0$. Furthermore, the characteristic speeds may even diverge. An example is given by the Keldysh equation [cf. Eq. (2.13)] [185, 220, 226]

$$t\,\partial_t^2\varphi(t,r) + \partial_r^2\varphi(t,r) = 0\ , \quad (3.5)$$

which has characteristic speeds $\pm\,(-t)^{-1/2}$ diverging as $t \to 0^-$. Finally, it has been shown that derivative self-interactions can lead to the formation of shocks/microshocks even when starting from smooth initial data, potentially leading to non-unique solutions and therefore to an ill-posed Cauchy problem [227, 228].

Solutions to these issues, however, have been put forward in recent years. Ref. [186] has shown that the Tricomi-type evolution system arising from the action of Eq. (3.3) can be avoided altogether if the coefficients of the derivative self-interactions satisfy suitable conditions. For example, accounting for a cubic term $(\nabla_\mu\varphi\nabla^\mu\varphi)^3$ is sufficient to avoid the loss of hyperbolicity.

Moreover, Ref. [186] and [113] have shown that for theories with this cubic term, a Keldysh-type breakdown of the Cauchy evolution typically occurs only during black hole collapse, for realistic initial data. However, the diverging characteristic speeds that define the Keldysh behavior are not pathological *per se*, but are simply due to a poor choice of gauge. Indeed, Ref. [180] has found a gauge (with non-vanishing shift) that maintains the characteristic speeds finite in stellar oscillations, during gravitational collapse and in binary neutron star mergers. Finally, the problem of shock formation can be avoided by writing the evolution equations as a hyperbolic conservation system, and by solving the latter using high-resolution shock capturing techniques [113, 180, 186].

The discriminant choice to perform numerical evolutions in self-interacting vector theories is therefore a careful selection of the coupling constants, so as to satisfy the conditions avoiding Tricomi type breakdowns of well-posedness [186]. If such conditions are not satisfied (as for the cases studied in [222–224]) an alternative possibility is to employ a "fixing-equation" [229] approach inspired by the Müller–Israel–Stewart formulation of viscous relativistic hydrodynamics [230–232]. These approaches have been successfully applied in [92, 154, 179, 193, 229, 233, 234] to ameliorate the stability of the fully numerical evolutions in theories with either changes of character of the Cauchy problem, higher-order derivatives, or derivative self-interactions. This method consists of modifying the field equations by introducing extra fields and "fixing equations" (i.e. drivers) for them. The fixing equations are devised such that on long timescales the evolution approximately matches that of the original effective field theory. Another possibility is to rely on the ultraviolet (UV) completion of the theory (when that is known) to continue the evolution past the Tricomi or Keldysh breakdown –as we did in Chapter 2. Unfortunately, for the most interesting cases (e.g. derivative self-interactions yielding screening mechanisms) a UV completion is not generally known.

Chapter 4

Robustness of kinetic screening against matter coupling

In this Chapter, we investigate static neutron star solutions in k-essence and allow for scalar first-order derivative self-interactions in the matter coupling. We assess the robustness of the kinetic screening mechanism present in these theories against general conformal couplings to matter. The latter include ones leading to the classical Damour-Esposito-Farèse scalarization, as well as ones depending on the kinetic term of the scalar field. We find that kinetic screening always prevails over scalarization, and that kinetic couplings with matter enhance the suppression of scalar gradients inside the star even more, without relying on the non-linear regime. Fine tuning the kinetic coupling with the derivative self-interactions in the action allows one to partially cancel the latter, resulting in a weakening of kinetic screening inside the star. This effect represents a novel way to break screening mechanisms inside matter sources, and provides new signatures that might be testable with astrophysical observations.

4.1 Motivation and outline

In Sec. 1.2.2, we have seen that the the observation of the binary NS merger GW170817, has placed stringent constraints on the theory space for scalar-tensor theories. Indeed, starting from the most general DHOST theories [85–87], consistency with the speed of GWs measured by GW170817 [172, 173], absence of GW decay into Dark Energy (DE) [108, 109], and non-linear stability of the propagating scalar mode [110] reduce the viable Lagrangian to the following form

$$S\left[g_{\mu\nu},\varphi,\Psi_m\right]=\int d^4x\sqrt{-g}\Big[\Phi\,R+K(\varphi,X)$$

$$+\frac{6}{\Phi}\left(\partial_X\Phi\right)^2\nabla^\mu\varphi\nabla_\mu\nabla_\rho\varphi\nabla^\rho\nabla^\nu\varphi\nabla_\nu\varphi\Bigg]+S_m[g_{\mu\nu},\Psi_m]\,, \quad (4.1)$$

where R and g are the Ricci scalar and metric determinant, φ is the scalar field (with $X\equiv\nabla_\mu\varphi\nabla^\mu\varphi$), and Ψ_m collectively describes the matter degrees of freedom. In the above expression, Φ and K are generic free functions of φ and X, and we have set $\hbar=1$. Performing a conformal transformation $g_{\mu\nu}\to\Phi^{-1}\,g_{\mu\nu}$ from the Jordan frame to the Einstein frame, together with a redefinition of the free function K, the action can be written as [cf. (1.11)]

$$S\left[g_{\mu\nu},\varphi,\Psi_m\right]=\int d^4x\sqrt{-g}\left[\frac{M_{\rm Pl}^2}{2}R+K(\varphi,X)\right]+S_m\left[\frac{g_{\mu\nu}}{\Phi(\varphi,X)},\Psi_m\right]\,, \quad (4.2)$$

where we have introduced the (reduced) Planck mass $M_{\rm Pl}^{-2}=\kappa=8\pi G$. The corresponding theory is usually referred to as k-essence [111, 112]. For the rest of this Chapter we will work in the Einstein frame and will denote quantities in the Jordan frame with a tilde hat (e.g. $\tilde{g}$).

We assume that there are only two energy scales involved in the action, one associated with the metric and the scalar field ($M_{\rm Pl}$) and the other with the derivatives of the scalar field (Λ). Moreover, as we did in Sec. 1.2, we will assume a shift symmetry for the action ($\varphi\to\varphi+\text{const.}$) which is only softly broken by a Planck suppressed scalar-matter interaction. Under these assumptions, we will only consider the lowest order non-linear terms in the free functions K and Φ, which read

$$K\left(X\right)=-\frac{1}{2}X+\beta\frac{X^2}{4\Lambda^4}\,, \quad (4.3)$$

$$\log\Phi\left(\varphi,X\right)=\alpha_1\frac{\varphi}{M_{\rm Pl}}+\alpha_2\frac{\varphi^2}{M_{\rm Pl}^2}+\lambda_1\frac{X}{2\Lambda^4}+\lambda_2\frac{X^2}{4\Lambda^8}\,, \quad (4.4)$$

where β,α_i,λ_i are $\mathcal{O}\left(1\right)$ dimensionless constants and the log function ensures $\Phi>0$ and thus the same metric signature in the Einstein and Jordan frames. In particular, recall that FJBD theory [114–116] is recovered in the case[1] $\beta=0$.

It is well known that when $\beta<0$ and $\log\Phi$ depends only linearly on φ, a screening mechanism referred to as k-mouflage (or kinetic screening) [120] suppresses the scalar force in the vicinity of a massive body, allowing for passing Solar System tests without imposing any bound on α_1 [113, 120, 179, 235]. Furthermore, time evolutions for (cubic) k-essence have been shown to be well-posed [179, 186] and numerical simulations of merging binary neutron stars with screening have been performed in Ref. [180].

[1]Strictly speaking, FJBD theory corresponds to $\beta=\lambda_{1,2}=0$. However, in this Chapter we use this terminology also for cases where $\lambda_{1,2}\neq0$.

On the contrary, in the absence of screening (i.e. $\beta \geq 0$), the same local tests constrain $|\alpha_1| < 5 \times 10^{-3}$ [157, 236]. This bound has led to investigating the effect of quadratic corrections in φ in the matter coupling, and to the discovery of spontaneous scalarization when $\alpha_2 \gtrsim 2$ [237, 238].

It is however unknown what the effect of this term is in the presence of screening. In principle, scalarization may still occur – as the quadratic term in φ in the matter coupling still tends to render the scalar tachyonically unstable [237–239] – and spoil the suppression of the scalar force. Likewise, the effect of X-dependent couplings with matter [c.f. Eq. (4.4)] on screened solutions is currently unknown. The aim of this work is to investigate these questions and assess the robustness of kinetic screening against matter couplings.

This Chapter is organized as follows. In Sec. 4.2, we present the covariant equations of motion for the class of models described by Eqs. (4.3) and (4.4). In Sec. 4.3.1, we describe our methodology to obtain fully relativistic static solutions through numerical integration of the equations of motion in spherical symmetry. In addition, in Sec. 4.3.2, we introduce an analytic model that captures the main features of the scalar configurations. Our main results are presented in Sec. 4.4. Finally, in Sec. 4.5, we summarize our findings and draw our conclusions. Details regarding the derivation of the equations of motion are relegated to Appendix C.1.

4.2 Field equations

Variation of action (4.2) with respect to $g_{\mu\nu}$ gives the equations of motion for the metric,

$$M_{\rm Pl}^2 G_{\mu\nu} = T^{(\varphi)}_{\mu\nu} + T_{\mu\nu} \,, \tag{4.5}$$

where $G_{\mu\nu}$ is the Einstein tensor, the stress-energy tensor of the scalar field is given by

$$T^{(\varphi)}_{\mu\nu} = K(X)\, g_{\mu\nu} - 2K'(X)\nabla_\mu\varphi\nabla_\nu\varphi \ , \tag{4.6}$$

and the matter stress-energy tensor is defined by [cf. (1.3)]

$$T^{\mu\nu} \equiv \frac{2}{\sqrt{-g}}\frac{\delta S_m}{\delta g_{\mu\nu}} \ , \tag{4.7}$$

with trace $T \equiv g_{\mu\nu}T^{\mu\nu}$.

Variation with respect to φ and the contracted Bianchi identity applied to Eq. (4.5) give rise to the scalar and matter equations of motion (see Appendix

C.1 for more details),

$$\nabla_\mu \left(\mathcal{K}\, \nabla^\mu \varphi\right) = \frac{1}{2}\mathcal{A}T \ , \tag{4.8}$$

$$\nabla_\mu \mathcal{T}^{\mu\nu} = -\frac{\mathcal{T}}{2\Phi}\nabla^\nu \Phi \ , \tag{4.9}$$

where we have defined

$$\mathcal{K} \equiv K'(X) + \mathcal{B}T \ , \tag{4.10}$$

$$\mathcal{T}^{\mu\nu} \equiv \Phi^{-3}\tilde{T}^{\mu\nu} = T^{\mu\nu} + 2\mathcal{B}T\nabla^\mu\varphi\nabla^\nu\varphi \ , \tag{4.11}$$

with trace $\mathcal{T} \equiv g_{\mu\nu}\mathcal{T}^{\mu\nu}$,

$$\mathcal{A} \equiv \frac{\partial_\varphi \Phi}{\mathcal{C}} \,, \quad \mathcal{B} \equiv \frac{\partial_X \Phi}{\mathcal{C}} \,, \quad \mathcal{C} \equiv -2\Phi\left(1 + \frac{X\,\partial_X\Phi}{\Phi}\right) \,, \tag{4.12}$$

and the Jordan-frame tensor is defined by

$$\tilde{T}^{\mu\nu} \equiv \frac{2}{\sqrt{-\tilde{g}}}\frac{\delta S_m}{\delta \tilde{g}_{\mu\nu}} \,. \tag{4.13}$$

Notice in particular that the dependence of Φ on X produces a matter redressing of $K'(X)$ in the scalar field equation and a disformal modification of the matter stress-energy tensor.

4.3 Methodology

4.3.1 Numerical integration

We describe matter as a perfect fluid in the Jordan frame by

$$\tilde{T}^{\mu\nu} = \left(\tilde{\rho} + \tilde{P}\right)\tilde{u}^\mu\tilde{u}^\nu + \tilde{P}\tilde{g}^{\mu\nu}, \tag{4.14}$$

with trace $\tilde{T} \equiv \tilde{g}_{\mu\nu}\tilde{T}^{\mu\nu}$, where $\tilde{u}^\mu$ is the 4-velocity of the fluid (normalized to -1) and the energy density $\tilde{\rho} = \tilde{\rho}_0\,(1+\tilde{\epsilon})$ is given in terms of the rest-mass density $\tilde{\rho}_0$ and the internal energy $\tilde{\epsilon}$.

We restrict to static solutions in spherical symmetry and write the line element in polar coordinates as

$$ds^2 = -N^2(r)\,dt^2 + a^2(r)\,dr^2 + r^2 d\Omega^2 \ , \tag{4.15}$$

where $d\Omega^2 = d\theta^2 + \sin^2\theta d\phi^2$. In addition to the scalar and matter equations, we use the tt- and rr-components of the Einstein equations (4.5). We will mainly

focus on neutron star matter, and thus we close the system by specifying a polytropic equation of state (EOS) $\tilde{P} = \tilde{K}\tilde{\rho}_0^{\tilde{\Gamma}}$ and $\tilde{P} = (\tilde{\Gamma} - 1)\tilde{\rho}_0\tilde{\epsilon}$, with adiabatic index $\tilde{\Gamma} = 2$ and $\tilde{K} = 123\, G^3 M_\odot^2$ in the Jordan frame.

The final Tolman–Oppenheimer–Volkoff (TOV) equations are a set of ordinary differential equations with schematic form

$$\boldsymbol{U}' = \boldsymbol{V}\left[\boldsymbol{U}, r\right] \ , \tag{4.16}$$

where $\boldsymbol{U} = (\varphi, \varphi', \tilde{P}, N, a)$ and the prime denotes the radial derivative. We do not write explicitly these equations as they are cumbersome and not particularly illuminating.

Regularity at the center of the star is imposed by solving the equations perturbatively around $r = 0$. In this way, the resulting independent integration constants are found to be $\{N(0), \varphi(0), \tilde{P}(0)\}$. The numerical integration is carried out outwards starting from a small but finite radius $r_0 > 0$. The lapse is initially chosen to be $N(0) = 1$ and is rescaled after the integration so that it approaches $N = 1$ at spatial infinity (this is possible by rescaling the time coordinate by a constant factor). Given a central pressure $\tilde{P}(0)$, the integration constant φ_0 is fixed by a shooting method so that φ asymptotes to zero at infinity. The location $r_\star$ of the surface of the star is determined by $\tilde{P}\left(r_\star\right) = 0$. The baryon mass in the Jordan frame is calculated as

$$\tilde{M}_b \equiv \int d^3\tilde{x}\sqrt{-\tilde{g}}\tilde{\rho}_0\tilde{u}^0 \tag{4.17}$$

whereas the scalar charge is calculated as [179, 237, 240]

$$\alpha_c \equiv \sqrt{\frac{4\pi}{G}}\frac{\varphi_1}{M_\infty} \ , \tag{4.18}$$

where φ_1 appears in the asymptotic expansion $\varphi(r) = \varphi_\infty + \varphi_1 r^{-1} + \mathcal{O}(r^{-2})$, and M_∞ is the gravitational mass in the Einstein frame appearing in the asymptotic expansion $N^2(r) = 1 - 2GM_\infty r^{-1} + \mathcal{O}(r^{-2})$.

4.3.2 Simplified analytic model

We complement our numerical analysis by introducing an analytical toy model for the scalar equation of motion, which, we anticipate, will allow us to reach values for the strong coupling scale relevant for Dark Energy, i.e. $\Lambda_{\rm DE} \sim 1\,\text{meV}$ (these values are hard to simulate numerically due to the hierarchy of scales involved [113, 179]). Moreover, our model will allow us to cross check and interpret certain features of the numerical scalar profiles presented in the next Section.

This model can be applied to all matter couplings in Eq. (4.4) but φ^2, because in the latter case the source of the scalar equation is a function of φ. Therefore, in that case the solution can only be obtained numerically as described in Sec. 4.3.1.

In more detail, we approximate the spacetime to be Minkoswki and consider a star described by the Tolman VII EOS [241],

$$\tilde{\rho}\,(r) \equiv \tilde{\rho}_c \left[1 - \left(\frac{r}{r_\star}\right)^2\right] \ , \tag{4.19}$$

where $r_\star$ is the star surface location and $\tilde{\rho}_c$ is a parameter specifying the central energy density. We then define[2]

$$\partial_\mu \chi \equiv \mathcal{K}\,(\varphi, X)\,\partial_\mu \varphi \ , \tag{4.20}$$

so that the scalar equation becomes

$$\nabla^2 \chi = -\hat{\alpha}\tilde{T} \ , \tag{4.21}$$

where $\hat{\alpha} \equiv \alpha_1/(4\Phi^2 M_{\rm Pl})$. Approximating $\tilde{T} \approx -\tilde{\rho}$ and $\Phi \approx 1$, one can solve Eq. (4.21) by making use of the Green function $\mathcal{G}(\boldsymbol{x}, \boldsymbol{x'}) \equiv -1/(4\pi|\boldsymbol{x} - \boldsymbol{x'}|)$ and obtain

$$\chi' = \begin{cases} \hat{\alpha}\tilde{\rho}_c \left(\dfrac{r}{3} - \dfrac{r^3}{5r_\star^2}\right), & r \leq r_\star \ , \\ \dfrac{2\hat{\alpha}\tilde{\rho}_c r_\star^3}{15 r^2}, & r_\star < r \ . \end{cases} \tag{4.22}$$

Finally, we invert Eq. (4.20) to obtain φ'.

As an illustration, and for the sake of simplicity of the analytic expressions, we present here the case where $\beta = \lambda_1 = 0$ and $\lambda_2 < 0$ in Eqs. (4.3)-(4.4). The extension to more general cases is straightforward. For this case, $\mathcal{K}$ can be written as

$$\mathcal{K} = -\frac{1}{2}\left(1 + \hat{\lambda}\tilde{T}X\right) \ , \tag{4.23}$$

where $\hat{\lambda} \equiv 2\lambda_2/(\Phi^2\Lambda^8)$, and the solution for φ' is given by the analytic inversion of Eq. (4.20), which corresponds to the real root $y \equiv \varphi'^2$ of the third-order polynomial

$$\left(1 - \hat{\lambda}\tilde{\rho}y\right)^2 y - 4\chi'^2 = 0 \ . \tag{4.24}$$

[2]Since we are looking at static solutions in spherical symmetry, the decomposition of $\mathcal{K}\,(\varphi, X)\,\partial_\mu\varphi$ in only the gradient part is complete.

The full solution is not particularly illuminating, however, it is instructive to examine separately the linear and non-linear regimes. The linear solution is relevant near the center of the star ($\varphi' \propto r$) and in the exterior ($\varphi' \propto r^{-2}$). In the not-so-deep interior of the star, however, the nonlinear term dominates and, if the density gradients are small, gives $\varphi' \propto r^{1/3}$.

4.4 Results

In this Section we illustrate neutron star solutions for the different terms in the conformal coupling (4.4). First, in Sec. 4.4.1, we consider the effect of a quadratic coupling in φ on screened solutions in k-essence, and we investigate whether scalarization can take place even in this scenario. Then, in Sec. 4.4.2, we study the effect of X-dependent couplings on FJBD theory and finally, in Sec. 4.4.3, we show the effect of the same kinetic couplings on k-essence theories that have screening.

4.4.1 Couplings to matter dependent on φ

We restrict to the part of Eq. (4.4) depending only on the scalar field and not on its derivatives, i.e. $\lambda_1 = \lambda_2 = 0$. In Fig. 4.1, we illustrate this case with an example of a generic solution with $|\alpha_{1,2}| \sim \mathcal{O}(1)$. We show the scalar gradient profile for FJBD theory with a linear coupling to matter (light-blue dashed) and with a quadratic one (purple dotdashed). The former is only shown for comparison as this case is ruled out by solar system constraints. The latter is usually referred to as the Damour-Esposito-Farèse (DEF) model, which leads to scalarized neutron stars. We also show, as a reference, the standard screened solution of k-essence [113], where only the linear coupling is present (red solid line). In this case, we observe the presence of a screening region (i.e. a change in slope which results in a suppression of the scalar force) between the first and last knee of the scalar gradient, with the location of the last knee (counting from the left) corresponding to the screening radius.

When we turn on a quadratic coupling in φ (orange dotted line), we observe no apparent difference with respect to the screened solution described above (red solid line). This is not surprising since higher-order couplings in φ are suppressed by the corresponding power of $M_{\rm Pl}$, which makes them irrelevant unless one hits the Planck scale. Note that this would be the case even in FJBD theory, unless one were to set $\alpha_1 = 0$ like in the example above, or to a very small value compatible with solar system constraints. In FJBD theory, the latter do indeed bound $|\alpha_1| < 5 \times 10^{-3}$, thus making the quadratic coupling dominant.

Although there is no need for a small α_1 coupling in k-essence (due to screening), it is nevertheless intriguing to investigate such possibility and address the question of whether scalarization can still take place. Setting $\alpha_1 = 0$ and leaving only the quadratic coupling active (in analogy to the DEF model), we find that the magnitude of the scalar gradient is uniformly suppressed (blue dashed line). The scalar field remains always in the linear regime [i.e. $\varphi'/\Lambda^2 \lesssim \mathcal{O}(1)$] and, as a consequence, when imposing a vanishing scalar field at infinity, the maximum of φ' can never exceed the value of Λ^2.

We empirically observe a uniform suppression that scales roughly as $\varphi' \propto \Lambda^2$, which in turn leads to a suppression of the scalar charge as $\alpha_c \propto \Lambda^2$ with respect to the DEF model. Therefore, we can conclude that, even if the non-linear regime of k-essence never kicks in when only a quadratic coupling with matter is present, there is still an overall suppression of the scalar force which depends on Λ. This implies a suppression of the scalar charge, which makes scalarization impossible in the presence of k-essence.

Let us now further investigate the origin of this uniform suppression and how it is affected by the boundary conditions. In Fig. 4.2, we plot the same cases as in Fig. 4.1, but instead of imposing a vanishing scalar field at infinity, we fix the central scalar field to the same constant value in all cases. We choose the value that was previously obtained for the k-essence profile with linear matter coupling (red solid line). Since the perturbative expansion around $r = 0$ is the same in FJBD theory and k-essence, we obtain two classes of solutions corresponding to the different matter couplings. Despite the same central scalar field, the value of the scalar field at infinity is now different for the two classes (due to the different field equations), and in the quadratic coupling case it does not vanish. This translates into larger scalar gradients, which make the k-essence solution with quadratic coupling enter the non-linear regime. Therefore, in order to excite k-essence non-linearities even with a quadratic coupling to matter, one would need a non-trivial scalar field boundary condition at infinity enhancing the scalar gradient.

4.4.2 FJBD and kinetic coupling with matter

We now study FJBD theory with a coupling to matter depending on the kinetic term X. Note that, in order to break the shift symmetry of the theory and avoid no-hair theorems (see e.g. Ref. [242]), we also need to maintain a dependence on φ, which we assume to be linear.

As an illustrative example, and to validate our analytic model, we begin by considering the case of only including the X^2 term in Φ. In Fig. 4.3, we show the numerical solution for the scalar gradient profile (blue dashed line) for $\lambda_2 =$

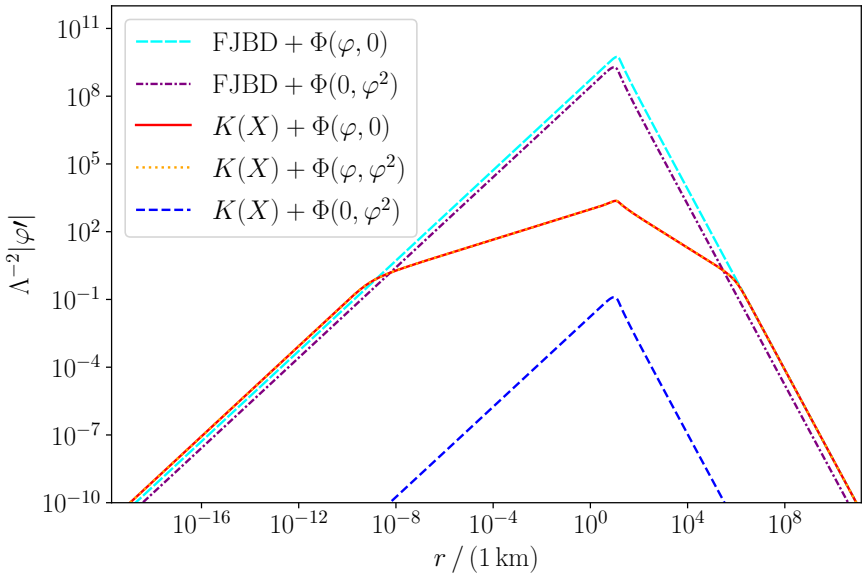

Figure 4.1: *Scalar profile for φ-dependent matter couplings.* Dashed cyan: Standard FJBD solution with parameters $(\beta, \alpha_1, \alpha_2) = (0, 1, 0)$. Dot dashed purple: DEF model with parameters $(\beta, \alpha_1, \alpha_2) = (0, 0, 9/4)$. Solid red: k-essence with $(\beta, \alpha_1, \alpha_2) = (-1, 1, 0)$. Dotted orange: k-essence with $(\beta, \alpha_1, \alpha_2) = (-1, 1, 9/4)$. Dashed blue: k-essence with $(\beta, \alpha_1, \alpha_2) = (-1, 0, 9/4)$. We choose stars with $\tilde{M}_b = 1.87\, M_\odot$, near the top of the $\beta = \alpha_1 = 0$ charge-mass curve. In all cases we use $\Lambda = 1\,\mathrm{keV}$.

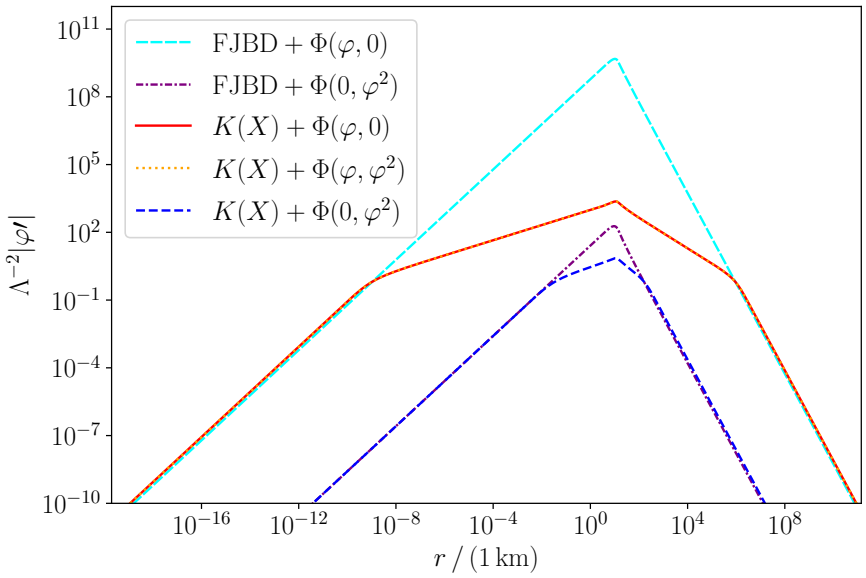

Figure 4.2: *Scalar profile for φ-dependent matter couplings with equal $\varphi(0)$.* Same cases as in Fig. 4.1. Here, however, we fix the boundary condition at the center to the same constant value $\varphi(0)/\Lambda = 1.709 \times 10^{-3}$.

-1 and $\Lambda \approx 10.3\,\mathrm{MeV}$. We observe a behavior similar to kinetic screening in the interior of the star, whereas in the exterior the scalar behaves linearly. For comparison, we show the solution in k-essence (green solid line) for $\beta = -1$ and $\Lambda = 0.38\,\mathrm{MeV}$, which comes from the matter redressing of the above energy scale, i.e. $\Lambda_{\mathrm{eff}}^4 = \Lambda^8/[2\tilde{\rho}\,(0)]$. In more detail, this effect can be understood by

noting that the quadratic term in the conformal coupling and in k-essence enter in the same way in the scalar equation (4.8), namely $2\mathcal{K}+1 \propto \lambda_2\tilde{\rho}X/\Lambda^8$ and $2\mathcal{K}+1 \propto \beta X/\Lambda^4$, respectively. The presence of $\tilde{\rho}$ in the first case is responsible for the different energy scale at which screening takes place. Moreover, since this effect is proportional to the density distribution, it fades away as the star surface is approached (as $\tilde{\rho} \to 0$), and thus it is not present in the exterior.

In Fig. 4.3 we also note the appearance of a "cusp" at the star surface, $r_\star \approx 14\,\mathrm{km}$, which arises from the connection between the non-linear (interior) and linear (exterior) behavior. Despite this feature, we have checked that all quantities (including the curvature invariants R, $R_{\mu\nu}R^{\mu\nu}$, and $R_{\mu\nu\rho\sigma}R^{\mu\nu\rho\sigma}$) remain regular at $r_\star$. From a practical point of view, numerically integrating this cusp is challenging, as one must make sure that the scalar gradient is resolved, and for lower values of Λ this becomes increasingly difficult to achieve.

In order to more easily capture the behavior at the star surface, and to cross-check our numerical scalar profiles, we resort to the analytical model introduced in Sec. 4.3.2. In Fig. 4.3, we show the scalar gradient profile (red dot dashed line) generated with the analytic model, where the parameters of the equation of state (4.19) are chosen to closely match the stellar radius and central density of the numerical integration profile. We observe that the scalar gradient predicted by this model is qualitatively similar to the numerical one (blue dashed line), with differences mainly due to the details of the EOS. Moreover, in the analytic model we can perform an expansion near the surface of the star to confirm that the scalar gradient approaches a finite value at the cusp. Expanding in $\Delta r \equiv r - r_\star$, as $\Delta r \to 0^-$, we obtain

$$\pm\varphi' = \pm\sqrt{y} = \frac{4}{15}\hat{\alpha}\tilde{\rho}_c r_\star + \frac{8}{3375}\hat{\alpha}\tilde{\rho}_c\left(225 + 16\hat{\lambda}\hat{\alpha}^2\tilde{\rho}_c^3 r_\star^2\right)\Delta r + \mathcal{O}\left[(\Delta r)^2\right] \ , \quad (4.25)$$

where the overall sign can be fixed by comparing with the interior solution.

Having validated our analytic model, we can now employ it to study scales relevant for Dark Energy. In Fig. 4.4, we show the scalar gradient profile (green solid line) for $\lambda_1 = \lambda_2 = -1$ in Eq. (4.4) and energy scale $\Lambda \sim \Lambda_{\rm DE} \sim 1\,\mathrm{meV}$. For comparison, we also plot (orange dashed line) the case studied above (i.e. $\lambda_1 = 0$ and $\lambda_2 = -1$), and (blue dotted line) the profile in k-essence ($\beta = -1$) with an equivalent strong-coupling scale $\Lambda \approx 3 \times 10^{-12}\,\mathrm{meV}$. In particular, we observe that the scalar field is always in the linear regime, with a different magnitude of the gradient inside and outside the star. The value inside is greatly suppressed, as compared to the value outside, due to the redressing of the linear term in the scalar equation inside matter.

To conclude this Section, and for completeness, we briefly summarize the

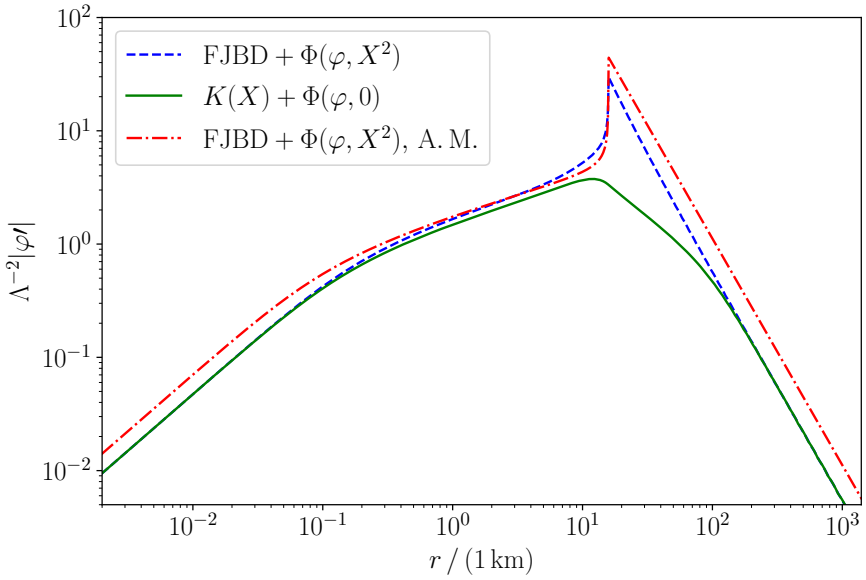

Figure 4.3: *FJBD theory with X^2-coupling to matter.* Dashed blue: scalar gradient profile for $(\beta, \alpha_1, \lambda_1, \lambda_2) = (0, 10^{-3}, 0, -1)$ and $\Lambda = 10.3\,\mathrm{MeV}$. Solid green: kinetic screening in k-essence with parameters $(\beta, \alpha_1, \lambda_1, \lambda_2) = (-1, 10^{-3}, 0, 0)$ – for the purposes of comparison we have used an energy scale $\Lambda = 0.38\,\mathrm{MeV}$. Red dash dot: scalar gradient profile obtained with the analytic model (A. M.) with parameters $(\beta, \alpha_1, \lambda_1, \lambda_2) = (0, 10^{-3}, 0, -1)$ and $\Lambda = 10.3\,\mathrm{MeV}$. We choose $\tilde{\rho}_c = \tilde{\rho}\,(0)$ and $r_\star$ as given by the integration in k-essence.

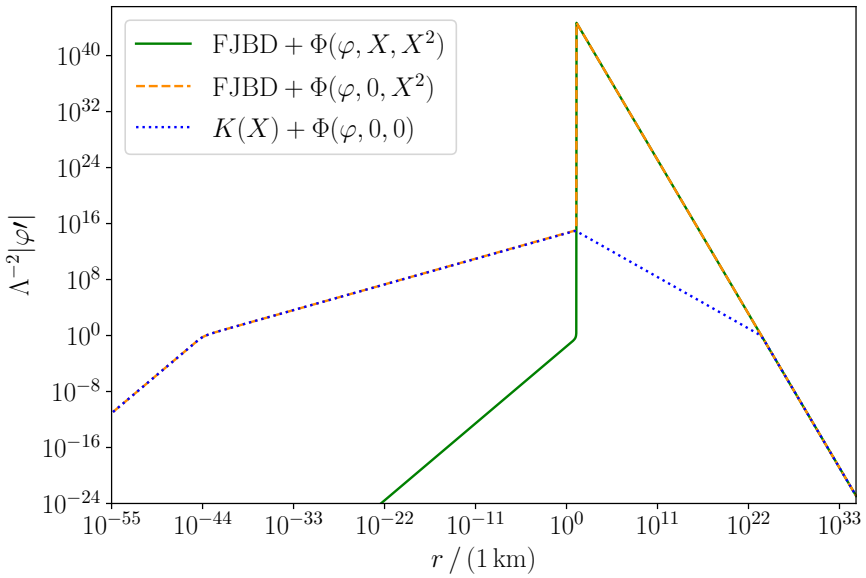

Figure 4.4: *FJBD theory with generic kinetic coupling to matter at DE scales.* Solid green: scalar gradient profile for $(\beta, \alpha_1, \lambda_1, \lambda_2) = (0, 1, -1, -1)$. Dashed orange: scalar gradient profile for $(\beta, \alpha_1, \lambda_1, \lambda_2) = (0, 10^{-3}, 0, -1)$. In both solutions, the energy scale is $\Lambda = 1\,\mathrm{meV}$. Dotted blue: for comparison, the k-essence screened solution with $(\beta, \alpha_1, \lambda_1, \lambda_2) = (-1, 10^{-3}, 0, 0)$ and $\Lambda = 3.6 \times 10^{-12}\,\mathrm{meV}$. The vertical axis is rescaled with respect to the latter value for Λ and, in all cases, we use the analytic model.

behavior for the positive signs of the kinetic couplings in Eq. (4.4). For $\lambda_1 > 0$, there is a location inside the star where $\mathcal{K} = 0$ and where the scalar gradient

diverges and changes sign. This is a pathological solution. Finally, for $\lambda_1 = 0, \lambda_2 > 0$, the solutions become pathological at the origin as the scalar field ceases to be regular (i.e. $\varphi'(0) \neq 0$). For the parameters of Fig. 4.4, but with $\lambda_2 = 1$, this occurs for $\Lambda \lesssim 100\,\mathrm{MeV}$.

4.4.3 k-essence and kinetic coupling with matter

In this Section, we rely on our analytic model to study the effects of kinetic coupling with matter in k-essence, for DE scales.

For $\lambda_1 < 0$, and regardless of the sign of λ_2, we observe an enhancement of the scalar suppression inside the star, in line with the previous discussion. In fact, as shown in Fig. 4.5 (solid blue), inside the star the scalar field remains always in the linear regime with a gradient uniformly suppressed as in the previous Section, while kinetic screening remains unchanged in the exterior of the star.

More interesting phenomenology occurs when $\lambda_1 = 0$ and $\lambda_2 > 0$. Indeed, in this case, the scalar gradient profile features a *weakening* of the kinetic screening inside the star, due to the partial cancellation of the non-linear terms coming from k-essence and from the matter coupling. In Fig. 4.5, we show this effect (green dashed line). For demonstrative purposes, and in order to maximize this effect, we chose a different energy scale for the matter coupling given by $\Lambda_{\rm eff}^8 \approx 2\Lambda^4\tilde{\rho}_c \approx (0.52\,\mathrm{keV})^8$. This effect is similar, although different in nature, to the partial breaking of the Vainshtein screening inside matter for beyond Horndeski [243, 244] and DHOST theories [174, 176, 177, 245]. Finally, for comparison, we also show (red dot dashed) the profile for a screened star in k-essence without kinetic coupling to matter.

4.5 Final comments

In this Chapter, we have investigated the effect of general matter couplings for k-essence scalar-tensor theories featuring kinetic screening of local scales. In Refs. [113, 179, 180], the standard linear coupling in φ was considered in studies of neutron star oscillations and mergers. We find here that this choice is robust against more general matter couplings, at least for the static configurations chosen as initial data. Indeed, we have explicitly shown that the inclusion of a quadratic term in φ does not affect significantly the solution. Moreover, even in a configuration *à la* DEF (i.e. with a matter coupling including only a quadratic term in φ), scalarization becomes negligible as the scalar gradient profile becomes even more suppressed (although always in the linear regime).

We have also explored couplings to matter depending explicitly on the kinetic term of the scalar field. Such terms arise from X-dependent conformal trans-

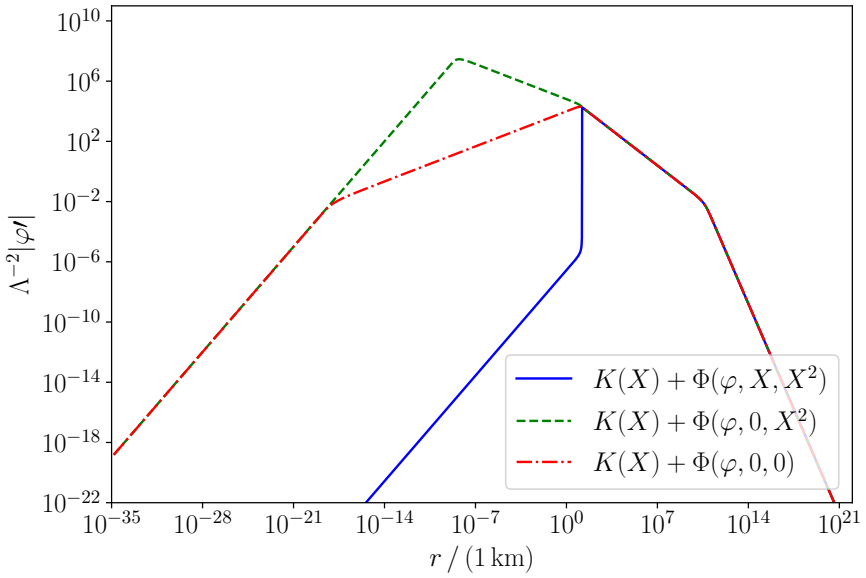

Figure 4.5: *k-essence and kinetic coupling with matter.* Solid blue: With parameters $(\beta,\alpha_1,\lambda_1,\lambda_2) = (-1,10^{-3},-1,1)$. Dashed green: With parameters $(\beta,\alpha_1,\lambda_1,\lambda_2) = (-1,10^{-3},0,1)$ and $\Lambda = 1\,\mathrm{meV}$ for the function $K(X)$, however, we choose a different energy scale $\Lambda \approx 0.52\,\mathrm{keV}$ in Φ for illustrative purposes, such that the cancellation effect is maximized. Dash dot red: $(\beta,\alpha_1,\lambda_1,\lambda_2) = (-1,10^{-3},0,0)$ and $\Lambda = 1\,\mathrm{meV}$. The parameters used for the equation of state $\{\tilde{\rho}_c, r_\star\}$ are taken to be the same as in Fig. 4.3.

formations of viable DHOST theories in the Jordan frame. We have identified healthy sectors of the parameter space, where the suppression of the scalar gradient inside the star is enhanced, while the theory is still in the linear regime. This in turn produces a sharp transition between the linear and non-linear regimes at the star surface, which is however devoid of pathologies.

Finally, interesting phenomenology arises when only a quadratic kinetic term is present in the matter coupling (together with the usual linear term in φ). In this case, there is a weakening of the kinetic screening inside stars, due to the partial cancellation of the non-linear terms coming from k-essence and from the matter coupling.

This new partial breaking of the screening mechanism inside matter has several consequences for stellar astrophysics, which can be used to test the model. For example, the Chandrasekhar mass limit [246], the burning process in brown and red dwarfs [247] and the mass-radius relation of white dwarfs [248] are all quantities sensitive to the gravitational force inside bodies. These observables have been used to place constraints on models which, like ours, break the screening inside matter. We plan to explore these effects and use them to constrain kinetic couplings in future work.

Part III

Constraining gravity with black hole images

Chapter 5

Separating astrophysics and geometry in black hole images

The observation of the shadow of the supermassive black hole M87* by the EHT is sensitive to the spacetime geometry near the circular photon orbit and beyond, and it thus has the potential to test GR in the strong field regime. Obstacles to this program, however, include degeneracies between putative deviations from GR and both the description of the accretion flow and the uncertainties on "calibration parameters", such as e.g. the mass and spin of the black hole. In this Chapter, we introduce a formalism, based on a principal component analysis, capable of reconstructing the black hole metric (i.e. the "signal") in an agnostic way, while subtracting the "foreground" due to the uncertainties in the calibration parameters and the modelling of the accretion flow. We apply our technique to simulated mock data for spherically symmetric black holes surrounded by a thick accretion disk. We show that separation of signal and foreground may be possible with next generation EHT-like experiments. Throughout this Chapter we set $G = c = 1$.

5.1 Motivation and outline

One possible way to look for deviations from GR is to test the Kerr hypothesis [43, 44, 249] –see Sec. 1.1.1. The recent measurement of the shadow of M87* is therefore particularly interesting to test the Kerr hypothesis and constrain possible deviations from it. Several theoretical works have connected the bright emission ring that is present in the reconstructed image with the impact parameter of the circular photon orbit [142, 250–262]. This feature in the image may therefore be used to connect the underlying BH spacetime with the observed image and therefore test the Kerr hypothesis.

Despite this large amount of existing theoretical work on the topic, a lively

discussion about the interpretation of BH shadow images is currently ongoing. More precisely, one question is how suited the shadow size alone (as opposed to the full image) is for testing deviations from the Kerr metric [Eq. (1.4)]. In Psaltis *et al.* [263], it was claimed that the 17 % constraint on the shadow size of M87*, as reported earlier by the EHT Collaboration in Refs. [264, 265], can be used to place constraints beyond the first post-Newtonian order of the BH metric. However, the basis and robustness of this conclusion have been critically discussed since then. Gralla [266] argued that uncertainties in the underlying astrophysics make tests of GR with the current observations not possible. Völkel *et al.* [144] showed that even if some underlying assumptions questioned by Gralla [266] and adopted in Psaltis *et al.* [263] are true, the bounds of Ref. [263] do not hold when higher order post-Newtonian orders are included in the analysis. Nevertheless, Völkel *et al.* [144], as well as Kocherlakota *et al.* [267], demonstrate that theory specific tests can be performed and allow for gaining information on the gravitational theory. The role of dimensional coupling constants in alternative theories of gravity has been studied by Glampedakis and Pappas [268].

Since the shadow size, as used in most previous works[1], is only a single number, it represents an immense reduction of the information that is encoded in the full image. For this reason, and because it is based on the connection between the impact parameter of the circular photon orbit and the image brightness, more advanced studies are needed.

Improvements of several aspects of the analysis have already been partially carried out in recent works. For instance, a multiple ring structure seems to appear in the shadow image at high angular resolution, although its observation would require measurements beyond current EHT capabilities, see e.g. Refs. [270–272]. Medeiros *et al.* [262] have also investigated deviations from circularity in non-Kerr spacetimes using a principal component analysis (PCA). Formal questions regarding the uniqueness of shadow images and the underlying BH geometry, from the point of view of geodesics, have been recently studied in Ref. [273].

Ideally, however, an analysis should take into account the whole image and simulate both the astrophysics and the background geometry at the same time. Treating this problem in its full complexity is far beyond of what is currently possible. State-of-the-art calculations combine general relativistic magneto-hydrodynamic (GRMHD) simulations of the matter with ray-tracing codes to construct images –see Ref. [11, 265]. However, even in the context of GR, the large computational cost associated to these calculations allows one to vary (at the same time) at most a few parameters describing the accretion flow physics and the geometry [11, 274]. Therefore, repeating these simulations for non-Kerr spacetimes is al-

[1] See Nampalliwar *et al.* [269] for a recent work including also the deviations from circularity.

ready challenging, even when backreaction on the geometry is neglected –see e.g. Refs. [275, 276]. Nevertheless, varying the accretion flow physics and allowing for non-Kerr geometries at the same time has been attempted before, although restricting to particular deformations of the metric [277].

In this Chapter, we present a framework that allows one to deal with deviations of both the accretion flow and the spacetime geometry from standard scenarios, showing that under suitable assumptions they can be both recovered/-constrained from the shadow image. In more detail, we perform a PCA, which allows us to probe small but very general (i.e. theory "agnostic") deviations from the Schwarzschild metric, while at the same time reconstructing the astrophysical accretion flow (which we assume to be spherical and with a simple emissivity profile). The PCA allows for working in a rather general set of basis functions, e.g. Gaussians or power laws. Although our matter description is not as sophisticated as current GRMHD simulations, we show for the first time how the background metric and simple astrophysical scenarios can be disentangled from one another and reconstructed singularly in an *inverse problem for the whole shadow image*. Our work is therefore extensible to incorporate more realistic models in the future.

Our main findings can be summarized as follows. We provide different mock images produced by our model as hypothetically observed data. These images have been produced by varying the emissivity profile and/or the BH metric. We have first demonstrated that the PCA reconstruction allows one to constrain the emissivity profile when the background is assumed to be Schwarzschild. Then we have also demonstrated that general deviations of the metric away from Schwarzschild can be recovered when the emissivity profile is well understood. In the final and most important application, we have demonstrated that when the functional form of the emissivity profile is assumed to be of a simple form, but with unknown parameters, it is possible to recover both the spacetime geometry (the "signal") in an agnostic way, as well as the emissivity profile (the "matter foreground").

This Chapter is organized as follows. In Sec. 5.2 we summarize our accretion model and the ray-tracing algorithm. In Sec. 5.3 we outline our numerical method to compute BH images and the PCA. Applications and results are reported in Sec. 5.4. A discussion of our findings is presented in Sec. 5.5, while our final conclusions are provided in Sec. 5.6.

5.2 Theory

In the following, we will give a brief overview of our modelling of accretion flows (in Sec. 5.2.1) and of ray-tracing around supermassive BHs (in Sec. 5.2.2).

5.2.1 Accretion model

Being a bright source for terrestrial and space observatories across different parts of the electromagnetic spectrum, M87* has been extensively observed in a variety of wavelengths [278]. The central BH mass can be estimated by modeling the dynamics of nearby gas [279] or stars [280]. Note that these methods give different BH mass values, but the recent EHT measurement of $M_{\rm BH} = (6.5 \pm 0.7) \times 10^9 M_\odot$ only agrees with the stellar dynamics measurement [265]. The environment of M87* is believed to be a geometrically thick and optically thin accretion disk [11], rather than a geometrically thin and optically thick one (such as e.g. the classic Novikov-Thorne model [281]). The photons observed by the EHT at 1.3 mm are thought to be produced by synchrotron radiation from the relativistic electrons in the hot accretion plasma [11, 264]. Moreover, M87* exhibits a visible jet, observable at all wavelengths, whose power has been used to disfavor zero-spin models [11, 282].

For our purposes, we employ a simplified toy model for the accretion flow. We assume a spherically symmetric and optically thin disk surrounding a spherically symmetric (i.e. non-rotating) BH with metric

$$ds^2 = g_{tt}(r)\, dt^2 + g_{rr}(r)\, dr^2 + r^2 d\theta^2 + r^2 \sin^2(\theta)\, d\phi^2, \tag{5.1}$$

where $g_{tt}(r)\, g_{rr}(r) = -B(r)^2$, with $B(r)$ being a free function. The power radiated by the disk can be characterized by the *emissivity* [283],

$$j_\nu(r) = \frac{dE}{dV\, dt\, d\nu}, \tag{5.2}$$

which we assume to be independent of the frequency ν. Motivated by radiatively inefficient accretion flow (RIAF) models [277, 284], we assume that the spatial distribution of the emissivity is well-described by a power law $j_\nu(r) \propto r^{-n}$, with $n \approx 1$.

We assume that the BH image is detected by a distant observer. Hence, the image can be described by the intensity $I_\nu(b)$, as a function of the impact parameter b of the null geodesics along which photons propagate. The intensity can be obtained by integrating the radiative transfer equations (here presented in the form of Ref. [285, 286]),

$$\frac{d}{d\lambda}\left(\frac{I_{\nu,\rm obs}}{\nu_{\rm obs}^3}\right) = \frac{j_\nu}{\nu^2} e^{-\tau_{\nu,\rm obs}}, \tag{5.3}$$

$$\frac{d\tau_{\nu,\rm obs}}{d\lambda} = \alpha_\nu \nu, \tag{5.4}$$

where $\nu = -\kappa_\mu u^\mu$, with κ^μ the photon's linear momentum and u^μ the 4-velocity

of the disk's fluid, is the photon's frequency as measured in the fluid's rest frame. The subscript "obs" denotes quantities in the observer's frame.

These equations are integrated from the matter source to the far away observer along null geodesics parametrized by the affine parameter λ. Since we make the assumption of a disk that is (perfectly) optically thin, we choose an absorption coefficient $\alpha_\nu = 0$, and we also neglect the Doppler shift due to the motion of the disk's fluid, i.e. we assume $u^\mu = (1/\sqrt{-g_{tt}}, 0, 0, 0)$. Furthermore, we assume that the observer measures $I_{\nu,\mathrm{obs}}(b)$ at a single frequency.[2] Hereinafter, for simplicity, we will drop the labels ν and "obs" in both the intensity and the emissivity.

5.2.2 Ray-tracing

The photons contributing to the BH image probe the spacetime along null geodesics. In the vicinity of a Schwarzschild BH, these photons are strongly lensed. For a critical impact parameter $b_{\mathrm{ph}} = 3\sqrt{3}\,M_{\mathrm{BH}}$, where M_{BH} is the mass of the BH, photons follow unstable circular orbits at a surface called the *photon sphere*. If no matter is present within this surface, this critical value of b_{ph} can be interpreted as the size of the BH *shadow*. [287]

In practice, although photons follow trajectories from the source to the observer, *ray-tracing* algorithms often integrate the geodesics and radiative transfer equations in the opposite direction – see e.g. Ref. [286]. In addition, although the geodesics equations are integrable in spherical symmetry (and in the Kerr spacetime), it is convenient to consider the standard second-order equations

$$\frac{d^2\kappa^\mu}{d\lambda^2} + \Gamma^\mu_{\rho\sigma}\frac{d\kappa^\rho}{d\lambda}\frac{d\kappa^\sigma}{d\lambda} = 0, \tag{5.5}$$

where $\Gamma^\mu_{\rho\sigma}$ are the Christoffel symbols. The advantages of this choice are that one avoids a special treatment at the turning points of the geodesics, and (as we will describe below) one can linearly perturb these equations in a straightforward way.

5.3 Methods

In this Section, we outline our PCA method. In more detail, in Sec. 5.3.1 we introduce the basis functions on which we decompose the accretion model and the deviations of the BH metric away from Schwarzschild. In Sec. 5.3.2, we present our (linearized) likelihood, and apply the PCA to it in Sec. 5.3.3. The role of priors is discussed in Sec. 5.3.4.

[2] In practice, the EHT measures *visibilities*, which correspond to the Fourier transform coefficients of the Stokes parameters of the image.

5.3.1 Choice of basis

Recalling the discussion in Sec. 1.4.1, a useful way to describe and test the multiple possible modified gravity solutions for BH geometries is to employ physically motivated parametrizations of the metric. In spherical symmetry, these can take the form of series of r^{-n} terms, with $n \neq 0$, like in the post-Newtonian (PN) series, or more complicated expressions, like in the Rezzolla-Zhidenko parametrization, where the metric coefficients are described by Padé approximants [138, 140]. One must be careful, however, that any particular parametrization may not be able to describe all possible *arbitrary* departures from GR, especially if only few parameters are left free to vary.[3] For instance, the PN expansion is valid only for mild gravitational fields, c.f. for instance Ref. [144], and an infinite number of terms would be needed to describe all possible conceivable BH metrics in the strong field region.

In the following, we therefore allow the deviations of the metric from the Schwarzschild solution to have an arbitrary form. Focusing on $g_{tt}(r)$ and assuming for simplicity a toy model where $B(r) \equiv 1$ (and hence $g_{tt}(r)\, g_{rr}(r) = -1$), one can write

$$g_{tt}(r) = g_{tt}^{(0)}(r) + \sum_i \alpha_i^{(tt)} \delta g_{tt}^{(i)}(r), \tag{5.6}$$

where $\alpha_i^{(tt)}$ are free coefficients, $g_{tt}^{(0)}(r)$ is the Schwarzschild solution, and the functions $\delta g_{tt}^{(i)}(r)$ form a suitable *basis* on which any smooth function defined on the (positive) real axis can be decomposed. The basis is sometimes referred to also as *frame*. A familiar example of basis functions is given by sines and cosines in Fourier analysis. Another example is provided by the Morlet-Gabor wavelets used in gravitational wave analysis pipelines [137]. This basis need not be orthogonal. For instance, in some of the applications described in the following, we choose the basis to consist of Gaussians (centered on different points on the real axis, labelled by a discrete index i, but with a non-vanishing overlap to enforce continuity of the reconstructed function).

In order to account for uncertainties in the astrophysical model, we can write a similar expression for the emissivity of the disk:

$$j(r) = j^{(0)}(r) + \sum_i \alpha_i^{(J)} \delta j^{(i)}(r), \tag{5.7}$$

[3] Note however that the Rezzolla-Zhidenko parametrization has proven very flexible in this respect, as it is capable of reproducing BH geometries in entire classes of theories [139] with relatively few parameters. However, those theories are not necessarily comprehensive of all possible deviations from GR that one can conceive.

where $\alpha_i^{(J)}$ are again free coefficients, and $\delta j^{(i)}(r)$ may be different from the metric basis functions.

5.3.2 Linearized model and likelihood

We approach the inverse problem of reconstructing the spacetime metric from the observed BH image within a Bayesian perspective. The expressions in Eqs. (5.6) and (5.7) will be the backbone of our model $I_M(\alpha, b)$ for the BH image. We will then seek to estimate the parameters $\boldsymbol{\alpha} = \left(\alpha_l^{(tt)}, \alpha_m^{(J)}\right)$ that best describe the BH image data $I_D(b)$. When the posterior probability can be approximated as Gaussian, one can further "clean" the reconstructed metric by means of a PCA.

We begin by describing our model for the BH image in more detail. We assume that the image consists of a finite number of data points at locations $b_1, \ldots, b_N$, where the associated intensity $\boldsymbol{I}_D = (I_{D,1}, \ldots, I_{D,N})$ is measured. We also assume that the data are subject to Gaussian measurement errors, which we assume to be constant and given by σ. As for our model, which we denote by $\boldsymbol{I}_M(\boldsymbol{\alpha}) = (I_M(\boldsymbol{\alpha}, b_1), \ldots, I_M(\boldsymbol{\alpha}, b_N))$, we integrate numerically the radiative transfer and geodesic equations [Eqs. (5.3) and (5.5)] assuming Eqs. (5.6) and (5.7). In particular, in order to render the posterior probability function Gaussian (i.e. quadratic in the parameters $\boldsymbol{\alpha}$) and apply the PCA technique, we linearize Eqs. (5.3) and (5.5) in $\boldsymbol{\alpha}$.

Physically, this amounts to assuming that the deviations from Schwarzschild and from our default emissivity model are small. (We do not report these linearized equations here as they are cumbersome and not particularly illuminating – see e.g. Appendix A of Ref. [288] for the linear perturbations of the geodesic equations.) In practice, the 14 first-order linearized equations for the variables

$$\{t, r, \phi, \dot{t}, \dot{r}, \dot{\phi}, \delta t, \delta r, \delta\phi, \delta\dot{t}, \delta\dot{r}, \delta\dot{\phi}, I^{(0)}, \delta I\}, \tag{5.8}$$

where $\dot{X} \equiv dX/d\lambda$, are integrated with a custom-made ray-tracing code written in C++ and employing an adaptive stepsize fourth order Runge-Kutta algorithm [289]. Therefore, the model can be written as

$$\boldsymbol{I}_M(\boldsymbol{\alpha}) = \boldsymbol{I}^{(0)} + \sum_{i=1}^{M} \alpha_i \delta\boldsymbol{I}, \tag{5.9}$$

where M is the total number of α_i parameters and $\delta\boldsymbol{I}$ are the image deviations corresponding to each of the individual basis functions.[4]

[4]Notice that the basis functions (dependent on the coordinate variable r) are mapped into an image space (dependent on the impact parameter variable b) by a nonlinear transformation or "transfer function". In many applications of the PCA (e.g. Ref. [290]) there is no such

In the Bayesian framework, the solution to the inverse problem, up to a normalization factor, is encoded in the posterior probability distribution, given by

$$p\left(\boldsymbol{\alpha}|\boldsymbol{I}_D\right) \propto p\left(\boldsymbol{I}_D|\boldsymbol{\alpha}\right) p\left(\boldsymbol{\alpha}\right), \tag{5.10}$$

where the likelihood follows from the assumption of Gaussian measurement errors and is given by

$$\log p\left(\boldsymbol{I}_D|\boldsymbol{\alpha}\right) = -\frac{\chi^2}{2}, \tag{5.11}$$

with

$$\chi^2 = \frac{1}{\sigma^2}\left(\boldsymbol{I}_D - \boldsymbol{I}_M\left(\boldsymbol{\alpha}\right)\right)^T\left(\boldsymbol{I}_D - \boldsymbol{I}_M\left(\boldsymbol{\alpha}\right)\right). \tag{5.12}$$

In addition, as explained below, we will assume Gaussian priors $p\left(\boldsymbol{\alpha}\right)$. This choice, coupled with the likelihood Eq. (5.12), yields Gaussian posteriors, which are suitable for PCA.

5.3.3 Principal Component Analysis

Since the model is linear in the parameters and the posterior probability is Gaussian, the maximum of the latter (i.e. the "most likely" parameters $\boldsymbol{\alpha}^\star$) can be obtained by solving a (possibly degenerate) linear system of equations of the form $\boldsymbol{F}\boldsymbol{\alpha} + \boldsymbol{q} = 0$, where the $M \times M$ matrix $\boldsymbol{F}$ (defined below) and the M-vector $\boldsymbol{q}$ are computed numerically with our ray-tracing code. (This is the most computationally expensive part of the framework since it involves computing a perturbed image for every basis function.) The errors associated with the parameters are in general correlated and are encoded in the Fisher (Hessian) matrix

$$F_{lm} = -\frac{1}{2}\frac{\partial^2}{\partial\alpha_l\partial\alpha_m}\log p\left(\boldsymbol{\alpha}|\boldsymbol{I}_D\right), \tag{5.13}$$

which, with our assumptions, becomes a constant matrix. Linear combinations of the parameters corresponding to the Fisher matrix orthonormal eigenvectors $\boldsymbol{e}^{(i)}$, however, have uncorrelated errors $\sigma^{(i)} = 1/\sqrt{2\lambda^{(i)}}$, where $\lambda^{(i)}$ are the corresponding eigenvalues.

The main idea behind the PCA is to clean the reconstruction of the model by keeping only the "largest" coefficients $\beta_i = \boldsymbol{\alpha}^\star \cdot \boldsymbol{e}^{(i)}$. This is akin to the procedure of cleaning a time series from noise by performing a Fourier transform, and then keeping only the Fourier terms with coefficients significantly different from zero.

mapping.

More precisely, we prescribe the selection criterion [290]

$$|\beta_i| \geq N_{\rm th}\sigma^{(i)}, \tag{5.14}$$

whereby we only retain the coefficients β_i that are inconsistent with zero at $N_{\rm th}$-th sigma level, with $N_{\rm th} \approx$ 1-3. The final estimate of the parameters is then given by

$$\boldsymbol{\alpha}^{\rm PCA} \equiv \sum_{|\beta_i|\geq N_{\rm th}\sigma^{(i)}} \left(\beta_i \ \pm \sigma^{(i)}\right) \boldsymbol{e}^{(i)}. \tag{5.15}$$

Explicitly, the reconstructed metric and emissivity are then given by

$$g_{tt}^{\rm PCA}(r) \equiv g_{tt}^{(0)}(r) + \sum_{|\beta_i|\geq N_{\rm th}\sigma^{(i)}} \left(\beta_i \ \pm \sigma^{(i)}\right) \eta^{(i),(tt)}(r), \tag{5.16}$$

$$j^{\rm PCA}(r) \equiv j^{(0)}(r) + \sum_{|\beta_i|\geq N_{\rm th}\sigma^{(i)}} \left(\beta_i \ \pm \sigma^{(i)}\right) \eta^{(i),(J)}(r), \tag{5.17}$$

where

$$\eta^{(i),(tt)}(r) \equiv \sum_k e_k^{(i),(tt)} \delta g_{tt}^{(k)}(r), \tag{5.18}$$

$$\eta^{(i),(J)}(r) \equiv \sum_k e_k^{(i),(J)} \delta j^{(k)}(r), \tag{5.19}$$

are the corresponding eigenfunctions. Here we have separated the eigenvectors $\boldsymbol{e}^{(i)} = \left(e_l^{(i),(tt)}, e_m^{(i),(J)}\right)$ according to their corresponding metric and emissivity indices. Note that because the coefficients β_i are uncorrelated Gaussian variables, the errors on the reconstructed metric and emissivity at a given location can be computed by propagating the errors $\sigma^{(i)}$ in quadrature. These errors will be reported in Sec. 5.4.

5.3.4 Priors

The use of priors in the reconstruction can enhance it by mitigating some of the degeneracies that may be present. First, the linear system needed to solve for $\boldsymbol{\alpha}^\star$, and thus to obtain $\boldsymbol{\alpha}^{\rm PCA}$, is in general degenerate. One way to tame this issue is by conditioning the Fisher matrix F_{lm}, i.e. by replacing $F_{lm} \to F_{lm} + \epsilon\, \delta_{lm}$, where δ_{lm} is the Kronecker delta and ϵ is suitably small [290]. From the Bayesian perspective, this can be interpreted as prescribing loose Gaussian priors for $\boldsymbol{\alpha}$ centered at zero. At least in the case of the metric, this is in line with the theoretical expectation that the parameters $\alpha_i^{(tt)}$, which describe the deviations from GR, should be small.

Proper priors on the coefficients of neighboring basis functions can also be used to enforce continuity [291]. More importantly, from a physical point of view, priors can be used to enforce the expectation that the metric deviations are well constrained at large distances, where the Newtonian limit of GR (but not necessarily its 1PN dynamics [144]) should be recovered. For the Gaussian basis functions uniformly distributed in radius that we will use below, we therefore include a prior of the form

$$p(\boldsymbol{\alpha}) \propto \exp\left[-\left(\frac{r_{(i)}}{M_{\rm BH}}\right)^n \sum_i \frac{\alpha_i^{(tt)\,2}}{2\sigma_r^2}\right], \tag{5.20}$$

with $n = 4$, constant σ_r and $r_{(i)}$ the location of the Gaussian basis function associated to $\alpha_i^{(tt)}$. Equivalently, this corresponds to the expectation that the deviations from GR enter at 1PN order or higher [144]. This prior has also the advantage that it stabilizes the reconstruction against fluctuations from different noise realizations. Finally, the choice of the reference functions $g_{tt}^{(0)}(r)$ and $j^{(0)}(r)$ constitutes an additional "theoretical prior".

5.4 Applications and results

We apply our framework to the following cases. First, in Sec. 5.4.1 we assume that the spacetime geometry is known and only the accretion flow, described by the emissivity, needs to be reconstructed. Second, in Sec. 5.4.2 we consider the opposite case in which the emissivity is assumed to be known, but the spacetime geometry needs to be reconstructed. Finally, in Sec. 5.4.3 we let both the spacetime geometry and the accretion flow model undetermined at the same time. In order to directly compare the results obtained in these three ways, we show the corresponding reconstructions in the same figures at the end of this Section. Since we do not realistically model the details of the noise in the simulated observations, in the following we will focus on injections in the noiseless approximation. This for instance standard when designing gravitational wave data analysis pipelines [292]. However, we have checked that the results are similar for explicit realizations of the Gaussian noise.

In the following, we also introduce the scales j_* and I_*, with units $[j_*] = [\text{energy}]\,[\text{length}]^{-3}$ and $[I_*] = [\text{length}]\,[j_*]$, as a normalizing scales for the emissivity and observed intensity.

5.4.1 Reconstructing the accretion flow

We fix the reference metric function to be that of the Schwarzschild geometry, $g_{tt}^{(0)}(r) = -(1 - 2M_{\rm BH}/r)$, without allowing for any deviations from it –i.e. only the astrophysical parameters $\alpha_i^{(J)}$ are allowed to vary. As for the reference emissivity, we choose it to be $j^{(0)}(r) = 0$ (i.e. we assume no prior knowledge of the emissivity). We produce the injection (i.e. the data) $\boldsymbol{I}_D$ from

$$g_{tt,D}(r) = g_{tt}^{(0)}(r), \qquad\qquad j_D(r) = 2j_* \frac{M_{\rm BH}}{r}. \tag{5.21}$$

We assume an optimistic resolution of $0.15\,M_{\rm BH}$ (potentially achievable with future space-based interferometers [293]). More precisely, we generate $N = 100$ data points uniformly distributed in the interval of impact parameters $[0, 15\,M_{\rm BH}]$, and assume an (uncorrelated) measurement error of $\sigma = 0.1\,I_*$. The basis is composed of 161 (unnormalized) Gaussians uniformly distributed in the interval of radii $[0, 100\,M_{\rm BH}]$, with root mean square (RMS) width of $1\,M_{\rm BH}$. We condition the Fisher matrix with $\epsilon = 1$, which can also be interpreted as a Gaussian prior, as discussed in Sec. 5.3.4.

In the upper panel of Fig. 5.1, in blue, we show the intensity profile for the injection Eq. (5.21), as a function of the impact parameter. One can clearly observe the effect of the photon sphere at $b \approx 5.2\,M_{\rm BH}$. In Fig. 5.2, with blue contours, we show the 2σ bands of the reconstructed emissivity profile for a PCA criterion parameter $N_{\rm th} = 1$. We observe good agreement with the injection (gray dashed lines) for most radii. The reconstruction, however, does not accurately reproduce the emissivity profile near the BH horizon at $r = 2\,M_{\rm BH}$. This disagreement is most likely due to the effect of gravitational redshift, which suppresses the intensity of the near-horizon Gaussian components. The widening of the reconstruction bands at $r \approx 14\,M_{\rm BH}$ occurs instead because the image data were provided in a finite interval –i.e. it is an "edge effect".

5.4.2 Reconstructing the geometry

In the following, we present the results of our framework when the accretion flow is assumed to be known and only the background metric is reconstructed –i.e. when only the parameters $\alpha_i^{(tt)}$ are allowed to vary.

For this example, the injection includes a deviation from GR in the metric, which is given by

$$g_{tt,D}(r) = g_{tt}^{(0)}(r) - 0.02\,\exp\left[-\frac{(r - 7\,M_{\rm BH})^2}{M_{\rm BH}^2}\right] - 0.8\left(\frac{M_{\rm BH}}{r}\right)^3,$$

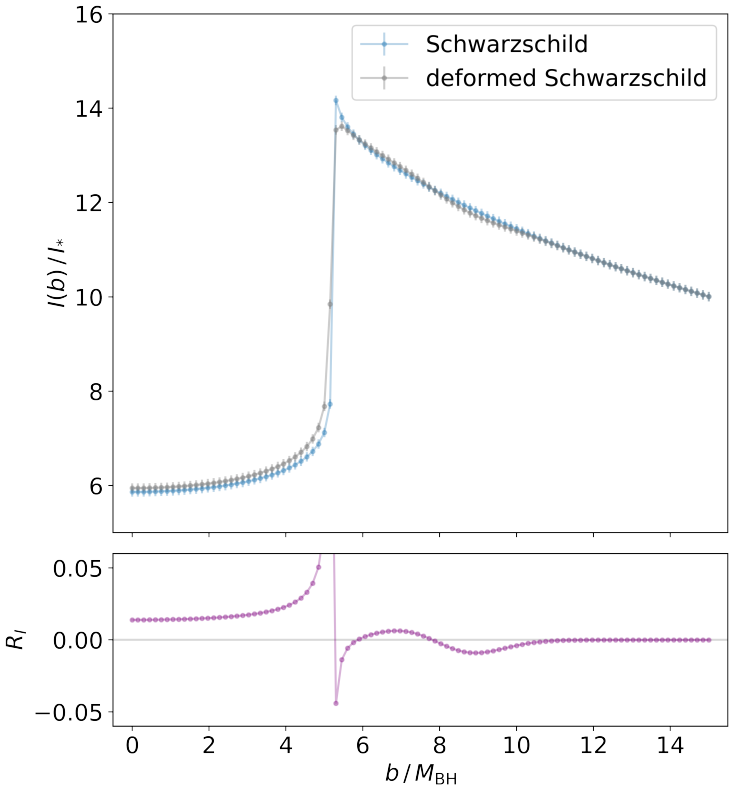

Figure 5.1: *Intensity profile for a deformed Schwarzschild metric.* Upper panel: Computed intensity profiles $I(b)$ used as "observations", as a function of the impact parameter b for the Schwarzschild metric (blue) and the deformed Schwarzschild metric (gray), with corresponding "measurement" error bars of $\pm 0.1\, I_*$. The scale I_* is used to normalize the intensity profile, and its units are given in the main text. The Schwarzschild intensity profile is used as input data for the example of Sec. 5.4.1, while the deformed Schwarzschild one is used in the examples of Secs. 5.4.2 and 5.4.3. Lower panel: Relative difference $R_I = (I_{\rm Sch} - I_{\text{def-Sch}})/I_{\rm Sch}$ of the images in the upper panel.

$$j_D(r) = j^{(0)}(r) = 2j_* \frac{M_{\rm BH}}{r}, \tag{5.22}$$

where $g_{tt}^{(0)}(r) = -(1 - 2M_{\rm BH}/r)$. For the sake of simplicity, we also set the reference function for the emissivity to be the same as the injection –although we could have chosen a slightly different profile without strongly affecting our results. The resolution and measurement errors are the same as in the previous example. We choose a basis of 161 Gaussians uniformly distributed in the interval $[0, 25\, M_{\rm BH}]$ and with RMS width of $0.5\, M_{\rm BH}$, supplemented by additional power law components r^{-n}, with $n = 1, 2, \ldots, 15$. To improve the conditioning of the Fisher matrix, we also rescale the coefficients $\boldsymbol{\alpha}$ so that the different entries in that matrix are roughly of the same order of magnitude. The r^{-1} power law accounts for the uncertainty in our knowledge of the mass, for which we assume a small prior measurement error of $\sigma_{M_{\rm BH}} = 0.01\, M_{\rm BH}$. Finally, we take $\epsilon = 10^{-3}$ for the conditioning of the Fisher matrix, and $\sigma_r^2 = 10^5$ for the large distance prior of Eq. (5.20).

The intensity profile used as data and produced from Eq. (5.22) is shown in the upper panel of Fig. 5.1, in gray. Here, one can observe the breakdown of the linear approximation to the full geodesics equation at $b \approx 5.2\,M_{\rm BH}$, where the linear approximation fails to reproduce the shift in the photon sphere projection away from the Schwarzschild solution, shown in blue. We will not worry about this spurious effect for the moment (as it concerns only few data points) and postpone a more thorough discussion of it to Sec. 5.5.1.

Let us also briefly comment about the features of the resulting image. In the lower panel of Fig. 5.1, we show the relative difference between the images of the upper panel of Fig. 5.1. Since the injected metric deformation [Eq. (5.22)] has a local minimum around $r \approx 7\,M_{\rm BH}$, one could naively expect that the absolute value of the relative difference should also have a local maximum there. However, a more involved structure is evident. The appearance of a hill and a trough in the intensity is mostly due to the derivatives of the metric deviation from Schwarzschild becoming larger and dominant at the location of the bump – indeed, this pattern resembles the shape of the derivative of a Gaussian function.

In Fig. 5.3, in blue, we show the 2σ reconstruction contours for the deviation of the metric from Schwarzschild. As before, we observe generally good agreement with the injection (gray dashed lines) for the $N_{\rm th} = 1$ PCA criterion. The reconstructed bump is clearly distinguishable from the power law component. The narrower error bands near the photon sphere at $r \approx 3\,M_{\rm BH}$ indicate greater sensitivity of the method to features in that region. As in the previous example, the goodness of the reconstruction deteriorates near the BH horizon ($r \approx 2\,M_{\rm BH}$) presumably due to the effect of gravitational redshift. Finally, we observe a slight oscillatory behavior around $r \approx 11\,M_{\rm BH}$. This happens because many of the eigenvectors (and consequently the eigenfunctions) of the Fisher matrix present oscillatory features. By including more components (i.e. lower $N_{\rm th}$ or smaller measurement error), these oscillatory components interfere and cancel out to give a better overall reconstruction.

5.4.3 Reconstructing astrophysics and geometry

Finally, we will now present the most interesting results of our framework. These correspond to cases in which both the spacetime and accretion flow are reconstructed at the same time –i.e. all of the parameters $\boldsymbol{\alpha}$ are allowed to vary. Since both aspects play an important role in the details of BH images, one might argue that it is not possible to constrain deviations in the metric when the exact details of the astrophysical model are not known –see for example Gralla [266]. In this section, we will show that if our "theoretical priors" are strong enough, it is in principle possible to disentangle the two types of contributions. Such strong

priors can be achieved by sufficient understanding of the underlying astrophysics and by reasonable constraints on the long distance behavior of the metric.

For this example, the injection and reference functions are the same as in Sec. 5.4.2. In this case, as expected, we find that there are degeneracies between the metric and the emissivity, when one considers a Gaussian basis for both functions. Indeed, one generically obtains degenerate reconstructions – i.e. profiles for the metric and emissivity that reproduce the data but do not correspond to the injection. Since these are "failed" reconstructions, we do not present them here.

In order to tighten our priors and mitigate this degeneracy, we assume that the radial distribution of the emissivity is well described by a power law (as in RIAF models), and thus allow only the amplitude and exponent to vary. Moreover, we linearize the emissivity in the deviation of the exponent away from the default reference value [which is set as in Eq. (5.22) for this example], so as to reduce to Eq. (5.7). We take the metric basis and priors to be the same as in the previous example, and perform the reconstruction with a PCA criterion $N_{\rm th} = 1$ as before.

In Fig. 5.2, we show the 2σ reconstruction contours of the emissivity in orange. Because of the tight "theoretical priors" that we assumed on the functional form of the the emissivity, the reconstruction is much better than the "agnostic" one. However, upon closer inspection, as can be seen from the inset, a slight bias is noticeable in the reconstruction. Part of it is due to the missing information weeded out by the PCA criterion. We have verified this by comparing reconstructions with different values of $N_{\rm th}$.

In Fig. 5.3, one can observe that the reconstruction of the metric deviation (in orange) recovers the injection as in the previous example. It also exhibits the narrower contour bands near $r \approx 3\,M_{\rm BH}$, and the slightly inaccurate reconstruction near the BH horizon at $r \approx 2\,M_{\rm BH}$, like before.

This example illustrates that a good, but not necessarily complete, understanding of the astrophysics may be sufficient to extract possible deviations from GR from the BH image. Although constraining the emissivity to follow a particular parametrization – here a power law – may seem rather restrictive, this is not necessarily the only way to mitigate the degeneracy. Alternative possibilities may include judiciously prescribing the priors of the astrophysical parameters –in the spirit of the metric prior of Eq. (5.20)–, or reducing the number of parameters in the metric by employing a particular ansatz – e.g. the Rezzolla-Zhidenko parametrization [138]. This second possibility, however, comes at the cost of being less general, however. We leave these possibilities to future extensions of this work.

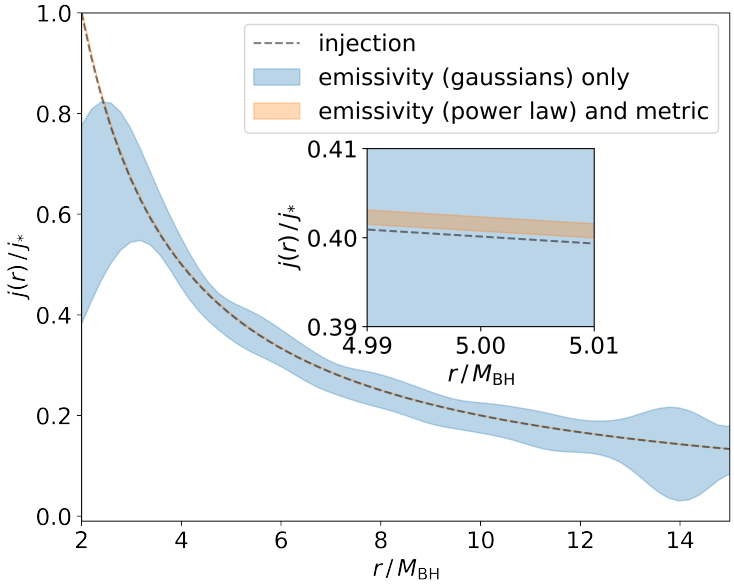

Figure 5.2: *Reconstruction of the emissivity.* Individual reconstruction of the emissivity when the metric is fixed (blue), and joint reconstruction (orange) when it is constrained to be a power law, corresponding respectively to the examples of Sec. 5.4.1 and 5.4.3. The scale j_* is used to normalize the emissivity and its units are given in the main text.

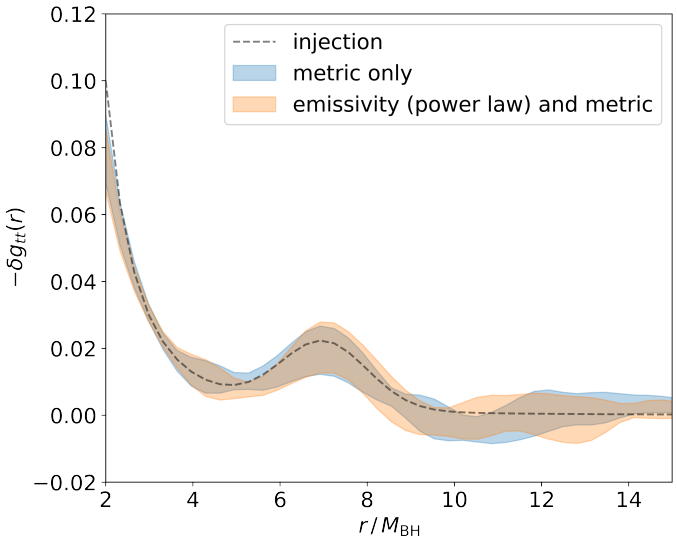

Figure 5.3: *Reconstruction of the metric deviation.* Individual reconstruction of the metric deviation from Schwarzschild, $\delta g_{tt}(r) = g_{tt}(r) - g_{tt}^{(0)}(r)$, when the emissivity is fixed (blue) and joint reconstruction (orange), corresponding respectively to the examples of Sec. 5.4.1 and 5.4.3.

5.5 Discussion

In this Section, we briefly comment about the relation between our framework and other existing approaches (Sec. 5.5.1). Some limitations and possible extensions of this work are discussed in Sec. 5.5.2. Finally, possible connections to the inverse problem in gravitational wave astronomy are mentioned in Sec. 5.5.3.

5.5.1 Comparison to other approaches

Many previous works on modified gravity constraints using the EHT measurements utilize only the size of the critical curve corresponding to the projection at infinity of the photon sphere [142, 250–262]. This is justified, because it has been argued that the size of the bright ring is a robust feature in the BH image [11, 263, 267]. However, whether the approach is to constrain the charges and coupling constants of particular solutions in modified theories of gravity (e.g. "exotic" Reissner–Nordström solutions [294, 295]), or to constrain the parameters in phenomenological parametrizations of the metric (e.g. the Rezzolla-Zhidenko parametrization [138]), the bounds that are obtained are generically degenerate and loose when many parameters are at play [144]. This is not surprising since the shadow size amounts to the measurement of a single number. Indeed, if our PCA framework is applied to the shadow size alone (see Appendix D.1), the only combination of parameters that can be constrained [c.f. Eq. (11) of Ref. [144]] is

$$\sum_{i=1}^{M} \alpha_i \delta g_{tt}^{(i)} \left(3\, M_{\rm BH}\right) . \tag{5.23}$$

In this Chapter, we have on the one hand exploited the whole intensity profile of the EHT BH image (although in a toy model and with mock data). On the other hand, to allow for generic deviations away from GR BHs, we have parametrized the metric in terms of a completely general superposition of basis functions. We have then performed a PCA analysis to obtain a smooth metric reconstruction, filtering out the components that cannot be significantly constrained. This technique has been applied before to describe the shape of the shadow of spinning BHs in non-Kerr metrics in Ref. [262]. However, unlike in previous applications, here it is used to reconstruct the spacetime geometry and the disk's emissivity using the whole intensity profile of the BH image.

5.5.2 Limitations and possible extensions

Although astrophysical BHs are believed to be simple (i.e. describable only by their mass and angular momentum [43, 44, 249, 296]), the modelling of their en-

vironments is fairly complex. In this Chapter, we have made a large number of simplifications (no spin, static and spherical accretion flow, etc.). Nevertheless, the inclusion of many of these environmental aspects is conceptually straightforward, although it would lead to computationally more intensive analyses.

We have made further simplifications regarding the observational data. In particular, we have assumed that the intensity profile is measured directly and that the associated errors are Gaussian and uncorrelated. The inclusion of *visibilities* – the observables that the EHT actually measures and which correspond to the Fourier transform coefficients of the image – is also possible in future extensions of the work presented in this Chapter. However, one would have to deal with additional errors due to the incomplete observational coverage of the visibility parameter space – see e.g. Fig. 2 of Ref. [264].

Regarding the actual calculation of the BH image, we have linearized the radiative transfer and geodesic equations [Eqs. (5.5) and (5.3)]. This step was essential in order to make the likelihood a Gaussian function and to allow us to apply the PCA technique (which relies on the Fisher matrix being constant). For the case of the metric, this is justified by the expectation that deviations from the GR solution are small. Similarly, the linearization is reasonable for the accretion parameters, provided that one has good prior knowledge of the astrophysical model.

Even in this case, however, some non-perturbative effects may be important. In particular, the linearization does not capture the shift in the position of the photon sphere or the BH horizon. Future work in this direction may include integration of the full non-linear equations and reconstruction with Markov Chain Monte Carlo (MCMC) techniques, along the line of Refs. [277, 297].

Finally, we also recall that we have considered a metric ansatz [Eq. (5.1)] satisfying $g_{tt}(r)\, g_{rr}(r) = -1$. It is well known that this condition does not hold in general [298]. Moreover, it is expected that BHs have spin – e.g. to power the jet seen in M87* [11, 282]. Therefore, a more rigorous analysis should necessarily include more than one independent metric function, leading to further degeneracy between them. A first step in this direction would be to consider the slowly rotating case, by assuming a fixed form of the mixed terms in the metric, i.e. $g_{t\phi}(r) = g_{\phi t}(r) = -M_{\rm BH}^2 a/r$, and linearizing Eqs. (5.3) and (5.5) in the dimensionless spin parameter a. In this case (even if the accretion flow is spherical) the radial symmetry of the BH image is broken and we expect that the angle of observation will become important in our ability to extract a with our PCA approach. In the most general case, once rotation and realistic accretion are considered, we expect that a good modelling of the astrophysical component, as well as appropriate priors that reflect our knowledge in the weak gravity regime,

will continue to be key in allowing to extract possible deviations of the spacetime geometry. Moreover, although more information in the BH image could potentially be extracted, additional strategies may be needed handle degeneracy in the parameter space. We leave this more challenging setup for future work.

5.5.3 Possible connections to gravitational waves

It is well known in the literature that BH *quasi-normal modes* in the eikonal approximation are closely related to the impact parameter of the BH shadow [299, 300]. An interesting question is therefore whether there is a gravitational wave analog to the BH image. Unlike the image, which depends strongly on the surrounding matter, gravitational waves couple only very weakly to the environment, which would allow for a much cleaner test of BH geometries.

One possibility would be to use the full, infinite set of BH quasi-normal modes [301–303]. However, the eikonal approximation only probes the spacetime near the maximum of the potential. Moreover, in general one cannot expect that the inverse spectrum problem is uniquely solvable, e.g., in GR axial and polar perturbations are isospectral, but the underlying Regge-Wheeler and Zerilli potentials are not the same (and other isospectral, and thus equivalent, potentials can be built with suitable transformations [304, 305]). While degeneracies remain, however, it is possible to put some constraints on the BH metric or the potential for quasi-normal modes, given a finite set of quasi-normal mode measurements (see e.g. [145, 306]).

Closely related to the quasi-normal mode spectrum are the *transmission and reflection coefficients*, which describe the frequency dependent wave propagation in the spacetime. These coefficients are computed over the whole exterior BH spacetime. In the Wentzel–Kramers–Brillouin (WKB) approximation [307] this can be done via integral equations, which one can attempt to invert to constrain the properties of the potentials [308–310]. This can also be connected to Hawking radiation [171]. Like for the quasi-normal modes, however, the problem is not uniquely invertible.

5.6 Final comments

In this Chapter, we have demonstrated that BH spacetimes and simple accretion models can be constrained at the same time from BH images. The general inverse problem of BH imaging involves the reconstruction of the astrophysical properties of the accretion disk, as well as possible deviations of the spacetime geometry from GR. Our analysis is a proof of principle, because it is only valid (strictly speaking)

for spherically symmetric spacetimes and it makes considerable simplifications for the accretion model and for the mock data. It is clear that realistic modelling of astrophysical processes, as well as of the EHT data analysis pipeline, exceed what can be described by our simple current framework. However, the detailed study of a simplified toy models is still of great value and interest, since it allows one to understand the fundamental aspects of the problem. This is also well demonstrated by the ongoing discussion about the interpretation of the bright emission ring observed by the EHT collaboration, and namely about whether that can be robustly identified with the impact parameter of the photon orbit, and thus be used to test the Kerr hypothesis [144, 263, 266–268].

In summary, our framework addresses the fundamental question of whether astrophysical uncertainties and degeneracies jeopardize tests of the Kerr hypothesis with EHT BH images. By deriving a linear model that describes the BH geometry in terms of a general superposition of basis functions (Gaussians and power laws), we have demonstrated that a PCA technique allows for reconstructing the spacetime geometry *and* the accretion model *simultaneously*, provided that sufficient theoretical priors are available on the latter.

Part IV

Black holes in the ultraviolet

Chapter 6

Black holes in ultraviolet-complete Hořava gravity

As we have hinted in Sec. 1.3, Hořava gravity is a proposal for completing general relativity in the ultraviolet by interactions that violate Lorentz invariance at very high energies. In this Chapter, we focus on (2+1)-dimensional projectable Hořava gravity, a theory which is renormalizable and perturbatively ultraviolet-complete, enjoying an asymptotically free ultraviolet fixed point. Adding a small cosmological constant to regulate the long distance behavior of the metric, we search for all circularly symmetric stationary vacuum solutions with vanishing angular momentum and approaching the de Sitter metric with a possible angle deficit at infinity. We find a two-parameter family of such geometries. Apart from the cosmological de Sitter horizon, these solutions generally contain another Killing horizon and should therefore be interpreted as black holes from the viewpoint of the low-energy theory. Contrary to naive expectations, their central singularity is not resolved by the higher derivative terms present in the action. It is unknown at present if these solutions form as a result of gravitational collapse. The only solution regular everywhere is just the de Sitter metric devoid of any black hole horizon. Throughout this Chapter, we use units in which $\hbar = c = 1$, and metric signature $-++$.

6.1 Motivation and outline

Despite huge efforts in the last few decades, the formulation of a quantum theory of gravitation remains elusive. In particular, there lingers the open question of how to put together a theory that reproduces the well-known and tested infrared (IR) behavior of GR at the scales of the solar system and cosmology, while having a consistent ultraviolet (UV) limit. While to describe many low-energy systems it is often enough to consider GR as an EFT, as we have described in Sec. 1.4.2,

where the low-energy Lagrangian is complemented with an infinite series of higher dimensional operators encoding the effect of UV physics, there are situations in which a full description (valid for all ranges of energies) is needed.

The most prominent of such situations is provided by the existence of singularities within GR. The latter are regions of divergent spacetime curvature, where strong quantum gravitational effects cannot be neglected. The most worrisome singularities are cosmological and those occurring in the interior of BHs. In this Chapter, we focus on the latter. Although there are reasons to believe that BH singularities may always be hidden behind a horizon [217], thus remaining inaccessible to exterior observers, they are nevertheless the endpoint of any world-line crossing the event horizon of a BH. Any observer falling into the BH will unavoidably hit the singularity, thus quitting the range of validity of any EFT of gravity. Resolving the dynamics of the spacetime in the high-curvature region near singularities will therefore require a theory of quantum gravity.

At present, we still do not have such a theory at our disposal. A possible candidate, which has attracted much interest in recent years, is quadratic gravity [311, 312], where the Einstein-Hilbert Lagrangian is complemented by adding terms quadratic in the Riemann tensor, which make it renormalizable [313–315]. However, this theory contains a ghost in the spectrum, as a consequence of the presence of four time derivatives in the action, leading to violation of unitarity or catastrophic instabilities at high energies. Moreover, BH solutions in quadratic gravity – such as the Schwarzschild metric, which is still a solution of the field equations [316, 317]– are not free of singularities. Therefore, resolution of curvature singularities within quadratic gravity would require a separate mechanism, unrelated to renormalizability.

A compelling workaround to the ghost problem was proposed in 2009 by Petr Hořava [14]. If the spacetime is endowed with a preferred time foliation, then one can construct a theory that has only higher order *spatial* derivatives thus avoiding the presence of a ghost. By including in the action all marginal and relevant operators under an anisotropic (Lifshitz) scaling[1]

$$t \to b^d\, t, \qquad x^i \to b\, x^i, \tag{6.1}$$

where b is constant and d is the number of spatial dimensions, one can make the theory power-counting renormalizable.

The presence of a time foliation, and thus that of a privileged time direction, make it natural to formulate the theory by using the Arnowitt-Deser-Misner

[1]Latin indices run over space dimensions only ($i = 1, ..., d$), while Greek indices include time.

(ADM) decomposition of the metric [127]

$$ds^2 = -N^2 dt^2 + \gamma_{ij}(dx^i + N^i dt)(dx^j + N^j dt), \tag{6.2}$$

where N and N^i are respectively the lapse function and shift vector, and γ_{ij} is the metric of the spatial hypersurfaces. The presence of a preferred foliation also breaks the full diffeomorphism invariance of GR. The gauge group of the theory reduces to *foliation preserving diffeomorphisms (FDiff)*, i.e. it consists of the direct product of time-dependent spatial diffeomorphisms and time re-parametrizations

$$t \to \tilde{t}(t), \quad x^i \to \tilde{x}^i(t, x), \tag{6.3}$$

where $\tilde{t}(t)$ is a monotonic function.

Locally, the presence of the preferred foliation breaks Lorentz invariance by allowing for dispersion relations with higher powers of the spatial momentum, i.e. $\omega^2 = c_1^2 k^2 + c_2^2 k^4 + ... + c_{2d}^2 k^{2d}$, with constant coefficients c_I. Lorentz invariance may only be recovered as an accidental symmetry in the IR, when higher derivatives are neglected and if the low-energy velocities c_1 flow to the same value for all particle species.

The splitting of *FDiff* into two distinct symmetries allows for formulating two versions of the theory, depending on how one deals with time re-parametrization invariance. In the *projectable* theory, one assumes that the lapse is independent of the spatial coordinates, i.e. a function $N(t)$ of time only. In that case, one can set its value to a constant, which can be chosen to be unity for convenience $[N(t) = 1]$, gauge fixing time re-parametrization invariance away.

After Hořava's seminal paper, there was a surge of activity in understanding the consequences of the theory, and its soundness as a proposal for quantum gravity. Soon, it was realized that the extra propagating scalar mode of the theory – present alongside the transverse-traceless graviton – was problematic. Although stable at high energies, in all dimensions higher than $d = 2$ it behaves as a tachyon in the IR, signaling that flat space is not a stable vacuum of the theory [128]. This can be solved by abandoning projectability and allowing the lapse $N(t, x^i)$ to be a function of all spacetime coordinates. This choice gives rise to a version of the theory known as *non-projectable Hořava gravity*. In this case, new terms are allowed in the Lagrangian, preventing the instability in the IR [125]. However, it comes at the cost of reintroducing time re-parametrization invariance as a full-fledged gauge symmetry. This causes the presence of an instantaneous propagating mode [128, 132] and complicates quantization of the model [318], although efforts to pursue this endeavor have not been spared [319–322].

On the other hand, the projectable model has been proven to be fully renormalizable in any spacetime dimension [124], preserving gauge invariance to all orders in the loop expansion [315]. Moreover, in $2+1$ dimensions it has been shown to be UV-complete [323], while propagating a stable non-trivial degree of freedom, thus representing a bona fide theory of quantum gravity in this dimensionality. There are also some hints that UV-completeness could hold in $3+1$ dimensions [324], although a proof is not yet available.

The existence of BHs has been extensively studied in the IR limit of non-projectable Hořava gravity, where the theory can be shown to be related to Einstein-Aether theory [134, 325, 326]. IR BH solutions have a structure similar to those of GR BHs, with a Killing horizon hiding a central singularity where every in-falling world-line ends [132, 327–330]. Additionally, they also possess a "universal horizon" [132, 327], i.e. a compact hypersurface of constant preferred time that surrounds the central singularity and from which no modes (even instantaneous ones) can escape. Its behavior mimics that of an event horizon in GR [331–333]. However, as mentioned, these are *low-energy solutions*, obtained by disregarding the higher derivative terms that should be important when an observer gets close to the singularity. A complete understanding of the interior of BHs and of the fate of the universal horizon would require to consider the full Lagrangian of the theory, carefully studying the effect of the UV-completing terms.

In this Chapter, we tie together all these issues, and study the effect of renormalizability on the resolution of curvature singularities in a controllable playground, that of *projectable Hořava gravity in* $2+1$ *spacetime dimensions*. As previously mentioned, this is a perturbative UV-complete theory, meaning that *it completely describes gravity, at any energy*.[2] The Lagrangian functional form of the theory should be valid up to arbitrary high energies – albeit with varying values for the coupling constants, as predicted by the renormalization group flow. If the solution to BH singularities is linked to the renormalizable character of the theory, without the need for any additional mechanism, it must then be contained within the dynamics dictated by the action. In other words, we use this model to address the following question: *does a UV-complete gravity theory resolve BH singularities?*

In this Chapter, we make the first steps in this direction and analyze all circularly symmetric vacuum solutions of the theory with vanishing angular momentum. Recall that GR in (2+1) dimensions does not have any BH solutions with flat or de Sitter asymptotics.[3] By contrast, we find that projectable Hořava grav-

[2] Up to, perhaps, presently unknown non-perturbative obstructions.

[3] BHs with anti-de Sitter (AdS) asymptotics do exist in the presence of a negative cosmological constant [334]. We do not consider this case in the context of projectable Hořava gravity

ity admits solutions that can be legitimately called BHs. We start by considering the low-energy limit of the theory and solve the equations of motion analytically when higher derivatives are neglected. The solutions present a Killing horizon and a curvature singularity at the origin of the coordinates. They therefore physically represent BHs, and one can use them as asymptotic solutions far from the center, where the curvature is small and neglecting higher-derivatives is a good approximation.

We will then attempt to extend our solutions numerically to the higher curvature region of the spacetime, including all the terms in the Lagrangian. By numerical investigation and analytic arguments, we show that there exist no vacuum solutions that are free of central curvature singularities and which reduce far from the center to the BH solutions found in the IR limit of the theory. In other words, we show that the higher-order derivatives, although they make the theory UV-complete and renormalizable, do not resolve the central singularity, at least classically. We will comment on the implications of this finding.

This Chapter is organized as follows. In Sec. 6.2 we review projectable Hořava gravity. In Sec. 6.3, we introduce our circularly symmetric and stationary ansatz, which we use to obtain BH solutions in the IR limit of the theory in Sec. 6.4. The embedding of these BH solutions into the full UV theory is discussed in Sec. 6.5, where we argue that such UV BH solutions necessarily present a curvature singularity at the center. This is further substantiated in Sec. 6.6 by utilizing a boundary-layer expansion. We discuss our findings and the mass of our BH solutions in Sec. 6.7.

6.2 Projectable Hořava gravity

We formulate Hořava gravity in terms of the ADM variables in Eq. (6.2). Under *FDiff* transformations the components of the metric behave as

$$\begin{aligned} N &\to N\frac{dt}{dt'}, \\ N^i &\to \left(N^j\frac{\partial x'^i}{\partial x^j} - \frac{\partial x'^i}{\partial t}\right)\frac{dt}{dt'}, \\ \gamma_{ij} &\to \gamma_{kl}\frac{\partial x^k}{\partial x'^i}\frac{\partial x^l}{\partial x'^j}. \end{aligned} \tag{6.4}$$

Their anisotropic scaling dimension under Eq. (6.1) is

$$[N] = [\gamma_{ij}] = 0, \qquad [N^i] = d - 1. \tag{6.5}$$

as the constant-lapse condition forces the AdS metric to be time dependent.

The requirement of *FDiff* invariance, time-reversal invariance, parity, power-counting renormalizability under Eq. (6.1) and absence of ghosts fixes the action to be

$$S = \frac{1}{\kappa} \int dt\ d^d x \sqrt{\gamma}\ N \left(K_{ij} K^{ij} - \lambda K^2 - \mathcal{V} \right), \tag{6.6}$$

where $\kappa = 16\pi G$ (notice that this convention is different that in Parts I-III) and λ are dimensionless coupling constants in the sense of Eq. (6.1) (i.e. they are invariant under that rescaling), and $\mathcal{V}$ contains all possible marginal and relevant operators with respect to the anisotropic scaling. Here, K_{ij} is the extrinsic curvature of the slices,

$$K_{ij} = \frac{1}{2N} \left(\partial_t \gamma_{ij} - \nabla_i N_j - \nabla_j N_i \right), \tag{6.7}$$

with ∇_i the covariant derivative compatible with γ_{ij}.

Hereinafter we will focus on the projectable model, thus from now on we will assume that $N(t)$ is independent of the spatial coordinates. We can therefore set it to $N(t) = 1$ by exploiting time reparametrization invariance, leaving time-dependent spatial diffeomorphisms as the only remaining gauge symmetry.[4] The potential $\mathcal{V}$ will thus be built exclusively out of *FDiff* invariants, constructed with the spatial metric and covariant derivatives. Its form in $d = 2$ is

$$\mathcal{V} = 2\Lambda + \mu R^2, \tag{6.8}$$

where R is the scalar curvature constructed from R_{ijkl}, the Riemann tensor of the spatial slices. Note that we are omitting a linear term in R, since it corresponds to the Gauss-Bonnet density in $d = 2$, thus being a total derivative. Here Λ is the cosmological constant which will serve as a regulator for the long-distance behavior of the BH solutions. The total action that we consider then takes the form

$$S = \frac{1}{\kappa} \int dt\ d^2 x \sqrt{\gamma}\ \left(K_{ij} K^{ij} - \lambda K^2 - \mu R^2 - 2\Lambda \right). \tag{6.9}$$

Although in $2+1$ dimensions GR propagates no local degrees of freedom, this is not the case for Hořava gravity. Due to the reduced symmetry group, there is an extra scalar degree of freedom in the spectrum of the theory, with dispersion relation

$$\omega^2 = 4\mu\ \frac{1-\lambda}{1-2\lambda}\ k^4 \tag{6.10}$$

[4] This implies disregarding the global Hamiltonian constraint $\delta S / \delta N = 0$.

around flat-space. Note the absence of k^2 term, as a consequence of the triviality of the piece linear in R in the Lagrangian. Unitarity and stability then require $\mu > 0$ and either $\lambda < \frac{1}{2}$ or $\lambda > 1$. We will consider the latter case throughout this Chapter, for reasons that will become clear in a moment.

When regarded as a quantum field theory, the action (6.9) corresponds to a renormalizable theory. Within perturbation theory, all UV divergences can be absorbed by a corresponding redefinition of the coupling constants. Correlation functions of observables are then essentially the same as their classical values, with κ, λ and μ replaced by $\kappa(k_*), \lambda(k_*), \mu(k_*)$, where k_* is a parameter that sets the interaction scale. The running of the couplings was computed in the one-loop approximation in Ref. [323] and reads

$$\frac{d\lambda}{d\log k_*} = \frac{15-14\lambda}{128\pi}\sqrt{\frac{1-2\lambda}{1-\lambda}}\ \tilde{\kappa} \tag{6.11a}$$

$$\frac{d\tilde{\kappa}}{d\log k_*} = -\frac{(16-33\lambda+18\lambda^2)}{128\pi(1-\lambda)^2}\sqrt{\frac{1-\lambda}{1-2\lambda}}\ \tilde{\kappa}^2, \tag{6.11b}$$

where we have defined $\tilde{\kappa} = \frac{\kappa}{\sqrt{\mu}}$. It can be shown that the flows of κ and μ are separately gauge dependent. However, those of $\tilde{\kappa}$ and λ are independent of the choice of gauge. This signals that only these parameters appear in correlation functions of gauge-invariant observables, and in physical observables of the theory.

The fact that the theory is stable against radiative corrections suggests a justification for attempting a classical treatment down to arbitrarily short scales. Indeed, the magnitude of quantum fluctuations can be estimated from the action (6.9) as follows. Setting that for fluctuations the action is of order unity, $\delta S \sim 1$, and assuming a regular geometry, we obtain

$$(\delta K_{ij})^2 \sim \frac{\kappa}{\tau l^2}\ , \qquad (\delta R)^2 \sim \frac{\kappa}{\mu\tau l^2}\ , \tag{6.12}$$

where τ and l are the characteristic time and length scales of the perturbations. The fluctuations of the extrinsic and intrinsic curvatures are related to the metric fluctuations as $\delta K_{ij} \sim \tau^{-1}\delta\gamma_{ij}$, $\delta R \sim l^{-2}\delta\gamma_{ij}$. Substituting into (6.12) and taking the product to get rid of τ and l, we obtain

$$\delta\gamma_{ij} \sim \sqrt{\tilde{\kappa}}\,, \tag{6.13}$$

which remains small at all scales, as long as $\tilde{\kappa}$ is small.

Note that the set of β-functions (6.11) contains a fixed point of the renormalization group flow in the region $\lambda > 1$ for the values

$$\lambda_\bullet = \frac{15}{14}, \qquad \tilde{\kappa}_\bullet = 0. \tag{6.14}$$

This shows that the theory enjoys asymptotic freedom at high energies, thus representing a perturbatively UV-complete quantum field theory. A second fixed point appears at $\lambda = 1/2$. However, in the vicinity of that point the expansion parameter is $\tilde{\kappa}(1-2\lambda)^{-\frac{1}{2}}$ and it remains arbitrary at one loop. Thus, it cannot be said whether this fixed point persists or not unless a two-loop computation is performed. We will therefore focus on the first fixed point.

After fixing the lapse to $N(t) = 1$ by using the projectability condition, the dynamical variables left in the theory are the shift N^i and the spatial metric γ_{ij}. Varying the action with respect to them, we get the following equations of motion

$$\mathcal{P}_i \equiv \nabla^j K_{ij} - \lambda \nabla_i K = 0, \tag{6.15a}$$

$$\begin{aligned}\mathcal{G}^{ij} \equiv & -D_t\left(K^{ij} - \lambda\gamma^{ij}K\right) - (1-2\lambda)KK^{ij} - 2K^{ik}K^j_k \\ & + \frac{1}{2}K^{kl}K_{kl}\gamma^{ij} + \frac{\lambda}{2}K^2\gamma^{ij} + \frac{\mu}{2}R^2\gamma^{ij} + 2\mu\Delta R\gamma^{ij} \\ & - 2\mu\nabla^i\nabla^j R - \Lambda\gamma^{ij} = 0\ ,\end{aligned} \tag{6.15b}$$

where we have used that $R^{ij} = R\gamma^{ij}/2$ in two dimensions. Here the covariant time derivative is defined as

$$D_t = \partial_t - \mathcal{L}_{\vec{N}}\ , \tag{6.16}$$

where $\mathcal{L}_{\vec{N}}$ is the Lie derivative along the shift vector, so that for a two-index tensor we have,

$$D_t A^{ij} = \partial_t A^{ij} - N^k\nabla_k A^{ij} + A^{ik}\nabla_k N^j + A^{jk}\nabla_k N^i\ . \tag{6.17}$$

On top of this and like in any gauge theory, local invariance under spatial time-dependent diffeomorphisms (6.4) imposes a "Bianchi" identity [327, 330, 335]

$$\nabla_j\mathcal{G}^{ji} + \gamma^{ij}D_t\mathcal{P}_j + K\mathcal{P}^i = 0\ . \tag{6.18}$$

We assume the cosmological constant to be small compared to the UV scale set by μ^{-1}, $\Lambda\mu \ll 1$. It is needed to regulate the long-distance behavior of the solutions. This is a peculiarity of (2+1) dimensions, where the gravitational field of a localized source does not vanish at infinity even in GR, persisting as a global angle deficit. We find that the problem gets aggravated in Hořava gravity, where in the limit $\Lambda \to 0$ the conical deficit grows indefinitely at large radii, despite the fact that all curvature invariants tend to zero. Introduction of non-vanishing Λ turns this into a well-behaved de Sitter asymptotics with a finite angle deficit.

6.3 Circularly symmetric spacetimes

In the following, we will write the equations of motion for a general non-rotating circularly symmetric and stationary ansatz. We use polar coordinates (r, θ) for the spatial slices and write the ADM metric in the preferred foliation as

$$ds^2 = (-1 + N_i N^i)dt^2 + 2N_i dx^i dt + \gamma_{ij} dx^i dx^j \,, \tag{6.19}$$

where we have already fixed $N(t) = 1$.

Stationarity of the solution imposes $\partial_t N^i = \partial_t \gamma_{ij} = 0$, while the requirement of circular symmetry enforces $N^\theta = 0$. Finally, any two-dimensional metric is conformally flat, implying that γ_{ij} can only depend on a single function $G(r)$. We thus adopt, without loss of generality, the ansatz

$$ds_2^2 = dr^2 + r^2 G(r)^2 d\theta^2 \tag{6.20}$$

for the two-dimensional spatial metric.

Putting all this together and defining $N^r = F(r)$, our ansatz for the full metric finally takes the form

$$ds^2 = (-1 + F(r)^2)dt^2 + 2F(r)dtdr + dr^2 + r^2 G(r)^2 d\theta^2. \tag{6.21}$$

This chart of coordinates is reminiscent of the well-known Gullstrand-Painlevé coordinates (see e.g. Ref. [336]) in standard solutions – e.g. the Schwarzschild metric and the Banados, Zanelli and Teitelboim (BTZ) BHs [334].

We now insert this ansatz into the equations of motion (6.15). From $\mathcal{P}_r$ and $\mathcal{G}_{\theta\theta}$ we obtain differential equations that are second order in derivatives for $F(r)$, and fourth order for $G(r)$. Since the precise form of the equations is cumbersome and not very illuminating, we relegate them to Appendix E.1. Schematically, their form is

$$E_1 \left[F, F', F'', G, G', G''\right] = 0, \tag{6.22a}$$

$$E_2 \left[F, F', F'', G, G', G'', G^{(3)}, G^{(4)}\right] = 0, \tag{6.22b}$$

where a prime denotes a derivative with respect to the argument of the function. From now on we will suppress the arguments for clarity whenever needed.

From $\mathcal{G}_{rr}$ we can in principle obtain another second order equation for $F(r)$. However, one can combine it with Eq. (6.22a) to eliminate $F''(r)$ and rewrite it as a constraint

$$E_3 \left[F, F', G, G', G'', G^{(3)}\right] = 0. \tag{6.23}$$

Furthermore, using the Bianchi identity (6.18), one can show that

$$E_3' + 2GrF'E_1 + \left(\frac{G'}{G} + \frac{1}{r}\right)(E_2 - 2E_3) = 0. \tag{6.24}$$

Therefore, we see that the system is *not* over-determined. The condition (6.24) implies that once the constraint equation (6.23) is imposed at a point, e.g. at a boundary r_0, then the constraint is propagated throughout r, provided that the equations of motion (6.22) are satisfied.

Close examination of Eqs. (6.22) and (6.23) reveals that they are invariant under constant rescalings of $G(r)$ (i.e., if (F, G) is a solution, also (F, kG), with k a constant rescaling factor, is a solution to the same theory). Thus, we can take advantage of this and further simplify the equations of motion by defining a new variable

$$\Gamma(r) = \frac{1}{r} + \frac{G'(r)}{G(r)}, \tag{6.25}$$

This reduces Eq. (6.22) to a third-order system in $\Gamma(r)$ of the form

$$\mathcal{E}_1 \equiv (\lambda - 1)\left(F'' + F'\Gamma + F\Gamma'\right) + F\Gamma' + F\Gamma^2 = 0, \tag{6.26a}$$

$$\begin{aligned}\mathcal{E}_2 \equiv \mu &\left(-8\Gamma''' - 16\Gamma\Gamma'' - 12\left(\Gamma'\right)^2 + 8\Gamma^2\Gamma' + 4\Gamma^4\right) \\ &+ (\lambda - 1)\left(2FF'' + \left(F'\right)^2 + 4FF'\Gamma + 2F^2\Gamma' + F^2\Gamma^2\right) \\ &+ 2FF'' + 2\left(F'\right)^2 - 2\Lambda = 0,\end{aligned} \tag{6.26b}$$

while the constraint (6.23) becomes a second-order equation in $\Gamma(r)$,

$$\begin{aligned}\mathcal{E}_3 \equiv \mu\left(8\Gamma\Gamma'' - 4\left(\Gamma'\right)^2 + 8\Gamma^2\Gamma' - 4\Gamma^4\right) + (\lambda - 1)&\left(-\left(F'\right)^2 - 2FF'\Gamma - F^2\Gamma^2\right) \\ &- 2FF'\Gamma + 2\Lambda = 0.\end{aligned} \tag{6.26c}$$

Henceforth, instead of dealing with the original equations $\mathcal{E}_1$ and $\mathcal{E}_2$, we can instead solve the system consisting of $\mathcal{E}_1$ and $\mathcal{E}_3$ (i.e. the system consisting of one of the evolution equation and the constraint equation), effectively dealing with a *second-order* system in both $F(r)$ and $\Gamma(r)$, and thus requiring only four integration constants. One can always do this because the Bianchi identity ensures that the remaining equation $\mathcal{E}_2$ will be satisfied by the solution.

In the case of vanishing cosmological constant Λ, we can identify two symmetries of the equations of motion (besides the aforementioned invariance under constant rescalings of G), corresponding to shifts and rescaling of the radial co-

ordinate. In more detail, the field equations are invariant under

$$F(r) \mapsto bF(b\,r + a), \tag{6.27a}$$

$$\Gamma(r) \mapsto b\Gamma(b\,r + a), \tag{6.27b}$$

with arbitrary constants a and b. This symmetry will play an important role in the numerical analysis of Sec. 6.5.

6.3.1 Black holes

We will define the concept of a BH from the perspective of an observer in the IR limit of the theory, in analogy to the general relativistic case. If we were dealing with GR, then a BH would be characterized by the presence of a trapped surface for null trajectories [337], i.e. for (massless) particles with dispersion relation $\omega = k$. The outermost of all trapped surfaces is usually referred to as the apparent horizon, which in stationary circularly symmetric configurations coincides with the Killing and event horizons. By analogy, we will assume that in the IR limit of Hořava gravity, massless particles move with dispersion relation $\omega = k + \mathcal{O}(k^2)$, and therefore we will borrow the same definition of a BH.

The Killing horizon can be identified by requiring the time-like Killing vector $\partial/\partial t$ to have vanishing norm at the position of the horizon. For our metric ansatz, this leads to the condition

$$\frac{\partial}{\partial t} \cdot \frac{\partial}{\partial t} = g_{tt} = -1 + F^2(r) = 0\,. \tag{6.28}$$

Since our ansatz for the metric is stationary, the Killing horizon coincides with the apparent horizon – which is defined in turn by the constant r surfaces becoming null $g^{\mu\nu}\partial_\mu r \partial_\nu r = 0$ [336] – and with the event horizon.

It is worth noting here an important difference with known BH solutions in *non-projectable* Hořava gravity [132, 327]. In that theory, solutions are characterized by the presence of a *universal horizon*, a compact surface that traps all signals, regardless of their dispersion relation. Its position can be identified by requiring the unit-vector orthogonal to the foliation,

$$U_\mu = -N\delta^t_\mu, \tag{6.29}$$

to become orthogonal to the Killing vector ∂_t (which is tangent to hypersurfaces of constant r), i.e.

$$U \cdot \frac{\partial}{\partial t} = -N = 0. \tag{6.30}$$

Because of the condition $N(t) = 1$, it is impossible for solutions in projectable Hořava gravity to present universal horizons. Thus, we can expect signals of arbitrary speed to be able to eventually probe the interior of the BH (as defined in the IR) and escape from it.

6.4 Black holes in the IR limit

We will now face the issue of obtaining circularly symmetric solutions to the equations of motion (6.26)–(6.26c). This is not an easy task in general. The non-linear character of the equations renders the problem hard to tackle analytically. However, there is a regime in which solutions can be found rather easily, namely the IR limit of the theory, which one can obtain by setting $\mu = 0$. Solutions obtained in this way will be valid whenever the spatial curvature of the slices is low. This corresponds to focusing on the region $r \gg \sqrt{\mu}$, where we expect this to happen and where higher derivative terms can be ignored.

We start by considering the combination $(\mathcal{E}_2 + \mathcal{E}_3)/2 - F\mathcal{E}_1$ of the equations, which yields

$$FF'' + (F')^2 - FF'\Gamma - F^2\Gamma' - F^2\Gamma^2 = 0. \tag{6.31}$$

Assuming that $F(r)$ is non-vanishing everywhere and introducing a new variable

$$Y = \Gamma - \frac{F'}{F}\,, \tag{6.32}$$

this equation can be cast into the simple form

$$-Y' + 2Y^2 - 3Y\Gamma = 0. \tag{6.33}$$

Note that the derivative of Γ has disappeared from the equation.

Let us first consider the solution $Y = 0$ to this equation, which implies $\Gamma = F'/F$. Substituting this relation in Eq. (6.26c) (with $\mu = 0$), we find that the function F is linear,

$$F = \pm r\sqrt{\frac{\Lambda}{2\lambda - 1}}. \tag{6.34}$$

Note that this solution exists for positive Λ only if $\lambda > 1/2$, and that it corresponds to a constant radial function

$$G(r) = G_\infty. \tag{6.35}$$

For $G_\infty = 1$, this reduces to the de Sitter metric, which is regular everywhere

and has a cosmological Killing horizon at

$$r_{\rm dS} = \sqrt{\frac{2\lambda - 1}{\Lambda}} \tag{6.36}$$

Other choices of G_∞ lead to an angle deficit and a conical singularity at the origin.

We now consider the case of non-vanishing solutions to Eq. (6.33), $Y \neq 0$. We assume $Y > 0$ without loss of generality.[5] From Eqs. (6.32) and (6.33), we can express Γ and F'/F in terms of Y and its derivative,

$$\Gamma = -\frac{Y'}{3Y} + \frac{2}{3}Y, \qquad\qquad \frac{F'}{F} = -\frac{Y'}{3Y} - \frac{Y}{3}. \tag{6.37}$$

The second of these equations can be integrated if we introduce a new function $X(r)$ such that

$$X' = Y\,, \tag{6.38}$$

yielding

$$F = \frac{C}{Y^{1/3}}\, e^{-X/3}\,, \tag{6.39}$$

where C is an integration constant. Substituting this and the first relation (6.37) into Eq. (6.26), we obtain a differential equation involving X and Y,

$$\begin{aligned} 0 = &- \frac{(4\lambda - 2)(Y')^2}{9Y^2} + \frac{(4\lambda - 2)Y'}{9} + \frac{(5 - \lambda)Y^2}{9} \\ &+ \frac{2\Lambda}{C^2}\, Y^{2/3}\, e^{2X/3}. \end{aligned} \tag{6.40}$$

Recalling that Y is the derivative of X, we observe that this is a second-order differential equation for the function $X(r)$. Importantly, this equation does not contain explicitly the variable r, and thus can be reduced to a first-order equation if we choose X to be our independent variable, instead of r. We therefore substitute

$$Y' = \frac{dY}{dX}\, X' = \frac{dY}{dX}\, Y \tag{6.41}$$

and obtain

$$0 = -\frac{2(2\lambda - 1)}{9}\left(\frac{dY}{dX}\right)^2 + \frac{2(2\lambda - 1)}{9} Y \frac{dY}{dX} + \frac{5 - \lambda}{9} Y^2$$

[5] Positive Y can always be achieved by changing the sign of r, as manifest from the definitions (6.32) and (6.25).

$$+\frac{2\Lambda}{C^2}Y^{2/3}e^{2X/3}. \tag{6.42}$$

This is further simplified by the definition $Y=\hat{Y}^{3/2}e^{X/2}$, which yields

$$-(2\lambda-1)\left(\frac{d\hat{Y}}{dX}\right)^2+\hat{Y}^2+\frac{4\Lambda}{C^2}=0. \tag{6.43}$$

Again, in the case of positive Λ (on which we focus in this Chapter) the solution exists only if $\lambda>1/2$. Solving for $\hat{Y}$ and substituting into the expression for Y we find

$$Y=\left(\pm\frac{2\sqrt{\Lambda}}{|C|}\sinh\frac{X-X_0}{\sqrt{2\lambda-1}}\right)^{3/2}e^{X/2}\,, \tag{6.44}$$

where X_0 is an integration constant, and the signs $\pm$ are chosen to have the expression in brackets positive. The constant X_0 can be absorbed in the shift of X and subsequent rescaling $C\mapsto Ce^{X_0/3}$, which leave both Y and F invariant. Therefore we set $X_0=0$ henceforward.

The solutions presents two branches corresponding to the plus/minus sign and positive/negative X. Let us focus on the case $X<0$ (we will comment on the branch with $X>0$ at the end of the section). Using Eqs. (6.38), (6.39) and the first of Eqs. (6.37), we obtain the solution in parametric form

$$\sqrt{\Lambda}\,r=\frac{B}{2}\int_{-\infty}^{X}\frac{e^{-X'/2}}{\left(\sinh\frac{-X'}{\sqrt{2\lambda-1}}\right)^{3/2}}dX', \tag{6.45a}$$

$$F=\pm B\frac{e^{-X/2}}{\left(\sinh\frac{-X}{\sqrt{2\lambda-1}}\right)^{1/2}}, \tag{6.45b}$$

$$rG=G_\infty B\sqrt{\frac{2\lambda-1}{\Lambda}}\frac{e^{X/2}}{\left(\sinh\frac{-X}{\sqrt{2\lambda-1}}\right)^{1/2}}, \tag{6.45c}$$

where we have introduced a new integration constant G_∞ and defined

$$B=\left(\frac{|C|^3}{2\sqrt{\Lambda}}\right)^{1/2}. \tag{6.46}$$

The $\pm$ in Eq. (6.45b) corresponds to the sign of the original integration constant C, which can be both positive or negative, whereas B is strictly positive. Note also that B is dimensionless and that the integral in Eq. (6.45a) converges at the lower end, as long as $\lambda<5$, and diverges as $X\to0^-$, so that r varies from 0 to $+\infty$. This is a relevant range for λ, as it includes the fixed point (6.14), and we will focus on it in the following.

Let us study the asymptotics of the solution (6.45). Consider first $X \to 0^-$, corresponding to $r \to +\infty$, which yields

$$\sqrt{\Lambda}\, r \approx (2\lambda-1)^{3/4}\frac{B}{\sqrt{-X}}, \tag{6.47a}$$

$$F \approx \pm(2\lambda-1)^{1/4}\frac{B}{\sqrt{-X}} \approx \pm\sqrt{\frac{\Lambda}{2\lambda-1}}\, r, \tag{6.47b}$$

$$rG \approx G_\infty \frac{(2\lambda-1)^{3/4}}{\sqrt{\Lambda}}\frac{B}{\sqrt{-X}} \approx G_\infty r. \tag{6.47c}$$

In these expressions we recognize the de Sitter metric [Eqs. (6.34) and (6.35)] with the deficit angle set by G_∞. The integration constant B has dropped out. Therefore, at sufficiently large radii, the solution given by Eq. (6.45) approaches the de Sitter geometry.

Second, we consider the other extreme $X \to -\infty$, corresponding to $r \ll B/\sqrt{\Lambda}$. In this limit, we obtain

$$\sqrt{\Lambda}\, r \approx \frac{2\sqrt{2\lambda-1}}{3-\sqrt{2\lambda-1}}\sqrt{2}B\exp\left[\left(\frac{3}{2\sqrt{2\lambda-1}}-\frac{1}{2}\right)X\right], \tag{6.48a}$$

$$F \approx \pm\sqrt{2}B\exp\left[\left(\frac{1}{2\sqrt{2\lambda-1}}-\frac{1}{2}\right)X\right] = \pm F_0(\sqrt{\Lambda}\, r)^{-\sigma}, \tag{6.48b}$$

$$\begin{aligned} G &\approx \frac{G_\infty B}{r}\sqrt{\frac{2(2\lambda-1)}{\Lambda}}\exp\left[\left(\frac{1}{2\sqrt{2\lambda-1}}+\frac{1}{2}\right)X\right] \\ &= G_0(\sqrt{\Lambda}\, r)^{2\sigma}, \end{aligned} \tag{6.48c}$$

where

$$\sigma = \frac{\lambda-2+\sqrt{2\lambda-1}}{5-\lambda} > 0\,, \tag{6.49}$$

$$F_0 = (\sqrt{2}B)^{1+\sigma}\left(\frac{3-\sqrt{2\lambda-1}}{2\sqrt{2\lambda-1}}\right)^{-\sigma}, \tag{6.50}$$

$$G_0 = G_\infty\sqrt{2\lambda-1}\,(\sqrt{2}B)^{-2\sigma}\left(\frac{3-\sqrt{2\lambda-1}}{2\sqrt{2\lambda-1}}\right)^{1+2\sigma}. \tag{6.51}$$

Remarkably, these solutions present a second Killing horizon besides the cosmological one, located at

$$r_H = \frac{F_0^{\frac{1}{\sigma}}}{\sqrt{\Lambda}}. \tag{6.52}$$

From the point of view of the low-energy theory, this solution then describes a black (white) hole for positive (negative) $F(r)$. The second horizon is well within the de Sitter radius (6.36) as long as $F_0 \ll 1$, which holds if $B \ll 1$. Note that

$B \ll 1$ also implies $G_0 \gg G_\infty$.

Were these solutions to be trusted in the whole spacetime, extrapolating them inwards would lead to curvature singularities at the origin, as can be seen in the different curvature scalars

$$K = -\left(\frac{F_0}{\Lambda^{\sigma/2}}\right)\frac{(1+\sigma)}{r^{1+\sigma}}, \tag{6.53}$$

$$R = -\frac{4\sigma(1+2\sigma)}{r^2}, \tag{6.54}$$

$$K_{ij}K^{ij} = \left(\frac{F_0^2}{\Lambda^{\sigma}}\right)\frac{(5\sigma^2+4\sigma+1)}{r^{2+2\sigma}}, \tag{6.55}$$

as well as in the full three-dimensional spacetime curvature

$$R^{(3)} = 2\sigma(1+2\sigma)\left[\left(\frac{F_0^2}{\Lambda^{\sigma}}\right)\frac{1}{r^{2+2\sigma}} - \frac{2}{r^2}\right], \tag{6.56}$$

where we have made use of the Gauss–Codazzi relations.

In light of all this, we refer to these solutions as "IR BHs". We can think of them as akin to the Schwarzschild–de Sitter BHs of GR. They are solutions to the low energy limit of a gravitational theory, and behind a horizon they include a region (near the center) where the description provided by the low-energy Lagrangian breaks down, and where one therefore needs to account for the dynamics of the full theory. In particular, in the case at hand we expect the effects of the μR^2 term to become important at a distance $r \sim \sqrt{\mu}$ from the center. This ensures that for any IR solution there is always a value of $\sqrt{\mu} \ll r_H$ for which the UV corrections are only important deep inside the geometry. Therefore, they do not modify the horizon, and the solution still appears as a BH to exterior observers.

Let us discuss the limit of vanishing cosmological constant $\Lambda \to 0$. If one keeps the combinations $B\Lambda^{-\frac{\sigma}{2(1+\sigma)}}$, $G_\infty\Lambda^{-\frac{\sigma^2}{(1+\sigma)}}$ fixed in this limit, the BH horizon radius r_H remains finite, whereas the de Sitter asymptotics are pushed to infinity. The solution (6.48b)-(6.48c) is then valid for arbitrary large radii. Note that the curvature invariants K, $K_{ij}K^{ij}$, R and $R^{(3)}$ of this solution vanish as $r \to \infty$, just like the projections of the Riemann tensor on the (normalized) timelike and spacelike Killing vectors (parallel respectively to ∂_t and ∂_θ). This implies that the asymptotic geometry is locally flat, but not globally such, because it presents an asymptotically increasing negative deficit angle due to the growth of the function G. This unappealing behavior is due to the peculiarity of the 2-dimensional spatial geometry, where a change of the circumference of a circle does not affect the local characteristics of space. We have seen how this long-distance behavior is regulated by the presence of a positive cosmological constant.

Finally, we comment on the $X > 0$ branch of solutions. A similar analysis shows that it also presents de Sitter asymptotics for $X \to 0^+$. However, the solutions in this branch do not have any additional Killing horizons, besides the cosmological one. Moreover, the metric function rG diverges at $r \to 0$, a behavior that appears rather pathological. For these reasons, we are not going to consider these solutions further in this Chapter.

6.5 Black holes in the UV-complete theory

We now analyze how the inclusion of the higher derivative terms affects the BH solutions found in the previous section. The higher derivative terms are important at distances $r \sim \sqrt{\mu} \ll 1/\sqrt{\Lambda}$. Therefore, in this section we neglect the cosmological constant and use Eqs. (6.48b), (6.48c) as the large-distance form of the solution. In other words, we will look for solutions of Eqs. (6.26a), (6.26c) with $\Lambda = 0$, which have asymptotics

$$F(r) = F_\infty r^{-\sigma}, \tag{6.57a}$$

$$\Gamma(r) = \frac{1+2\sigma}{r}, \tag{6.57b}$$

at $r \to \infty$, where F_∞ is a constant. To simplify notations, we will from now on measure distances in units of $\sqrt{\mu}$, which corresponds to formally setting $\mu = 1$ in the equations.

Based on generic arguments, one may expect a renormalizable UV-complete theory including higher order spatial derivatives to allow for "resolving" the central curvature singularity of BHs, which is also present in the aforementioned IR solutions (see e.g. Ref. [133] for a mention of this possibility). In the following, we will therefore try to seek BH solutions to the UV-complete theory that implement this feature.

In principle, the singularity could be resolved in (at least) three possible ways: *(a)* the full solution may have a regular center at $r = 0$; *(b)* the full solution may extend all the way down to $r = -\infty$, where it may open up into another asymptotic region, thus describing a wormhole configuration; *(c)* the full solution extends all the way down to $r = -\infty$, with the metric function rG and all curvature invariants remaining bounded: this would describe the resolution of the singularity into an infinite throat.

To see if any of these options gets realized, we start by counting the number of free parameters in the solution of the system (6.26a), (6.26c) once the large-distance asymptotics (6.57) are fixed. We linearize the functions F, Γ around

their asymptotics by writing

$$F(r) = F_\infty r^{-\sigma}\big(1 + f(r)\big), \tag{6.58a}$$

$$\Gamma(r) = \frac{1+2\sigma}{r}\big(1 + g(r)\big)\,, \tag{6.58b}$$

where we assume f and g to be small at large r. Substituting this into Eqs. (6.26a), (6.26c) and expanding to linear order in f and g we find a system of two second-order linear equations, whose general solution reads (see Appendix E.2 for details),

$$f = f_\infty r^{-2(1-\sigma)} + C_1\frac{\sigma}{r} + C_2 + C_3 f_3(r) + C_4 f_4(r), \tag{6.59a}$$

$$g = g_\infty r^{-2(1-\sigma)} + C_1\frac{1}{r} + C_3 g_3(r) + C_4 g_4(r)\,. \tag{6.59b}$$

Here the coefficients f_∞, g_∞ are fixed in terms of λ and F_∞ and correspond to a particular solution of the linear system. Notice that consistency of the asymptotic expansion requires that these solutions decrease at $r \to \infty$, which implies $\sigma < 1$. This requirement is satisfied if $\lambda < 5/2$, which includes the interesting fixed point (6.14).

The coefficients C_I in Eqs. (6.59) are arbitrary. The parameters C_1, C_2 correspond to the symmetry (6.27) of the equations, spontaneously broken by the asymptotic form (6.58). One easily recognizes in the linearly independent solutions they multiply the results of an infinitesimal shift and rescaling of the asymptotics (6.58). The two remaining linearly independent solutions (f_3, g_3) and (f_4, g_4) are oscillating and can be found analytically in the limit $(\lambda - 1) \ll 1$ using a version of the WKB expansion [141] (see Appendix E.2). Importantly, the amplitude of g_3 and g_4 grows at large r, destroying the desired asymptotic behavior. To satisfy the boundary conditions at infinity, we have to set $C_3 = C_4 = 0$. Thus, we conclude that imposing the large-distance asymptotics (6.58) leaves only 2 free parameters C_1, C_2, both corresponding to the exact symmetries of the equations.

As the next step, we include non-linear corrections to the asymptotic expansion. Motivated by the results of our linearized analysis, we use an ansatz for F and Γ in the form of a double series in inverse powers of r,

$$F(r) = F_\infty r^{-\sigma}\left[1 + \sum_{n,m}\frac{f_{(n,m)}}{r^{n+m\sigma}}\right], \tag{6.60a}$$

$$\Gamma(r) = \frac{1+2\sigma}{r}\left[1 + \sum_{n,m}^{\infty}\frac{g_{(n,m)}}{r^{n+m\sigma}}\right], \tag{6.60b}$$

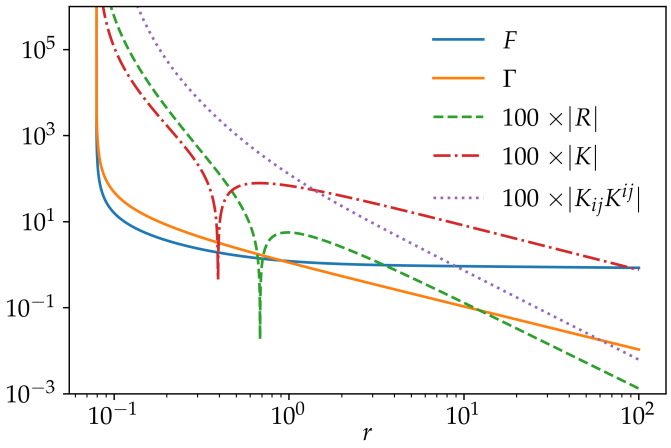

Figure 6.1: *Radial profile of the metric functions and curvature invariants.* Metric functions integrated inwards and the corresponding curvature invariants for $F_\infty = 1$, $f_{(1,0)} = 0$ and $\lambda = \frac{15}{14}$. The qualitative behavior of the solution is the same for other values of λ.

with n, and m integers such that $n + m\sigma > 0$. Plugging this ansatz into the equations of motion, the latter can be solved perturbatively in powers of r^{-1}, in terms of only two integration constants F_∞ and $f_{(1,0)}$.

We now fix $F_\infty = 1$, $f_{(1,0)} = 0$ and numerically integrate Eqs. (6.26a), (6.26c) from large r towards the center. The result is shown in Fig. 6.1. We see that F and Γ monotonically grow as r decreases and diverge at a finite value of r. (Note however that the areal radius $|rG|$ goes to zero as F and Γ diverge, i.e. the area of the singularity vanishes.) The curvature invariants also diverge at that point, indicating that the BH singularity persists even after the inclusion of the higher derivative terms. Notice that varying F_∞ and $f_{(1,0)}$ will not change this result, aside from rescalings/shifts of the solutions. As discussed above, these parameters correspond to exact symmetries that cannot turn a singular behavior into a regular one.

However, it is still premature at this point to claim the absence of a regular solution with certainty because of the following caveat in the above argument. It is logically possible that the divergence observed in the numerical solution is due to a spurious admixture (produced by numerical errors) of modes that are regular throughout the spacetime and modes that are instead singular. Thus, we need to further scrutinize our numerical procedure to ensure its stability.

Let us focus on the possibility that the BH might have a regular center (option *(a)* above). We thus impose regularity by assuming that $F(r)$ and $G(r)$ are analytic near $r = 0$, with respectively only odd and even powers of r [205][6].

[6]This is needed to ensure that the metric (6.21) is C^∞ at the center when expressed in Cartesian coordinates, but is also automatically implied by the field equations themselves.

Absence of an angle deficit at $r = 0$ would also require $G = 1$ there, but that condition can be imposed without loss of generality because the field equations are homogeneous in G, [i.e., as already mentioned, if (F, G) is a solution, also (F, kG), with k a constant rescaling factor, is a solution to the same theory]. This ansatz implies, for F and Γ, the functional form

$$F(r) = \sum_{n=0}^{\infty} F_{2n+1} r^{2n+1}, \tag{6.61a}$$

$$\Gamma(r) = \frac{1}{r} + \sum_{n=0}^{\infty} \Gamma_{2n+1} r^{2n+1}. \tag{6.61b}$$

Replacing this ansatz in the field equations (6.26) and (6.26c) we find that the coefficients F_{2n+1} and Γ_{2n+1} are all given in terms of two integration constants, F_1 and Γ_1. We have checked that the resulting perturbative solution leads to regular curvature invariants $K_{ij}K^{ij}$, K, R and $R^{(3)}$ at the origin. Note that because we have fixed the center to be at $r = 0$, in the numerical investigation below we will not be allowed to use the shift symmetry [parameter a in Eqs. (6.27a)–(6.27b)], whereas we will exploit the rescaling symmetry [parametrized by b in Eqs. (6.27a)–(6.27b)].

The strategy is to use the perturbative solution (6.61), valid near the center, to provide initial data for F and Γ at some small radius $r \ll 1$, and integrate numerically outwards (once the integration constants F_1, Γ_1 have been chosen). Similarly, one can use the IR solution (6.60) (fixing the integration constants F_∞, $f_{(1,0)}$) to provide initial data at a finite radius $r \gg 1$ for a numerical integration inwards. One then matches the two solutions smoothly at some fixed radius $r_m \sim 1$, where both solutions are regular, by imposing

$$\Delta F|_{r_m} = \Delta F'|_{r_m} = \Delta\Gamma|_{r_m} = \Delta\Gamma'|_{r_m} = 0, \tag{6.62}$$

where

$$\Delta X|_{r_m} = X_{\rm out}(r_m) - X_{\rm in}(r_m) \tag{6.63}$$

refers to the difference between the values of the function $X(r)$ when approaching the matching point r_m from the two directions. Equivalently, one can think of this problem as that of finding the root(s) of the system

$$\mathbf{F}(\mathbf{p}) = 0, \tag{6.64}$$

where $\mathbf{p} = \left(F_1, \Gamma_1, F_\infty, f_{(1,0)}\right)$ and the components of $\mathbf{F}$ are the jumps shown in (6.62).

As mentioned earlier, the symmetry under rescaling of coordinates can still be used to eliminate one of the four integration constants [F_∞, $f_{(1,0)}$ for the outer solution and F_1, Γ_1 for the inner one]. We choose for instance to set $F_1 = 1$. The system we have to solve is then overdetermined: we have four junction conditions (6.62) for three parameters. Thus, one does not expect existence of a regular solution on general grounds. To verify this, we consider three of the junction conditions given by Eq. (6.62), and we solve them (with a Newton-Raphson method) in our three variables Γ_1, F_∞ and $f_{(1,0)}$. We then check whether the fourth junction condition is satisfied (to within numerical errors) and it is not. We have checked that this result is stable against the choice of the initial guess of the Newton-Raphson algorithm.

Based on this overwhelming evidence, we can therefore conclude that there exist no regular solutions approaching at large radii the IR BHs that we identified previously, even if we allow for a conical defect at the center. This result excludes option *(a)* outlined in the beginning of the section.

Let us now consider option *(b)*. In that case, the metric function $rG(r)$ must diverge at both $r = \pm\infty$, remaining finite and non-vanishing in between. This implies that its logarithmic derivative $\Gamma(r)$ must change sign at finite $r = r_*$. However, this is impossible due to Eq. (6.26c). If $\Gamma(r_*) = 0$, the left-hand side of this equation becomes a sum of strictly negative terms, implying that also $F'(r_*)$ and $\Gamma'(r_*)$ must vanish. The latter means that $\Gamma(r)$ does not actually cross zero, and we arrive at a contradiction[7].

Option *(c)* still remains a logical possibility. We have not attempted to rule out robustly for generic values of λ, as we did with option *(a)*. However, given our experience in the structure of solutions to Eqs. (6.26a), (6.26c), we believe it is unlikely. This is corroborated by the analysis in the limit $(\lambda - 1) \ll 1$ presented in the next section.

6.6 A perturbative expansion in $(\lambda - 1)$

Let us now give an additional analytic argument showing that no regular UV extension to our IR BH solutions exists. The interesting UV fixed point of the renormalization group flow (6.14) is close to $\lambda = 1$ and, at least along some of the flow lines, λ further approaches 1 when the theory flows towards IR [323]. This motivates to study the behavior of the solutions by performing a perturbative expansion in $\epsilon \equiv \lambda - 1$.

[7] One can be more careful and Taylor expand $\Gamma(r)$ in the vicinity of r_* to see its behavior in more detail. One then obtains $\Gamma(r) \propto (r - r_*)^2$, which confirms that $\Gamma(r)$ does not change sign.

According to standard techniques dealing with differential equations with small parameters in front of the highest derivatives, we introduce a rescaled coordinate $\tilde{r} = r/\epsilon^{1/2}$. Recalling that $\sigma \approx (\lambda - 1)/2$ in the desired limit, the asymptotics (6.57b) and (6.60b) for $\Gamma(r)$ suggest the following ansatz,

$$\Gamma(\tilde{r}) = \frac{1 + \epsilon\tilde{g}(\tilde{r})}{\epsilon^{1/2}\,\tilde{r}}, \tag{6.65}$$

where the function $\tilde{g}$ is of order one and will interpolate between small and large $\tilde{r}$. We will see shortly that this ansatz provides the most general solution to the field equations (6.26a), (6.26c) in the relevant limit $\epsilon \ll 1$. Notice that the divergence of $\Gamma(\tilde{r})$ at $\tilde{r} = 0$ excludes the wormhole *(b)* and throat *(c)* scenarios.

Substituting the ansatz into $\mathcal{E}_1$ and $\mathcal{E}_3$ and retaining only the leading terms in ϵ, we obtain

$$F'' + \frac{F'}{\tilde{r}} - \frac{F}{\tilde{r}^2}(1 - \tilde{r}\tilde{g}' - \tilde{g}) = 0, \tag{6.66a}$$

$$\frac{8\tilde{g}''}{\tilde{r}} - \frac{16\tilde{g}}{\tilde{r}^3} - 2FF' = 0, \tag{6.66b}$$

where now the derivatives are taken with respect to $\tilde{r}$. Note that, despite a lot of simplifications, this is still a system of two second-order differential equations, like the original system (6.26a), (6.26c). Its general solution contains four arbitrary integration constants, implying that we have not lost any solutions in making the ansatz (6.65).

Equation (6.66b) can be integrated once, yielding

$$8\left(\frac{\tilde{g}'}{\tilde{r}} + \frac{\tilde{g}}{\tilde{r}^2}\right) - F^2 = A, \tag{6.67}$$

where the integration constant A must be fixed by suitable boundary conditions. Since $\sigma \sim \epsilon/2$ as $\epsilon \to 0$, the asymptotics (6.57) correspond to the boundary conditions

$$F \to F_\infty\ , \quad \tilde{g} \to 1 \quad \text{at} \ \ \tilde{r} \to +\infty, \tag{6.68}$$

from which one obtains $A = -F_\infty$. We can use the scaling transformation [corresponding to the parameter b in Eqs. (6.27)] to set $F_\infty = 1$ and hence $A = -1$. Moreover, from Eq. (6.67) we also obtain a sub-leading term in F,

$$F(\tilde{r}) = 1 + \frac{4}{\tilde{r}^2} + \mathcal{O}\left(\frac{1}{\tilde{r}^3}\right). \tag{6.69}$$

The combination of $\tilde{g}$ and its derivative in Eq. (6.67) is the same as in

Eq. (6.66a). By combining the two equations one then obtains a closed second-order equation for $F(\tilde{r})$

$$F'' + \frac{F'}{\tilde{r}} + \left(\frac{F^2-1}{8} - \frac{1}{\tilde{r}^2}\right)F = 0. \tag{6.70}$$

This is still a non-linear differential equation, which, to the best of our knowledge, cannot be solved analytically. Nevertheless, its numerical analysis is straightforward. Starting from large $\tilde{r}$ with the boundary conditions (6.69) and integrating inwards, we find that F diverges, producing a curvature singularity at the center.

Alternatively, we can assume existence of a regular center. From the expansion (6.61) near $\tilde{r} = 0$, it follows that the corresponding boundary conditions are

$$F \approx \tilde{F}_1 \tilde{r}, \quad \tilde{g} \approx \Gamma_1 \tilde{r}^2 \,, \tag{6.71}$$

where $\tilde{F}_1 = \epsilon^{1/2} F_1$ and $\Gamma_1 = -1/24$ is fixed from Eq. (6.67) by using the boundary condition at spatial infinity ($A = -1$). We have numerically integrated Eq. (6.70) from $\tilde{r} = 0$ with initial conditions $F(0) = 0$, $F'(0) = \tilde{F}_1$ and scanned over different values of the single free parameter $\tilde{F}_1$. We have observed that the solution always oscillates at large $\tilde{r}$ around 1 or -1 with a non-vanishing amplitude, and cannot be matched to the asymptotics (6.68). This once again rules out the possibility of a regular center inside the IR BH.

6.7 Discussion

Many puzzles of quantum gravity are related to BHs. To set up the stage for addressing these puzzles in a UV-complete theory, we looked for circularly symmetric stationary non-rotating vacuum solutions in $(2+1)$-dimensional Hořava gravity. We found that in the presence of a positive cosmological constant the theory possesses, unlike $(2+1)$-dimensional GR, a family of solutions with two Killing horizons: the outer cosmological horizon, and the inner horizon that corresponds to a BH from the low-energy perspective. At large distances the solutions asymptotically approach de Sitter spacetime with a possible finite angle deficit. In the limit of vanishing cosmological constant the asymptotic spacetime is locally flat, but features a global growing (negative) deficit angle.

Motivated by the conjecture that the good quantum properties of Hořava gravity may lead to resolution of BH singularities (see e.g. Ref. [133, 338]), we scrutinized the regularity of our BH solutions. We found that they are singular at the center, similar to BHs in GR, implying that no resolution of singularities occurs in the pure vacuum theory. Stated differently, we have ruled out the

existence of regular classical solutions in pure $(2+1)$-dimensional Hořava gravity ("gravitational solitons") with BH-type Killing horizons.

Our results can have several interpretations. It can be that the BH solutions we found are merely physically irrelevant. A more interesting possibility is that they may form as the geometry describing the exterior of collapsing matter configurations. In that case, the fate of the central singularity will depend on the dynamics of matter. For example, the latter can form a compact remnant inside the Killing horizon, smoothing out the metric at the center. Alternatively, regular solutions may be dynamical (see e.g. Ref. [339, 340]). For instance, matter can bounce back from the center, in which case the BH solution will correspond to transient configurations.[8]

In this context it is instructive to discuss the gravitational energy of the BH solutions. Recall first that we did not impose the global Hamiltonian constraint following from the variation of the action with respect to the lapse $N(t)$,

$$\frac{\delta S}{\delta N} = 0 \quad \Rightarrow \quad \int d^2x\sqrt{\gamma}\big(K_{ij}K^{ij} - \lambda K^2 + \mu R^2 + 2\Lambda\big) = 0.$$

We find this constraint meaningless for spacetimes with non-compact spatial slices, like in our case: a positive energy in one region of space can be compensated by a negative contribution from another region infinitely far away. An alternative viewpoint is that we have studied the version of the theory where the lapse is set to $N = 1$ from the start and there is no gauge freedom of time-reparametrization. Therefore, the theory possesses a well-defined notion of local and global energy, given by the Hamiltonian.

Applying the Legendre transform to the Lagrangian (6.9), we find the Hamiltonian of pure Hořava gravity,

$$\begin{aligned}\mathcal{H} =& \frac{1}{\kappa}\int d^2x\sqrt{\gamma}\ \left(K_{ij}K^{ij} - \lambda K^2 + \mu R^2 + 2\Lambda\right) \\ & - \frac{2}{\kappa}\int d^2x\sqrt{\gamma}\,\mathcal{P}_i N^i + \frac{1}{\kappa}\oint d\Sigma^i q_i,\end{aligned} \tag{6.72}$$

where

$$q_i = 2N_i\left(K^{ij} - \lambda K\gamma^{ij}\right), \tag{6.73}$$

and $d\Sigma^i$ denotes the line element vector on the boundary at spatial infinity. Notice that we do not include any York–Gibbons–Hawking term [341, 342] neither in the action, nor in the Hamiltonian. This is justified, since the field equations

[8] Such bounce is in principle classically allowed in Hořava gravity, because the Killing horizon is not the true event horizon for high-energy modes that propagate with arbitrarily high velocities.

are fourth-order in spatial derivatives of the metric γ_{ij} and thus the variational principle requires fixing both $\delta\gamma_{ij}$ and its derivatives on the spatial boundary to zero. The variation of the action (6.9) is then well-defined without any boundary term. The Hamiltonian (6.72) does not include the contribution of matter, which, as we argued, must be considered in the full physical setup. However, we can use it to compute the energy arising from the gravitational field outside matter configurations.

To simplify further discussion, let us set $\Lambda = 0$. Then, for stationary solutions, like our BH metric, the gravitational energy can be cast into a boundary integral using the following relation,

$$\sqrt{\gamma}\big(K_{ij}K^{ij} - \lambda K^2 + \mu R^2\big) = \sqrt{\gamma}\,\gamma_{ij}\mathcal{G}^{ij} + (1-2\lambda)\partial_t(\sqrt{\gamma}\,K) + \sqrt{\gamma}\,\nabla_i l^i, \quad (6.74)$$

where

$$l^i = (2\lambda - 1)N^i K - 2\mu\nabla^i R\,. \quad (6.75)$$

Thus, using Gauss law we can write

$$\mathcal{H}_{\rm tot} = \mathcal{H}_{\rm out} + \mathcal{H}_{\rm center} + \mathcal{O}\left(\mathcal{P}_i, \mathcal{G}^{ij}\right), \quad (6.76)$$

where

$$\mathcal{H}_{\rm out} = \frac{1}{\kappa}\oint d\Sigma^i (l_i + q_i)\,, \quad (6.77)$$

the term $\mathcal{H}_{\rm center}$ includes possible matter contribution in the central region, as well as the integral of l_i over the line encompassing this region, and $\mathcal{O}\left(\mathcal{P}_i, \mathcal{G}^{ij}\right)$ denotes terms that vanish on shell (in vacuum and away from singularities). The long-distance contribution $\mathcal{H}_{\rm out}$ is evaluated using the asymptotics $F = F_\infty r^{-\sigma}$, $G = \hat{G}_\infty r^{2\sigma}$ at $r \to \infty$ with the result

$$\mathcal{H}_{\rm out} = \frac{2\pi}{\kappa} F_\infty^2 \hat{G}_\infty\,(1+3\sigma)\,. \quad (6.78)$$

We observe that this contribution is finite and positive.

The finiteness of the BH gravitational energy is consistent with the proposal that this metric can form outside matter configurations during gravitational collapse. To investigate this possibility in more detail, one would need to follow the dynamics of time-dependent spherical collapse in this theory. Unlike in the infrared limit of Hořava gravity, where gravitational collapse has been studied in several works [135, 343–346], numerical simulations in the UV theory are complicated by the presence of higher (spatial) derivatives, which would require to carefully examine the character of the resulting (non-linear) system of partial dif-

ferential equations, the well-posedness of the Cauchy problem, etc. Clearly, more work is needed in this direction.

Part V

Conclusion

Summary

The increasing availability of data from experiments probing strong gravity (GW interferometers, VLBI and binary pulsar observations) has motivated a renewed interest in computing predictions in the strong field for *both* GR and alternative theories.

Throughout this Thesis we have considered theories inspired by the puzzles of Dark Energy (for which k-essence arose as a viable dynamical explanation) and by the search for a theory of quantum gravity (for which Hořava gravity arose as a promising recent candidate). For these theories, we have explored a diverse range of phenomena, including: the nonlinear consequences of the presence of new dynamical scalar degrees of freedom, how the self-interactions of such scalars can shield matter configurations from fifth forces, and how higher-derivatives may restore regularity to the BH interior. We have also addressed theory-independent ways to interpret data from BH images, an approach that may be practically convenient given the large variety of available theories beyond GR. We recap the results presented in each Part below.

Part II. In Chapter 2, we have seen that the nonlinear self-interactions in k-essence that produce kinetic screening (required to have the theory explain Dark Energy and at the same time satisfy local gravitational constraints), may also become an obstacle to the well-posedness of the initial-value problem and stable dynamical evolutions –the latter is necessary, for example, to obtain predictions for the gravitational waveform from binary mergers. Indeed, these nonlinear interactions may lead to a change of character of the scalar equation of motion from hyperbolic to parabolic/elliptic, which we characterized as either Tricomi-type or Keldysh-type breakdowns. We have illustrated two ways to restore well-posedness to the Cauchy problem for quadratic k-essence. The first was to resort to a UV completion of the theory at higher-energy (shorter scales), when it is known, that admits a well-posed initial-value-problem. The second was through the "fixing-the-equations" approach, which modifies the equations of motion in a way designed to damp high-frequency modes suspect of causing the Cauchy breakdown. We have shown an example where it can explicitly be observed how

both of these approaches allow to evolve past the point where there used to be a Tricomi-type breakdown. Moreover, the direct comparison in our study between the UV solution and "fixed" solution provided a "sanity check" of the "fixing-the-equations" approach –indeed we observed the same qualitative behavior for both. The latter point is relevant as the "fixing-the-equations" approach can be readily applied to cases where no UV completions are available, such as the screening branch of quadratic k-essence, as well as other alternative theories of gravity.

The above results are part of a larger effort in the community, to extend numerical relativity evolutions to theories beyond GR –see Ref. [347] for a review of the state-of-the art in the field. One of the ultimate goals in this area is to compute the accurate waveforms necessary to compare alternative theories of gravity with experimental GW data on the same footing as GR –i.e. beyond null tests. Moreover, in Chapter 3, we have shown that a spin-off of these investigations (as well as of Refs. [113, 179, 180, 185, 186, 202]) is that the techniques that have been found to be useful for k-essence may be extended to other theories, such as massive vectors with nonlinear potentials –where the longitudinal mode behaves essentially like k-essence.

With respect to static matter configurations, in Chapter 4, we have studied the resilience of kinetic screening against general matter couplings –most previous work in the literature focused on linear matter couplings. However, we have seen that the most general k-essence model, not ruled out by current constraints on GW propagation, allows for couplings to matter dependent on the kinetic term of the scalar. Our results show that kinetic screening is dominant when quadratic terms are included in the matter coupling, as in Damour-Esposito-Farèse theory. On the other hand, effects form kinetic-dependent terms in the matter coupling are confined to the interior of the star, and maintain kinetic screening in the exterior. Kinetic-dependent effects may however be tested with other stellar physics probes (e.g. mass-radius relations or burning processes). With regards to future dynamical evolutions of stars with kinetic-dependent matter couplings, one needs to take into account new terms mixing the principal parts of the scalar and matter equations. Nevertheless, we expect the techniques of Chapter 2 to be of use.

Part III. The framework presented in Chapter III goes in the direction of generalizing and improving previous attempts to constrain gravity using the size of the bright ring in BH images obtained with VLBI. In particular, we have attempted to address recent concerns on the role of uncertainty in the astrophysics modelling for tests of GR with BH images.

We have done so by tackling the general inverse problem of BH imaging in a

simplified setting (spherical symmetry, small deformations confined to one metric function and simplified accretion). Using mock observation data, we have set out to reconstruct (both independently and simultaneously) the metric and the emissivity profile of the accretion matter, which we parameterized in a theory-independent way using a basis of Gaussian functions and power laws. Part of the degeneracy between the large number of parameters in the model was dealt with the application of a Principal Component Analysis (PCA), which selects the most relevant combinations of the basis functions that can be extracted from the input data. This allowed us to recover the metric and emissivity for the case when only one of them was allowed to vary.

Further, we have highlighted that theoretical priors may be critical to overcome the degeneracy between geometry and accretion physics. And we have demonstrated that with such priors, both the metric and the astrophysics can be recovered simultaneously in our simplified model. However, more work needs to be carried out before our framework can be applied to realistic data. In this direction, future studies may improve the modelling of accretion (possibly informed with GR magneto-hydrodynamics simulation data), include spin, and apply a non-linear generalization of the PCA (to extend beyond small deformations of the GR solutions).

Also in the direction of improving tests of gravity with BH images we note recent work by Ref. [348], where (in addition to the shadow size) the peak image intensity contrast was included in order to address the issue of degeneracy. Further work studying the relation between geometry and astrophysics in BH images was carried out in Refs. [12, 349–351].

Part IV. In Chapter 6, we have addressed a yet unresolved issue relating QG and BHs. Namely, whether (and how) QG resolves the singularity in the interior of BHs. In light of recent results showing that (2+1) projectable Hořava gravity is both renormalizable and UV-complete, we have attempted to find regular solutions in the full nonlinear theory in a simplified setting (circular-symmetry, restriction to stationary solutions and treating the theory in the classical field theory sense). Despite initial expectations that higher spatial derivatives (which give rise to modified dispersion relations) in Hořava gravity might lead to regular interiors, we have found that all circularly symmetric solutions (reducing to IR BHs) are singular at the origin.

However, regular solutions may possibly be found by relaxing some of our assumptions, e.g. by including Lifshitz matter (i.e. matter consistent with the symmetries of Hořava gravity) or by looking for non-stationary solutions. Future work may consider the question of whether these solutions may be formed from

gravitational collapse. Nevertheless, steps in this direction need to deal with the well-posedness of the Cauchy problem for this type of theories. Long-term directions may include the search for regular BHs in the full non-projectable version of Hořava gravity in $3+1$ dimensions.

Appendix A

In this Appendix, we present the strongly hyperbolic formulation used in Chapter 2 to study the evolution of the metric degrees of freedom.

A.1 The $Z4$ formulation

The covariant field equations in the $Z4$ formulation [352] are given by [55]

$$G_{\mu\nu} + \nabla_\mu Z_\nu + \nabla_\nu Z_\mu - \nabla_\sigma Z^\sigma g_{\mu\nu} + \kappa_1 \left(n_\mu Z_\nu + n_\nu Z_\mu + \kappa_2 n_\sigma Z^\sigma g_{\mu\nu}\right) = 8\pi G\, T_{\mu\nu} \ , \quad \text{(A.1)}$$

where $G_{\mu\nu}$ is the Einstein tensor, $T_{\mu\nu}$ is the stress-energy tensor of the matter content, Z^μ is a 4-vector, n_μ is the unit normal covector to the time slices, and κ_1 and κ_2 are constants. The terms associated to κ_1 and κ_2 are introduced in a convenient way to enforce the decay of constraint violations associated to Z^μ, and are called *constraint damping terms*. Provided $\kappa_1 > 0$ and $\kappa_2 > -1$, these constraint damping terms help drive solutions to (A.1) to those of GR, which are recovered when $Z^\mu \equiv 0$ [55].

In this formulation, the Hamiltonian and momentum constraints are naturally included in the system of evolution equations, and the requirement that these constraints hold at an initial time $t = 0$ is equivalent to $Z^\mu|_{t=0} = \partial_t Z^\mu|_{t=0} = 0$. It can be shown that these constraints evolve (ignoring the constraint damping terms) according to $\Box Z_\mu + R_{\mu\nu} Z^\nu = 0$ [55].

In the $3+1$ decomposition,

$$ds^2 = -\alpha^2\, dt^2 + \gamma_{ij}(dx^i + \beta^i\, dt)(dx^j + \beta^j\, dt) \ , \quad \text{(A.2)}$$

Eq. (A.1) becomes [55]

$$(\partial_t - \mathcal{L}_\beta)\, \gamma_{ij} = -2\alpha K_{ij} \ , \quad \text{(A.3a)}$$

$$(\partial_t - \mathcal{L}_\beta)\, K_{ij} = -\nabla_i \alpha_j + \alpha \Big[R_{ij} + \nabla_i Z_j + \nabla_j Z_i$$

$$- 2K_{ij}^2 + (\mathrm{tr}K - 2\Theta)\, K_{ij} - \kappa_1 (1+\kappa_2)\, \Theta\gamma_{ij}\Big] \\ - 8\pi\alpha\Big[S_{ij} - \frac{1}{2}(\mathrm{tr}S - \tau)\,\gamma_{ij}\Big]\,, \tag{A.3b}$$

$$(\partial_t - \mathcal{L}_\beta)\,\Theta = \frac{\alpha}{2}\Big[\mathrm{tr}R + 2\nabla_k Z^k + (\mathrm{tr}K - 2\Theta)\,\mathrm{tr}K - \mathrm{tr}\left(K^2\right) \\ - 2Z^k\alpha_k/\alpha - \kappa_2(2+\kappa_2)\Theta - 16\pi\tau\Big]\,, \tag{A.3c}$$

$$(\partial_t - \mathcal{L}_\beta)\,Z_i = \alpha\Big[\nabla_j\left(K_i{}^j - \delta_i{}^j\mathrm{tr}K\right) + \partial_i\Theta \\ - 2K_i{}^j Z_j - \Theta\alpha_i/\alpha - \kappa_1 Z_i - 8\pi S_i\Big]\,, \tag{A.3d}$$

where γ_{ij} is the spatial metric, K_{ij} is the extrinsic curvature, $\Theta \equiv n_\mu Z^\mu$ is the normal projection of Z^μ, and the projections of the stress-energy tensor are defined as $\tau \equiv T^{\mu\nu}n_\mu n_\nu$, $S_i \equiv T_i^\mu n_\mu$ and $S_{ij} \equiv T_{ij}$.

A.2 The $Z3$ system

The solutions of Eq. (A.3) are invariant under the variable redefinition $K_{ij} \to K_{ij} + (n/2)\Theta\gamma_{ij}$. A family of $Z3$ systems is obtained by performing such transformation and breaking this symmetry by enforcing $\Theta \equiv 0$ and $n = 4/3$ [353, 354].

In spherical symmetry, the $Z3$ system used to perform the simulations of Chapter 2 is given by [212, 213]

$$\partial_t A_r = -\partial_r[\alpha\, trK]\,, \tag{A.4a}$$

$$\partial_t D_{rr}{}^r = -\partial_r[\alpha\, K_r{}^r]\,, \tag{A.4b}$$

$$\partial_t D_{r\theta}{}^\theta = -\partial_r[\alpha\, K_\theta{}^\theta]\,, \tag{A.4c}$$

$$\partial_t Z_r = -\partial_r[2\,\alpha\, K_\theta{}^\theta] + 2\alpha\Big\{(K_r{}^r - K_\theta{}^\theta)\Big(D_{r\theta}{}^\theta + \frac{1}{r}\Big) \\ - K_r{}^r\Big[Z_r + \frac{1}{4r}\Big(1 - \frac{g_{rr}}{g_{\theta\theta}}\Big)\Big] \\ + A_r K_\theta{}^\theta + \frac{1}{4r}\frac{g_{rr}}{g_{\theta\theta}}(K_\theta{}^\theta - K_r{}^r) - 4\pi S_r\Big\}\,, \tag{A.4d, A.4e}$$

$$\partial_t K_r{}^r = -\partial_r\Big[\alpha g^{rr}\Big(A_r + \frac{2}{3}D_{r\theta}{}^\theta - \frac{4}{3}Z_r\Big)\Big] + \alpha\Big\{(K_r{}^r)^2 + \frac{2}{3}K_\theta{}^\theta(K_r{}^r - K_\theta{}^\theta) \\ - g^{rr}D_{rr}{}^r A_r + \frac{1}{3r}[g^{rr}(D_{rr}{}^r - A_r - 4Z_r) + g^{\theta\theta}(D_{r\theta}{}^\theta - A_r)] \\ + \frac{2}{3}g^{rr}\Big[Z_r + \frac{1}{4r}\Big(1 - \frac{g_{rr}}{g_{\theta\theta}}\Big)\Big](2D_{rr}{}^r - 2D_{r\theta}{}^\theta - A_r) \\ - \frac{2}{3}g^{rr}\Big(D_{r\theta}{}^\theta + \frac{1}{r}\Big)(D_{rr}{}^r - A_r) + 8\pi\Big(\frac{\tau}{6} - \frac{S_r{}^r}{2} + S_\theta{}^\theta\Big)\Big\}\,, \tag{A.4f}$$

$$\partial_t K_\theta{}^\theta = -\partial_r\Big[\alpha g^{rr}\Big(-\frac{1}{3}D_{r\theta}{}^\theta + \frac{2}{3}Z_r\Big)\Big] + \alpha\Big\{\frac{1}{3}K_\theta{}^\theta(-K_r{}^r + 4K_\theta{}^\theta) \\ + \frac{1}{6r}[g^{rr}(A_r - 2D_{rr}{}^r - 4Z_r) + g^{\theta\theta}(A_r - 2D_{r\theta}{}^\theta)]$$

$$
\begin{aligned}
&- \frac{2}{3} g^{rr} \Big[Z_r + \frac{1}{4r} \Big(1 - \frac{g_{rr}}{g_{\theta\theta}} \Big) \Big] (D_{rr}{}^{r} - D_{r\theta}{}^{\theta} - 2A_r) \\
&+ \frac{1}{3} g^{rr} \Big(D_{r\theta}{}^{\theta} + \frac{1}{r} \Big) (D_{rr}{}^{r} - 4A_r) + 8\pi \Big(\frac{\tau}{6} + \frac{S_r{}^{r}}{2} \Big) \Big\} ,
\end{aligned} \tag{A.4g}
$$

where the variables A_j, $D_{ij}{}^{k}$ have been defined Eq .(2.30).

Appendix B

B.1 Weak data example

In this Appendix, we show results for the case with weak initial data corresponding to parameters $r_c = 55\,L_\Lambda$, $\sigma = 15\,L_\Lambda$, and $A = 0.02\,L_\Lambda$ [Eq. (2.43)], and the same values for the coupling constants as in the main text (Sec. 4.4). During the evolution, an ingoing pulse bounces off the origin and is dispersed as it propagates outwards. No apparent sound or black hole horizons are formed.

In Fig. B.1, we show the spatial maximum and minimum values of the eigenvalues of the effective metric and of the characteristic speeds, where no Cauchy breakdown is observed. Consistently with the discrepancy measure $\mathbb{E}_{AB}[\pi]$ in Fig. B.2, the scalar profiles show agreement across the board in Fig. B.3. For this initial data, the evolution remains in the linear/EFT regime at all times.

B.2 Constraint propagation in the "fixed" theory

In the "fixed" theory, the equations of motion do not automatically imply the conservation of the stress-energy tensor. Indeed, the right hand side of

$$\nabla^\mu T^{(\pi)}_{\mu\nu} = 2\nabla_\nu\pi\nabla^\mu\left[\left(\Sigma - K'(X)\right)\nabla_\mu\pi\right] + \text{term prop. to Eq. (2.27)} \tag{B.1}$$

is not formally zero when the equations of motion are used. However, if the "driver" equation [c.f. Eq. (2.28)] is such that $\Sigma \approx K'(X)$, an approximate conservation equation for $T^{(\pi)}_{\mu\nu}$ is expected, i.e. $\nabla^\mu T^{(\pi)}_{\mu\nu} \approx 0$.

In order to see the effect on the propagation of the constraint equations, we follow Ref. [205] (see also Ref. [355]). We begin by defining the projections of Einstein equations $E_{\mu\nu} \equiv G_{\mu\nu} - \kappa\, T^{(\pi)}_{\mu\nu} = 0$, given by

$$\begin{aligned} \mathcal{H} &\equiv n^\mu n^\nu E_{\mu\nu}\ , \\ \mathcal{M}_\mu &\equiv -n^\rho P_\mu{}^\sigma E_{\rho\sigma}\ , \\ \mathcal{E}_{\mu\nu} &\equiv P_\mu{}^\rho P_\nu{}^\sigma E_{\rho\sigma}\ , \end{aligned} \tag{B.2}$$

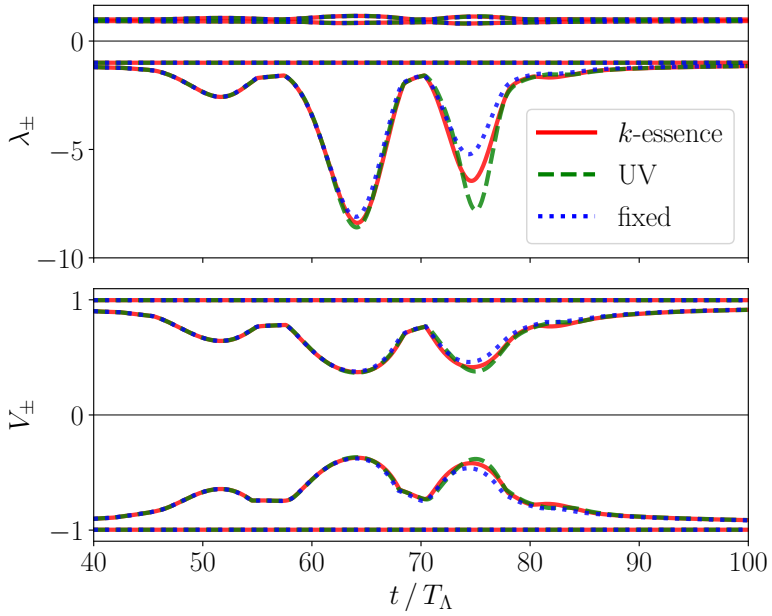

Figure B.1: *Character of the k-essence scalar equation (weak initial data).* First panel: the minimum and maximum values of the eigenvalues of the effective metric in k-essence (red solid line), the $U(1)$ UV completion (green dashed line) and the "fixed" theory (blue dotted line). For the last two, the effective metric is not a fundamental quantity but "emergent" at low energies. From top to bottom: $\max(\lambda_+)$, $\min(\lambda_+)$, $\max(\lambda_-)$, $\min(\lambda_-)$. Second panel: the minimum and maximum values of the characteristic speeds. In this panel, from top to bottom: $\max(V_+)$, $\min(V_+)$, $\max(V_-)$, $\min(V_-)$.

where n^μ is the vector normal to the foliation and $P_\mu{}^\sigma = \left(\delta^\sigma_\mu + n_\mu n^\sigma\right)$ is the spatial projector. Therefore, the Hamiltonian and momentum constraints can be expressed as $\mathcal{H} = 0$ and $\mathcal{M}_\mu = 0$, respectively. The evolution equations for the metric are instead $\mathcal{E}_{\mu\nu} = 0$. Finally, the evolution of the Hamiltonian and momentum constraints can be obtained from the projections of $\nabla^\mu \left(G_{\mu\nu} - \kappa\, T^{(\pi)}_{\mu\nu}\right)$ and are given by,

$$n^\nu \nabla_\nu \mathcal{H} = -D^\nu \mathcal{M}_\nu - \mathcal{E}_{\mu\nu} D^\mu n^\nu + \mathcal{L}_{\mathcal{H}}\left(\mathcal{H}, \mathcal{M}_\sigma\right) + \kappa\, n^\nu\, \nabla^\mu T^{(\pi)}_{\mu\nu}\,, \tag{B.3}$$

$$n^\nu \nabla_\nu \mathcal{M}_\mu = -D^\nu \mathcal{E}_{\mu\nu} - \mathcal{E}_{\mu\nu} n^\lambda \nabla_\lambda n^\nu + \mathcal{L}_{\mathcal{M}_\mu}\left(\mathcal{H}, \mathcal{M}_\sigma\right) - \kappa\, P_\mu{}^\sigma \nabla^\lambda T^{(\pi)}_{\sigma\lambda}\,, \tag{B.4}$$

respectively, where and $\mathcal{L}_{\mathcal{H}}$ and $\mathcal{L}_{\mathcal{M}_\mu}$ are zero for vanishing arguments, and D the spatial covariant derivative. Thus, an approximate conservation of the constraints ($n^\nu \nabla_\nu \mathcal{H} \approx 0$ and $n^\nu \nabla_\nu \mathcal{M}_\mu \approx 0$) happens if *(i)* they are satisfied initially, *(ii)* we use the equations of motion, and *(iii)* the driver equation ensures that $\Sigma \approx K'(X)$ during the evolution.

In contrast, for k-essence and the $U(1)$ UV completion, the stress energy tensor is conserved, and thus $n^\nu \nabla_\nu \mathcal{H} = n^\nu \nabla_\nu \mathcal{M}_\mu = 0$, when the equations of motion are used.

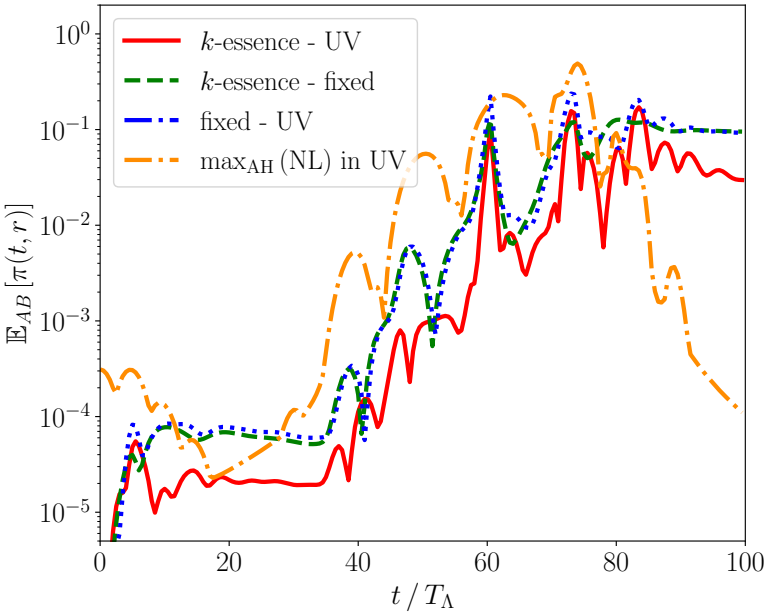

Figure B.2: *Discrepancy of the k-essence scalar (weak initial data).* The discrepancy measure $\mathbb{E}_{AB}$ of the k-essence scalar π for theories A vs. B, defined in Eq. (2.50); namely, k-essence vs. $U(1)$ UV completion (red solid line), k-essence vs. "fixed" theory (green dashed line), and "fixed" theory vs. $U(1)$ UV completion (blue dot-dashed line). For completeness, we plot $\max_{\rm AH}$ (NL) in the $U(1)$ UV completion (orange dot-dashed line).

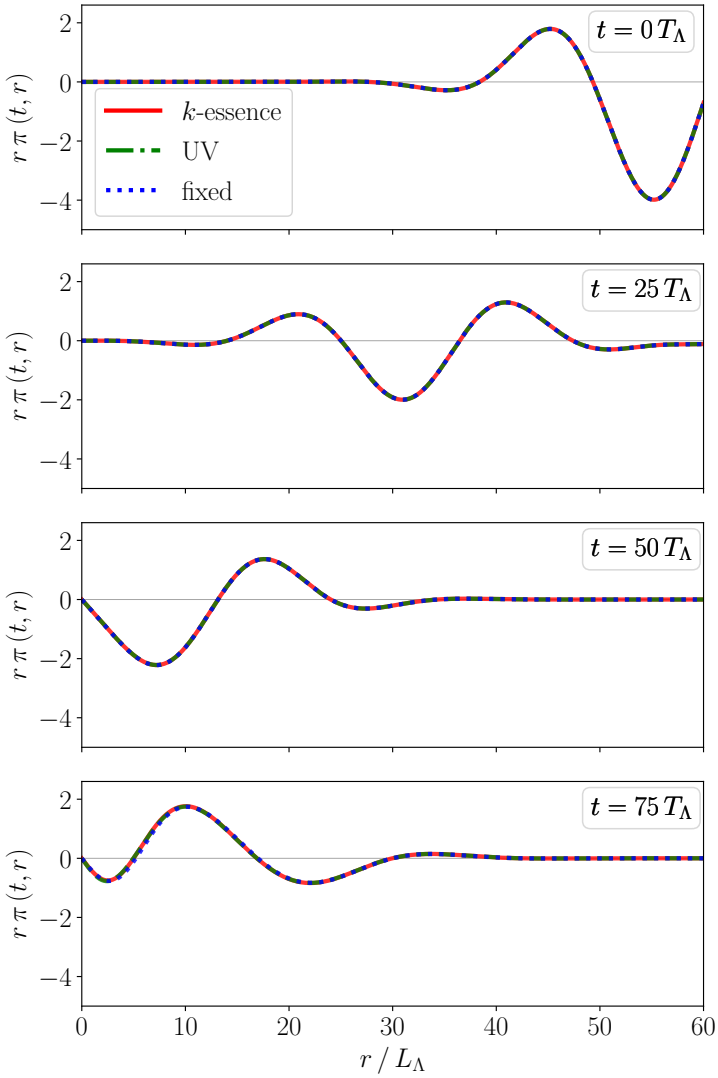

Figure B.3: *Dynamics of the pulse in the linear/EFT regime (weak initial data).* Time snapshots of the k-essence scalar for representative times from $t = 0$ to $t = 75\,T_\Lambda$ for k-essence (red solid lines), the phase field of the $U(1)$ UV completion (green dashed lines) and the π-scalar of the "fixed" theory (blue dotted lines).

Appendix C

C.1 Derivation of the scalar and matter equations

Variation of the action with respect to φ and the Bianchi identity applied to Eq. (4.5) give

$$\nabla_\mu \left(\mathcal{K}\nabla^\mu\varphi\right) = -\frac{\tilde{T}}{4\Phi^3}\partial_\varphi\Phi \ , \tag{C.1}$$

$$\nabla_\mu \left[T^{\mu\nu} + T^{(\varphi)\,\mu\nu}\right] = 0 \ , \tag{C.2}$$

respectively, where

$$\mathcal{K} \equiv K'(X) - \frac{\tilde{T}}{2\Phi^3}\partial_X\Phi \ , \tag{C.3}$$

$\tilde{T} \equiv \tilde{g}_{\mu\nu}\tilde{T}^{\mu\nu}$ is the trace of the matter stress-energy tensor in the Jordan frame, and $\tilde{g}_{\mu\nu} \equiv \Phi^{-1}g_{\mu\nu}$ is the metric in the Jordan frame.

The disformal relation (4.11) arises due to the factor

$$\frac{\delta\tilde{g}_{\mu\nu}}{\delta g_{\rho\sigma}} = \frac{1}{\Phi}\delta^\rho_\mu\delta^\sigma_\nu + \frac{\partial_X\Phi}{\Phi^2}g_{\mu\nu}\nabla^\rho\varphi\nabla^\sigma\varphi \ . \tag{C.4}$$

These equations can be written as Eqs. (4.8)-(4.12) by using the (disformal) relation (4.11), and by substituting Eq. (C.1) into Eq. (C.2).

Appendix D

D.1 Black hole shadow with PCA

In this appendix we apply the PCA framework to the shadow size of a non-rotating BH and conclude that only one combination of parameters can be meaningfully constrained. We will ignore the effect of spin as in Ref. [267].

The impact parameter $b_{\rm ph}$ and radial location $r_{\rm ph}$ of the photon sphere are obtained by solving the system $V\left(r_{\rm ph}, b_{\rm ph}\right) = \partial V\left(r_{\rm ph}, b_{\rm ph}\right)/\partial r = 0$, where $V(r, b)$ is the effective potential of null rays in spherical symmetry. Remarkably, $V(r)$ is only sensitive to the $g_{tt}(r)$ metric function, and therefore, no constraints can be placed on an independent function $g_{rr}(r)$. Explicitly, this system becomes [144]

$$r_{\rm ph} = \frac{2g_{tt}(r_{\rm ph})}{g'_{tt}(r_{\rm ph})}, \qquad\qquad b^2_{\rm ph} = -\frac{4g_{tt}(r_{\rm ph})}{\left[g'_{tt}(r_{\rm ph})\right]^2}. \tag{D.1}$$

For the Schwarzschild metric, these equations can be easily solved to obtain $r^{\rm Sch}_{\rm ph} = 3\,M_{\rm BH}$ and $b^{\rm Sch}_{\rm ph} = 3\sqrt{3}\,M_{\rm BH}$.

A deformed Schwarzschild metric introduces deviations on the photon sphere radius $\delta r_{\rm ph}$ and impact parameter $\delta b_{\rm ph}$. By linearizing Eqs. (D.1), they are found to be

$$\begin{aligned}
\delta r_{\rm ph} &= -\frac{3}{8}\left[3r_s^2\,\delta g'_{tt}\left(r^{\rm Sch}_{\rm ph}\right) - 4r_s\,\delta g_{tt}\left(r^{\rm Sch}_{\rm ph}\right)\right], \\
\delta b_{\rm ph} &= \frac{9}{4}\sqrt{3}\,r_s\,\delta g_{tt}\left(r^{\rm Sch}_{\rm ph}\right),
\end{aligned} \tag{D.2}$$

where $r_s = 2\,M_{\rm BH}$ and where we can describe $\delta g_{tt}(r)$ as a sum of M basis terms with parameters α_i as in Eq. (5.6) in the main text. Our model for the impact parameter – the only observable– will then be $b_M\left(\boldsymbol{\alpha}\right) = b^{\rm Sch}_{\rm ph} + \delta b_{\rm ph}\left(\boldsymbol{\alpha}\right)$.

We compare with a measurement $b^{\rm Sch}_{\rm ph} \pm \sigma$, with error $\sigma \approx 0.17\,b^{\rm Sch}_{\rm ph}$ [263], by writing the likelihood

$$\log p(\boldsymbol{\alpha}|b^{\rm Sch}_{\rm ph}) = -\frac{\left(b_M\left(\boldsymbol{\alpha}\right) - b^{\rm Sch}_{\rm ph}\right)^2}{2\sigma^2}. \tag{D.3}$$

For flat priors, the Fisher matrix (5.13) becomes

$$F_{ij} \propto \delta g_{tt}^{(i)}\left(r_{\rm ph}^{\rm Sch}\right)\delta g_{tt}^{(j)}\left(r_{\rm ph}^{\rm Sch}\right), \tag{D.4}$$

which has only one non-zero eigenvalue, corresponding to the eigenvector

$$\boldsymbol{e}^{(1)} \propto \left(\delta g_{tt}^{(1)},\ldots,\delta g_{tt}^{(M)}\right)|_{r_{\rm ph}^{\rm Sch}}. \tag{D.5}$$

Then, the only combination [c.f. Eq. (11) of Ref. [144]] we can constrain with the EHT measurement is

$$\left|\sum_{i=1}^{M}\alpha_i\delta g_{tt}^{(i)}\left(r_{\rm ph}^{\rm Sch}\right)\right| \lesssim 0.17. \tag{D.6}$$

Appendix E

E.1 Equations of motion

In this Appendix, we provide explicit expressions for the field equations in terms of the metric functions $F(r)$ and $G(r)$, using the same notation as in the main text. In more detail, the explicit expressions for Eqs. (6.15) are

$$E_1 = (\lambda-1)\left(r^2\left(GF'G' + G\left(GF'' + FG''\right) - F\left(G'\right)^2\right) + G^2rF' - FG^2\right) + FGr^2G'' + 2FGrG', \quad \text{(E.1)}$$

$$\begin{aligned} E_2 = (\lambda-1)\Bigg[&Gr^3\left(F\left(2G\left(GF'' + FG''\right) - F\left(G'\right)^2\right) + G^2\left(F'\right)^2 + 4FGF'G'\right) \\ &+ 2FG^2r^2\left(2GF' + FG'\right) - F^2G^3r\Bigg] \\ &+ \mu\Bigg[4r^3\left(-4\left(G'\right)^2G'' + 4GG^{(3)}G' + G\left(3\left(G''\right)^2 - 2GG^{(4)}\right)\right) \\ &- 16r^2\left(-4GG'G'' + 2\left(G'\right)^3 + G^2G^{(3)}\right) \\ &+ 16Gr\left(2GG'' - \left(G'\right)^2\right) - 32G^2G'\Bigg] + 2G^3r^3\left(\left(F'\right)^2 + FF''\right) \\ &- 2G^3r^3\Lambda\,, \end{aligned} \quad \text{(E.2)}$$

while the constraint (6.23) is

$$\begin{aligned} E_3 = (\lambda-1)\left[-2FG^2r^2\left(GF' + FG'\right) - Gr^3\left(GF' + FG'\right)^2 - F^2G^3r\right] \\ + \mu\Bigg[r^3\left(-8\left(G'\right)^2G'' + 8GG^{(3)}G' - 4G\left(G''\right)^2\right) \\ + 8r^2\left(-GG'G'' - 2\left(G'\right)^3 + G^2G^{(3)}\right) \end{aligned}$$

$$+ 16Gr\left(GG'' - 3\left(G'\right)^2\right) - 16G^2G'\Bigg] - 2FG^3r^2F' - 2FG^2r^3F'G' + 2G^3r^3\Lambda\ . \quad \text{(E.3)}$$

E.2 Linearized analysis at large radius

To study the asymptotics of the general solution of the system $(\mathcal{E}_1, \mathcal{E}_3)$ at large r, we substitute the expansion (6.58) and linearize, assuming the functions f, g and their first derivatives are small ($f, g \ll 1$ and $rf', rg' \ll 1$). We do not need to make any assumptions about the second derivatives of f and g. Proceeding in this way, we obtain the system of linear equations

$$(\lambda-1)f'' + \frac{(\lambda-1)}{r}f' + \frac{\lambda(1+2\sigma)}{r}g' + \\ + \frac{(1+2\sigma)^2 - (\lambda-1)\sigma(\sigma+1)}{r^2}g = 0, \quad \text{(E.4a)}$$

$$8(1+2\sigma)^2 g'' + \frac{16\sigma(1+2\sigma)^2}{r}g' \\ - 2(\lambda+\sigma+\lambda\sigma)F_\infty^2 r^{1-2\sigma}f' \\ - (\lambda-1)(1+4\sigma+3\sigma^2)F_\infty^2 r^{-2\sigma}g \\ = \frac{16\sigma(1+2\sigma)^2(2+\sigma)}{r^2}. \quad \text{(E.4b)}$$

Note that in deriving Eq. (E.4) we have assumed that $\sigma < 1$ and neglected terms of order $O(r^{-2}g)$ in Eq. (E.4b), which are small compared to the terms we have kept.

We are now interested in the solutions of this system at large $r \gg 1$. A particular solution is provided by

$$f = f_\infty r^{-2(1-\sigma)}, \qquad g = g_\infty r^{-2(1-\sigma)}, \quad \text{(E.5)}$$

where the coefficients f_∞, g_∞ are determined from the linear algebraic equations,

$$4(\lambda-1)(1-\sigma)^2 f_\infty + \\ + (1-2\lambda+5\sigma-3\lambda\sigma+5\sigma^2+3\lambda\sigma^2)g_\infty = 0, \quad \text{(E.6)}$$

$$4(\lambda+\sigma+\lambda\sigma)(1-\sigma)f_\infty + \\ - (\lambda-1)(1+4\sigma+3\sigma^2)g_\infty = \frac{16\sigma(1+2\sigma)^2(2+\sigma)}{F_\infty^2}. \quad \text{(E.7)}$$

In particular, at $\lambda - 1 \ll 1$ we have $f_\infty = 4(\lambda-1)/F_\infty^2$, $g_\infty = 0$.

It is straightforward to see that two solutions of the homogeneous system at

large r have the form

$$f = \frac{\sigma}{r}, \qquad g = \frac{1}{r}, \qquad \text{and} \quad f = \text{const}, \qquad g = 0. \tag{E.8}$$

As discussed in the main text, they correspond to the shift and rescaling of the non-linear solution.

The two other solutions cannot in general be found analytically. Still, they can be derived in the limit $(\lambda - 1) \ll 1$. To simplify the subsequent analysis, we set $F_\infty = 1$, as can always be achieved by the symmetry transformation (6.27).

We observe that the highest derivative term in Eq. (E.4a) is multiplied by a small quantity, which suggests using the Wentzel–Kramers–Brillouin (WKB) expansion [141]. The derivatives of a function should be treated as enhanced by a factor $1/\sqrt{\lambda - 1}$ compared to the function itself. We will need both the leading and the subleading terms in the expansion in powers of $\sqrt{\lambda - 1}$. With this in mind and recalling that $\sigma \approx (\lambda - 1)/2$, we simplify Eqs. (E.4), keeping only the relevant terms:

$$(\lambda - 1) f'' + \frac{\lambda - 1}{r} f' + \frac{g'}{r} + \frac{g}{r^2} = 0, \tag{E.9a}$$

$$8g'' - 2r^{1-2\sigma} f' = 0 \tag{E.9b}$$

The form of the equations suggests the following ansatz,

$$f = (f_0 + \sqrt{\lambda - 1} f_1 + \ldots) \exp\left(\frac{iQ}{\sqrt{\lambda - 1}}\right), \tag{E.10a}$$

$$g = \sqrt{\lambda - 1}\,(g_0 + \sqrt{\lambda - 1} g_1 + \ldots) \exp\left(\frac{iQ}{\sqrt{\lambda - 1}}\right), \tag{E.10b}$$

We first consider the leading order, which corresponds to terms $O(1)$ and $O(1/\sqrt{\lambda - 1})$ in Eqs. (E.9a) and (E.9b), respectively. At this order, we obtain

$$-(Q')^2 f_0 + \frac{iQ'}{r} g_0 = 0, \tag{E.11a}$$

$$-2ir^{1-2\sigma} Q' f_0 - 8(Q')^2 g_0 = 0. \tag{E.11b}$$

As f_0, g_0 are non-vanishing by assumption, the system must be degenerate, giving the condition

$$(Q')^2 = \frac{r^{-2\sigma}}{4}. \tag{E.12}$$

Choosing the positive root, we find $Q = r^{1-2\sigma}/2$ and

$$g_0 = -\frac{i}{2} r^{1-\sigma} f_0\,. \tag{E.13}$$

The fact that Q is real implies that the solution is quickly oscillating.

To find the behavior of the amplitude, we need to go to the next WKB order. This corresponds to terms $O(\sqrt{\lambda-1})$ in Eq. (E.9a) and $O(1)$ in Eq. (E.9b). Using that $Q'' = O(\lambda-1)$, we obtain

$$2iQ'f_0' + \frac{iQ'}{r}f_0 + \frac{g_0'}{r} + \frac{g_0}{r^2} - (Q')^2 f_1 + \frac{iQ'}{r}g_1 = 0, \tag{E.14a}$$

$$16iQ'g_0' - 2r^{1-2\sigma}f_0' - 2iQ'r^{1-2\sigma}f_1 - 8(Q')^2 g_1 = 0 \tag{E.14b}$$

Next, we multiply the second equation by $iQ'r^{-1+2\sigma}/2$ and add it to the first one. This eliminates the functions f_1 and g_1, so that we are left with an equation containing only f_0 and g_0. Using further the relation (E.13), we obtain a differential equation for f_0,

$$f_0' + \frac{(1-\sigma)f_0}{2r} = 0. \tag{E.15}$$

We then obtain that $f_0 \propto r^{-(1-\sigma)/2}$ and $g_0 \propto r^{(1-\sigma)/2}$, where the latter is a growing function of the radial coordinate.

The above analysis shows that for $(\lambda-1) \ll 1$ two linearly independent solutions of the system (E.4) oscillate with a growing amplitude. By solving the system numerically we have found that this qualitative behavior persists at finite $(\lambda-1)$ as long as $\lambda \lesssim 5/2$.

Let us make the following comment. At first sight, it may be surprising to find oscillatory asymptotics in stationary perturbations of a time-independent background. Normally, one would expect such perturbations to obey an elliptic equation, which should lead to solutions that exponentially grow or decay at large r. The fact that the perturbations are instead oscillating in r seems to suggest that the spatial part of the eigenmode equation in the BH background has turned hyperbolic, and one may worry if this leads to a rapid gradient instability when the time evolution is included. In more detail, the WKB result (E.12) could suggest that the dispersion relation for the short-wavelength modes at small $(\lambda-1)$ has changed from (6.10) to

$$\omega^2 = 4\mu(\lambda-1)\,k^4 - F^2(r)\,k^2\,, \tag{E.16}$$

where we have used that $r^{-\sigma} = F(r)$. This would imply an instability on time scale $\tau_{\rm inst} \sim F/\sqrt{\mu(\lambda-1)}$, which would be catastrophic.

Fortunately, this is not the case. The reason is that our BH background is stationary, rather than static, i.e. it has non-vanishing shift vector. Therefore, the time derivative operator in any field equations gets modified by an admixture of a term with spatial derivatives (cf. Eq. (6.16)), $\partial_t \mapsto \partial_t - N^i\partial_i + \ldots$, where dots stand for term without derivatives acting on the field. As a consequence,

the dispersion relation for short-wavelength modes takes the form

$$\big(\omega - F(r)\,k\big)^2 = 4\mu(\lambda - 1)k^4\,, \tag{E.17}$$

which for $\omega = 0$ is the same as Eq. (E.16). But now ω never becomes imaginary, and no catastrophic instabilities develop. Notice that this does not prove the absence of long-wavelength instabilities that are, anyway, less harmful.

List of Figures

Bibliography

[1] B. P. Abbott *et al.*, "Observation of Gravitational Waves from a Binary Black Hole Merger," *Phys. Rev. Lett.*, vol. 116, no. 6, p. 061102, 2016.

[2] R. A. Hulse and J. H. Taylor, "Discovery of a pulsar in a binary system," *Astrophys. J.*, vol. 195, pp. L51–L53, 1975.

[3] J. H. Taylor and J. M. Weisberg, "A new test of general relativity: Gravitational radiation and the binary pulsar PS R 1913+16," *Astrophys. J.*, vol. 253, pp. 908–920, 1982.

[4] B. P. Abbott *et al.*, "Tests of general relativity with GW150914," *Phys. Rev. Lett.*, vol. 116, no. 22, p. 221101, 2016. [Erratum: Phys.Rev.Lett. 121, 129902 (2018)].

[5] B. P. Abbott *et al.*, "Tests of General Relativity with GW170817," *Phys. Rev. Lett.*, vol. 123, no. 1, p. 011102, 2019.

[6] B. Abbott *et al.*, "Tests of General Relativity with the Binary Black Hole Signals from the LIGO-Virgo Catalog GWTC-1," *Phys. Rev. D*, vol. 100, no. 10, p. 104036, 2019.

[7] R. Abbott *et al.*, "Tests of general relativity with binary black holes from the second LIGO-Virgo gravitational-wave transient catalog," *Phys. Rev. D*, vol. 103, no. 12, p. 122002, 2021.

[8] R. Abbott *et al.*, "Tests of General Relativity with GWTC-3," 12 2021.

[9] K. Akiyama *et al.*, "First M87 Event Horizon Telescope Results. I. The Shadow of the Supermassive Black Hole," *Astrophys. J.*, vol. 875, no. 1, p. L1, 2019.

[10] K. Akiyama *et al.*, "First Sagittarius A* Event Horizon Telescope Results. I. The Shadow of the Supermassive Black Hole in the Center of the Milky Way," *Astrophys. J. Lett.*, vol. 930, no. 2, p. L12, 2022.

[11] K. Akiyama *et al.*, "First M87 Event Horizon Telescope Results. V. Physical Origin of the Asymmetric Ring," *Astrophys. J. Lett.*, vol. 875, no. 1, p. L5, 2019.

[12] K. Akiyama *et al.*, "First Sagittarius A* Event Horizon Telescope Results. VI. Testing the Black Hole Metric," *Astrophys. J. Lett.*, vol. 930, no. 2, p. L17, 2022.

[13] K. Akiyama *et al.*, "First M87 Event Horizon Telescope Results. VIII. Magnetic Field Structure near The Event Horizon," *Astrophys. J. Lett.*, vol. 910, no. 1, p. L13, 2021.

[14] P. Horava, "Quantum Gravity at a Lifshitz Point," *Phys. Rev. D*, vol. 79, p. 084008, 2009.

[15] P. Amaro-Seoane *et al.*, "Laser Interferometer Space Antenna," 2 2017.

[16] M. Kramer *et al.*, "Strong-Field Gravity Tests with the Double Pulsar," *Phys. Rev. X*, vol. 11, no. 4, p. 041050, 2021.

[17] B. P. Abbott *et al.*, "GW170817: Observation of Gravitational Waves from a Binary Neutron Star Inspiral," *Phys. Rev. Lett.*, vol. 119, no. 16, p. 161101, 2017.

[18] B. P. Abbott *et al.*, "Gravitational Waves and Gamma-rays from a Binary Neutron Star Merger: GW170817 and GRB 170817A," *Astrophys. J. Lett.*, vol. 848, no. 2, p. L13, 2017.

[19] J. Hadamard, "Sur les problemes aux derivees partielles et leur signification physique," *Princeton university bulletin*, pp. 49–52, 1902.

[20] D. Lovelock, "The Einstein tensor and its generalizations," *J. Math. Phys.*, vol. 12, pp. 498–501, 1971.

[21] D. Lovelock, "The four-dimensionality of space and the einstein tensor," *J. Math. Phys.*, vol. 13, pp. 874–876, 1972.

[22] E. Berti *et al.*, "Testing General Relativity with Present and Future Astrophysical Observations," *Class. Quant. Grav.*, vol. 32, p. 243001, 2015.

[23] J. M. Ezquiaga and M. Zumalacárregui, "Dark Energy in light of Multi-Messenger Gravitational-Wave astronomy," *Front. Astron. Space Sci.*, vol. 5, p. 44, 2018.

[24] A. Einstein, "The Foundation of the General Theory of Relativity," *Annalen Phys.*, vol. 49, no. 7, pp. 769–822, 1916.

[25] A. Einstein, "On the electrodynamics of moving bodies," *Annalen Phys.*, vol. 17, pp. 891–921, 1905.

[26] C. M. Will, *Theory and Experiment in Gravitational Physics*. Cambridge University Press, 9 2018.

[27] D. Hilbert, "Die Grundlagen der Physik. 1.," *Gott. Nachr.*, vol. 27, pp. 395–407, 1915.

[28] I. Newton, *Philosophiæ Naturalis Principia Mathematica*. 1687.

[29] V. Cardoso and P. Pani, "Testing the nature of dark compact objects: a status report," *Living Rev. Rel.*, vol. 22, no. 1, p. 4, 2019.

[30] R. M. Wald, *General Relativity*. Chicago, USA: Chicago Univ. Pr., 1984.

[31] C. Bambi, "Astrophysical Black Holes: A Review," *PoS*, vol. MULTIF2019, p. 028, 2020.

[32] M. Miyoshi, J. Moran, J. Hernstein, L. Greenhill, N. Nakai, P. Diamond, and M. Inoue, "Evidence for a black hole from high rotation velocities in a subparsec region of NGC4258," *Nature*, vol. 373, pp. 127–129, 1995.

[33] M. Volonteri, "The Formation and Evolution of Massive Black Holes," *Science*, vol. 337, p. 544, 2012.

[34] B. P. Abbott and et al., "Gw151226: Observation of gravitational waves from a 22-solar-mass binary black hole coalescence," *Phys. Rev. Lett.*, vol. 116, p. 241103, Jun 2016.

[35] J. D. Bekenstein, "Black holes and entropy," *Phys. Rev. D*, vol. 7, pp. 2333–2346, 1973.

[36] J. D. Bekenstein, "Generalized second law of thermodynamics in black hole physics," *Phys. Rev. D*, vol. 9, pp. 3292–3300, 1974.

[37] S. W. Hawking, "Particle Creation by Black Holes," *Commun. Math. Phys.*, vol. 43, pp. 199–220, 1975. [Erratum: Commun.Math.Phys. 46, 206 (1976)].

[38] R. Penrose, "Gravitational collapse: The role of general relativity," *Riv. Nuovo Cim.*, vol. 1, pp. 252–276, 1969. [Gen. Rel. Grav.34,1141(2002)].

[39] K. Schwarzschild, "On the gravitational field of a mass point according to Einstein's theory," *Sitzungsber. Preuss. Akad. Wiss. Berlin (Math. Phys.)*, vol. 1916, pp. 189–196, 1916.

[40] R. P. Kerr, "Gravitational field of a spinning mass as an example of algebraically special metrics," *Phys. Rev. Lett.*, vol. 11, pp. 237–238, 1963.

[41] R. H. Boyer and R. W. Lindquist, "Maximal analytic extension of the Kerr metric," *J. Math. Phys.*, vol. 8, p. 265, 1967.

[42] E. T. Newman, R. Couch, K. Chinnapared, A. Exton, A. Prakash, and R. Torrence, "Metric of a Rotating, Charged Mass," *J. Math. Phys.*, vol. 6, pp. 918–919, 1965.

[43] D. Robinson, "Uniqueness of the Kerr black hole," *Phys. Rev. Lett.*, vol. 34, pp. 905–906, 1975.

[44] W. Israel, "Event horizons in static vacuum space-times," *Phys. Rev.*, vol. 164, pp. 1776–1779, 1967.

[45] S. W. Hawking, "Black holes in the Brans-Dicke theory of gravitation," *Commun. Math. Phys.*, vol. 25, pp. 167–171, 1972.

[46] E. Berti, V. Cardoso, and A. O. Starinets, "Quasinormal modes of black holes and black branes," *Class. Quant. Grav.*, vol. 26, p. 163001, 2009.

[47] W. Baade and F. Zwicky, "Remarks on super-novae and cosmic rays," *Phys. Rev.*, vol. 46, pp. 76–77, Jul 1934.

[48] H. A. Buchdahl, "General Relativistic Fluid Spheres," *Phys. Rev.*, vol. 116, p. 1027, 1959.

[49] W.-C. Chen and J. Piekarewicz, "Compactness of Neutron Stars," *Phys. Rev. Lett.*, vol. 115, no. 16, p. 161101, 2015.

[50] A. Lyne, F. Graham-Smith, and B. Stappers, *Pulsar Astronomy*. Cambridge Astrophysics, Cambridge University Press, 5 ed., 2022.

[51] V. Paschalidis and N. Stergioulas, "Rotating Stars in Relativity," *Living Rev. Rel.*, vol. 20, no. 1, p. 7, 2017.

[52] J. W. T. Hessels, S. M. Ransom, I. H. Stairs, P. C. C. Freire, V. M. Kaspi, and F. Camilo, "A radio pulsar spinning at 716-hz," *Science*, vol. 311, pp. 1901–1904, 2006.

[53] K. Yagi and N. Yunes, "Approximate Universal Relations for Neutron Stars and Quark Stars," *Phys. Rept.*, vol. 681, pp. 1–72, 2017.

[54] J. R. Oppenheimer and G. M. Volkoff, "On massive neutron cores," *Phys. Rev.*, vol. 55, pp. 374–381, 1939.

[55] C. Bona, C. Palenzuela-Luque, and C. Bona-Casas, *Elements of Numerical Relativity and Relativistic Hydrodynamics*, vol. 783. 2009.

[56] D. Baumann, *Cosmology*. Cambridge University Press, 7 2022.

[57] E. Di Valentino, O. Mena, S. Pan, L. Visinelli, W. Yang, A. Melchiorri, D. F. Mota, A. G. Riess, and J. Silk, "In the realm of the Hubble tension—a review of solutions," *Class. Quant. Grav.*, vol. 38, no. 15, p. 153001, 2021.

[58] N. Aghanim *et al.*, "Planck 2018 results. I. Overview and the cosmological legacy of Planck," *Astron. Astrophys.*, vol. 641, p. A1, 2020.

[59] S. Perlmutter *et al.*, "Measurements of Ω and Λ from 42 high redshift supernovae," *Astrophys. J.*, vol. 517, pp. 565–586, 1999.

[60] A. G. Riess, A. V. Filippenko, W. Li, and B. P. Schmidt, "An indication of evolution of type ia supernovae from their risetimes," *Astron. J.*, vol. 118, pp. 2668–2674, 1999.

[61] S. W. Hawking and R. Penrose, "The Singularities of gravitational collapse and cosmology," *Proc. Roy. Soc. Lond. A*, vol. 314, pp. 529–548, 1970.

[62] A. H. Guth, "The Inflationary Universe: A Possible Solution to the Horizon and Flatness Problems," *Phys. Rev. D*, vol. 23, pp. 347–356, 1981.

[63] V. A. Rubakov, M. V. Sazhin, and A. V. Veryaskin, "Graviton Creation in the Inflationary Universe and the Grand Unification Scale," *Phys. Lett. B*, vol. 115, pp. 189–192, 1982.

[64] A. Einstein, "Approximative Integration of the Field Equations of Gravitation," *Sitzungsber. Preuss. Akad. Wiss. Berlin (Math. Phys.)*, vol. 1916, pp. 688–696, 1916.

[65] A. Einstein, "Über Gravitationswellen," *Sitzungsber. Preuss. Akad. Wiss. Berlin (Math. Phys.)*, vol. 1918, pp. 154–167, 1918.

[66] P. R. Saulson, "Josh Goldberg and the physical reality of gravitational waves," *Gen. Rel. Grav.*, vol. 43, pp. 3289–3299, 2011.

[67] M. Maggiore, *Gravitational Waves. Vol. 1: Theory and Experiments*. Oxford Master Series in Physics, Oxford University Press, 2007.

[68] E. Newman and R. Penrose, "An Approach to gravitational radiation by a method of spin coefficients," *J. Math. Phys.*, vol. 3, pp. 566–578, 1962.

[69] D. M. Eardley, D. L. Lee, A. P. Lightman, R. V. Wagoner, and C. M. Will, "Gravitational-wave observations as a tool for testing relativistic gravity," *Phys. Rev. Lett.*, vol. 30, pp. 884–886, 1973.

[70] R. Abbott *et al.*, "GWTC-3: Compact Binary Coalescences Observed by LIGO and Virgo During the Second Part of the Third Observing Run," 11 2021.

[71] B. P. Abbott *et al.*, "Optically targeted search for gravitational waves emitted by core-collapse supernovae during the first and second observing runs of advanced LIGO and advanced Virgo," *Phys. Rev. D*, vol. 101, no. 8, p. 084002, 2020.

[72] R. Abbott *et al.*, "All-sky search for continuous gravitational waves from isolated neutron stars using Advanced LIGO and Advanced Virgo O3 data," 1 2022.

[73] K. G. Arun *et al.*, "New horizons for fundamental physics with LISA," *Living Rev. Rel.*, vol. 25, no. 1, p. 4, 2022.

[74] P. Amaro-Seoane *et al.*, "Astrophysics with the Laser Interferometer Space Antenna," 3 2022.

[75] J. Antoniadis *et al.*, "The International Pulsar Timing Array second data release: Search for an isotropic gravitational wave background," *Mon. Not. Roy. Astron. Soc.*, vol. 510, no. 4, pp. 4873–4887, 2022.

[76] C. J. Moore, R. H. Cole, and C. P. L. Berry, "Gravitational-wave sensitivity curves," *Class. Quant. Grav.*, vol. 32, no. 1, p. 015014, 2015.

[77] M. D. Schwartz, *Quantum Field Theory and the Standard Model.* Cambridge University Press, 3 2014.

[78] R. P. Woodard, "Ostrogradsky's theorem on Hamiltonian instability," *Scholarpedia*, vol. 10, no. 8, p. 32243, 2015.

[79] G. W. Horndeski, "Second-order scalar-tensor field equations in a four-dimensional space," *Int. J. Theor. Phys.*, vol. 10, pp. 363–384, 1974.

[80] K. Hinterbichler, M. Trodden, and D. Wesley, "Multi-field galileons and higher co-dimension branes," *Phys. Rev. D*, vol. 82, p. 124018, 2010.

[81] D. Pirtskhalava, L. Santoni, E. Trincherini, and F. Vernizzi, "Weakly Broken Galileon Symmetry," *JCAP*, vol. 09, p. 007, 2015.

[82] J. Gleyzes, D. Langlois, F. Piazza, and F. Vernizzi, "Healthy theories beyond Horndeski," *Phys. Rev. Lett.*, vol. 114, no. 21, p. 211101, 2015.

[83] J. Gleyzes, D. Langlois, F. Piazza, and F. Vernizzi, "Exploring gravitational theories beyond Horndeski," *JCAP*, vol. 02, p. 018, 2015.

[84] M. Zumalacárregui and J. García-Bellido, "Transforming gravity: from derivative couplings to matter to second-order scalar-tensor theories beyond the Horndeski Lagrangian," *Phys. Rev. D*, vol. 89, p. 064046, 2014.

[85] D. Langlois and K. Noui, "Degenerate higher derivative theories beyond Horndeski: evading the Ostrogradski instability," *JCAP*, vol. 02, p. 034, 2016.

[86] M. Crisostomi, K. Koyama, and G. Tasinato, "Extended Scalar-Tensor Theories of Gravity," *JCAP*, vol. 1604, p. 044, 2016.

[87] J. Ben Achour, M. Crisostomi, K. Koyama, D. Langlois, K. Noui, and G. Tasinato, "Degenerate higher order scalar-tensor theories beyond Horndeski up to cubic order," *JHEP*, vol. 12, p. 100, 2016.

[88] T. Kobayashi, M. Yamaguchi, and J. Yokoyama, "Generalized G-inflation: Inflation with the most general second-order field equations," *Prog. Theor. Phys.*, vol. 126, pp. 511–529, 2011.

[89] J. L. Ripley and F. Pretorius, "Gravitational collapse in einstein dilaton-gauss–bonnet gravity," *Classical and Quantum Gravity*, vol. 36, p. 134001, Jun 2019.

[90] T. P. Sotiriou and S.-Y. Zhou, "Black hole hair in generalized scalar-tensor gravity," *Phys. Rev. Lett.*, vol. 112, p. 251102, 2014.

[91] H. O. Silva, H. Witek, M. Elley, and N. Yunes, "Dynamical Descalarization in Binary Black Hole Mergers," *Phys. Rev. Lett.*, vol. 127, no. 3, p. 031101, 2021.

[92] N. Franchini, M. Bezares, E. Barausse, and L. Lehner, "Fixing the dynamical evolution in scalar-Gauss-Bonnet gravity," 5 2022.

[93] A. Dima, E. Barausse, N. Franchini, and T. P. Sotiriou, "Spin-induced black hole spontaneous scalarization," 6 2020.

[94] D. D. Doneva and S. S. Yazadjiev, "New Gauss-Bonnet Black Holes with Curvature-Induced Scalarization in Extended Scalar-Tensor Theories," *Phys. Rev. Lett.*, vol. 120, no. 13, p. 131103, 2018.

[95] D. Bettoni, J. M. Ezquiaga, K. Hinterbichler, and M. Zumalacárregui, "Speed of Gravitational Waves and the Fate of Scalar-Tensor Gravity," *Phys. Rev. D*, vol. 95, no. 8, p. 084029, 2017.

[96] D. Blas, M. M. Ivanov, I. Sawicki, and S. Sibiryakov, "On constraining the speed of gravitational waves following GW150914," *JETP Lett.*, vol. 103, no. 10, pp. 624–626, 2016.

[97] J. Beltran Jimenez, F. Piazza, and H. Velten, "Evading the Vainshtein Mechanism with Anomalous Gravitational Wave Speed: Constraints on Modified Gravity from Binary Pulsars," *Phys. Rev. Lett.*, vol. 116, no. 6, p. 061101, 2016.

[98] G. D. Moore and A. E. Nelson, "Lower bound on the propagation speed of gravity from gravitational Cherenkov radiation," *JHEP*, vol. 09, p. 023, 2001.

[99] B. P. Abbott *et al.*, "Properties of the binary neutron star merger GW170817," *Phys. Rev. X*, vol. 9, no. 1, p. 011001, 2019.

[100] B. P. Abbott *et al.*, "Multi-messenger Observations of a Binary Neutron Star Merger," *Astrophys. J. Lett.*, vol. 848, no. 2, p. L12, 2017.

[101] C. de Rham and S. Melville, "Gravitational Rainbows: LIGO and Dark Energy at its Cutoff," *Phys. Rev. Lett.*, vol. 121, no. 22, p. 221101, 2018.

[102] P. Creminelli and F. Vernizzi, "Dark Energy after GW170817 and GRB170817A," *Phys. Rev. Lett.*, vol. 119, no. 25, p. 251302, 2017.

[103] J. M. Ezquiaga and M. Zumalacárregui, "Dark Energy After GW170817: Dead Ends and the Road Ahead," *Phys. Rev. Lett.*, vol. 119, no. 25, p. 251304, 2017.

[104] T. Baker, E. Bellini, P. G. Ferreira, M. Lagos, J. Noller, and I. Sawicki, "Strong constraints on cosmological gravity from GW170817 and GRB 170817A," *Phys. Rev. Lett.*, vol. 119, no. 25, p. 251301, 2017.

[105] J. Sakstein and B. Jain, "Implications of the Neutron Star Merger GW170817 for Cosmological Scalar-Tensor Theories," *Phys. Rev. Lett.*, vol. 119, no. 25, p. 251303, 2017.

[106] J. Gleyzes, D. Langlois, F. Piazza, and F. Vernizzi, "Essential Building Blocks of Dark Energy," *JCAP*, vol. 08, p. 025, 2013.

[107] G. Cusin, M. Lewandowski, and F. Vernizzi, "Nonlinear Effective Theory of Dark Energy," *JCAP*, vol. 04, p. 061, 2018.

[108] P. Creminelli, M. Lewandowski, G. Tambalo, and F. Vernizzi, "Gravitational Wave Decay into Dark Energy," *JCAP*, vol. 1812, p. 025, 2018.

[109] P. Creminelli, G. Tambalo, F. Vernizzi, and V. Yingcharoenrat, "Resonant Decay of Gravitational Waves into Dark Energy," *JCAP*, vol. 10, p. 072, 2019.

[110] P. Creminelli, G. Tambalo, F. Vernizzi, and V. Yingcharoenrat, "Dark-Energy Instabilities induced by Gravitational Waves," *JCAP*, vol. 05, p. 002, 2020.

[111] T. Chiba, T. Okabe, and M. Yamaguchi, "Kinetically driven quintessence," *Phys. Rev. D*, vol. 62, p. 023511, 2000.

[112] C. Armendariz-Picon, V. F. Mukhanov, and P. J. Steinhardt, "A Dynamical solution to the problem of a small cosmological constant and late time cosmic acceleration," *Phys. Rev. Lett.*, vol. 85, pp. 4438–4441, 2000.

[113] L. ter Haar, M. Bezares, M. Crisostomi, E. Barausse, and C. Palenzuela, "Dynamics of screening in modified gravity," 9 2020.

[114] M. Fierz, "On the physical interpretation of P.Jordan's extended theory of gravitation," *Helv. Phys. Acta*, vol. 29, pp. 128–134, 1956.

[115] P. Jordan, "The present state of Dirac's cosmological hypothesis," *Z. Phys.*, vol. 157, pp. 112–121, 1959.

[116] C. Brans and R. H. Dicke, "Mach's principle and a relativistic theory of gravitation," *Phys. Rev.*, vol. 124, pp. 925–935, 1961.

[117] A. A. H. Graham and R. Jha, "Nonexistence of black holes with noncanonical scalar fields," *Phys. Rev. D*, vol. 89, no. 8, p. 084056, 2014. [Erratum: Phys.Rev.D 92, 069901 (2015)].

[118] L. Hui and A. Nicolis, "No-Hair Theorem for the Galileon," *Phys. Rev. Lett.*, vol. 110, p. 241104, 2013.

[119] P. Brax, "Screening mechanisms in modified gravity," *Class. Quant. Grav.*, vol. 30, p. 214005, 2013.

[120] E. Babichev, C. Deffayet, and R. Ziour, "k-Mouflage gravity," *Int. J. Mod. Phys. D*, vol. 18, pp. 2147–2154, 2009.

[121] T. Jacobson and D. Mattingly, "Gravity with a dynamical preferred frame," *Phys. Rev. D*, vol. 64, p. 024028, 2001.

[122] M. Gasperini, "Repulsive gravity in the very early universe," *Gen. Rel. Grav.*, vol. 30, pp. 1703–1709, 1998.

[123] T. Jacobson, "Extended Horava gravity and Einstein-aether theory," *Phys. Rev. D*, vol. 81, p. 101502, 2010. [Erratum: Phys.Rev.D 82, 129901 (2010)].

[124] A. O. Barvinsky, D. Blas, M. Herrero-Valea, S. M. Sibiryakov, and C. F. Steinwachs, "Renormalization of Hořava gravity," *Phys. Rev. D*, vol. 93, no. 6, p. 064022, 2016.

[125] D. Blas, O. Pujolas, and S. Sibiryakov, "Consistent Extension of Horava Gravity," *Phys. Rev. Lett.*, vol. 104, p. 181302, 2010.

[126] E. Barausse, T. Jacobson, and T. P. Sotiriou, "Black holes in Einstein-aether and Horava-Lifshitz gravity," *Phys. Rev. D*, vol. 83, p. 124043, 2011.

[127] R. Arnowitt, S. Deser, and C. W. Misner, "Dynamical structure and definition of energy in general relativity," *Phys. Rev.*, vol. 116, pp. 1322–1330, Dec 1959.

[128] D. Blas, O. Pujolas, and S. Sibiryakov, "Models of non-relativistic quantum gravity: The Good, the bad and the healthy," *JHEP*, vol. 04, p. 018, 2011.

[129] M. Visser, "Power-counting renormalizability of generalized Horava gravity," 12 2009.

[130] J. W. Elliott, G. D. Moore, and H. Stoica, "Constraining the new Aether: Gravitational Cerenkov radiation," *JHEP*, vol. 08, p. 066, 2005.

[131] J. Bhattacharyya, M. Colombo, and T. P. Sotiriou, "Causality and black holes in spacetimes with a preferred foliation," *Class. Quant. Grav.*, vol. 33, no. 23, p. 235003, 2016.

[132] D. Blas and S. Sibiryakov, "Horava gravity versus thermodynamics: The Black hole case," *Phys. Rev. D*, vol. 84, p. 124043, 2011.

[133] D. Blas and E. Lim, "Phenomenology of theories of gravity without Lorentz invariance: the preferred frame case," *Int. J. Mod. Phys. D*, vol. 23, p. 1443009, 2015.

[134] E. Barausse, T. P. Sotiriou, and I. Vega, "Slowly rotating black holes in Einstein-Aether theory," *Phys. Rev.*, vol. D93, no. 4, p. 044044, 2016.

[135] N. Franchini, M. Herrero-Valea, and E. Barausse, "On distinguishing between General Relativity and a class of khronometric theories," 3 2021.

[136] A. Adam, P. Figueras, T. Jacobson, and T. Wiseman, "Rotating black holes in Einstein-aether theory," *Class. Quant. Grav.*, vol. 39, no. 12, p. 125001, 2022.

[137] N. J. Cornish, T. B. Littenberg, B. Bécsy, K. Chatziioannou, J. A. Clark, S. Ghonge, and M. Millhouse, "Bayeswave analysis pipeline in the era of gravitational wave observations," *Physical Review D*, vol. 103, Feb 2021.

[138] L. Rezzolla and A. Zhidenko, "New parametrization for spherically symmetric black holes in metric theories of gravity," *Phys. Rev. D*, vol. 90, p. 084009, Oct 2014.

[139] R. A. Konoplya and A. Zhidenko, "General parametrization of black holes: the only parameters that matter," 2020.

[140] R. Konoplya, L. Rezzolla, and A. Zhidenko, "General parametrization of axisymmetric black holes in metric theories of gravity," *Phys. Rev. D*, vol. 93, no. 6, p. 064015, 2016.

[141] C. M. Bender and S. A. Orszag, *Advanced Mathematical Methods for Scientists and Engineers*. McGraw-Hill, 1977.

[142] Z. Younsi, A. Zhidenko, L. Rezzolla, R. Konoplya, and Y. Mizuno, "New method for shadow calculations: Application to parametrized axisymmetric black holes," *Phys. Rev. D*, vol. 94, no. 8, p. 084025, 2016.

[143] R. Konoplya and A. Zhidenko, "Analytical representation for metrics of scalarized Einstein-Maxwell black holes and their shadows," *Phys. Rev. D*, vol. 100, no. 4, p. 044015, 2019.

[144] S. H. Völkel, E. Barausse, N. Franchini, and A. E. Broderick, "EHT tests of the strong-field regime of General Relativity," 11 2020.

[145] S. H. Völkel and E. Barausse, "Bayesian Metric Reconstruction with Gravitational Wave Observations," *Phys. Rev. D*, vol. 102, no. 8, p. 084025, 2020.

[146] A. Cardenas-Avendano, S. Nampalliwar, and N. Yunes, "Gravitational-wave versus X-ray tests of strong-field gravity," *Class. Quant. Grav.*, vol. 37, no. 13, p. 135008, 2020.

[147] S. Nampalliwar, S. Xin, S. Srivastava, A. B. Abdikamalov, D. Ayzenberg, C. Bambi, T. Dauser, J. A. Garcia, and A. Tripathi, "Testing General Relativity with X-ray reflection spectroscopy: The Konoplya-Rezzolla-Zhidenko parametrization," 3 2019.

[148] C. Cheung, P. Creminelli, A. L. Fitzpatrick, J. Kaplan, and L. Senatore, "The Effective Field Theory of Inflation," *JHEP*, vol. 03, p. 014, 2008.

[149] G. Franciolini, L. Hui, R. Penco, L. Santoni, and E. Trincherini, "Effective Field Theory of Black Hole Quasinormal Modes in Scalar-Tensor Theories," *JHEP*, vol. 02, p. 127, 2019.

[150] L. Hui, A. Podo, L. Santoni, and E. Trincherini, "Effective Field Theory for the perturbations of a slowly rotating black hole," *JHEP*, vol. 12, p. 183, 2021.

[151] W. D. Goldberger and I. Z. Rothstein, "An Effective field theory of gravity for extended objects," *Phys. Rev. D*, vol. 73, p. 104029, 2006.

[152] S. Endlich, V. Gorbenko, J. Huang, and L. Senatore, "An effective formalism for testing extensions to General Relativity with gravitational waves," *JHEP*, vol. 09, p. 122, 2017.

[153] N. Sennett, R. Brito, A. Buonanno, V. Gorbenko, and L. Senatore, "Gravitational-Wave Constraints on an Effective Field-Theory Extension of General Relativity," *Phys. Rev. D*, vol. 102, no. 4, p. 044056, 2020.

[154] R. Cayuso and L. Lehner, "Nonlinear, noniterative treatment of EFT-motivated gravity," *Phys. Rev. D*, vol. 102, no. 8, p. 084008, 2020.

[155] L. Blanchet, "Gravitational Radiation from Post-Newtonian Sources and Inspiralling Compact Binaries," *Living Rev. Rel.*, vol. 17, p. 2, 2014.

[156] I. I. Shapiro, "Fourth Test of General Relativity," *Phys. Rev. Lett.*, vol. 13, pp. 789–791, 1964.

[157] B. Bertotti, L. Iess, and P. Tortora, "A test of general relativity using radio links with the Cassini spacecraft," *Nature*, vol. 425, pp. 374–376, 2003.

[158] U. J. Le Verrier, "Theorie du mouvement de Mercure," *Annales de l'Observatoire de Paris*, vol. 5, p. 1, Jan. 1859.

[159] A. Einstein, "Explanation of the Perihelion Motion of Mercury from the General Theory of Relativity," *Sitzungsber. Preuss. Akad. Wiss. Berlin (Math. Phys.)*, vol. 1915, pp. 831–839, 1915.

[160] R. Abuter *et al.*, "Detection of the Schwarzschild precession in the orbit of the star S2 near the Galactic centre massive black hole," *Astron. Astrophys.*, vol. 636, p. L5, 2020.

[161] K. Nordtvedt, "Equivalence Principle for Massive Bodies. 2. Theory," *Phys. Rev.*, vol. 169, pp. 1017–1025, 1968.

[162] K. Nordtvedt, "Testing relativity with laser ranging to the moon," *Phys. Rev.*, vol. 170, pp. 1186–1187, 1968.

[163] J. Lense and H. Thirring, "Über den Einfluß der Eigenrotation der Zentralkörper auf die Bewegung der Planeten und Monde nach der Einsteinschen Gravitationstheorie," *Physikalische Zeitschrift*, vol. 19, p. 156, Jan. 1918.

[164] H. Thirring, "Über die Wirkung rotierender ferner Massen in der Einsteinschen Gravitationstheorie.," *Physikalische Zeitschrift*, vol. 19, p. 33, Jan. 1918.

[165] J. M. Weisberg and Y. Huang, "Relativistic Measurements from Timing the Binary Pulsar PSR B1913+16," *Astrophys. J.*, vol. 829, no. 1, p. 55, 2016.

[166] L. Shao, N. Sennett, A. Buonanno, M. Kramer, and N. Wex, "Constraining nonperturbative strong-field effects in scalar-tensor gravity by combining pulsar timing and laser-interferometer gravitational-wave detectors," *Phys. Rev. X*, vol. 7, no. 4, p. 041025, 2017.

[167] G. Voisin, I. Cognard, P. C. C. Freire, N. Wex, L. Guillemot, G. Desvignes, M. Kramer, and G. Theureau, "An improved test of the strong equivalence principle with the pulsar in a triple star system," *Astron. Astrophys.*, vol. 638, p. A24, 2020.

[168] A. Buonanno, B. Iyer, E. Ochsner, Y. Pan, and B. S. Sathyaprakash, "Comparison of post-Newtonian templates for compact binary inspiral signals in gravitational-wave detectors," *Phys. Rev. D*, vol. 80, p. 084043, 2009.

[169] E. Barausse, C. Palenzuela, M. Ponce, and L. Lehner, "Neutron-star mergers in scalar-tensor theories of gravity," *Phys. Rev. D*, vol. 87, p. 081506, 2013.

[170] P. Kocherlakota *et al.*, "Constraints on black-hole charges with the 2017 EHT observations of M87*," *Phys. Rev. D*, vol. 103, no. 10, p. 104047, 2021.

[171] S. H. Völkel, R. Konoplya, and K. D. Kokkotas, "Inverse problem for Hawking radiation," *Phys. Rev. D*, vol. 99, no. 10, p. 104025, 2019.

[172] B. Abbott *et al.*, "Gravitational Waves and Gamma-rays from a Binary Neutron Star Merger: GW170817 and GRB 170817A," *Astrophys. J. Lett.*, vol. 848, no. 2, p. L13, 2017.

[173] B. Abbott *et al.*, "GW170817: Observation of Gravitational Waves from a Binary Neutron Star Inspiral," *Phys. Rev. Lett.*, vol. 119, no. 16, p. 161101, 2017.

[174] D. Langlois, R. Saito, D. Yamauchi, and K. Noui, "Scalar-tensor theories and modified gravity in the wake of GW170817," *Phys. Rev. D*, vol. 97, no. 6, p. 061501, 2018.

[175] M. Crisostomi and K. Koyama, "Self-accelerating universe in scalar-tensor theories after GW170817," *Phys. Rev.*, vol. D97, no. 8, p. 084004, 2018.

[176] M. Crisostomi and K. Koyama, "Vainshtein mechanism after GW170817," *Phys. Rev. D*, vol. 97, no. 2, p. 021301, 2018.

[177] A. Dima and F. Vernizzi, "Vainshtein Screening in Scalar-Tensor Theories before and after GW170817: Constraints on Theories beyond Horndeski," *Phys. Rev. D*, vol. 97, no. 10, p. 101302, 2018.

[178] E. Babichev, "Emergence of ghosts in Horndeski theory," *JHEP*, vol. 07, p. 038, 2020.

[179] M. Bezares, L. ter Haar, M. Crisostomi, E. Barausse, and C. Palenzuela, "Kinetic screening in non-linear stellar oscillations and gravitational collapse," 5 2021.

[180] M. Bezares, R. Aguilera-Miret, L. ter Haar, M. Crisostomi, C. Palenzuela, and E. Barausse, "No evidence of kinetic screening in merging binary neutron stars," 7 2021.

[181] A. Vainshtein, "To the problem of nonvanishing gravitation mass," *Phys. Lett. B*, vol. 39, pp. 393–394, 1972.

[182] E. Babichev and C. Deffayet, "An introduction to the Vainshtein mechanism," *Class. Quant. Grav.*, vol. 30, p. 184001, 2013.

[183] J. Khoury and A. Weltman, "Chameleon cosmology," *Phys. Rev. D*, vol. 69, p. 044026, 2004.

[184] K. Hinterbichler and J. Khoury, "Symmetron Fields: Screening Long-Range Forces Through Local Symmetry Restoration," *Phys. Rev. Lett.*, vol. 104, p. 231301, 2010.

[185] L. Bernard, L. Lehner, and R. Luna, "Challenges to global solutions in Horndeski's theory," *Phys. Rev. D*, vol. 100, no. 2, p. 024011, 2019.

[186] M. Bezares, M. Crisostomi, C. Palenzuela, and E. Barausse, "K-dynamics: well-posed initial value 1+1 evolutions in K-essence," 8 2020.

[187] R. Akhoury, D. Garfinkle, and R. Saotome, "Gravitational collapse of k-essence," *JHEP*, vol. 04, p. 096, 2011.

[188] C. D. Leonard, J. Ziprick, G. Kunstatter, and R. B. Mann, "Gravitational collapse of K-essence Matter in Painlevé-Gullstrand coordinates," *JHEP*, vol. 10, p. 028, 2011.

[189] R. Gannouji and Y. R. Baez, "Critical collapse in K-essence models," *JHEP*, vol. 07, p. 132, 2020.

[190] C. P. Burgess and M. Williams, "Who You Gonna Call? Runaway Ghosts, Higher Derivatives and Time-Dependence in EFTs," *JHEP*, vol. 08, p. 074, 2014.

[191] A. Adams, N. Arkani-Hamed, S. Dubovsky, A. Nicolis, and R. Rattazzi, "Causality, analyticity and an IR obstruction to UV completion," *JHEP*, vol. 10, p. 014, 2006.

[192] J. Cayuso, N. Ortiz, and L. Lehner, "Fixing extensions to general relativity in the nonlinear regime," *Physical Review D*, vol. 96, Oct 2017.

[193] G. Allwright and L. Lehner, "Towards the nonlinear regime in extensions to GR: assessing possible options," *Class. Quant. Grav.*, vol. 36, no. 8, p. 084001, 2019.

[194] E. Babichev, "Formation of caustics in k-essence and Horndeski theory," *JHEP*, vol. 04, p. 129, 2016.

[195] E. Babichev and S. Ramazanov, "Caustic free completion of pressureless perfect fluid and k-essence," *JHEP*, vol. 08, p. 040, 2017.

[196] S. Mukohyama and R. Namba, "Partial UV Completion of $P(X)$ from a Curved Field Space," *JCAP*, vol. 02, p. 001, 2021.

[197] H. Friedrich and A. Rendall, "The cauchy problem for the einstein equations," in *Einstein's Field Equations and Their Physical Implications* (B. G. Schmidt, ed.), (Berlin, Heidelberg), pp. 127–223, Springer Berlin Heidelberg, 2000.

[198] O. A. Reula, "Hyperbolic methods for Einstein's equations," *Living Rev. Rel.*, vol. 1, p. 3, 1998.

[199] O. Sarbach and M. Tiglio, "Continuum and Discrete Initial-Boundary-Value Problems and Einstein's Field Equations," *Living Rev. Rel.*, vol. 15, p. 9, 2012.

[200] D. Hilditch, "An Introduction to Well-posedness and Free-evolution," *Int. J. Mod. Phys. A*, vol. 28, p. 1340015, 2013.

[201] Y. Foures-Bruhat, "Theoreme d'existence pour certains systemes derivees partielles non lineaires," *Acta Mat.*, vol. 88, pp. 141–225, 1952.

[202] J. L. Ripley and F. Pretorius, "Hyperbolicity in spherical gravitational collapse in a horndeski theory," *Physical Review D*, vol. 99, Apr 2019.

[203] J. M. Stewart, "Signature change, mixed problems and numerical relativity," *Class. Quant. Grav.*, vol. 18, pp. 4983–4995, 2002.

[204] J. Goldstone, A. Salam, and S. Weinberg, "Broken symmetries," *Phys. Rev.*, vol. 127, pp. 965–970, Aug 1962.

[205] M. Alcubierre, *Introduction to 3+1 numerical relativity*. International series of monographs on physics, Oxford: Oxford Univ. Press, 2008.

[206] L. Lehner. Private communication, October 2021.

[207] C. Bona, T. Ledvinka, and C. Palenzuela, "A 3+1 covariant suite of numerical relativity evolution systems," *Phys. Rev. D*, vol. 66, p. 084013, 2002.

[208] C. Bona, L. Lehner, and C. Palenzuela-Luque, "Geometrically motivated hyperbolic coordinate conditions for numerical relativity: Analysis, issues and implementations," *Phys. Rev. D*, vol. 72, p. 104009, 2005.

[209] D. Alic, C. Bona, C. Bona-Casas, and J. Masso, "Efficient implementation of finite volume methods in Numerical Relativity," *Phys. Rev. D*, vol. 76, p. 104007, 2007.

[210] C. Bona, J. Masso, E. Seidel, and J. Stela, "A New formalism for numerical relativity," *Phys. Rev. Lett.*, vol. 75, pp. 600–603, 1995.

[211] W. R. Inc., "Mathematica, Version 12.2." Champaign, IL, 2020.

[212] A. Bernal, J. Barranco, D. Alic, and C. Palenzuela, "Multi-state Boson Stars," *Phys. Rev.*, vol. D81, p. 044031, 2010.

[213] S. Valdez-Alvarado, C. Palenzuela, D. Alic, and L. A. Ureña-López, "Dynamical evolution of fermion-boson stars," *Physical Review D*, vol. 87, Apr 2013.

[214] G. Raposo, P. Pani, M. Bezares, C. Palenzuela, and V. Cardoso, "Anisotropic stars as ultracompact objects in General Relativity," *Phys. Rev.*, vol. D99, no. 10, p. 104072, 2019.

[215] A. Dima, M. Bezares, and E. Barausse, "Dynamical chameleon neutron stars: Stability, radial oscillations, and scalar radiation in spherical symmetry," *Phys. Rev. D*, vol. 104, p. 084017, Oct 2021.

[216] C. Bona, C. Bona-Casas, and J. Terradas, "Linear high-resolution schemes for hyperbolic conservation laws: TVB numerical evidence," *J. Comput. Phys.*, vol. 228, pp. 2266–2281, 2009.

[217] R. Penrose, "Gravitational collapse: The role of general relativity," *Riv. Nuovo Cim.*, vol. 1, pp. 252–276, 1969.

[218] N. Kaloper, A. Padilla, P. Saffin, and D. Stefanyszyn, "Unitarity and the Vainshtein Mechanism," *Phys. Rev. D*, vol. 91, no. 4, p. 045017, 2015.

[219] H. S. Reall and C. M. Warnick, "Effective field theory and classical equations of motion," 5 2021.

[220] P. Figueras and T. França, "Gravitational Collapse in Cubic Horndeski Theories," *Class. Quant. Grav.*, vol. 37, no. 22, p. 225009, 2020.

[221] P. Figueras and T. França, "Black Hole Binaries in Cubic Horndeski Theories," 12 2021.

[222] K. Clough, T. Helfer, H. Witek, and E. Berti, "The problem with Proca: ghost instabilities in self-interacting vector fields," 4 2022.

[223] Z.-G. Mou and H.-Y. Zhang, "A singularity problem for interacting massive vectors," 4 2022.

[224] A. Coates and F. M. Ramazanoğlu, "The intrinsic pathology of self-interacting vector fields," 5 2022.

[225] K. Aoki and M. Minamitsuji, "Resolving pathology of self-interacting Proca field: a case study of Proca star," 6 2022.

[226] J. L. Ripley and F. Pretorius, "Hyperbolicity in Spherical Gravitational Collapse in a Horndeski Theory," *Phys. Rev.*, vol. D99, no. 8, p. 084014, 2019.

[227] H. S. Reall, N. Tanahashi, and B. Way, "Shock Formation in Lovelock Theories," *Phys. Rev. D*, vol. 91, no. 4, p. 044013, 2015.

[228] N. Tanahashi and S. Ohashi, "Wave propagation and shock formation in the most general scalar–tensor theories," *Class. Quant. Grav.*, vol. 34, no. 21, p. 215003, 2017.

[229] J. Cayuso, N. Ortiz, and L. Lehner, "Fixing extensions to general relativity in the nonlinear regime," *Phys. Rev. D*, vol. 96, no. 8, p. 084043, 2017.

[230] I. Muller, "Zum Paradoxon der Warmeleitungstheorie," *Z. Phys.*, vol. 198, pp. 329–344, 1967.

[231] W. Israel, "Nonstationary irreversible thermodynamics: A Causal relativistic theory," *Annals Phys.*, vol. 100, pp. 310–331, 1976.

[232] W. Israel and J. M. Stewart, "Thermodynamics of nonstationary and transient effects in a relativistic gas," *Physics Letters A*, vol. 58, pp. 213–215, Sept. 1976.

[233] M. Gerhardinger, J. T. Giblin, A. J. Tolley, and M. Trodden, "A Well-Posed UV Completion for Simulating Scalar Galileons," 5 2022.

[234] G. Lara, M. Bezares, and E. Barausse, "UV completions, fixing the equations, and nonlinearities in k-essence," *Phys. Rev. D*, vol. 105, no. 6, p. 064058, 2022.

[235] P. Brax and P. Valageas, "Small-scale Nonlinear Dynamics of K-mouflage Theories," *Phys. Rev.*, vol. D90, no. 12, p. 123521, 2014.

[236] C. M. Will, "The Confrontation between General Relativity and Experiment," *Living Rev. Rel.*, vol. 17, p. 4, 2014.

[237] T. Damour and G. Esposito-Farese, "Tensor multiscalar theories of gravitation," *Class. Quant. Grav.*, vol. 9, pp. 2093–2176, 1992.

[238] T. Damour and G. Esposito-Farese, "Nonperturbative strong field effects in tensor - scalar theories of gravitation," *Phys. Rev. Lett.*, vol. 70, pp. 2220–2223, 1993.

[239] N. Andreou, N. Franchini, G. Ventagli, and T. P. Sotiriou, "Spontaneous scalarization in generalised scalar-tensor theory," *Phys. Rev. D*, vol. 99, no. 12, p. 124022, 2019. [Erratum: Phys.Rev.D 101, 109903 (2020)].

[240] C. Palenzuela, E. Barausse, M. Ponce, and L. Lehner, "Dynamical scalarization of neutron stars in scalar-tensor gravity theories," *Phys. Rev. D*, vol. 89, no. 4, p. 044024, 2014.

[241] R. C. Tolman, "Static solutions of Einstein's field equations for spheres of fluid," *Phys. Rev.*, vol. 55, pp. 364–373, 1939.

[242] A. Lehebel, E. Babichev, and C. Charmousis, "A no-hair theorem for stars in Horndeski theories," *JCAP*, vol. 07, p. 037, 2017.

[243] T. Kobayashi, Y. Watanabe, and D. Yamauchi, "Breaking of Vainshtein screening in scalar-tensor theories beyond Horndeski," *Phys. Rev. D*, vol. 91, no. 6, p. 064013, 2015.

[244] E. Babichev, K. Koyama, D. Langlois, R. Saito, and J. Sakstein, "Relativistic Stars in Beyond Horndeski Theories," *Class. Quant. Grav.*, vol. 33, no. 23, p. 235014, 2016.

[245] M. Crisostomi, M. Lewandowski, and F. Vernizzi, "Vainshtein regime in scalar-tensor gravity: Constraints on degenerate higher-order scalar-tensor theories," *Phys. Rev. D*, vol. 100, no. 2, p. 024025, 2019.

[246] R. K. Jain, C. Kouvaris, and N. G. Nielsen, "White Dwarf Critical Tests for Modified Gravity," *Phys. Rev. Lett.*, vol. 116, no. 15, p. 151103, 2016.

[247] J. Sakstein, "Hydrogen Burning in Low Mass Stars Constrains Scalar-Tensor Theories of Gravity," *Phys. Rev. Lett.*, vol. 115, p. 201101, 2015.

[248] I. D. Saltas, I. Sawicki, and I. Lopes, "White dwarfs and revelations," *JCAP*, vol. 05, p. 028, 2018.

[249] S. Hawking, "Black holes in general relativity," *Commun. Math. Phys.*, vol. 25, pp. 152–166, 1972.

[250] R. Takahashi, "Black hole shadows of charged spinning black holes," *Publ. Astron. Soc. Jap.*, vol. 57, p. 273, 2005.

[251] T. Johannsen and D. Psaltis, "Testing the No-Hair Theorem with Observations in the Electromagnetic Spectrum: II. Black-Hole Images," *Astrophys. J.*, vol. 718, pp. 446–454, 2010.

[252] D. Psaltis and T. Johannsen, "Sgr A*: The Optimal Testbed of Strong-Field Gravity," *J. Phys. Conf. Ser.*, vol. 283, p. 012030, 2011.

[253] L. Amarilla and E. F. Eiroa, "Shadow of a rotating braneworld black hole," *Phys. Rev. D*, vol. 85, p. 064019, 2012.

[254] A. E. Broderick, T. Johannsen, A. Loeb, and D. Psaltis, "Testing the No-Hair Theorem with Event Horizon Telescope Observations of Sagittarius A*," *Astrophys. J.*, vol. 784, p. 7, 2014.

[255] D. Psaltis, F. Ozel, C.-K. Chan, and D. P. Marrone, "A General Relativistic Null Hypothesis Test with Event Horizon Telescope Observations of the black-hole shadow in Sgr A*," *Astrophys. J.*, vol. 814, no. 2, p. 115, 2015.

[256] T. Johannsen, A. E. Broderick, P. M. Plewa, S. Chatzopoulos, S. S. Doeleman, F. Eisenhauer, V. L. Fish, R. Genzel, O. Gerhard, and M. D. Johnson, "Testing General Relativity with the Shadow Size of Sgr A*," *Phys. Rev. Lett.*, vol. 116, no. 3, p. 031101, 2016.

[257] D. Psaltis, N. Wex, and M. Kramer, "A Quantitative Test of the No-Hair Theorem with Sgr A* using stars, pulsars, and the Event Horizon Telescope," *Astrophys. J.*, vol. 818, no. 2, p. 121, 2016.

[258] P. V. P. Cunha, C. A. R. Herdeiro, E. Radu, and H. F. Runarsson, "Shadows of Kerr black holes with scalar hair," *Phys. Rev. Lett.*, vol. 115, no. 21, p. 211102, 2015.

[259] P. V. Cunha, C. A. R. Herdeiro, B. Kleihaus, J. Kunz, and E. Radu, "Shadows of Einstein–dilaton–Gauss–Bonnet black holes," *Phys. Lett. B*, vol. 768, pp. 373–379, 2017.

[260] D. Psaltis, "Testing General Relativity with the Event Horizon Telescope," *Gen. Rel. Grav.*, vol. 51, no. 10, p. 137, 2019.

[261] P. V. Cunha, C. A. Herdeiro, and E. Radu, "Spontaneously Scalarized Kerr Black Holes in Extended Scalar-Tensor–Gauss-Bonnet Gravity," *Phys. Rev. Lett.*, vol. 123, no. 1, p. 011101, 2019.

[262] L. Medeiros, D. Psaltis, and F. Özel, "A Parametric model for the shapes of black-hole shadows in non-Kerr spacetimes," *Astrophys. J.*, vol. 896, no. 1, p. 7, 2020.

[263] D. Psaltis *et al.*, "Gravitational Test beyond the First Post-Newtonian Order with the Shadow of the M87 Black Hole," *Phys. Rev. Lett.*, vol. 125, p. 141104, Oct 2020.

[264] K. Akiyama *et al.*, "First M87 Event Horizon Telescope Results. I. The Shadow of the Supermassive Black Hole," *Astrophys. J.*, vol. 875, no. 1, p. L1, 2019.

[265] K. Akiyama *et al.*, "First M87 Event Horizon Telescope Results. VI. The Shadow and Mass of the Central Black Hole," *Astrophys. J. Lett.*, vol. 875, no. 1, p. L6, 2019.

[266] S. E. Gralla, "Can the EHT M87 results be used to test general relativity?," 10 2020.

[267] P. Kocherlakota *et al.*, "Constraints on black-hole charges with the 2017 EHT observations of M87*," *Phys. Rev. D*, vol. 103, no. 10, p. 104047, 2021.

[268] K. Glampedakis and G. Pappas, "Can supermassive black hole shadows test the Kerr metric?," 2 2021.

[269] S. Nampalliwar and S. Kumar, "Theory-agnostic tests of gravity with black hole shadows," 8 2021.

[270] S. E. Gralla, A. Lupsasca, and D. P. Marrone, "The shape of the black hole photon ring: A precise test of strong-field general relativity," *Phys. Rev. D*, vol. 102, p. 124004, Dec 2020.

[271] A. E. Broderick, P. Tiede, D. W. Pesce, and R. Gold, "Measuring Spin from Relative Photon Ring Sizes," 5 2021.

[272] M. Wielgus, "Photon rings of spherically symmetric black holes and robust tests of non-Kerr metrics," 9 2021.

[273] H. C. D. Lima, Junior., L. C. B. Crispino, P. V. P. Cunha, and C. A. R. Herdeiro, "Can different black holes cast the same shadow?," *Phys. Rev. D*, vol. 103, no. 8, p. 084040, 2021.

[274] F. H. Vincent, M. Wielgus, M. A. Abramowicz, E. Gourgoulhon, J. P. Lasota, T. Paumard, and G. Perrin, "Geometric modeling of M87* as a Kerr black hole or a non-Kerr compact object," *Astron. Astrophys.*, vol. 646, p. A37, 2021.

[275] Y. Mizuno, Z. Younsi, C. M. Fromm, O. Porth, M. De Laurentis, H. Olivares, H. Falcke, M. Kramer, and L. Rezzolla, "The Current Ability to Test Theories of Gravity with Black Hole Shadows," *Nat. Astron.*, vol. 2, no. 7, pp. 585–590, 2018.

[276] L. R. Weih, H. Olivares, and L. Rezzolla, "Two-moment scheme for general-relativistic radiation hydrodynamics: a systematic description and new applications," *Mon. Not. Roy. Astron. Soc.*, vol. 495, no. 2, pp. 2285–2304, 2020.

[277] A. E. Broderick, T. Johannsen, A. Loeb, and D. Psaltis, "Testing the no-hair theorem with event horizon telescope observations of sagittarius a*," *The Astrophysical Journal*, vol. 784, p. 7, Feb 2014.

[278] J. C. Algaba *et al.*, "Broadband Multi-wavelength Properties of M87 during the 2017 Event Horizon Telescope Campaign," *Astrophys. J. Lett.*, vol. 911, no. 1, p. L11, 2021.

[279] J. L. Walsh, A. J. Barth, L. C. Ho, and M. Sarzi, "The M87 Black Hole Mass from Gas-dynamical Models of Space Telescope Imaging Spectrograph Observations," *Astrophys. J.*, vol. 770, p. 86, 2013.

[280] K. Gebhardt, J. Adams, D. Richstone, T. R. Lauer, S. M. Faber, K. Gültekin, J. Murphy, and S. Tremaine, "The Black Hole Mass in M87 from Gemini/NIFS Adaptive Optics Observations," , vol. 729, p. 119, Mar. 2011.

[281] *Black holes (Les astres occlus)*, vol. 23 of *Les Houches Summer School*, (New York, NY), Gordon and Breach, Jan. 1973.

[282] B. Jeter and A. E. Broderick, "Reconciling EHT and Gas Dynamics Measurements in M87: Is the Jet Misaligned at Parsec Scales?," *Astrophys. J.*, vol. 908, no. 2, p. 139, 2021.

[283] G. B. Rybicki and A. P. Lightman, *Radiative Processes in Astrophysics*. 1986.

[284] A. E. Broderick, V. L. Fish, S. S. Doeleman, and A. Loeb, "Evidence for Low Black Hole Spin and Physically Motivated Accretion Models from Millimeter VLBI Observations of Sagittarius A*," *Astrophys. J.*, vol. 735, p. 110, 2011.

[285] Z. Younsi, K. Wu, and S. V. Fuerst, "General relativistic radiative transfer: formulation and emission from structured tori around black holes," *Astronomy & Astrophysics*, vol. 545, p. A13, Aug 2012.

[286] T. Bronzwaer, J. Davelaar, Z. Younsi, M. Mościbrodzka, H. Falcke, M. Kramer, and L. Rezzolla, "RAPTOR I: Time-dependent radiative transfer in arbitrary spacetimes," *Astron. Astrophys.*, vol. 613, p. A2, 2018.

[287] S. E. Gralla, D. E. Holz, and R. M. Wald, "Black Hole Shadows, Photon Rings, and Lensing Rings," *Phys. Rev. D*, vol. 100, no. 2, p. 024018, 2019.

[288] S. E. Gralla, "Second Order Gravitational Self Force," *Phys. Rev. D*, vol. 85, p. 124011, 2012.

[289] W. H. Press, S. A. Teukolsky, W. T. Vetterling, and B. P. Flannery, *Numerical Recipes in C (2nd Ed.): The Art of Scientific Computing*. USA: Cambridge University Press, 1992.

[290] M. Pieroni and E. Barausse, "Foreground cleaning and template-free stochastic background extraction for LISA," *JCAP*, vol. 07, p. 021, 2020. [Erratum: JCAP 09, E01 (2020)].

[291] H. O. Silva, J. Sakstein, L. Gualtieri, T. P. Sotiriou, and E. Berti, "Spontaneous scalarization of black holes and compact stars from a Gauss-Bonnet coupling," *Phys. Rev. Lett.*, vol. 120, no. 13, p. 131104, 2018.

[292] C. L. Rodriguez, B. Farr, V. Raymond, W. M. Farr, T. B. Littenberg, D. Fazi, and V. Kalogera, "Basic Parameter Estimation of Binary Neutron Star Systems by the Advanced LIGO/Virgo Network," *Astrophys. J.*, vol. 784, p. 119, 2014.

[293] M. D. Johnson, A. Lupsasca, A. Strominger, G. N. Wong, S. Hadar, D. Kapec, R. Narayan, A. Chael, C. F. Gammie, P. Galison, and et al., "Universal interferometric signatures of a black hole's photon ring," *Science Advances*, vol. 6, p. eaaz1310, Mar 2020.

[294] D. Garfinkle, G. T. Horowitz, and A. Strominger, "Charged black holes in string theory," *Phys. Rev. D*, vol. 43, p. 3140, 1991. [Erratum: Phys.Rev.D 45, 3888 (1992)].

[295] G. Gibbons and K.-i. Maeda, "Black Holes and Membranes in Higher Dimensional Theories with Dilaton Fields," *Nucl. Phys. B*, vol. 298, pp. 741–775, 1988.

[296] B. Carter, "Axisymmetric Black Hole Has Only Two Degrees of Freedom," *Phys. Rev. Lett.*, vol. 26, pp. 331–333, 1971.

[297] A. E. Broderick *et al.*, "THEMIS: A Parameter Estimation Framework for the Event Horizon Telescope," *Astrophys. J.*, vol. 897, no. 2, p. 139, 2020.

[298] T. Jacobson, "When is g tt g rr = 1?," *Classical and Quantum Gravity*, vol. 24, p. 5717–5719, Nov 2007.

[299] V. Ferrari and B. Mashhoon, "New approach to the quasinormal modes of a black hole," *Phys. Rev. D*, vol. 30, pp. 295–304, Jul 1984.

[300] H. Yang, D. A. Nichols, F. Zhang, A. Zimmerman, Z. Zhang, and Y. Chen, "Quasinormal-mode spectrum of Kerr black holes and its geometric interpretation," *Phys. Rev. D*, vol. 86, p. 104006, 2012.

[301] K. D. Kokkotas and B. G. Schmidt, "Quasinormal modes of stars and black holes," *Living Rev. Rel.*, vol. 2, p. 2, 1999.

[302] H.-P. Nollert, "Quasinormal modes: the characteristic `sound' of black holes and neutron stars," *Classical and Quantum Gravity*, vol. 16, pp. R159–R216, nov 1999.

[303] E. Berti, V. Cardoso, and A. O. Starinets, "Quasinormal modes of black holes and black branes," *Classical and Quantum Gravity*, vol. 26, p. 163001, jul 2009.

[304] S. Chandrasekhar, *The mathematical theory of black holes*. 1985.

[305] K. Glampedakis, A. D. Johnson, and D. Kennefick, "Darboux transformation in black hole perturbation theory," *Phys. Rev. D*, vol. 96, no. 2, p. 024036, 2017.

[306] S. H. Völkel and K. D. Kokkotas, "Scalar Fields and Parametrized Spherically Symmetric Black Holes: Can one hear the shape of space-time?," *Phys. Rev.*, vol. D100, no. 4, p. 044026, 2019.

[307] C. M. Bender and S. A. Orszag, *Advanced Mathematical Methods for Scientists and Engineers*. New York: McGraw-Hill, 1978.

[308] M. W. Cole and R. H. Good, "Determination of the shape of a potential barrier from the tunneling transmission coefficient," *Phys. Rev. A*, vol. 18, pp. 1085–1088, 1978.

[309] J. C. Lazenby and D. J. Griffiths, "CLASSICAL INVERSE SCATTERING IN ONE-DIMENSION," *Am. J. Phys.*, vol. 48, pp. 432–436, 1980.

[310] S. C. Gandhi and C. J. Efthimiou, "Inversion of gamow's formula and inverse scattering," *American Journal of Physics*, vol. 74, no. 7, pp. 638–643, 2006.

[311] K. S. Stelle, "Classical Gravity with Higher Derivatives," *Gen. Rel. Grav.*, vol. 9, pp. 353–371, 1978.

[312] A. Salvio, "Quadratic Gravity," *Front. in Phys.*, vol. 6, p. 77, 2018.

[313] K. Stelle, "Renormalization of Higher Derivative Quantum Gravity," *Phys. Rev. D*, vol. 16, pp. 953–969, 1977.

[314] E. Fradkin and A. A. Tseytlin, "Renormalizable asymptotically free quantum theory of gravity," *Nucl. Phys. B*, vol. 201, pp. 469–491, 1982.

[315] A. O. Barvinsky, D. Blas, M. Herrero-Valea, S. M. Sibiryakov, and C. F. Steinwachs, "Renormalization of gauge theories in the background-field approach," *JHEP*, vol. 07, p. 035, 2018.

[316] H. Lu, A. Perkins, C. Pope, and K. Stelle, "Black Holes in Higher-Derivative Gravity," *Phys. Rev. Lett.*, vol. 114, no. 17, p. 171601, 2015.

[317] W. Nelson, "Static Solutions for 4th order gravity," *Phys. Rev. D*, vol. 82, p. 104026, 2010.

[318] W. Donnelly and T. Jacobson, "Hamiltonian structure of Horava gravity," *Phys. Rev. D*, vol. 84, p. 104019, 2011.

[319] D. Orlando and S. Reffert, "On the Renormalizability of Horava-Lifshitz-type Gravities," *Class. Quant. Grav.*, vol. 26, p. 155021, 2009.

[320] G. Giribet, D. L. Nacir, and F. D. Mazzitelli, "Counterterms in semiclassical Horava-Lifshitz gravity," *JHEP*, vol. 09, p. 009, 2010.

[321] G. D'Odorico, F. Saueressig, and M. Schutten, "Asymptotic Freedom in Hořava-Lifshitz Gravity," *Phys. Rev. Lett.*, vol. 113, no. 17, p. 171101, 2014.

[322] J. Bellorín and B. Droguett, "Quantization of the non-projectable $2+1D$ Horava theory: The second-class constraints," 12 2019.

[323] A. O. Barvinsky, D. Blas, M. Herrero-Valea, S. M. Sibiryakov, and C. F. Steinwachs, "Hořava Gravity is Asymptotically Free in 2 + 1 Dimensions," *Phys. Rev. Lett.*, vol. 119, no. 21, p. 211301, 2017.

[324] A. O. Barvinsky, M. Herrero-Valea, and S. M. Sibiryakov, "Towards the renormalization group flow of Horava gravity in $(3+1)$ dimensions," *Phys. Rev. D*, vol. 100, no. 2, p. 026012, 2019.

[325] T. Jacobson and D. Mattingly, "Einstein-Aether waves," *Phys. Rev. D*, vol. 70, p. 024003, 2004.

[326] T. Jacobson, "Undoing the twist: The Hořava limit of Einstein-aether theory," *Phys. Rev. D*, vol. 89, p. 081501, 2014.

[327] E. Barausse, T. Jacobson, and T. P. Sotiriou, "Black holes in Einstein-aether and Horava-Lifshitz gravity," *Phys. Rev.*, vol. D83, p. 124043, 2011.

[328] E. Barausse and T. P. Sotiriou, "Slowly rotating black holes in Horava-Lifshitz gravity," *Phys. Rev.*, vol. D87, p. 087504, 2013.

[329] E. Barausse and T. P. Sotiriou, "Black holes in Lorentz-violating gravity theories," *Class. Quant. Grav.*, vol. 30, p. 244010, 2013.

[330] O. Ramos and E. Barausse, "Constraints on Hořava gravity from binary black hole observations," *Phys. Rev.*, vol. D99, no. 2, p. 024034, 2019.

[331] M. Herrero-Valea, S. Liberati, and R. Santos-Garcia, "Hawking Radiation from Universal Horizons," 12 2020.

[332] P. Berglund, J. Bhattacharyya, and D. Mattingly, "Mechanics of universal horizons," *Phys. Rev. D*, vol. 85, p. 124019, 2012.

[333] P. Berglund, J. Bhattacharyya, and D. Mattingly, "Towards Thermodynamics of Universal Horizons in Einstein-æther Theory," *Phys. Rev. Lett.*, vol. 110, no. 7, p. 071301, 2013.

[334] M. Banados, C. Teitelboim, and J. Zanelli, "The Black hole in three-dimensional space-time," *Phys. Rev. Lett.*, vol. 69, pp. 1849–1851, 1992.

[335] T. Jacobson, "Initial value constraints with tensor matter," *Class. Quant. Grav.*, vol. 28, p. 245011, 2011.

[336] A. B. Nielsen and M. Visser, "Production and decay of evolving horizons," *Class. Quant. Grav.*, vol. 23, pp. 4637–4658, 2006.

[337] R. Penrose, "Gravitational Collapse and Space-Time Singularities," , vol. 14, pp. 57–59, Jan. 1965.

[338] J. Chojnacki and J. H. Kwapisz, "Finite action principle and horava-lifshitz gravity: early universe, black holes and wormholes," 2021.

[339] K. Izumi and S. Mukohyama, "Stellar center is dynamical in Horava-Lifshitz gravity," *Phys. Rev. D*, vol. 81, p. 044008, 2010.

[340] S. Mukohyama, "Horava-Lifshitz Cosmology: A Review," *Class. Quant. Grav.*, vol. 27, p. 223101, 2010.

[341] G. W. Gibbons and S. W. Hawking, "Action Integrals and Partition Functions in Quantum Gravity," *Phys. Rev. D*, vol. 15, pp. 2752–2756, 1977.

[342] J. W. York, Jr., "Role of conformal three geometry in the dynamics of gravitation," *Phys. Rev. Lett.*, vol. 28, pp. 1082–1085, 1972.

[343] D. Garfinkle, C. Eling, and T. Jacobson, "Numerical simulations of gravitational collapse in Einstein-aether theory," *Phys. Rev. D*, vol. 76, p. 024003, 2007.

[344] J. Bhattacharyya, A. Coates, M. Colombo, and T. P. Sotiriou, "Evolution and spherical collapse in Einstein-Æther theory and Hořava gravity," *Phys. Rev. D*, vol. 93, no. 6, p. 064056, 2016.

[345] M. Saravani, N. Afshordi, and R. B. Mann, "Dynamical Emergence of Universal Horizons during the formation of Black Holes," *Phys. Rev. D*, vol. 89, no. 8, p. 084029, 2014.

[346] R. Akhoury, D. Garfinkle, and N. Gupta, "White holes in Einstein-aether theory," *Class. Quant. Grav.*, vol. 35, no. 3, p. 035006, 2018.

[347] J. L. Ripley, "Numerical relativity for Horndeski gravity," 7 2022.

[348] P. Kocherlakota and L. Rezzolla, "Distinguishing gravitational and emission physics in black hole imaging: spherical symmetry," *Mon. Not. Roy. Astron. Soc.*, vol. 513, no. 1, pp. 1229–1243, 2022.

[349] A. M. Bauer, A. Cárdenas-Avendaño, C. F. Gammie, and N. Yunes, "Spherical Accretion in Alternative Theories of Gravity," *Astrophys. J.*, vol. 925, no. 2, p. 119, 2022.

[350] Z. Younsi, D. Psaltis, and F. Özel, "Black Hole Images as Tests of General Relativity: Effects of Spacetime Geometry," 11 2021.

[351] F. Ozel, D. Psaltis, and Z. Younsi, "Black Hole Images as Tests of General Relativity: Effects of Plasma Physics," 11 2021.

[352] C. Bona, T. Ledvinka, C. Palenzuela, and M. Zacek, "General covariant evolution formalism for numerical relativity," *Phys. Rev. D*, vol. 67, p. 104005, 2003.

[353] C. Bona, T. Ledvinka, C. Palenzuela, and M. Zacek, "A Symmetry breaking mechanism for the Z4 general covariant evolution system," *Phys. Rev. D*, vol. 69, p. 064036, 2004.

[354] D. Alic, *Theoretical issues in Numerical Relativity simulations*. PhD thesis, Universitat de les Illes Balears. Departament de Física, 2009.

[355] S. Frittelli, "Note on the propagation of the constraints in standard 3+1 general relativity," *Phys. Rev. D*, vol. 55, pp. 5992–5996, May 1997.